New Metal Chelators for Chelation Therapy in Neurodegenerative Diseases

by MAHMOUD EL SAFADI

Thesis submitted in fulfilment of the requirements for
the degree of

Doctor of Philosophy

under the supervision of
Associate Professor ANDREW MCDONAGH
Dr TRISTAN RAWLING

University of Technology Sydney
School of Mathematical and Physical Sciences

March 2021

CERTIFICATE OF ORIGINAL AUTHORSHIP

I, *Mahmoud El Safadi* declare that this thesis, is submitted in fulfilment of the requirements for the award of *Doctor of Philosophy*, in the *School of Mathematical and Physical Sciences* at the University of Technology Sydney.

This thesis is wholly my own work unless otherwise referenced or acknowledged. In addition, I certify that all information sources and literature used are indicated in the thesis.

This document has not been submitted for qualifications at any other academic institution.

This research is supported by an Australian Government Research Training Program.

Signature: Production Note:
Signature removed prior to publication.

Date: 05.03.2021

ACKNOWLEDGEMENT

In the year of this thesis, 2020, the world experienced a life-threatening situation due to the Covid-19 pandemic leading governments to implement extreme measures such as quarantines and lockdowns. I have faced many difficulties in the last year of my PhD journey. I sincerely thank all the people mentioned below for their exceptional efforts and support during this unpredictable time.

Firstly, I would like to thank Associated Professor Andrew McDonagh for the continuing support of my PhD and related research, for his patience, inspiration and huge knowledge. His guidance helped me throughout my research and writing this thesis. I could not have imagined a better PhD research advisor and mentor.

Also, I would like to thank my Co-supervisor Dr Tristan Rawling, for his informative feedback and motivation, as well as for the hard question that led me to extend my study from different perspectives.

I would also like to thank Dr Ronald Shimmon, who gave access to the laboratory and research facilities. Without his precious encouragement, this work would not be possible.

I take this opportunity to express my deepest gratitude to Dr. Adam Southon, for his support and valuable discussions in the cell culture biological study.

I want to thank the University of Technology Sydney for allowing following my passion for chemistry research and give me access to the facilities I needed to finish my PhD.

A special thanks to my family. Words cannot express how grateful I am to my mother Mouminah Taha, and father Nasser El Safadi for all of the sacrifices that you have made on my behalf. Your prayer for me was what sustained me thus far. I would also like to thank all of my friends, especially Susan Shimmon, who incented me to strive towards my goal.

In the end, I would like to express appreciation to my beloved wife Hanan El Wardani who spent sleepless nights with and was always my support in the moments when there was no one to answer my queries.

Contents

List of Figures

List of Schemes

List of tables

List of Abbreviations

Å: Angstrom

δ: Chemical Shift (NMR)

λ: Wavelength

ν_{max}: Maximum absorbance

$[M]^+$: Molecular ion

$[M+H]^+$: Protonated molecular ion

8-HQ: 8-Hydroxyquinoline

Aβ: Amyloid-beta

AD: Alzheimer's disease

ADMET: Absorption, Distribution, Metabolism, Excretion, and Toxicity

AICD: APP intracellular domain

ALA: Alanine

AMPA: 2- amino- 3- (3-hydroxy 5-methyl- isoxazol-4-yl propanoic acid

APP: Amyloid precursor protein

ASP: Aspartic acid

ATP: Adenosine triphosphate

BBB: Blood-brain barrier

BCA: Bicinchoninic acid assay

BSA: Bovine Serum Albumin

$CDCl_3$: Deuterated chloroform

CNS: Central nervous system

COX17: Cytochrome oxidase coper chaperone

CQ: Clioquinol

CTR1: Copper transport protein

Cyclam: 1,4,8,11-Tetraazacyclotetradecane or 14 ane- N4

Cyclen: 1, 4, 7, 10-tetrazacyclododecane or 12 ane- N4

d: Doublet (NMR)

dd: Doublet of doublets (NMR)

DA: Dopamine

DAT: Dopamine transporter

DFP: Deferiprone

DPPH: 2,2-diphenyl-1-picrylhydrazyl

DMSO: Dimethyl sulfoxide

DNA: Deoxyribonucleic acid

FTIR: Fourier transform infrared spectroscopy

GABA: Gamma-amino butyric acid

GC: Gas chromatography

GLU: Glutamic acid

HIS: Histidine

HRMS: High resolution mass spectroscopy

Hz: Hertz

IC50: The half maximal inhibitory concentration

ITC: Isothermal titration colorimetry

J: Coupling constant (NMR)

M: Multiplet (NMR)

m/z: Mass to charge ratio

MAO: Monoamine oxidase inhibitory

mg: Milligrams

mL: Millilitre

mmol: Millimole

MLCT: Metal ligand charge transfer

MS: Mass spectroscopy

MTF: Membrane- bound transferrin

MTT: Microculture Tetrazolium Assay

NMDA: N-Methyl-D-aspartic acid

NMR: Nuclear magnetic resonance

NTBI: Non transferrin-bound iron

ORTEP: Oak Ridge Thermal Ellipsoid Plot Program

PBS: Phosphate-buffered saline

PD: Parkinson's Disease

PEAs: Phenylethylamines

PSA: Polar surface area

q: quartet (NMR)

Q-TOF: Quadrupole Time-of-Flight

R_f: Retention factor

RNA: Ribonucleic acid

ROS: Reactive oxygen species

SERT: Serotonin transporter

SFN: Small fibre neuropathy

s: Singlet (NMR)

SOD: Superoxide dismutase

SN: Substantia nigra

TETA: Triethylenetetramine

TF-Fe^{3+}: Iron-bound transferrin

TLC: Thin layer chromatography

Tyr: Tyrosinase

UV: Ultraviolet

Publications from This Thesis

M. E Safadi, M. Bhadbhade, R. Shimmon, A. T. Baker, A. M. McDonagh.

Cyclen-based chelators for the inhibition of Aβ aggregation: Synthesis, antioxidant and aggregation evaluation.

Inorganica Chimica Acta, 467**, 2017** 343-350. https://doi.org/10.1016/j.ica.2017.07.060.

ABSTRACT

In this thesis, a series of four new metal chelating compounds (**MS1-4**) based on the cyclen macrocycle that bear pendant arms to modify the molecules' properties are evaluated as candidate drugs for Alzheimer's disease. These compounds have been designed to bind to the misregulated metals associated with Alzheimer's disease. The corresponding Cu^{2+}, Zn^{2+} and Ni^{2+} complexes were synthesized and characterized to examine the ability of the chelators to bind to the metal centres. $A\beta_{40}$ de-aggregation by the cyclen compounds was assessed using turbidometry, and the re-solubilization of $A\beta_{40}$ was also examined. The results show that the cyclen compounds have the ability to effectively chelate Cu^{2+} and Zn^{2+} metal ions and de-aggregate $A\beta_{40}$ that has been aggregated due to the presence of these ions. The antioxidant properties of the cyclen compounds were tested using the DPPH scavenging assay, and the results show that some of the compounds can decrease oxidative stress especially MS1 with IC_{50} equals to 71 µM. Molecular modelling studies revealed the behaviour of the cyclen compounds within the E2 domain of APP and its interaction with Cu and Zn. Pharmacokinetics parameters were also promising for the compounds. Overall, these compounds exhibit promising properties as candidates for the treatment of Alzheimer's disease.

A study of drug candidates for Parkinson's disease investigated a series of new iron chelating compounds based on deferiprone and 8-hydroxyquinoline that have amphetamine-like structures. This work addresses a significant problem in Parkinson's disease research, the issue of targeted delivery of chelating compounds into dopaminergic cells where iron may accumulate. The corresponding Fe^{2+} complexes were synthesised and characterised to examine the ability of the chelators to bind to metal centres. Thermodynamic parameters between the chelators and iron were calculated by using Isothermal titration calorimetry.

The results show that 8-hydroxyquinoline-based compounds are more potent chelators than deferiprone-based compounds. N27 dopaminergic cell culture study was conducted to investigate whether the chelators can be transported within cells to prevent dopaminergic cell death caused by iron toxicity. The 8-hydroxyquinoline-based compounds showed the most promising results to rescue dopaminergic cells from iron-induced stress. The antioxidant properties of the compounds were tested using the DPPH scavenging assay, and the results show that 8-hydroxyquinoline-based compounds were superior in decreasing oxidative stress compared to the deferiprone-based compounds. Overall, 8-hydroxyquinoline-based compounds showed favourable properties as candidates for future Parkinson's disease research.

Chapter 1

Alzheimer's Disease and Parkinson's Disease

Chapter 1: Alzheimer's Disease and Parkinson's Disease

1.1. Introduction

Neurodegenerative diseases are a group of disabling chronic disorders characterised by progressive and selective neuronal loss in the central or peripheral nervous system. Serious age-related neurodegenerative disorders including Alzheimer's disease (AD) and Parkinson's disease (PD) contribute to dementia, a leading cause of illness worldwide, and a significant public health challenge with spiralling healthcare costs.

Metal dyshomeostasis and the accumulation of metals (Cu, Zn and Fe) are common features in many neurodegenerative diseases, including Alzheimer's and Parkinson's Diseases.

AD can cause severe dementia. It is marked by extracellular deposition of Aβ peptides in the form of senile plaques and intracellular aggregation of a binding protein (tau) as brain tangles. Misregulated zinc and copper ions can cause senile plaque to develop by interacting with neurons containing Aβ and contribute to oxidative stress.

Parkinson's disease (PD) is a progressive neurodegenerative disease with severe dopamine neuron degeneration in the substantia nigra. Iron accumulation associated with the DA neuron damage, oxidative stress in the SN, and the highest PD-like motor deficits.

Many studies indicate that abnormal metal homeostasis is an important pathogenic factor in these neurodegenerative diseases. Several studies have explored the potential of chelating agents capable of trapping redox-active metals. An effective chelating agent in AD and PD care must have low molecular weight, chelation selectivity, prevent depletion of other metal ions, and be able to tear off pathogen protein metal ions.

1.1.1. Significance of the project

This thesis addresses two major neurodegenerative diseases, AD and PD, with a view to investigate some new metal chelators that may have therapeutic effects. Macrocyclic compounds can reduce copper ions levels in the brain (Pavuluru and Luo, 2019). At the same time, 8-hydroxyquinoline can bind to Zn and Cu ions that are attached to Aβ and decrease the associated toxicity (Moret *et al*., 2006, Cherny *et al*., 2001). 8-Hydroxy quinoline has hydrophobic and antioxidant character and readily crosses the blood-brain barrier (BBB) (Cherny *et al*., 2001). Thus, binding quinoline moieties to cyclen units may assist in chelating Cu and Zn and reduce the oxidative stress that is caused by these misregulated metals. Here, new multifunctional compounds targeted at AD are explored that can cross the BBB, de-aggregate plaques, and reduce oxidative stress in the brain.
In the case of Parkinson's disease, deferiprone and 8-hydroxyquinoline have high selectivity towards iron (Mounsey and Teismann, 2012) but are not targeted to the brain (nor the appropriate region of the brain).

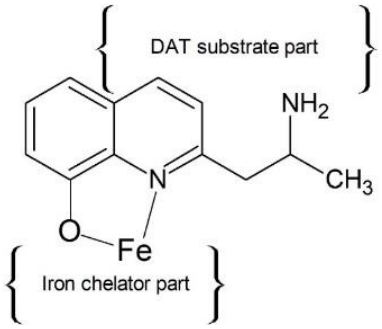

Figure 1: Example of a multifunctional compound examined in this work complexed to iron.

To address this problem, a novel idea that utilises 8-hydroxyquinoline or deferiprone-based chelators targeted to the SN using an amphetamine-like DAT substrate was developed (Figure 1). It is hypothesized that the amphetamine-like chelators bind to DAT and can be

transferred to dopaminergic cells, the target cells of the current work. The iron-chelating moieties (8-hydroxyquinoline or deferiprone) may then chelate iron in the N27 dopaminergic cells, providing therapeutic benefit.

1.1.2. Project aims

As shown above, the use of chelating compounds to address neurodegenerative diseases is attracting significant attention. Some of the mechanisms that underpin the role of metals in diseases such as AD and PD have started to become to be understood. This opens a pathway to trial new chelating compounds that may work to alleviate some of the effects, or slow the progress of these diseases. The aims of this work fall broadly into two areas. First, this work will investigate new metal chelators to bind metal ions associated with AD. Second, a new strategy to employ amphetamine-like chelators will be explored. It is important to note that the scope of this work will not extend into any *in-vivo* models.

Therefore, the specific aims of this thesis are:

- To synthesise and characterise cyclen-based chelators with appropriate redox properties and lipophilicity to reduce oxidative stress and bind specific metal ions.
- To synthesise and characterise the Cu, Zn and Ni complexes of the new cyclen chelators
- To model the ability of the cyclen-based compounds to pass the BBB as well as their interactions with metals and Aβ
- To measure the ability of the compounds to de-aggregate Aβ proteins *in-vitro*
- To measure the antioxidant activity of the cyclen-based compounds

and

- To synthesise and characterise new iron chelators that possess amphetamine-like structures
- To synthesise and characterise complexes between the chelators and iron

- To examine the chelation affinity of the new chelators via ITC and UV-Vis
- To assess the ability of the new chelators to protect N27 dopaminergic cells against iron-mediated degeneration

1.2. Alzheimer's disease

Alzheimer's disease (AD) was first described by Alois Alzheimer in 1901 after meeting a 51-year-old patient who had progressive memory loss, cognitive decline and impeded movement (Goedert and Spillantini, 2006). Post mortem examination of the brain revealed the existence of senile plaques and neurofibrillary tangles (Goedert and Spillantini, 2006, Agnihotri and Aruoma, 2020). Senile plaques are extracellular deposits of Aβ (a collection of peptides), whereas neurofibrillary tangles are composed of defective tau filaments that are joined together inside neurons to form a tangle (Wippold *et al*., 2008)

Senile plaque is formed by the interaction of misregulated metal ions and the Aβ protein. This interaction can catalyse the production of reactive oxygen species (ROS) that induce oxidative stress in the brain (Guilloreau *et al*., 2007). The Aβ aggregation, the metal-amyloid interaction, the toxicity of the misregulated metal ions and ROS together play an essential role in the progression of AD (Masters *et al*., 2006).

There is currently a significant amount of research aimed at uncovering how plaques are formed, aggregated, accumulated, and cleared from the body. The metal-Aβ interaction is important as this plays a role in developing and increasing plaques. Concept drugs have been developed that can prevent the linkage between metals and the Aβ protein or cleave the bond between them. In this regard, metal chelation has been found to be an important and useful method to decrease oxidative stress and the prevalence of Aβ protein (Rodríguez-Rodríguez *et al*., 2009, Wichur *et al*., 2020, Yang *et al*., 2020).

1.2.1. *Hypotheses relating to AD pathogenesis*

There are three main hypotheses regarding the factors contributing to Alzheimer's disease that are relevant to this project: the Aβ hypothesis, the metal ion hypothesis, and the oxidative stress hypothesis (Kepp, 2012, Cristóvão *et al*., 2020, Tabner *et al*., 2011)

The amyloid hypothesis

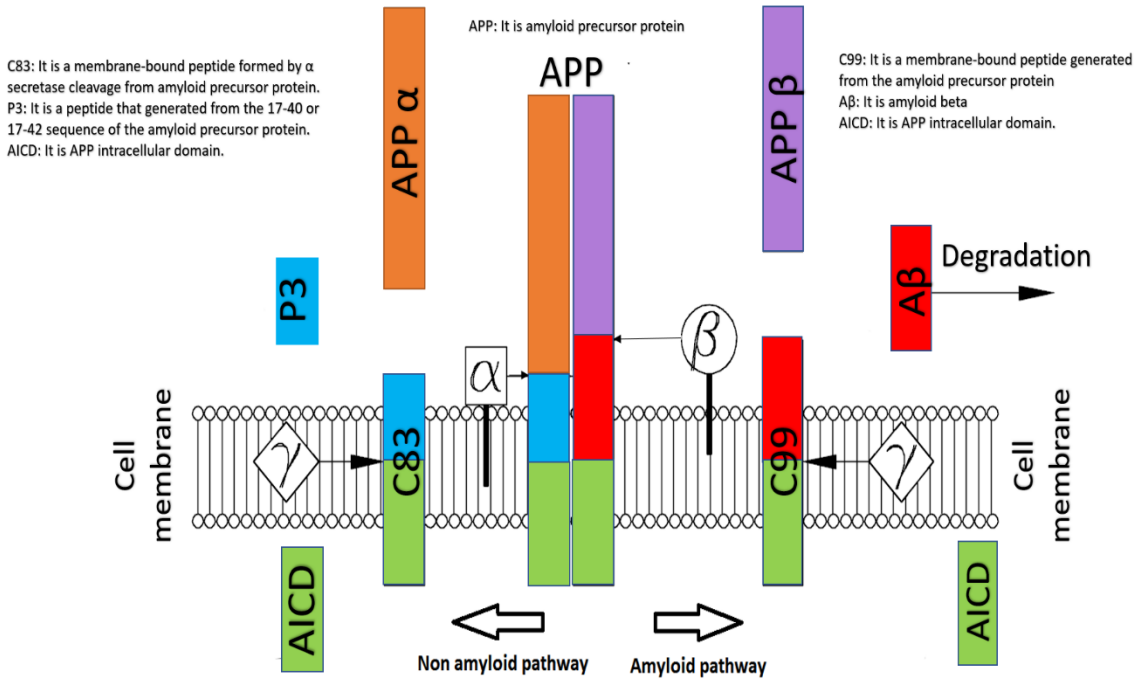

Figure 2: Amyloid precursor protein cleavage

Normally Aβ peptides are derived from amyloid precursor protein (APP) (Rodríguez-Rodríguez *et al*., 2009, Watt *et al*., 2010). APP is located in the cell membrane and consists of an N-extracellular terminal, a short C-intracellular terminal, a single hydrophobic transmembrane domain and a metal-binding site (Bush *et al*., 1994), and there are two methods for APP cleavage (Figure 2). The first of these is the non-amyloidogenic pathway, in which α-secretase convert APP to soluble APP*α* and the membrane-bound C83, which is turn cleaved into p3 and AICD protein by *γ*-secretase (Watt *et al*., 2010, Chow *et al*., 2010).

The second is the amyloidogenic pathway, which starts when β-secretase cleaves APP to APPβ and C99 terminal. γ-Secretase cleaves C99 to Aβ, which is normally degraded by zinc metalloproteases (NEP, IDE) (Chow *et al*., 2010, Watt *et al*., 2010, Singh *et al*., 2013), after which LRP1 escorts the Aβ degradation products out of the brain (Singh *et al*., 2013).

When CNS levels of copper reach more than 0.4 mM, Aβ regulation is impaired. The increased concentration of metal ions encourages the Aβ peptide to adhere to itself and resist proteolytic digestion by zinc metalloproteases. The accumulated Aβ can then further aggregate in the presence of Cu and Zn to form plaques (Guilloreau *et al*., 2007, Bush *et al*., 1994).

The metal ion hypothesis.

The metal ion hypothesis asserts that metal ions, in particular copper and zinc, are a significant factor responsible for the aggregation of Aβ through a metal-protein binding process that leads to the formation of cytotoxic plaques that cause neuronal cell death (Brewer, 2011, Singh *et al*., 2013). Although metal ions play a vital role in the brain and other organs (Osredkar and Sustar, 2011), excess amounts of metals caused by aging factors can lead to metal disruption. Aβ aggregation in the brain occurs by a complexation process which increases the number of senile plaques and tangles, and subsequent AD symptoms (Watt *et al*., 2010).

Roles of copper and zinc in healthy brains.

Copper plays five vital roles in brain cells. It binds with CTR1 membrane transporter protein which allows the copper to enter the cell. Copper's roles are to (i) bind with COX17 protein that helps the copper to reach the mitochondria where it cooperates with cytochrome c oxidase to produce energy for the cell, (ii) link with copper/ZnSOD enzyme that is

responsible for transforming free radicals into hydrogen peroxide, (iii) unite with ATOX1 protein to move the copper to the endoplasmic reticulum and Golgi apparatus that is loaded for transportation between neurons, (iv) bind to the MTF protein to make the RNA synthesis for intracellular signalling. Excess copper binds to ATP7a and ATP7b in which it passes outside the membrane for an extracellular role (white, 2014, Scheiber *et al*., 2014).

Normally, metals are supplied from daily nutrients and are not stored in the body. Metal levels are regulated to avoid increases or decreases in the brain via the metal homeostasis system, which uses specific transporters (Zheng and Monnot, 2012). These transporters are divided into two families. One group is responsible for transporting metals to the cells (after ingestion) to help the cell perform its functions by binding to a specific protein, for example, binding to copper/ZnSOD protein to breaks the free radicals (Smith *et al*., 2006, Zhang *et al*., 2008). The other transports are glutamatergic neurotransmitter which binds the metals from the presynaptic vesicle to the postsynaptic one. These metals are responsible for learning, cognition, and memory functions (Tyszka-Czochara *et al*., 2014).

Low levels of the metal lead to an increase of the free radicals inside the cell (absence of radical controls) and consequently to cell death, whereas a high level of metal in the brain leads to disturbing the receptors and that prevents them from doing their job correctly and causes neurotoxicity. Therefore, the transporters are essential to balance the levels of metals in the brain via the metal homeostasis system (Zhang *et al*., 2008).

Copper and zinc in the Alzheimer's brain:

After the formation of Aβ by the cleavage of APP through the amyloidogenic pathway, the Aβ is cleared from the brain via LRP1 protein. This process protects the brain from Aβ aggregation (Singh *et al*., 2013). However, copper and zinc species are one of the main

factors that increase the progression of AD by preventing the clearance of the Aβ protein in the brain by trapping them within the BBB to form plaques (Kepp, 2012, Brewer, 2011).

Copper and zinc may be ingested from drinking water carried in old pipes and from food like nuts, red meat, fruits, vegetables and shellfish. After a time, these metals may accumulate in the brain capillaries and the BBB (Netzer, 2013). These accumulated metal ions may reduce the level of LRP1 that is responsible for clearing the Aβ. At the same time, the accumulated free copper and zinc stimulates the production of extracellular Aβ by binding the active site of α-secretase in APP, contributes to its aggregation and formation of insoluble plaques (Singh *et al*., 2013).

Inside the brain cell, metal homeostasis is disrupted because the copper and zinc that are released from the cell may be trapped by the extracellular Aβ that is accumulated outside the cell (Bourassa and Miller, 2012).

Studies of zinc and copper complexes with the Aβ protein show that copper coordinates Aβ through four coordinating bonds: two imidazole nitrogens from His-6 and His 13/14, one N-terminal amine nitrogen from Asp-1, and carbonyl oxygen from Ala-2. Sometimes there is a fifth bond from the oxygen of Asp1 (Figure 3C) (Kepp, 2012). Other studies have reported that copper binds Aβ via Tyr-10 instead of Ala-2 (Figure 3A) (Curtain *et al*., 2001), whereas zinc coordinates the Aβ via His-13, His-14, His-6 and Glu-11 (Kepp, 2012).

After the metal binds Aβ forming a monomeric compound, the aggregation of Aβ starts by creating a new coordination bond between imidazole ring of His6 with the other copper atom from the other copper-Aβ complex to form a dimer compound (Figure 3 B) (Curtain *et al*., 2001). The bioavailability of copper and zinc inside the cell starts to reduce due to extracellular metal-Aβ interaction which leads to decrease the metal-protein cellular activity

(mitochondrial protein, Golgi protein and other cellular proteins), then oxidative stress is obtained (Rossi *et al*., 2004).

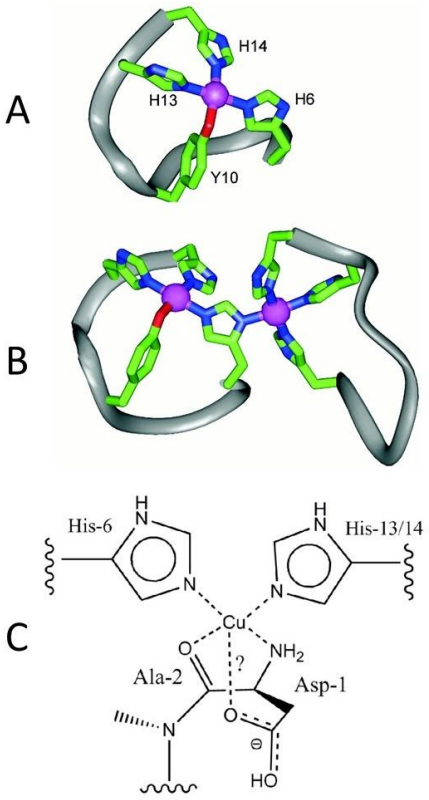

Figure 3: Models of the coordination site(s) of copper bound to Aβ (Kepp, 2012, Curtain et al., 2001).

The oxidative stress hypothesis:

The oxidative stress hypothesis states that mitochondrial dysfunction is the primary reason for oxidative stress in the brain (Bhat *et al*., 2015). After the spread of free metal ions in the brain and reducing the cellular metal-protein interaction, the oxidative balance is disturbed by increasing the level of reactive oxygen species beyond the antioxidant defences. This oxidative disruption forms advanced glycation end products, nitration and lipid peroxidation products. These products are responsible for the mitochondrial dysfunction, apoptosis and

then cell death (Tramutola *et al*., 2017, Rossi *et al*., 2004, Markesbery, 1997, Chauhan and Chauhan, 2006).

It is important to note that each of the three hypotheses discussed above are not entirely unrelated to each other. Some of the important relationships between the Alzheimer's disease hypotheses are shown in Figure 4. For example, ROS in the oxidative stress hypothesis stimulate β secretase to form Aβ via the amyloid pathway and is responsible for metal dyshomeostasis. However, each of these hypotheses leads to cell death and cognitive decline.

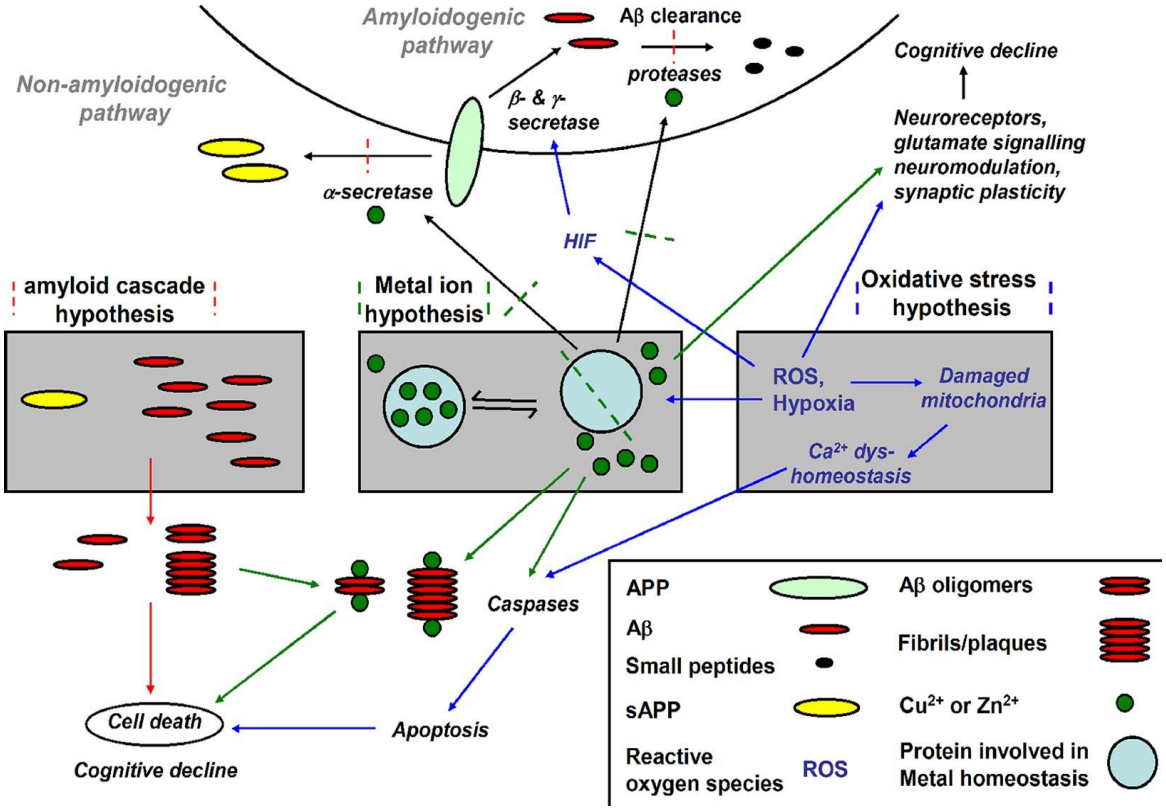

Figure 4: An overview of three hypotheses of factors relating to Alzheimer's disease (Kepp, 2012).

1.2.2. Therapeutic chemical compounds for AD

Antioxidants:

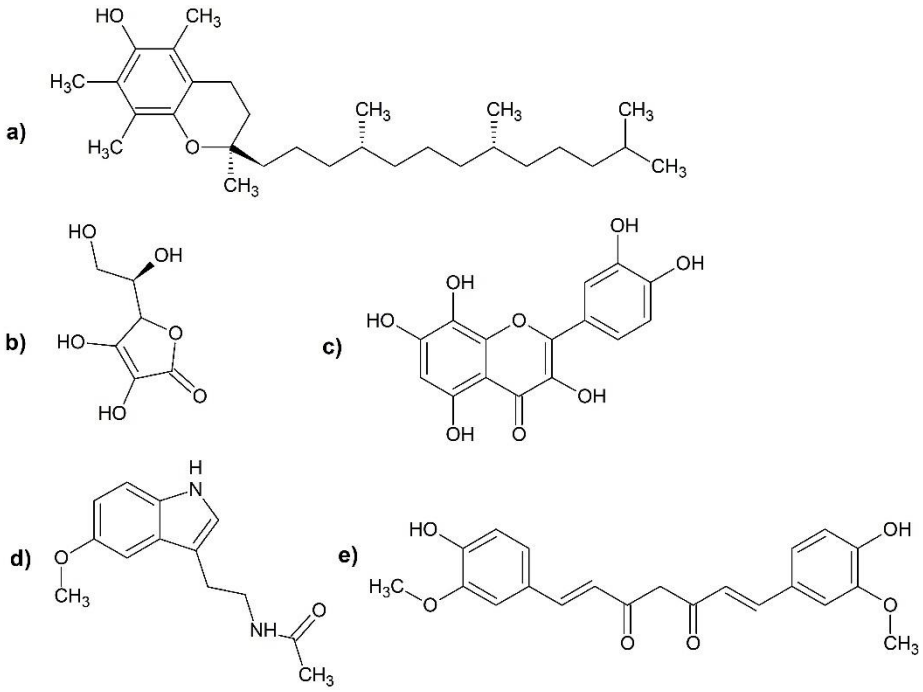

Figure 5: The molecular structures of some common antioxidant compounds.

Antioxidants help protect the brain against AD by reducing oxidative stress (Zandi *et al*., 2004). For example, vitamin E (α-tocopherol) (Figure 5 a) and vitamin C (ascorbic acid) (Figure 5 b) may have a positive effect on AD (Morris *et al*., 1998). The neuroprotective role of ascorbic acid is not only based on free-radical trapping but also on the suppression of pro-inflammatory genes, mitigating neuroinflammation, the chelation of iron, copper, and zinc, and on the reduction of Aβ (Monacelli *et al*., 2017). Similarly, Gossypin (3,3',4',5,7,8-hexahydroxyflavone 8-glu-coside) (Figure 5 c) was shown to reduce oxidative stress however it weakens the neurotoxicity made by Aβ (25-35), and it reduces lipid peroxidation originated by Fe^{2+} (Yoon *et al*., 2004). Melatonin (Figure5 d) is a good anti-oxidative stress agent and is a major secretory product of the pineal gland (but maybe liberated from other organs as well). Melatonin plays a vital role against the Aβ lesion in the brain and can be

effective against free radicals (hydroxyl radicals, peroxynitrite anions and peroxy radicals) (Zatta *et al*., 2003). Curcumin ((1E, 6E) 1, 7-bis (4-hydroxy-3-methoxyphenyl)-1, 6 heptadiene-3, 5 dione) (Figure 5 e) targets many diseases such as cellular oxidative stress. This antioxidant compound may interfere with antioxidant enzymes such as superoxide dismutase, catalase, and glutathione peroxidase and it is served as a Michael acceptor by reacting with glutathione and thioredoxin that reduces intracellular GCH in the cells (Shishodia *et al*., 2005).

Metal chelating compounds:

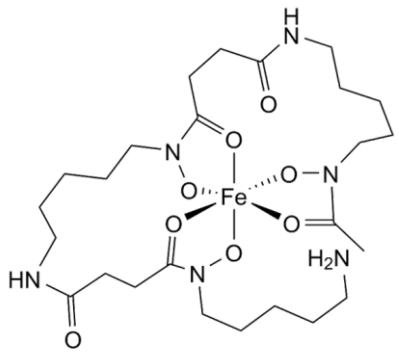

Figure 6: Desferrioxamine-iron complex.

Another type of therapy involves chelating unregulated metal ions. This chelation process reduces the aggregation of Aβ the initiation of oxidative stress (Sampson *et al*., 2014). Desferrioxamine (N'-[5-(acetyl-hydroxy-amino) pentyl]-N [5-[3-(5-aminoopentyl hydroxycarbamoy 10 propanoylamino] pentyl]-N-hydroxy-butane diamide) contains three hydroxamic acid groups from inside, and a free amino group, which has a basic character. This ligand has a high affinity towards free iron (Figure 6) as well as copper and zinc, with which it forms stable complexes that slow down the development of Alzheimer's disease (Smith *et al*., 2007, Keberle, 1964).

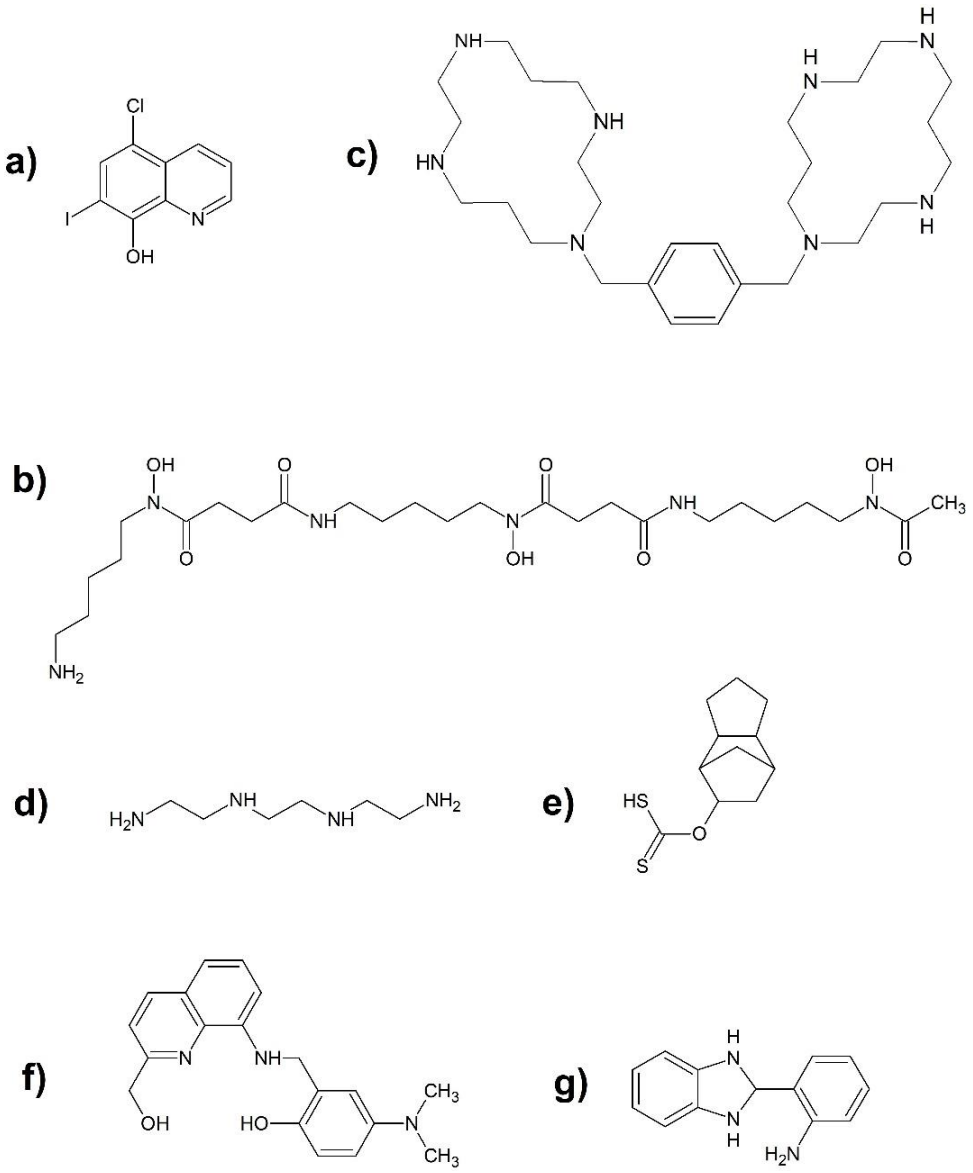

Figure 7: The molecular structures of some metal-binding compounds

Saturated macrocyclic polyamines (Figure 7c) can target many diseases such as HIV (Rusconi *et al*., 2004), inflammatory diseases (Alzheimer's disease) and cancer (De Clercq, 2003, Moret *et al*., 2006). Macrocyclic compounds have the ability to reduce copper levels in the brain and maintain the homeostatic activity in the blood by metal-ligand chelation process (Figure 8) (Moret *et al*., 2006). TETA (triethylenetetramine) (Figure 7d) is used in the treatment of metal disorders such as Wilson's disease, but this compound is highly hydrophilic which inhibit it passing through BBB of the brain (Cherny *et al*., 2001).

Tricyclodecan-9-yl-xanthogenate (Figure 7e) protects the brain against Aβ peptide and reduces oxidative stress (reactive oxygen species, protein oxidation and lipid peroxidation) and thus is a useful therapy for AD (Perluigi *et al*., 2006).

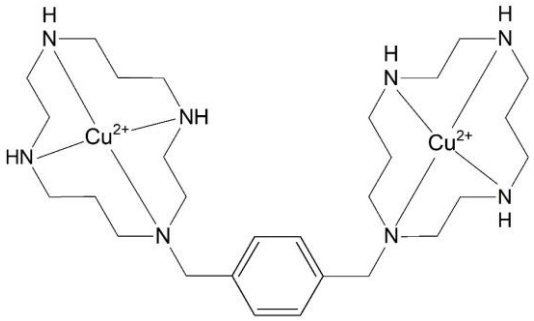

Figure 8: Cu (1,1'-Xylyl bis-1,4,8,11-tetraaza cyclotetradecane).

Clioquinol (5-chloro-7-iodo-8-hydroxyquinoline) (Figure 7a) has a hydrophobic character and readily crosses the BBB. Thus, clioquinol can bind to zinc and copper that are attached to Aβ and decrease the toxicity of the Aβ. On the other hand, clioquinol-copper complexes (Figure 9) can increase the level of biological copper in the brain and has been shown to redistribute copper (Moret *et al*., 2006, Cherny *et al*., 2001).

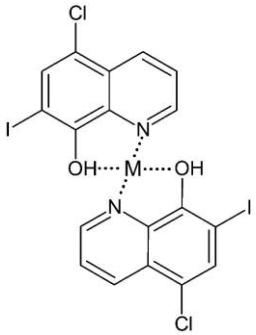

Figure 9: Structure of a metal (M) clioquinol complex.

The multifunctional ligand 4-(dimethylamino)-2-(((2-(hydroxymethyl) quinolin-8-yl)-amino) -methyl) phenol (Figure 7 f) plays a vital role as a metal chelator, Aβ inhibitor, and ROS formation controller, as well as its potential to cross BBB (Lee *et al*., 2014). Another example

of a multifunctional drug is 2-(2,3-dihydro-1H-benzimidazol-2-yl)aniline (Figure 7g) that has a good affinity towards Aβ, readily crosses the BBB and has a good chelation affinity towards copper and zinc (a tetrahedral geometry) through the nitrogen electron donor atom. In addition, the presence of the NH group pendant arm provides it with antioxidant property.

Multifunctional metal-binding ligands:

Multifunctional ligand metal-chelators play a significant role in targeting AD lesions. The multifunctionality arises from properties such as good metal-ligand chelation, low molecular weight, low toxicity and a lipophilic nature to cross BBB. Investigations into these ligands are still in progress, and there are many examples on derivatives of multifunctional ligands: 1,10-phenanthroline, macrocyclic polyamine, carbonyl oxalamide, tetrahydrosalen (Figure 10) (Rodríguez-Rodríguez *et al*., 2012).

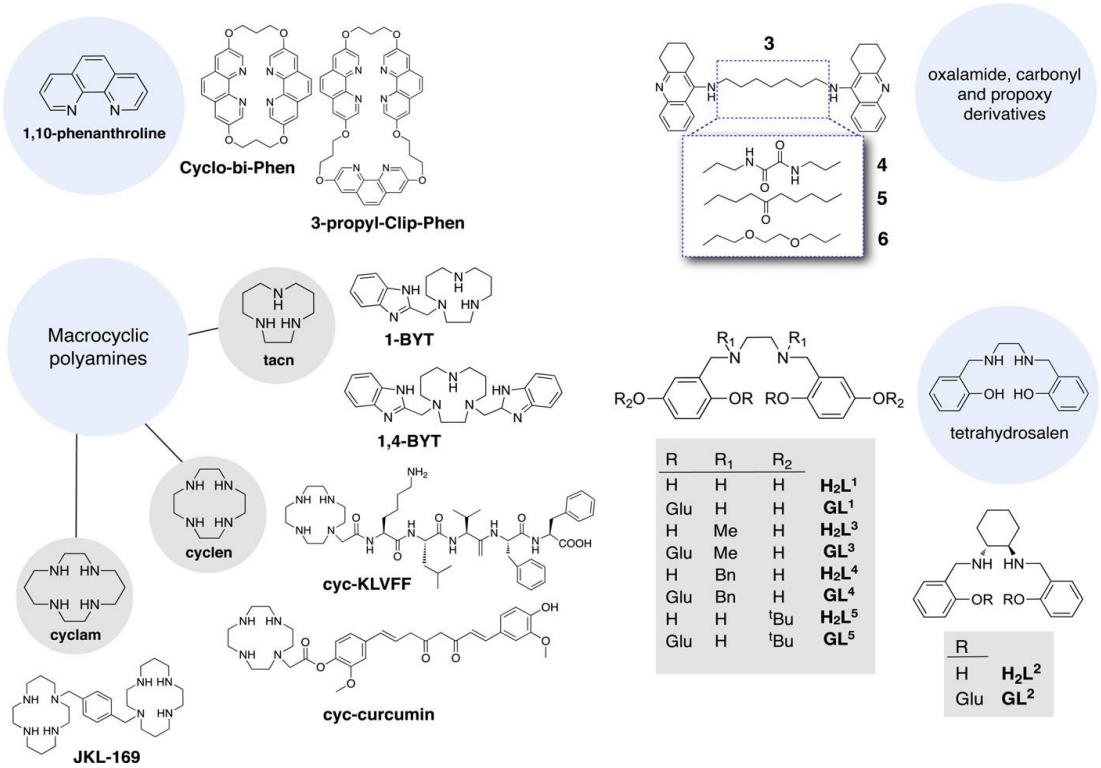

Figure 10: Multifunctional metal-binding ligands (Rodríguez-Rodríguez et al., 2012).

1.2.3. Coordination chemistry of macrocyclic polyamine derivatives:

Saturated macrocyclic polyamines have been studied since the 1960s and may be used as ligands to chelate transition metals. Polyamine macrocycles form stable complexes through coordination of the basic nitrogen atoms (Kimura, 1992). The stability of the transition metal complexes is affected by the size of the chelating rings, complex conformers, and macrocyclic pendant arms.

Size of the chelating rings:

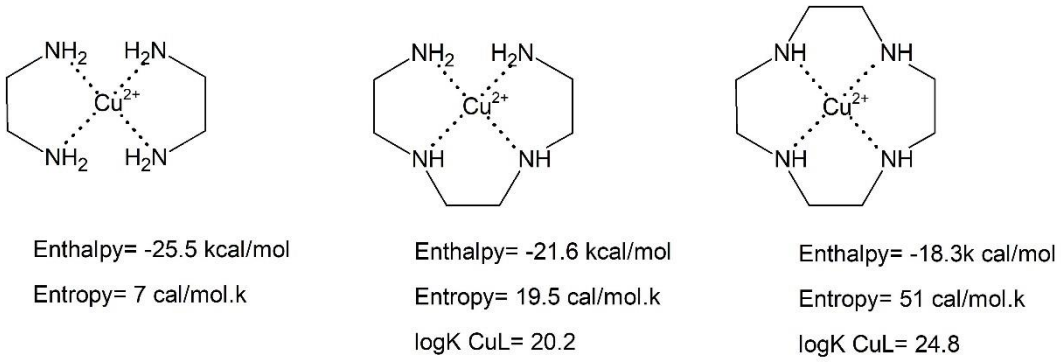

Figure 11: Stability data for some copper(II) complexes.

Generally, as the number of chelating rings increases, the complex stability increases. When the number of chelating rings increases, the entropy increases, and so log K for the complex increases (Figure 11) (Kimura, 1992, Hancock and Martell, 1989). The selectivity of metals changes according to macrocycle cavity size. The "ligand design" rule states: "The increase of chelate ring size from five-membered to six-membered ring will favour ligand selectivity for small over large metal ions" (Hancock *et al*., 1996, Hancock and Martell, 1989) (Figure 12). By changing the ligand from cyclen (compound **1** in Figure 12) to cyclam (compound **2** in Figure 12), with a large metal, the stability of the ligand will decrease, and *vice versa*. So upon changing from **1** to **2**, $\Delta\log k_1$ for the complex decreases with increase of the metal size

so that the stability of the larger metal complex increases with the small macrocyclic cavity (Hancock and Martell, 1989).

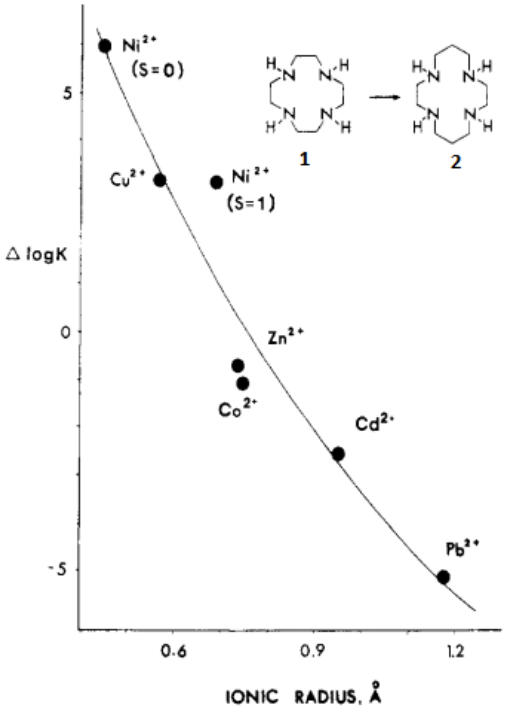

Figure 12: Plot showing ΔlogK vs ionic radius for several metal ions (Hancock and Martell, 1989).

Cyclen complex conformers:

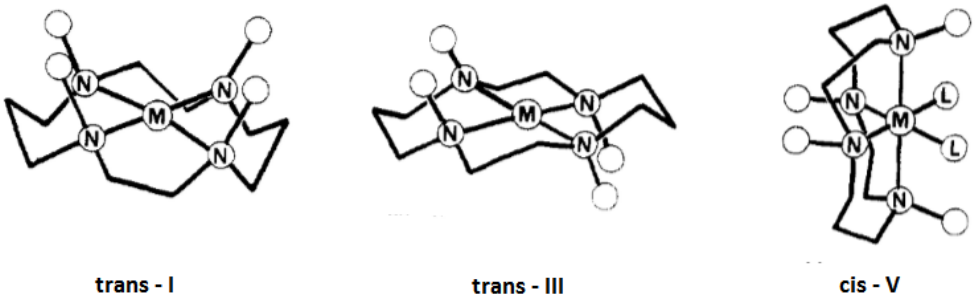

Figure 13: Conformers of cyclen complexes (Hancock et al., 1996).

The flexibility of the large macrocycle cavity allows it to bind to a range of metals of different sizes. Three main conformers of the cyclen molecules have been identified: trans-I, trans-III and cis-V (Figure 13)(Hancock and Martell, 1989). Computational studies have

shown that these ligands change their conformer according to the size of the metal. Figure 14 shows that the trans-I conformation has a lower energy than that of trans-III regardless of the metal size or the M-N bond length. Thus trans-I, in which the metal is pushed out of the plane, is the only conformer that occurs in the case of M (cyclen) (DeSimone *et al.*, 1980). In the case of M (cyclen) (Figure 14), there are regions in which different conformers are dominant. If M-N bond lengths lie between 1.96 and 2.17 Å, the trans-III the dominant conformer. If the M-N bond length is less than 1.96 or greater than 2.17 Å, the trans-I conformer is dominant (Hancock, 1990).

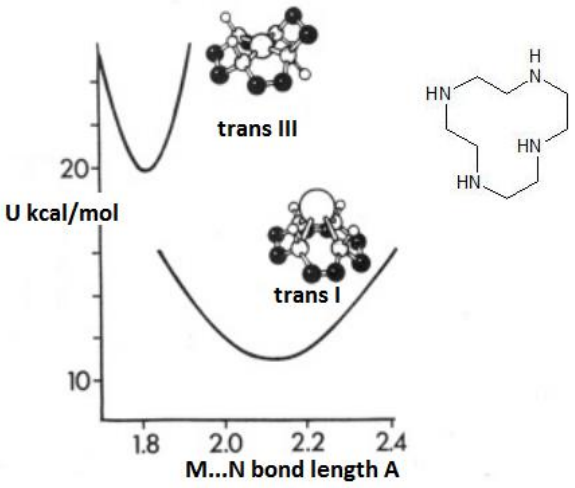

Figure 14: Strain energy, U, of the trans-I and trans-III conformers of M (cyclen) as function of final energy minimized M-N bond length (Hancock et al., 1996).

Macrocycles with pendant arms

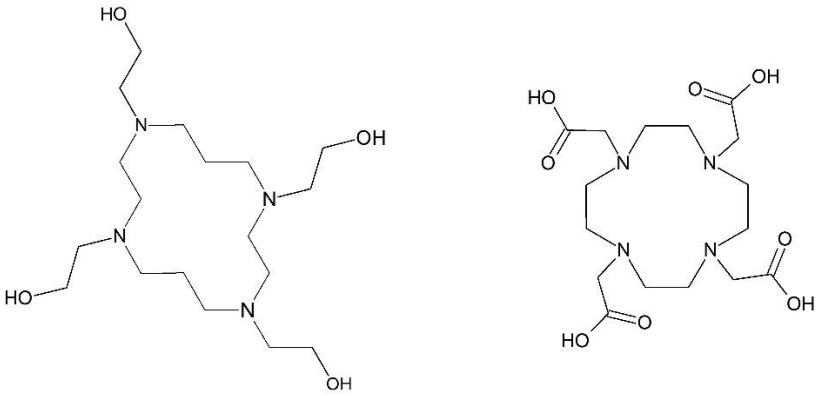

Figure 15: Macrocycles with pendant arms.

Macrocycles with pendant donor groups have been examined to tune the selectivity of the ligands. Oxygen-containing pendant arms including, for example, hydroxyethyl groups (Figure 15) decrease the complex stability with small metal ions and increase complex stability with large metals such as Pb^{2+} (Hancock *et al*., 1996). Figure 16 shows how the addition of neutral oxygen donor groups (N-hydroxyethyl groups) to the macrocycle affects complex stability for a range of metals (Hancock and Martell, 1989).

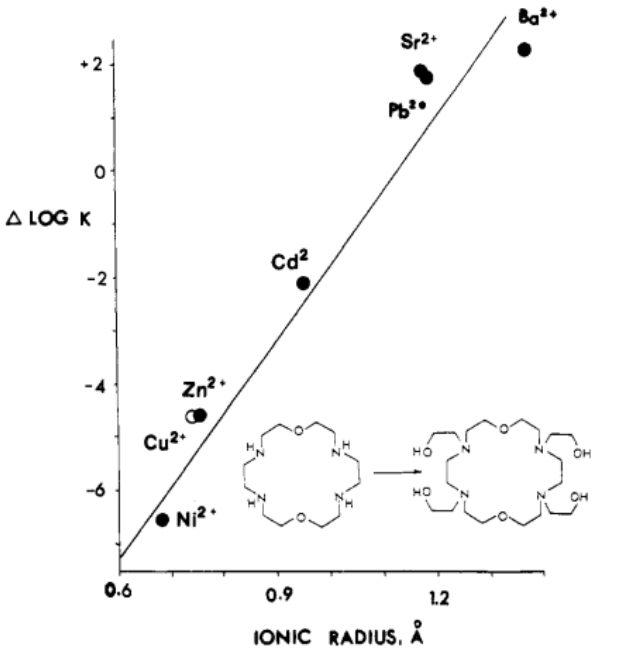

Figure 16: The stability of complexes of 18-aneN_2O_4 (Hancock and Martell, 1989).

1.3. Parkinson's disease

Parkinson's disease (PD) was first described by James Parkinson in 1817 (Khandhar and Marks, 2007). It is the second most common neurodegenerative disease after Alzheimer's disease (De Lau and Breteler, 2006). It affects 1-2 per 1000 of the population (Tysnes and Storstein, 2017) and 1% of the population of age 60 years and above (Tysnes and Storstein, 2017).

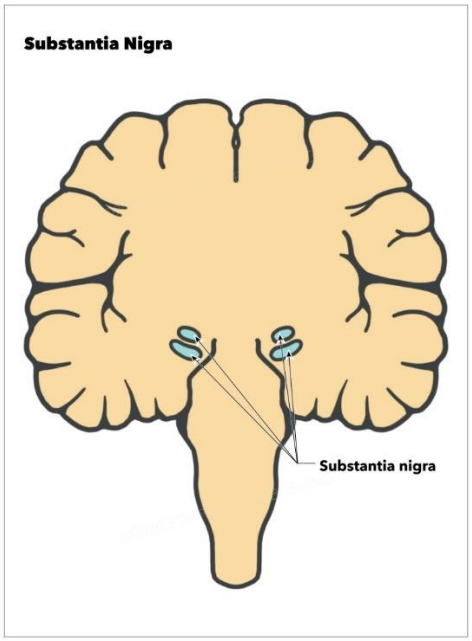

Figure 17: Diagram to the human brain showing the location of the Substantia Nigra (Sonne and Beato, 2018).

PD involves dopaminergic neuron death in the Substantia Nigra (Tysnes and Storstein) (Figure 17) (Trist *et al*., 2019). Symptoms of Parkinson's disease appear when the level of dopaminergic neurons reduces to 70-80% of their original amount (Mounsey and Teismann, 2012). Dopamine belongs to catecholamine and phenethylamine families and plays many essential roles in mammals. Dopamine is a neurotransmitter that sends signals from the body to the brain. Inside the brain, dopamine plays important roles in executive functions,

motor control, motivation, arousal, reinforcement, and reward, as well as lower-level functions including lactation, sexual gratification, and nausea. Dopamine 's right balance is important for both physical and mental wellbeing (Alam *et al*., 2020)

PD is a combination of many factors, including aggregation of a toxic protein, inflammation, changes in iron homoeostasis and oxidative stress (Mounsey and Teismann, 2012).

In the central nervous system (CNS), iron together with specific proteins is involved in essential processes such as myelin production, oxygen transportation, synthesis of neurotransmitters, mitochondrial respiration and oxidative phosphorylation (Ward *et al*., 2014). The biological function of iron relies on its redox potential, which allows reversible transitions between the ferrous (Fe^{2+}) and the ferric (Fe^{3+}) states, thereby catalysing electron transfer reactions (Belaidi and Bush, 2016). Iron is essential inside the CNS, but iron can be toxic and lead to neurodegeneration oxidative stress in the case of iron overload, and neurodegeneration hypomyelination in the case of iron deficiency (Mounsey and Teismann, 2012) (Belaidi and Bush, 2016). Cellular iron is complexed inside metalloproteins that permit electron-transfer responses and decrease ROS, which can cause DNA and protein damage, lipid peroxidation, and cellular death as observed in neurodegenerative illnesses (Belaidi and Bush, 2016).

1.3.1. The role of iron in PD

Iron in healthy cells.

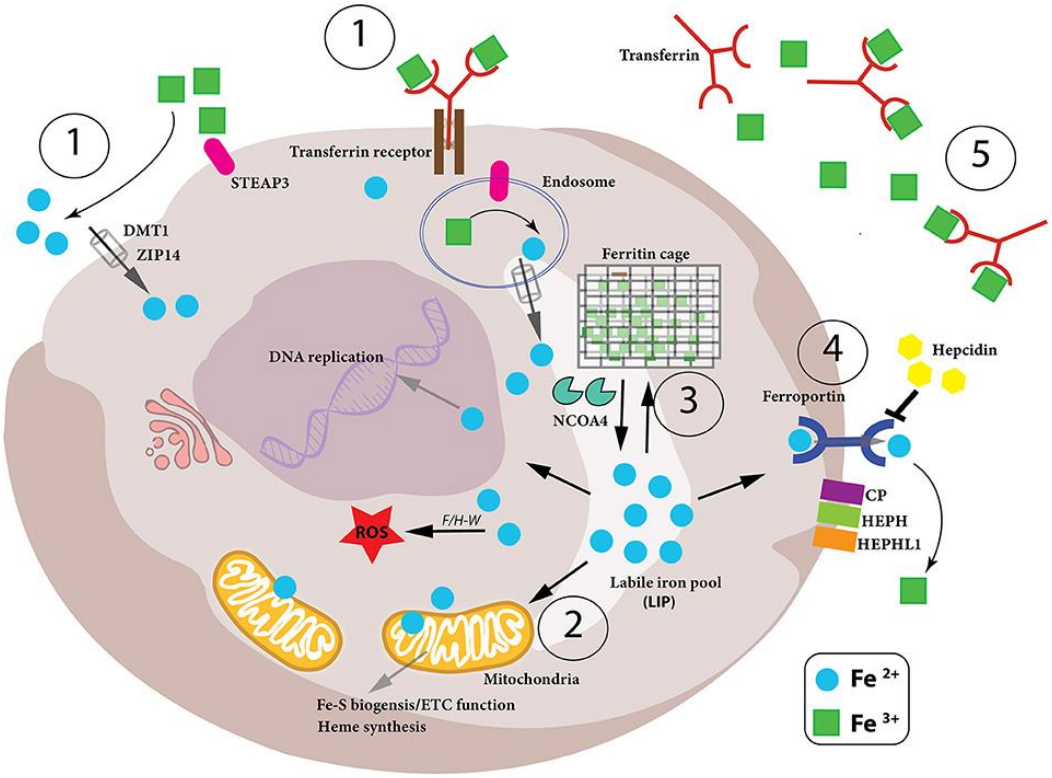

Figure 18: The role of iron in healthy cells (Cronin et al., 2019).

The levels of intracellular iron are strictly regulated because too little or too much can affect the cell's health. Therefore, (1) iron absorption, (2) use, (3) storage and (4) export (Cronin *et al*., 2019) (Figure 18) must be handled in a coordinated manner, as well as the conversion of iron oxidation states (Fe^{2+} and Fe^{3+}) in the cell. (1) Iron-bound transferrin (TF-Fe^{3+}) and non-transferrin-bound iron (NTBI) imported into cell by iron transporters (DMT1 and ZIP14) (McKie *et al*., 2001). STEAP3 is a ferrireductase, reducing Fe^{3+} to Fe^{2+} (Maines, 1988), which can then be imported. (2) Once within the cell, bioavailable and more soluble Fe^{2+} is used for various biological processes – DNA replication, ROS development by Fenton / Haber-Weiss (F / H-W) chemistry, mitochondrial bioenergetics, Fe-S and heme biosynthesis, as well as plenty of proteins that use the metal to perform their functions (Yanatori *et al*., 2016). (3)

Fe^{2+} ion is dangerous because of its role in ROS development. Therefore, it needs to be stored while being readily available for use. This is accomplished by a specific ferritin protein arrangement called the "ferritin cage," which stores the more inert, insoluble Ferric ion. When intracellular levels are small, NCOA4 signals this ferritin cage for degradation, releasing the stored iron. (4) When intracellular iron levels are depleted, iron must be removed from the cell. The iron exporter ferroportin (FPN) does this when the Fe^{2+} ion is oxidised to Fe^{3+} (via CP, HEPH, HEPHL). (5) Eventually, Fe^{3+} is then bound to pass (Tf-Fe^{3+}) and begins circulation again (Muckenthaler *et al*., 2017). Notably, hepcidin is a liver-controlled iron hormone. When systemic iron levels are high in the blood, hepcidin is released and contributes to cell FPN degradation preventing cellular iron release into the blood. Conversely, when blood iron levels are low, hepcidin expression is reduced. (Cronin *et al*., 2019).

Iron in PD

Iron concentration increases in the brain with age due to multiple factors such as leaky BBB, neuroinflammation, inefficient chelation of iron in the brain and compromised iron homeostasis. The selective increase in iron content with age in the substantia nigra (Tysnes and Storstein, 2017), putamen, globus pallidus and cortices makes these neurons vulnerable to oxidative stress-induced neurodegeneration (Correia *et al*., 2014).

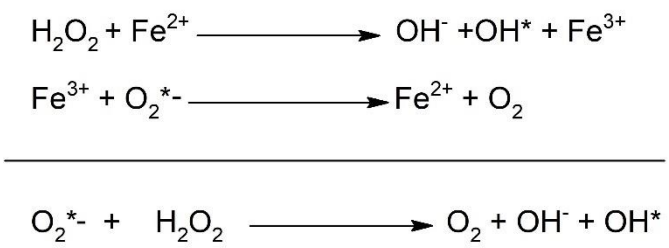

Figure 19: Key reactions involving Fenton chemistry

Excess free iron can generate ROS, which interacts with different cell components, including genetic materials and proteins. ROS can also cause releases of iron from the sulphur-iron mitochondria cluster and other iron storage sources and accelerate neurodegeneration. ROS species are produced via Fenton chemistry (Figure 19). An examination of iron species in the SN of PD sufferers found a Fe^{2+}: Fe^{3+} ratio of 2:1, whereas healthy subjects had a 1:2 Fe^{2+}: Fe^{3+} ratio (Riederer *et al*., 1988).

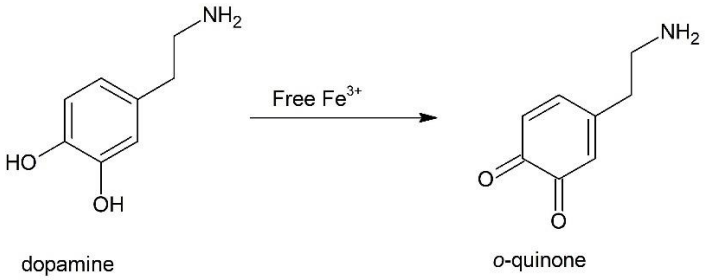

Figure 20: Formation of toxic o-quinone from dopamine

Dopamine is oxidised in enzymes or by iron to create a highly reactive toxic dopamine-quinone (Figure 20). Quinone is considered most reactive of all other oxidised products. Quinone is stable at pH 2.0, but at physiological pH it can transform further into different reactive species, for example, aminochrome, Leukoaminochrome, and 5,6-indolequinone (Linert and Jameson, 2000). These oxidised dopamine products can have multiple neurotoxic reactions, as shown below (Figure 21) (Zucca *et al*., 2017).

The toxicity of dopamine-metal complexes toward dopaminergic neurons depends on cell absorption ability. Dopamine oxidation by Fe^{3+} ions raises the quantity of Fe^{2+}, exacerbating oxidative stress further (Cronin *et al*., 2019).

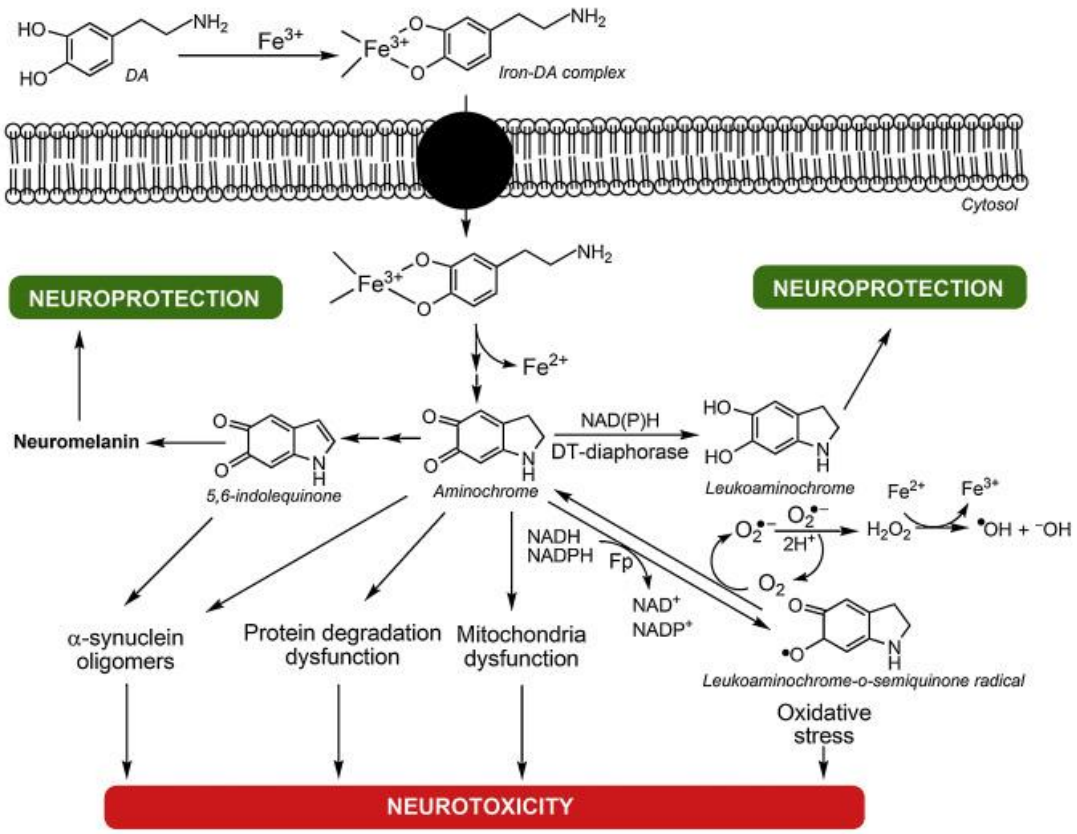

Figure 21: Neurotoxicity pathways involving the iron-dopamine complex (Zucca et al., 2017).

1.3.2. Parkinson's disease: Therapeutic modality

Iron chelators

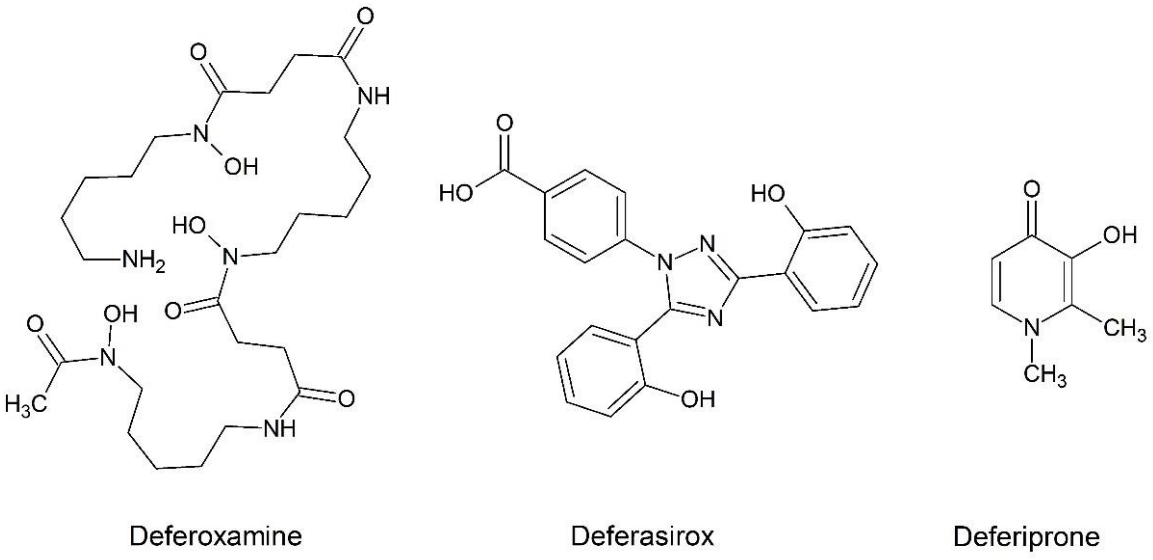

Figure 22: Some commercially available iron chelators

Iron chelation has been proposed as a method for managing PD (Fabbri *et al*., 2020). Clinically, there are many metal chelators such as Deferoxamine (DFO), deferiprone (DFP), deferasirox and penicillamine (Figure 22) to manage systemic metal dyshomeostasis. DFP was the first oral iron chelator reported for clinical use (Ward *et al*., 2012) (Singh *et al*., 2019).

Recently developed iron chelators have desirable properties such as mitochondrial targeting, centres for interaction between iron-reactive oxygen species and the ability to quench free Fenton-producing radicals. These chelators should also have mild iron-binding affinities, sufficient to chelate misregulated iron in the brain. The candidate chelators should be aimed for neuronal forms to minimise adverse side effects during the long-term therapy (Nuñez and Chana-Cuevas, 2018). Based on trials using the iron chelators deferiprone and PBT2, therapies designed to minimise iron in some brain areas have benn proposed with feasible metalloneurobiology action to delay or discourage PD from progressing (Nuñez and Chana-Cuevas, 2018).

Hydroxypyridinone analogs

Hydroxypyridinone compounds are important heterocyclic bidentate ligands for "hard" metal ions, including Fe^{3+}. Deferiprone is a member of the 3-hydroxy-4-pyridinone class that is commonly used as an iron-chelating agent. This class of powerful chelators can be derived from natural sources and can be conveniently refined to modulate complex physicochemical / biological properties, with low toxicity and good biocompatibility (Santos *et al*., 2012).

Hydroxypyridinone compounds have a heterocyclic 6-membered ring scaffold that provides several practical substitution sites at various ring locations, allowing regulation of their

bioavailability and association with many biological targets. A multitude of derivatives was developed for various applications in biomedicine.

8-Hydroxyquinoline (8-HQ) analogs

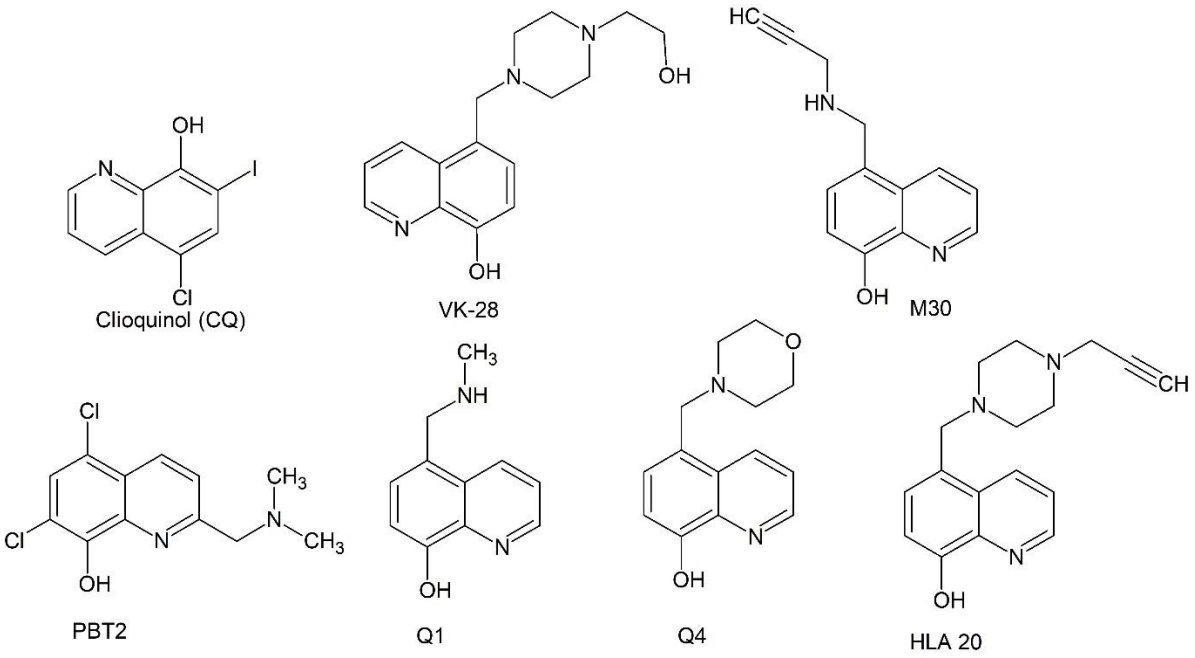

Figure 23: 8-Hydroxyquinoline (8-HQ) analogues.

Many 8-HQ variants showed significant neurodegeneration therapeutic ability. Clioquinol (Figure 23) is an iodinated 8-hydroxyquinoline (8-HQ) that is successful in arresting the metal-induced neurotoxicity in Parkinsonic animals. This mechanism can entail a redox silencing of reactive Fe^{2+}, or prevention of peptide fibrillation similar to Aβ (Finkelstein *et al*., 2016). VK-28 is a strong iron chelator, has good brain permeability, is MAO (monoamine oxidase) inhibitory and has neuroprotective properties (Youdim *et al*., 2004). M30 is also brain permeable with good MAO inhibitory properties and *in-vivo* efficacy in animal models (Gal *et al*., 2005) as well as chelating capability in PD brain SNPc regions (Gal *et al*., 2006). HLA20 is a chlorinated cell permeable 8-hydroxyquinoline analogue. It has a higher affinity for iron compared to copper. Chelators with higher selectivity for iron are of interest as

antioxidant-type drugs if excessive iron stores and iron-mediated production of free radicals in the brain are associated with neurodegenerative diseases (Zheng *et al*., 2005). PBT2 is an 8-hydroxyquinoline derivative without iodine-induced toxic effects due to the absence of a C-7 iodine atom. PBT2, a second-generation MPAC, has an extra tertiary amine in the structure potentially responsible for enhanced solubility and efficacy in preclinical studies. Oral PBT2 to Tg2576 mice decreased Aβ aggregates and plaques. PBT2 treatment significantly decreased oligomeric Aβ in double-transgenic APP / PS1 mice. However, Phase II clinical trials showed promising activity (Singh *et al*., 2019). Two novel 8HQ iron chelators, Q1 and Q4, decreased mitochondrial iron accumulation and oxidative stress in PD cell and animal models (Singh *et al*., 2019).

Dopamine transporter (DAT) ligands

Dopamine transporter (DAT) is a transmembrane protein in the central nervous system that transports dopamine from the synaptic cleft to the cytosol. DAT activity affects many facets of brain function, including perception, cognitive control, motivation, behavioural reinforcement and economic analysis (Salamone *et al*., 2009, Montague and Berns, 2002, Greengard, 2001)

DAT is a key focus of numerous psychostimulant, nootropic and antidepressant medications, as well as some illicit substances, including the highly addictive cocaine stimulant. Traditionally, DAT ligands (substrates) are classified into two categories: cocaine-like antagonists and amphetamine-like substrates (Altaf *et al*., 2015, Montague and Berns, 2002) In neuronal transmission, the structurally related serotonin and dopamine transporters (SERT and DAT) play an important role. Their principle role, i.e. the re-uptake of synaptic cleft neurotransmitters, has been extensively studied (Goldberg *et al*., 2003, Hilber *et al*.,

2005, Seidel *et al*., 2005, Shi *et al*., 2008) although the precise process of their substratum selectivity remains unclear. Phenylethylamines (PEAs) are SERT and DAT ligands (Schmitt *et al*., 2013, Sitte and Freissmuth, 2010). The interplay of bioactivity values and other structural properties of PEAs may therefore give rise to new perspectives about the selectivity of monoamine transporters.

A study by Baumann *et al.* in which the pEC_{50} values of SERT and DAT substrates were analysed, provided an indication of PEAs' selectivity profile (Rothman and Baumann, 2003, Cozzi *et al*., 2013) (Seddik *et al*., 2013). Some details can be taken from this study (Seddik *et al*., 2013): 1. Amphetamine α-methylene chirality does not affect the selectivity of SERT/DAT. 2. In both transporters the (S)-enantiomers of the amphetamine analogues are the most active enantiomers.

Amphetamine is considered a potent DAT and SERT substrate because of its planar conformation, molecular size and the presence of an aromatic ring and nitrogen on the aryl side-chain. These properties are the prerequisite physicochemical properties of a competitive DAT substrate because its similar to the monamines (dopamine). Comparing the relative potencies of S and R amphetamine, Heikkila *et al*. and Easton *et al*. stated that S-isomer was around fourfold more effective than R-isomer as a dopamine transporter substrate (Easton *et al*., 2007, Heikkila *et al*., 1975, Heal *et al*., 2013).

The chemical structure, particularly amphetamine's 3-dimensional (3-D) composition, is crucial in determining the pharmacological effects underpinning its major therapeutic benefits and also its responsibility for recreational abuse. Amphetamine is a medication class called 'β-phenylethylamines. Although it was synthesised several decades before the finding that monoamines, i.e. noradrenaline (norepinephrine), dopamine and 5-

hydroxytryptamine (5-HT; serotonin), were main neurotransmitters in the central and peripheral nervous systems.

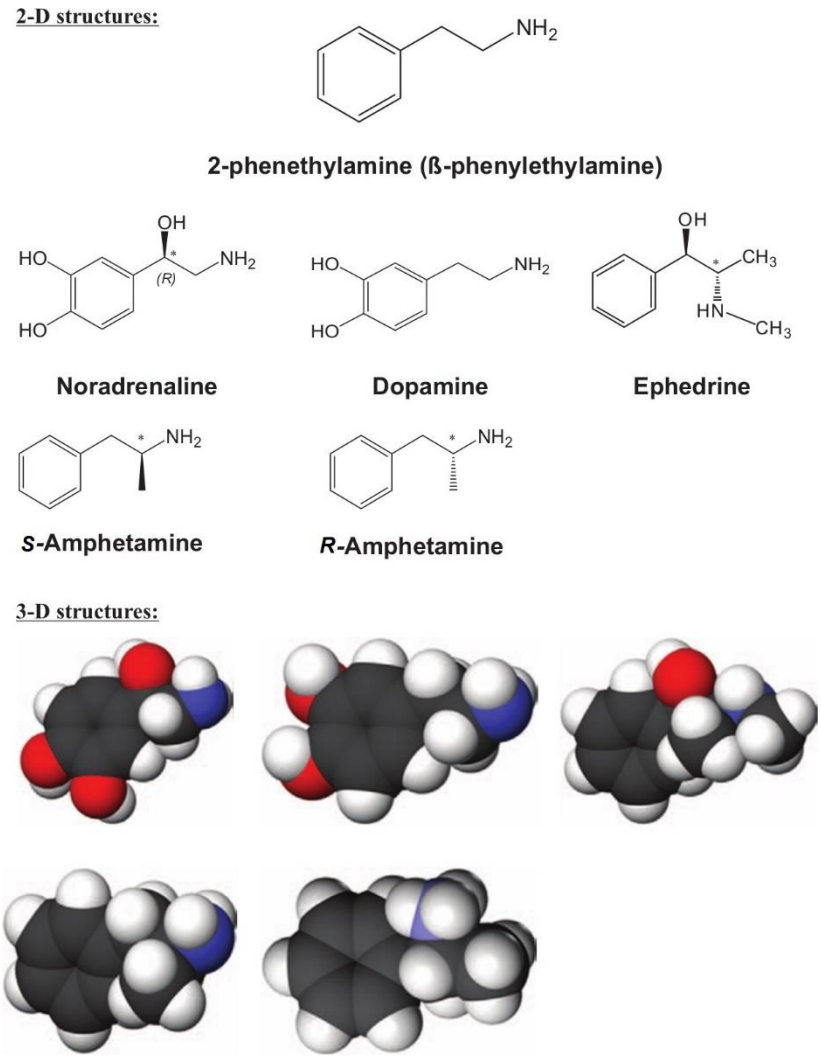

Figure 24: Chemical structures of various biologically active phenylethylamines (Heal et al., 2013).

As shown in Figure 24, the similarity between catecholamine neurotransmitter chemical structures, noradrenaline and dopamine, ephedrine, and amphetamine isomers is abundantly clear (Heal *et al*., 2013).

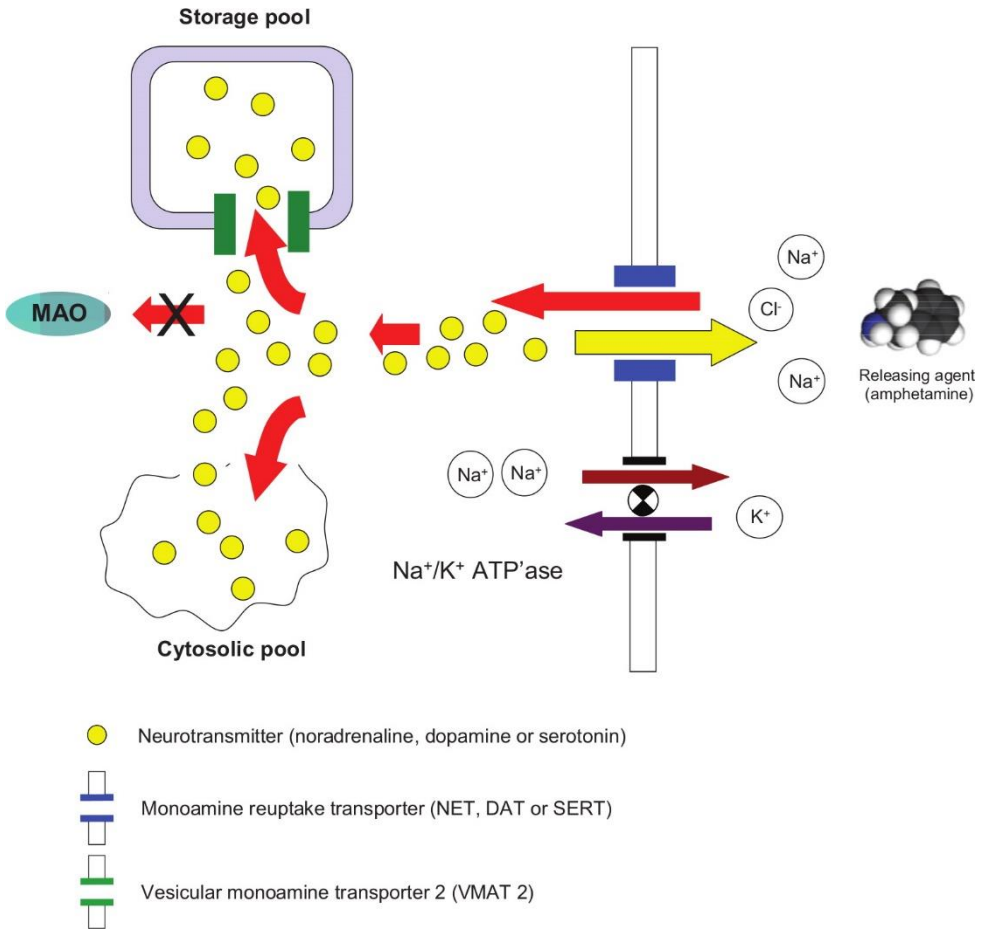

Figure 25: Transferring amphetamine to presynaptic nerve terminals (Heal et al., 2013).

Figure 25 shows the process of transferring monoamines and amphetamine to presynaptic nerve terminals. One molecule of monoamine neurotransmitter or amphetamine binds two Na^+ ions and one Cl^- ion, and the resultant molecular complex is dynamically transferred by the related monoamine reuptake transporter (DAT or SERT) to the presynaptic terminal (Fei *et al*., 2008, Fleckenstein *et al*., 2009) (Ramamoorthy *et al*., 2011).

Therefore, combining the ideas presented above (iron chelators for PD therapy) with those outlined in this section may lead to a new type of targeted iron chelator – the amphetamine-like chelator.

Chapter 2

Experimental

Chapter 2. Experimental

2.1. General

Reagents and analytical grade solvents were purchased from commercial sources. Dichloromethane, triethylamine and acetonitrile were dried by refluxing over calcium hydride for several hours. Toluene was dried by standing over sodium wire for two days.

The Aβ40 peptide (purity >95%) was purchased from GL Biochem Ltd (Shanghai). A BCA protein assay kit was purchased from Thermo Scientific.

N27 rat dopaminergic neural cells were obtained from Millipore (product number: SCC048). Glutamax was obtained from Thermo Fisher (product number:61870-036). Foetal calf serum was obtained from Bovogen, Keilor East, Australia. Penicillin/Streptomycin from Thermo Fisher (product number: 15140122). MTT was obtained from Sigma Aldrich (product number: M5655).

^{1}H and ^{13}C NMR spectra were recorded using an Agilent 500 MHz spectrometer (499.86 MHz ^{1}H, 125.70 MHz ^{13}C) using deuterated chloroform ($CDCl_3$) as solvent unless otherwise specified. Low-resolution mass spectra were obtained on an Agilent 6890GC fitted with 5% polysilphenylene, 95% polydimethylsiloxane column, and an Agilent 5973n MS spectrometer. High-resolution mass spectra were obtained on an Agilent 6510 Accurate Mass Q-TOF Mass Spectrometer, equipped with an ESI source. TLC analysis was performed using aluminium-backed Merck 60 GF_{254} silica gel or Merck 60 GF_{254} neutral alumina gel with UV detection at 254 nm. Compounds were purified by column chromatography using either neutral alumina or silica gel (40 – 63 μm).

UV-Vis recorded using an Agilent Technologies Cary 60 spectrometer (Santa Clara, CA, USA). Infrared spectra were collected using thermos scientific FT-IR(ATR) spectrometer Nicolet

6700 spectrometer in the range of 4000-600 cm-1 signals are given as (cm^{-1}).

Suitable single crystals were selected for crystallographic studies using a polarizing microscope (Leica M165Z), mounted on a MicroMount (MiTeGen, USA) consisting of a thin polymer tip with a wicking aperture. The X-ray diffraction measurements were carried out on a Bruker kappa-II CCD diffractometer at 150 K by using IμS Incoatec Microfocus Source with Mo-Kα radiation (λ = 0.710723 Å). The single crystal, mounted on the goniometer using cryo loops for intensity measurements, was coated with paraffin oil and then quickly transferred to the cold stream using an Oxford Cryo stream attachment. Symmetry related absorption corrections using the program SADABS(Bruker, 2001) were applied and the data were corrected for Lorentz and polarisation effects using Bruker APEX2 software(Bruker, 2007). The structure was solved by direct methods, and the full-matrix least-square refinement was carried out using Shelxl (Sheldrick, 2008) in Olex2(OLEX, 2009). The non-hydrogen atoms were refined anisotropically. The molecular graphic was generated using program Olex2 (OLEX, 2009).

Modelling and pharmacokinetic parameters were calculated using Discovery Studio 4.5 (Accelrys, San Diego, CA, USA).

2.2. Synthesis and characterisation of cyclen-based compounds

2.2.1. Synthesis of 2,3,5,6,8,9-hexahydrodiimidazo[1,2-a:2',1'-c] pyrazine (MSOG)

This procedure is a modification of the method reported by Weismann and Reed (Weisman and Reed, 1996). Triethylenetetramine (1.21 g, 8.32 mmol) was dissolved in absolute ethanol (10ml) and placed in a 100 ml three-necked round bottom flask equipped with a magnetic stir bar, condenser, dropping funnel and a nitrogen inlet. The top of the condenser was connected to a safety flask and the flask was connected to two fritted gas washing

bottles each containing 50 ml of 30% aqueous sodium hydroxide to scrub the hydrogen sulfide produced by the reaction. Dithiooxamide (1.00 g, 8.32 mmol) dissolved in ethanol (5 ml) was added in one portion via a dropping funnel to the round bottom flask and the reaction mixture was stirred at reflux for 4 hours under nitrogen. The evolution of gas (hydrogen sulphide and ammonia) was observed as bubbles through the scrubbing solutions. The mixture was cooled to room temperature and stirred for 3 hrs under nitrogen to allow residual hydrogen sulfide to dissipate. The solvent was then removed using a rotary evaporator. The crude product was dissolved in chloroform (15 ml) followed by gravity filtration of the solution through a glass wool plug. The solvent was removed using a rotary evaporator. The product was dissolved in boiling toluene (5.00 ml) and filtered using a glass wool plug. The crude product was purified by sublimation to give white crystals (0.900 g, 0.00549 mol). Yield: 66%; R*f* (1:3 hexane/ethanol) 0.63; ^{1}H NMR (δ, 500 MHz, $CDCl_3$) 3.86(t, *J*= 9.5 Hz, 4H, H11,6), 3.34(t, *J*= 9.0 Hz, 4H, H12,5), 3.25(s, 4H, H2,3); ^{13}C NMR ($CDCl_3$) δ: 139, 54.1, 52.1, 45.3; GCMS: 164 $(M)^+$, 136 $(C_6N_4H_8)^+$, 109 $(C_4N_4H_5)^+$, 68.0 $(C_3N_2H_4)^+$, 42.0 $(C_2N_2H_4)^+$

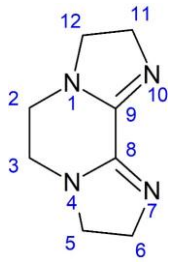

2.2.2. Synthesis of of N,N,N – tri(toluene-4-sulfonyl) diethylenetriamine (MS0C)

This procedure is a modification of the method reported by Wilson *et al* (Wilson *et al*., 2007). Diethylene triamine (2.00 g, 0.0194 mol) was dissolved in de-ionised water (12.5 ml) and sodium hydroxide pellets (2.40 g, 0.0600 mol) were added at room temperature. Diethyl ether (15.0 ml) was added and the solution was stirred vigorously. The solution was cooled in an ice bath and toluene-4-sulfonyl chloride (11.5 g, 0.0603 mol) was added. The reaction was stirred for 1 hour at 0 °C. The white precipitate that formed was collected by filtration and washed with diethyl ether (25.0 ml). The crude product was purified by

recrystallization from chloroform to give a white solid (10.2 g, 0.0180 mol), yield: 90%; ^{1}H NMR (δ,500 MHz, $CDCl_3$) 7.76(m, 4H, H35,31,24,28), 7.63(d, *J* = 8.5 Hz, 2H, H2,6), 7.31(m, 6H, H34,32,25,27,3,5), 3.20-3.14 (m, 8H, H18,17,12,13), 2.44(s, 9H, H36,37,9).

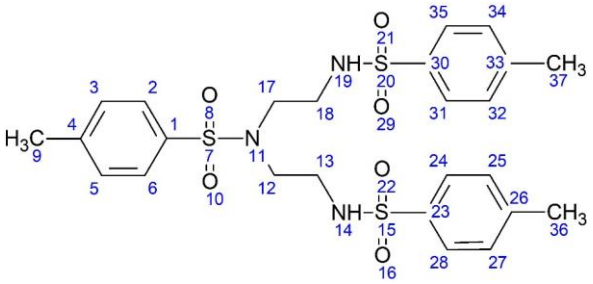

2.2.3. Synthesis of N,O,O – tri(toluene-4-sulfonyl) diethanolamine (MS0D)

This procedure is a modification of the method reported by Wilson *et al.* (Wilson *et al*., 2007). Toluene-4-sulfonyl chloride (11.45 g, 0.06 mol) was dissolved in dichloromethane (15 ml) and placed in a 50 ml round bottom flask. The solution was cooled down to 0 °C and diethanolamine (2.10 g, 0.0199 mol), benzyltriethylammonium chloride (1.82 g, 7.99 mmol) and 30% NaOH (2.40 g in 15.0 ml of water) were added. The solution was stirred vigorously at room temperature for 1 hr. The mixture was then added to water (30.00 ml) and the organic phase was separated from the aqueous phase, washed with water (3 x 15.0 ml), and dried using anhydrous magnesium sulfate. After filtering, the solvent was removed in vacuo to give a white solid (9.90 g, 0.0170 mol), yield: 87%; ^{1}H NMR (δ, 500 MHz, $CDCl_3$) 7.77(d, *J* =9.0 Hz, 4H, H35,31,2,6), 7.62(d, *J* = 9.0 Hz, 2H, H24,28), 7.37 (d, *J* = 8.0 Hz, 4H, H34,32,3,5), 7.3(m, 2H, H25,27), 4.11 (t, *J* = 6.0Hz , 4H, H17,10), 3.37 (t, *J* = 6.0Hz , 4H, H18,9), 2.46(s, 6H, H37,14), 2.43(s, 3H, H36).

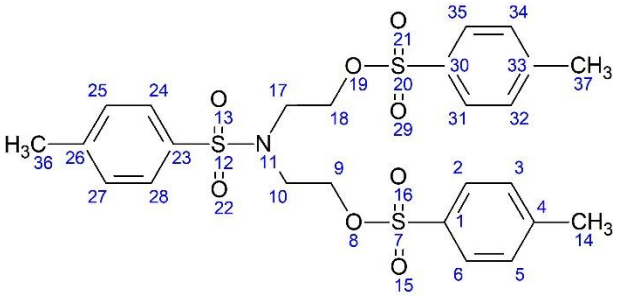

2.2.4. Synthesis of 1, 4, 7, 10- tetrakis(toluene-4-sulfonyl)-1,4,7,10-tetrazacyclododecane (MS0E)

This procedure is a modification of the method reported by Wilson *et al.* (Wilson *et al*., 2007). *N, N, N*–Tri (toluene-4-sulfonyl) diethylene triamine (0.800 g, 1.10 mmol), caesium

carbonate (1.36 g, 4.20 mmol) and *N,N*-dimethylformamide (30.0 ml) were placed in a 250 ml round bottom flask. A solution of *N, O, O*-tri(toluene-4-sulfonyl) diethanolamine (0.560 g, 1.10 mmol) and *N,N*- dimethylformamide (12.5 ml) was added dropwise with stirring over three hours. The reaction mixture was stirred for five days and then concentrated using a rotary evaporator. Dichloromethane (15 ml) and water (15 ml) were added to the residue and the mixture transferred to a separating funnel. The organic phase was separated, and the aqueous phase was washed with dichloromethane (10.0 ml). The combined organic phases were washed with saturated aqueous sodium chloride and dried using anhydrous magnesium sulfate. Solvent was removed in vacuo and the crude product was recrystallised from methanol to give a colourless solid (0.620 g, 0.780mmol), yield: 71%; ^{1}H NMR (δ, 500 MHz, $CDCl_3$) 7.71(d, *J*=8.5 Hz, 8H, H30,34,37,41,44,48,23,27), 7.35(d, *J*= 8.0 Hz, 8H, H31,33,38,40,45,47,24,26), 3.44(br s, 16H, H2,3,5,6,8,9,11,12), 2.45(s, 12H, H49,50,51,52).

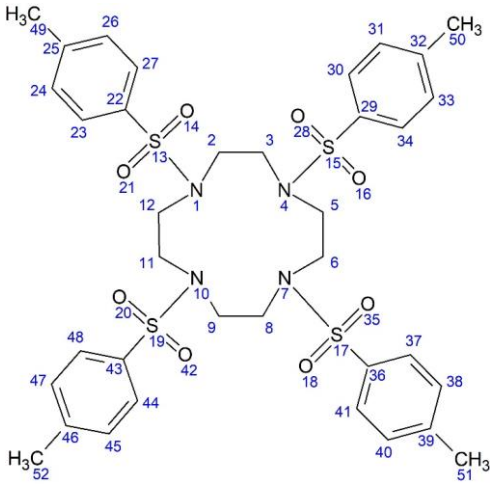

2.2.5. Synthesis of 1, 4, 7, 10-Tetrazacyclododecane (cyclen) (MS0)

Method 1

This procedure is a modification of the method reported by Weismann and Reed (Weisman and Reed, 1996). 2, 3, 5, 6, 8, 9-Hexahydrodiimidazo pyrazine (0.900 g, 5.48 mmol) was added to a 50 ml, two neck round bottom flask equipped with a condenser and rubber septum. The flask was purged with nitrogen gas and placed in an ice bath. Diisobutyl aluminium hydride solution (21.8 ml, 1.50 M) was added *via* syringe. The mixture was refluxed under nitrogen for 16 hrs. After cooling to room temperature toluene (20.0 ml) was

added and the reaction quenched by the dropwise addition of aqueous potassium hydroxide (2.00 ml, 3M). When gas evolution ceased, another 35.0 ml of the aqueous potassium hydroxide solution was added in one portion the mixture was transferred to separating funnel. The aqueous phase was separated, followed by addition of chipped ice with chloroform. The combined organic phase was dried using anhydrous sodium sulfate, filtered, and concentrated using a rotary evaporator. The crude compound was purified by sublimation to yield a white product. Yield: 51%; ^{1}HNMR (δ,500 MHz, $CDCl_3$) 2.69(s, 16H, H2,3,5,6,8,9,11,12), 1.62 (s (br), 4H, H1,4,7,10); ^{13}C NMR ($CDCl_3$) δ: 46.1.

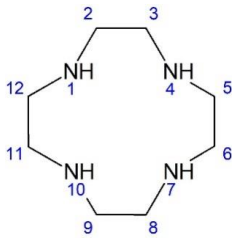

Method 2

This procedure is a modification of the method reported by Wilson *et al* (Wilson *et al*., 2007). 1, 4, 7, 10- tetrakis(toluene-4-sulfonyl)-1,4,7,10-tetrazacyclododecane (0.120 g, 0.240 mmol) and 1.3g was dissolved in 30 ml of acetic acid and 10 ml of hydrobromic acid then transferred to 100 ml round bottom flask that is equipped with condenser. The mixed solution was refluxed for 2 days. Then the reaction was cooled down and concentrated in *vacuo*. The crude compound was dissolved in dichloromethane and water, then transferred to the separatory funnel. The collected organic phase was dried by sodium sulfate, then filtered and concentrated by rotary evaporator. The product was recrystallised from hot toluene to get white solid yield: 39%.

2.2.6. Synthesis of 2-bromomethyl-8-hydroxyquinoline (MS1B)

2-Formyl-8-hydroxyquinoline (2.00 g, 0.0100 mol) was dissolved in methanol (25.0 mL) in a 50 mL round bottom flask. Sodium borohydride (0.500 g, 0.0130 mol) was added gradually and the reaction stirred for 5 hours at room temperature. The solvent was removed using a

rotary evaporator and then water (25.0 mL) was added. The resultant solution was neutralized using aqueous hydrochloric acid (2.00 M) and then extracted with ethyl acetate (3 x 50.0 mL) and the organic phase dried over sodium sulfate. The mixture was filtered, and the solvent was evaporated by rotary evaporator to yield 2-hydroxymethyl-8-hydroxyquinoline (**MS1A**) (1.66 g, 95%), which was used without further purification. 2-Hydroxymethyl-8-hydroxyquinoline (1.66 g, 9.50 mmol) was added to a 25 ml round bottom flask and concentrated hydrobromic acid (16.0 mL) was added dropwise. The mixture was stirred at reflux for 4 hours and then cooled in an ice bath. Aqueous sodium carbonate (2.00 M) was added until pH 7. The mixture was extracted with dichloromethane (3 x 50.0 mL) and the organic layer was dried over sodium sulfate, filtered, and the solvent was evaporated using a rotary evaporator. The crude product was purified by silica gel column chromatography eluting with hexane: ethyl acetate (1:1) to give pure 2-bromomethyl-8-hydroxyquinoline as a pale-yellow solid (1.40 g, 7.79 mmol). Yield 82%. Note: This compound was found to decompose upon standing in air after 2 days. RF silica gel (hexane: ethyl acetate (1:1)) = 0.92; ^{1}H NMR (δ, 500 MHz, $CDCl_3$) 8.18 (d, *J*= 8.5 Hz, 1H, H4), 8.06 (s, 1H, H13), 7.59 (d, *J*= 8.5Hz, 1H, H6), 7.47 (t, *J* = 8.5 Hz, 1H, H7), 7.34 (d, *J*= 8.0 Hz, 1H, H3), 7.20 (d, *J*=8.0 Hz, 1H, H8), 4.71 (s, 2H, H11). ^{13}C NMR (δ, 125.7 MHz, $CDCl_3$) 154.9, 152.2, 137.6, 128.5, 127.8. 122, 117.8, 110.8, 33.9; HRMS $[M+H]^+$ calc. $C_{10}H_8ONBr$ 237.9862, Found 237.9868.

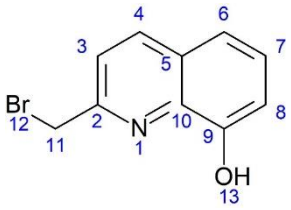

2.2.7. Synthesis of 2-bromo-N-(2-(pyridin-2-yl)ethyl) acetamide (MS2A)

2-(Pyridin-2-yl)ethan-1-amine (2.44 ml, 20.0 mmol) and triethylamine (2.78 mL, 20.0 mmol) were dissolved in anhydrous dichloromethane (25ml) and then cooled to -10°C. A solution of bromoacetyl bromide (1.74 ml, 20.0 mmol) in anhydrous dichloromethane (10.0 ml) was

added dropwise. The mixture was stirred for 1 h under a nitrogen atmosphere at -10 °C and then for 2 hours at room temperature. The reaction mixture was extracted with aqueous sodium bicarbonate and the aqueous phase extracted with dichloromethane (3 x 50.0 mL). The combined organic extracts were dried with anhydrous potassium carbonate the solvent was removed using a rotary evaporator to give a pale-yellow oil (3.93 g, 0.0160 mmol). Yield 81%; RF silica gel (chloroform: methanol: hexane) = 0.775;^{1}H NMR (δ, 500 MHz, $CDCl_3$) 8.55 (dd, *J*= 5.5, 1.5 Hz, 1H, H6), 7.67 (s, 1H, H9), 7.63 (td, *J*= 7.5, 2.0 Hz, 1H, H4), 7.17 (m, 2H, H3,5), 3.86 (s, 2H,H12), 3.71 (q, *J*=6.0 Hz, 2H,H8), 3.02 (t, *J*= 6.0Hz, 2H,H7) ppm; ^{13}C NMR 166.0, 159.4, 149.4, 136.9, 123.6, 121.9, 39.4, 36.4, 29.5 ppm; HRMS $[M]^+$ calculated for $C_9H_{11}N_2OBr$ 242.0055 Found 242.0063.

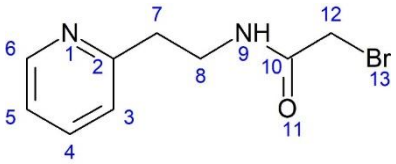

2.2.8. Synthesis of bis(2-hydroxyethyl)carbamic bromide (MS4A)

Using the procedure described above and using diethanolamine (1.92 mL, 20 mL) instead of 2-(pyridin-2-yl)ethan-1-amine. Yellow oil (4.07 g, 18.0 mmol). Yield 90%; ^{1}H NMR (δ, 500 MHz, $CDCl_3$) 4.04 (s, 2H, H10) ppm, 3.83 (m, 4H, H5,3), 3.54 (m, 4H, H2,6); ^{13}C NMR (δ, 125.7 MHz, $CDCl_3$) 169.4, 59.9, 49.5, 26.4; HRMS $[M+H]^+$ calculated for $C_6H_{12}NO_3Br$ 226.0073 Found 226.0079.

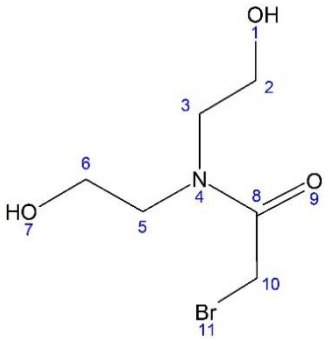

Typical procedure for the synthesis of MS1-4

2.2.9. Synthesis of N-(2-methyl-8-hydroxyquinoline)-1,4,7,10-tetrazacyclododecane (MS1)

1,4,7,10-Tetrazacyclododecane (0.288 g, 1.68 mmol) was dissolved in anhydrous acetonitrile (20.0 ml) in a two-necked round bottom flask (50 ml) containing potassium carbonate (0.580 g, 4.20 mmol)). Separately, 2-bromomethyl-8-hydroxyquinoline (0.200 g, 0.840 mmol, a cyclen:alkylbromide ratio of 2:1) was dissolved in anhydrous acetonitrile (10.0 ml) and was added dropwise to the 1,4,7,10-tetrazacyclododecane solution over 2 hours under nitrogen gas and at reflux. After 48 hours the mixture was cooled and filtered. The crude product was purified by column chromatography (silica gel) eluting with dichloromethane: methanol: ammonia (83:15:2) to give a dark yellow oil (0.165 g, 0.504 mmol). Yield: 60%; RF silica gel (dichloromethane: methanol: ammonia 83:15:2) = 0.56. ^{1}H NMR (δ, 500 MHz, $CDCl_3$) 2.78-2.92 (m, 16H, H2,3,5,6,8,9,11,12), 4.02 (s, 2H, H13), 7.14 (d, *J*=7.0 Hz, 1H, H18), 7.21 (d, *J*= 8.0 Hz, 1H, H23), 7.28 (d, *J*= 9.0 Hz, 1H, H20), 7.32 (t, *J*= 8.0 Hz, 1H, H19), 8.02 (d, *J*= 9.0 Hz, 1H, H22) ppm. ^{13}C NMR (δ, 125.7 MHz, $CDCl_3$) 45.4, 45.9, 46.3, 46.8, 52.6, 112, 117, 120.5, 127, 127, 136, 152, 160 ppm; HRMS $[M+H]^+$ calculated for $C_{18}H_{27}ON_5$ 330.2288 Found 330.2291; FTIR (neat) 3418, 3078, 2994, 2920, 2850, 1669, 1632, 1569, 1473, 1358, 771.0.cm^{-1}.

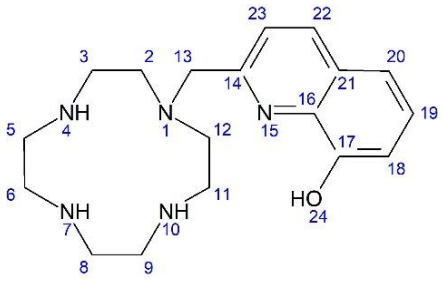

2.2.10. Synthesis of N-[2-(pyridin-2-yl)ethyl] acetamide-1,4,7,10-tetrazacyclododecane (MS2)

Using 2-bromo-*N*-(2-(pyridin-2-yl)ethyl) acetamide, the crude product was purified by column chromatography (alumina) eluting with chloroform: methanol: 3:1 to give a brown oil (65%). RF alumina (chloroform: methanol 3:1) = 0.26; ^{1}H NMR (δ, 500 MHz, $CDCl_3$) 8.53 (dd, *J*= 5.5, 1.0 Hz, 1H, H21) , 8.14 (s, 1H, H16), 7.61 (td, *J*= 7.5, 1.5 Hz, 1H, H23) 7.21 (d, 1H,

J= 7.5 Hz, H24), 7.13 (t, 1H, *J*= 7.5 Hz, H22), 3.68 (m, 2H, H17), 3.12 (s, 2H, H13), 3.04 (t, *J*= 8.5 Hz, 2H, H18), 2.57-2.77 (m, 16H, H2,3,5,6,8,9,11,12) ppm. ^{13}C NMR (δ, 125.7 MHz, $CDCl_3$) 160, 149, 137, 124, 122, 59.5, 53.3, 47.4, 46.9, 45.9, 37.6, 29.8 ppm. HRMS $[M+H]^+$ calculated for $C_{17}H_{30}N_6O$ 335.2554 Found 335.2558; FTIR (neat) 3418, 3180, 3078, 2920, 1669, 1632, 1595, 1473, 1437, 1358, 771.0 cm^{-1}.

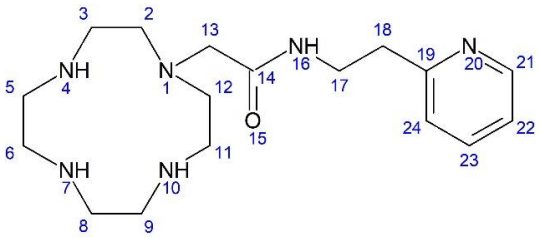

2.2.11. Synthesis of N-[3-(pyridin-4-yl)propyl]-1,4,7,10-tetrazacyclododecane (MS3)

Using 4-(3-bromopropyl)pyridine, the crude product was purified by silica gel column chromatography eluting with dichloromethane: methanol: ammonia 82:15:2 to give a white solid (62%). RF silica gel 0.26; ^{1}H NMR (δ, 500 MHz, $CDCl_3$) δ = 8.45 (d, *J*= 6.0 Hz, 2H, H18,20), 7.14 (d, 2H, *J*=6.0Hz, 2H, H17,21), 2.78 (t, *J*=5.0 Hz, 2H, H13), 2.54-2.63 (m, 16H, H2,3,5,6,8,9,11,12), 2.46 (t, *J*=7.5 Hz, 2H, H15), 1.80 (m, 2H, H14) ppm; ^{13}C NMR (δ, 125.7 MHz, $CDCl_3$): 151, 150, 124, 54, 51.5, 46.8, 45.8, 44.9, 33.1, 28.1 ppm; HRMS $[M+H]^+$ calculated for $C_{16}H_{29}N_5$ 292.2496 Found 292.2506; FTIR (neat) 3417, 2920, 2850, 1659, 1604, 1453, 1261, 801.0 cm^{-1}.

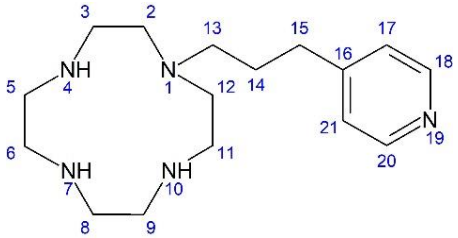

2.2.12. Synthesis of N-(bis(2-hydroxyethyl)carbamic bromide)-1,4,7,10-tetrazacyclododecane (MS4)

Using bis(2-hydroxyethyl)carbamic bromide, the crude product was washed with hot hexane and then with hot toluene to give an orange oil (61%). ^{1}H NMR (δ, 500 MHz, $CDCl_3$) δ = 3.70 (m, 4H, H17, 20), 3.66 (t, *J*= 5.0 Hz, 2H, H21), 3.46 (t, *J*= 4.5 Hz, 2H, H18), 3.41 (s, 2H, H13), 2.57-2.78 (m, 16H, 2,3,5,6,8,9,11,12)

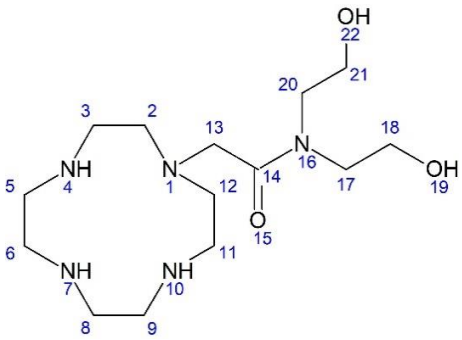

ppm; ^{13}C NMR (δ, 125.7 MHz, $CDCl_3$): 171.9, 59.4, 59.1, 52.4, 49.7, 49.3, 46.2, 45.7, 45, 44.5 ppm; HRMS $[M+H]^+$ calculated for $C_{14}H_{31}N_5O_3$ 318.2499 Found 318.2516; FTIR (neat) 3377, 2934, 2851, 2361, 1635, 1559, 1457, 1292, 1071 cm^{-1}.

Typical procedure for the synthesis of Zn and Ni complexes of MS1-4

2.2.13. Synthesis of MS1:Zn

N-(2-methyl-8-hydroxyquinoline)-1,4,7,10-tetrazacyclododecane (**MS1**, 30.0 mg, 0.0911mmol) was dissolved in methanol (~1.00 mL) and $ZnCl_2$ (12.42 mg, 0.0911 mmol) was dissolved in water (~1.00 mL). The metal salt solution was added dropwise to the methanolic solution to get **MS1**:Zn stock solution. Crystals suitable for X-ray diffraction were grown by diffusion of acetone into the methanol/water solution in a sealed vessel. Yield of bright green solid (80 %). ^1H NMR (δ, 500 MHz, D_2O) 8.52 (d, *J*= 8.5 Hz, 1H) 7.59 (m, 2H), 7.42 (t, *J*= 8.5 Hz, 1H), 7.33 (dd, *J*=8.0, 2.0 Hz, 1H), 4.40 (s, 2H), 2.87-3.24 (m, 16H) ppm; ^{13}C NMR (δ, 125.7 MHz, D_2O): = 46.5, 46.8, 47.0, 56.0, 60.9, 116, 121, 123, 130, 131, 131, 143, 160, 143, 131, 131, 130, 123, 121, 116, 60.9, 56, 47, 46.8, 46.5 ppm; HRMS $[M]^+/2$ calculated for $ZnC_{18}H_{27}ON_5$ 196.5748 Found 196.5750 with % abund. *m/z* 196.5750 (100), 197.0766 (21.62), 197.5737 (60.1), 198.0747 (21.23), 198.5731 (42.59), 199.0732 (8.81); FTIR (neat) 3416, 3215, 1621, 1462, 1384, 1144, 756.0 cm^{-1}; UV (MeOH, ε(M^{-1}, cm^{-1})) 340 (260), 252 (14218), 205 (13270)

2.2.14. Synthesis of MS2:Zn

Yellow solid (82%). ^1H NMR (δ, 500 MHz, D_2O) δ = 8.48 (d, *J*= 4.5 Hz, 1H), 7.88 (td, *J*= 7.5, 2.0 Hz, 1H), 7.39 (m, 2H), 3.69 (t, *J*= 6.5 Hz, 2H), 3.43 (s, 2H), 3.04 (m, 2H), 2.65-2.97 (m, 16H) ppm; ^{13}C NMR, δ = 175.1, 160.4, 150.5, 141.4, 127.2, 125.2, 58.3, 56.7, 48.7, 47.3, 46.9, 42.1, 38.6 ppm; HRMS $[M]^+/2$ calculated for $ZnC_{17}H_{30}N_6O$ 199.0881 Found 199.0890 with %

abund. *m/z* 199.0890 (100), 199.5899 (20.96), 200.0874 (60.24), 200.5881 (20.83), 201.0868 (42.54), 201.588(8.54), 202.0877(2.23); FTIR (neat) 3469, 3285, 2930 1657, 1641, 1552, 1484, 1442, 1384, 772.0 cm^{-1}; UV (MeOH, ε(M^{-1}, cm^{-1})) 350 (190), 262 (12727), 208 (14182).

2.2.15. Synthesis of MS3:Zn

White solid (75%). ^{1}H NMR (D_2O), δ: 8.44 (d, *J*= 6.0 Hz, 2H), 7.54 (d, 2H, *J*=6.0Hz), 3.05(m, 2H), 2.92-2.99 (m, 16H), 2.71 (t, *J*=7.0 Hz, 2H), 1.950 (m, 2H) ppm; ^{13}C NMR δ: 151.2, 150.6, 127.6, 54.71, 52.2, 47, 46, 44.9, 34.7, 25.2 ppm; HRMS $[M]^+$ /2 calculated for $ZnC_{16}H_{29}N_5$ 177.5852 Found 177.5794 with % abund. *m/z* 177.5794 (100), 178.0871 (19.47) 178.5842 (59.76), 179.0854 (19.88), 179.5843 (42.12); FTIR (neat) 3465, 3271, 2937, 1616, 1443 1296, 1091, 860.0 cm^{-1}, UV (MeOH, ε(M^{-1}, cm^{-1})) 355 (110), 255 (5360), 207 (11504).

2.2.16. Synthesis of MS4:Zn

Yellow solid (81%). ^{1}H NMR (D_2O) δ = , 3.87 (s, 2H) ppm, 3.80 (t, *J*= 5.5Hz, 4H), 3.67 (t, *J*= 5.5 Hz, 2H) 3.57 (t, *J*= 5.5 Hz, 2H), 2.78-3.11 (m, 16H) ppm; ^{13}C NMR δ: 176.7, 61, 60.6, 58.7, 58.3, 51.5, 50.7, 49.1, 47.7, 46.4 ppm; HRMS $[M]^+$/2 calculated for $ZnC_{14}H_{31}N_5O_3$ 190.5854 Found 190.5890 with % abund. *m/z* 190.5890(100), 191.091(17.44) 191.5875 (60.02), 192.0884 (18.77), 192.5869 (42.12); FTIR (neat) 3421, 3261, 2932, 1616, 1559, 1457, 1297, 1091 cm^{-1}; UV (MeOH, ε(M^{-1}, cm^{-1})) 350 (210), 204 (7173).

2.2.17. Synthesis of MS1:Ni

Using $NiSO_4 \cdot 7H_2O$, a yellow solid was obtained (78 %). HRMS $[M]^+$/2 calculated for $NiC_{18}H_{27}ON_5$ 193.5779 Found 193.5774 with % abund. *m/z* 193.5774 (100), 194.0797 (21.64), 194.5763 (40.92), 195.1595 (10.2), 195.5753 (6.67); FTIR (neat) 3249, 3220, 2362, 1653, 1457, 1384, 1098, 794.0 cm^{-1}; UV (MeOH, ε(M^{-1}, cm^{-1})) 320 (190), 260 (4800), 244 (4533), 202 (6533)

2.2.18. Synthesis of MS2:Ni

Using $NiSO_4 \cdot 7H_2O$, a white solid was obtained (71%). HRMS $[M]^+/2$ calculated for $NiC_{17}H_{30}N_6O$ 196.0912 Found 196.0919 with % abund. *m/z* 196.0919 (100), 196.5932 (20.96), 197.0898 (40.83), 197.5908 (9.93), 198.0890 (6.58), 198.5901(1.22), 199.0891(1.48); FTIR (neat) 3423, 3285, 2941, 1637, 1642, 1596, 1472, 1389, 777.0 cm^{-1}; UV (MeOH, ε(M^{-1}, cm^{-1})) 370 (155), 262 (4545), 207 (13182).

2.2.19. Synthesis of MS3:Ni

Using $NiSO_4 \cdot 7H_2O$, a bright blue solid was obtained (86%). HRMS $[M]^+/2$ calculated for $NiC_{16}H_{29}N_5$ 174.5883 Found 174.5878 with % abund. *m/z* 174.5878(100), 175.0866(19.47) 175.5821 (40.32), 176.0854 (9.28), 176.5823 (6.36); FTIR (neat) 3321, 2361, 1624, 1145, 1096, 766.0 cm^{-1}; UV (MeOH, ε(M^{-1}, cm^{-1})) 365 (165), 254 (4000), 207 (12000).

2.2.20. Synthesis of MS4:Ni

Using $NiSO_4 \cdot 7H_2O$ a bright green solid was obtained (85%). HRMS $[M]^+/2$ calculated for $NiC_{14}H_{31}N_5O_3$ 187.5885 Found 187.5884 with % abund. *m/z* 187.5884(100), 188.0898(17.45) 188.5866 (40.58), 189.0872 (8.56), 189.5852 (6.42); FTIR (neat) 3258, 1616, 1457, 1098 cm^{-1}; UV (MeOH, ε(M^{-1}, cm^{-1})) 360 (180), 206 (12760)

Typical procedure for the synthesis of copper complexes of MS1-4

2.2.21. Synthesis of MS1:Cu

N-(2-methyl-8-hydroxyquinoline)-1,4,7,10-tetrazacyclododecane (**MS1,** 30.00 mg, 0.0911mmol) was dissolved in methanol (~1.00 mL) and separately $CuSO_4.5H_2O$ (22.8 mg, 0.0911 mmol) was dissolved in methanol (~1.00 mL). The copper(II) sulfate solution was added to the solution containing the chelator dropwise to get **MS1**:Cu stock solution.

Crystals suitable for X-ray diffraction were grown by diffusion of diethyl ether into the methanolic solution in a sealed vessel. Yield of green solid (82 %). HRMS $[M]^+/2$ calculated for $CuC_{18}H_{27}ON_5$ 196.0756 Found 196.0756 with % abund. *m/z* 196.0756 (100), 196.5766 (21.62), 197.0748 (47.05), 197.5758 (9.83); FTIR (neat) 3446, 3211, 2928, 1653, 1559, 1457, 1384, 1117, 982.0, 619.0 cm^{-1}; UV (MeOH, ε(M^{-1}, cm^{-1})) 646 (143), 253 (8333), 204 (8095)

2.2.22. Synthesis of MS2:Cu

Blue solid (75%). HRMS $[M]^+/2$ calculated for $CuC_{17}H_{30}N_6O$ 198.5883 Found 198.5898 with % abund. *m/z* 198.5898 (100), 199.0903 (20.96), 199.5884(46.92), 200.0894 (9.52), 200.5905 (1.06); FTIR (neat) 3442 2941, 1640, 1477, 1443, 1115, 771.0, 619.0 cm^{-1}; UV (MeOH, ε(M^{-1}, cm^{-1})) 616 (97), 262 (6818), 207 (8727).

2.2.23. Synthesis of MS3:Cu

Blue solid (91%). HRMS $[M]^+/2$ calculated for $CuC_{16}H_{29}N_5$ 177.0854 Found 177.0858 with % abund. *m/z* 177.0871(100), 177.5872(19.47) 178.0850 (46.41), 178.5863 (8.79); FTIR (neat) 3408, 2935, 1658, 1612, 1448, 1292, 812.0 cm^{-1}; UV (MeOH, ε(M^{-1}, cm^{-1})) 621 (186), 257 (3200), 204 (4000)

2.2.24. Synthesis of MS4:Cu

Blue solid (77%); HRMS $[M]^+/2$ calculated for $CuC_{14}H_{31}N_5O_3$ 190.0856 Found 190.0855 with % abund. *m/z* 190.0855(100), 190.5885(17.44) 191.0868 (46.66), 191.5878 (7.94); FTIR (neat) 3224, 2933, 1611, 1457, 1291, 1116 cm^{-1}; UV (MeOH, ε(M^{-1}, cm^{-1})) λ 603 (194), 272 (3670), 200 (10229)

2.3. Synthesis and characterization of deferiprone-based compounds

2.3.1. 3-(benzyloxy)-2-methyl-4H-pyran-4-one (MS5C)

Sodium hydroxide (2.00 ml, 7.00 M) was added with stirring to a solution of 2-methyl-3-hydroxy-4-pyrone (1.78 g, 14.0 mmol) in methanol (18 ml), followed by the addition of benzyl bromide (1.91 mL, 16 mmol). The mixture was stirred at reflux for 6 hours. The solvent was then removed to afford an orange oil. The crude compound was dissolved in dichloromethane (20 ml) and transferred to a 100 ml separating funnel. The organic phase washed five times with sodium hydroxide (30ml, 5%). The organic phase was separated then washed with brine (30ml). The organic phase was dried using anhydrous sodium sulfate, filtered, and the solvent removed using a rotary evaporator to give a light yellow oil (2.57 g, 11.9 mmol). Yield 85%; ^{1}H NMR (δ, 500 MHz, $CDCl_3$) 7.60 (d, *J*= 5.5, 1H, H2), 7.41-7.34(m, 5H, H11,12,13,14,15), 6.37(d, *J*= 6.0, 1H, H3), 5.16(s, 2H, H9), 2.09(s, 3H, H16).

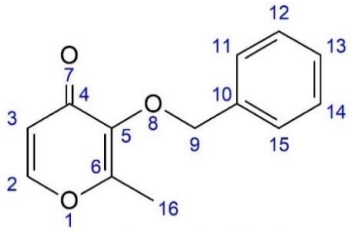

2.3.2. R/S-tert-Butyl{1-[3-(benzyloxy)-2-methyl-4-oxopyridin-1(4H)-yl]propan-2-yl}carbamate (MS5A)

3-(Benzyloxy)-2-methyl-4H-pyran-4-one (0.170 g, 0.785 mmol) and *rac-tert*-butyl(1-aminopropan-2-yl)carbamate (0.150 g, 0.860 mmol) were placed in a single neck round bottom flask and dissolved in ethanol:water (20 mL, 2:3). Sodium hydroxide (2.80 mL, 2.00 M) was added dropwise with stirring at 0 °C. The reaction mixture was stirred at room temperature for 24 h. The volume of the solution was reduced using a rotary evaporator followed by addition of water (20 mL). The mixture was extracted three times with chloroform (20mL). The organic phases were combined and washed three times with brine. The organic phase was separated and dried using sodium sulfate. The solvent was filtered

and then evaporated using a rotary evaporator. The crude compound was purified using column chromatography with two solvent systems. First, ethyl acetate: hexane (3:1) was used to elute impurities. Dichloromethane: methanol (9:1) was used to elute the target compound. Removal of the solvent gave a yellow oil (0.100 g, 0.270 mmol). Yield 35%; ^{1}H NMR (δ, 500 MHz, $CDCl_3$) 7.43-7.3 (m, 5H, H18,19,20,21,22), 7.17 (d, 1H, *J*=7.5 Hz, H2), 6.4(d, *J*=7.5Hz, 1H, H3), 5.24(s, 2H, H16), 3.93(m, 1H, H8), 3.82-3.64(m, 2H, H7), 2.18(s, 3H, H23), 1.42(s, 9H, H13,27,26), 1.13(d, *J*=7.0 Hz, 3H, H24), ^{13}C NMR δ: 173, 155, 146, 140, 138, 129, 128, 128, 117, 80.00, 73.0, 58.0, 46.3, 28.3, 18.0, 13.0; HRMS $[M+H]^+$calc. $C_{21}H_{29}N_2O_4$ 373.2127, found 373.2124.

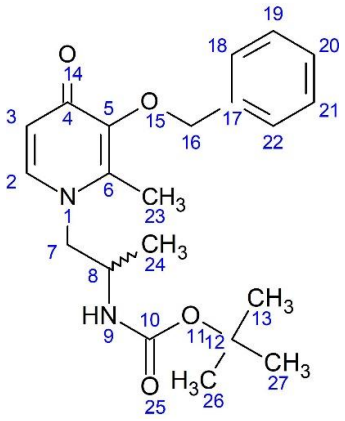

2.3.3. tert-butyl {(2R)-1-[3-(benzyloxy)-2-methyl-4-oxopyridin-1(4H)-yl]propan-2-yl}carbamate (MS6A)

3-(Benzyloxy)-2-methyl-4H-pyran-4-one (0.130 g, 0.601 mmol) and tert-butyl [(2R)-1-aminopropan-2-yl]carbamate (0.130 g, 0.746 mmol) were placed in a single neck round bottom flask and dissolved in ethanol:water (20 mL, 2:3). Sodium hydroxide (2.80 mL, 2.00 M) was added dropwise with stirring at 0 °C. The reaction mixture was stirred at room temperature for 24 h. The volume of the solution was reduced using a rotary evaporator followed by addition of water (20 mL). The mixture was extracted three times with chloroform (20mL). The organic phases were combined and washed three times with brine. The organic phase was separated and dried using sodium sulfate. The solvent was filtered and then evaporated using a rotary evaporator. The crude compound was purified using column chromatography with two solvent systems. First, ethyl acetate: hexane (3:1) was

used to elute impurities. Dichloromethane: methanol (9:1) was used to elute the target compound. Removal of the solvent gave a yellow oil (89.5mg, 0.240 mmol). Yield 40%; ^{1}H NMR (δ, 500 MHz, $CDCl_3$) 7.43-7.28 (m, 5H, H18,19,20,21,22), 7.18 (d, 1H, *J*=7.5 Hz, H2), 6.40(d, *J*=7.5Hz, 1H, H3), 5.22(s, 2H, H16), 3.90(m, 1H, H8), 3.84-3.65(m, 2H, H7), 2.17(s, 3H, H23), 1.41(s, 9H, H13,27,26), 1.13(d, *J*=7.0Hz, 3H, H24), ^{13}C NMR δ: 173, 155, 146, 140, 138, 129, 128, 128, 117, 80.00, 73.0, 58.0, 46.3, 28.3, 18.0, 13.0; HRMS $[M+H]^{+}$calc. $C_{21}H_{29}N_2O_4$ 373.2127, found 373.2128.

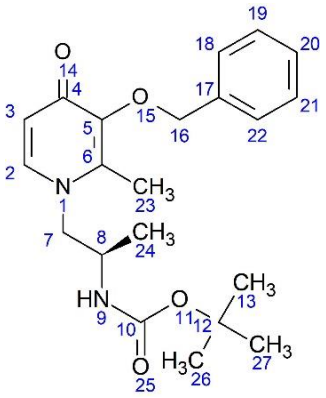

2.3.4. tert-butyl {(2S)-1-[3-(benzyloxy)-2-methyl-4-oxopyridin-1(4H)-yl]propan-2-yl}carbamate (MS7A)

3-(Benzyloxy)-2-methyl-4H-pyran-4-one (0.200 g, 0.925 mmol) and tert-butyl [(2S)-1-aminopropan-2-yl]carbamate (0.35 0g, 2.00 mmol) were placed in a single neck round bottom flask and dissolved in ethanol:water (20 mL, 2:3). Sodium hydroxide (3.50 mL, 2.00 M) was added dropwise with stirring at 0 °C. The reaction mixture was stirred at room temperature for 24 h. The volume of the solution was reduced using a rotary evaporator followed by addition of water (30 mL). The mixture was extracted three times with chloroform (30mL). The organic phases were combined and washed three times with brine. The organic phase was separated and dried using sodium sulfate. The solvent was filtered and then evaporated using a rotary evaporator. The crude compound was purified using column chromatography with two solvent systems. First, ethyl acetate: hexane (3:1) was used to elute impurities. Dichloromethane: methanol (9:1) was used to elute the target compound. Removal of the solvent gave a yellow oil (141 mg, 0.379 mmol). Yield 41%; ^{1}H

NMR (δ, 500 MHz, $CDCl_3$) 7.43-7.28 (m, 5H, H18,19,20,21,22), 7.17 (d, 1H, *J*=7.5 Hz, H2), 6.40(d, *J*=7.5Hz, 1H, H3), 5.24(s, 2H, H16), 3.94(m, 1H, H8), 3.84-3.64(m, 2H, H7), 2.18(s, 3H, H23), 1.41(s, 9H, H13,27,26), 1.13(d, *J*=7.0Hz, 3H, H24), ^{13}C NMR δ: 174, 155, 146, 140, 138, 129, 128, 128, 117, 80.00, 73.0, 58.0, 46.3, 28.3, 18.0, 13.0; HRMS $[M+H]^+$calc. $C_{21}H_{29}N_2O_4$ 373.2127, found 373.2118.

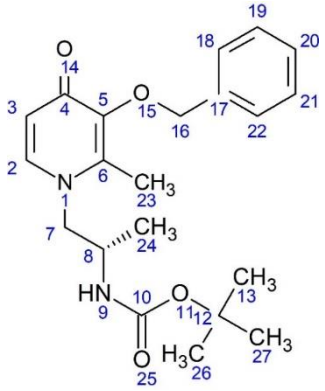

2.3.5. 1-(2-aminoethyl)-3-(benzyloxy)-2-methylpyridin-4(1H)-one (MS8A)

3-(Benzyloxy)-2-methyl-4H-pyran-4-one (0.200 g, 0.925 mmol) and ethane-1,2-diamine (0.615 g, 4.63 mmol) were placed in a single neck round bottom flask and dissolved in ethanol:water (30 mL, 2:3). Sodium hydroxide (16.0 mL, 2.00 M) was added dropwise with stirring at 0 °C. The reaction mixture was stirred at room temperature for 24 h. The volume of the solution was reduced using a rotary evaporator followed by addition of water (30 mL). The mixture was extracted three times with chloroform (30mL). The organic phases were combined and washed three times with brine. The organic phase was separated, dried using sodium sulfate and filtered. The solvent was then evaporated using a rotary evaporator. The crude compound was purified using column chromatography with dichloromethane: methanol: ammonia 83:15:2. Removal of the solvent gave a light brown oil (83.43 mg, 0.323 mmol). Yield 35%; ^1H NMR (δ, 500 MHz, $CDCl_3$) 7.42-7.27 (m, 5H, H14, 15, 16, 17, 18), 7.26 (d, 1H, *J*=6.5 Hz, H2), 6.44(d, *J*=7.0 Hz, 1H, H3), 5.23(s, 2H, H12), 3.82(t, *J*=6.0 Hz, 2H, H7), 2.96(t, *J*=6.5Hz, 2H, H8), 2.12(s, 3H, H19), ^{13}C NMR δ: 173, 146, 141, 139, 137, 129, 128, 128, 117, 73.0, 56.0, 42.0, 12.5; HRMS $[M+H]^+$calc. $C_{15}H_{19}N_2O_2$ 259.1447, found 259.1442

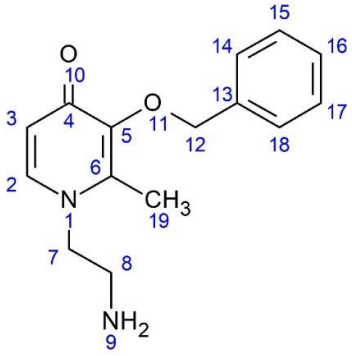

2.3.6. 3-(benzyloxy)-2-methyl-1-(2-methylpropyl)pyridin-4(1H)-one (MS9A)

3-(Benzyloxy)-2-methyl-4H-pyran-4-one (0.170 g, 0.785 mmol) and 2-methylpropan-1-amine (78.0 µL, 0.785 mmol) were placed in a single neck round bottom flask and dissolved in ethanol:water (20 mL, 2:3). Sodium hydroxide (2.81 mL, 2.00 M) was added dropwise with stirring at 0 °C. The reaction mixture was stirred at room temperature for 24 h. The volume of the solution was reduced using a rotary evaporator followed by addition of water (30 mL). The mixture was extracted three times with chloroform (30mL). The organic phases were combined and washed three times with brine. The organic phase was separated and dried using sodium sulfate. The solvent was filtered and then evaporated using a rotary evaporator. The crude compound was purified using column chromatography with two solvent systems. First, ethyl acetate: hexane (3:1) was used to elute impurities. Dichloromethane: methanol (9:1) was used to elute the target compound. Removal of the solvent gave an orange oil (198 mg, 0.73 mmol). Yield 92.9%; ^{1}H NMR (δ, 500 MHz, $CDCl_3$) 7.42-7.27 (m, 5H, H14, 15, 16, 17, 18), 7.14 (d, 1H, *J*=7.5 Hz, H2), 6.42(d, *J*=7.5Hz, 1H, H3), 5.25(s, 2H, H12), 3.55(d, *J*=7.5Hz, 2H, H7), 2.07(s, 3H, H19), 1.9(m, 1H, H8), 0.9(d, *J*=6.5Hz, 6H, H9, 20), ^{13}C NMR δ: 173, 146, 139, 138, 129, 128, 128, 117, 72.9, 60.8, 29.7, 19.6, 12.6; HRMS $[M+H]^+$calc. $C_{17}H_{22}NO_2$ 272.1651, found 272.1650.

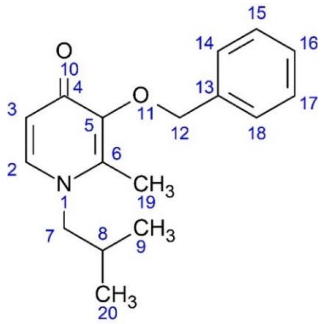

2.3.7. 1-(2-ammoniopropyl)-3-(benzyloxy)-4-hydroxy-2-methylpyridinium (MS5B)

tert-Butyl[1-[3-(benzyloxy)-2-methyl-4-oxopyridin-1(4H)-yl]propan-2-yl]carbamate (0.100 g, 0.270 mmol) was dissolved in diethyl ether (7.00mL) and placed in a 50 mL round bottom flask flushed with nitrogen gas and sealed with a septum. Hydrogen chloride in diethyl ether (10.00 mL, 2.00 M) was added to the flask by syringe. After 3 hours, a fine yellow powder

had formed. The volatile components were removed using rotary evaporator to give a yellow solid (70.1 mg, 0.256 mmol). Yield 95%; ^{1}H NMR (δ, 500 MHz, DMSO) 8.47 (s, 3H, H20a,b,c), 8.35 (d, 1H, *J*=7.0 Hz, H5), 7.48-7.37(m, 5H, H11,12,13,14,15), 7.20(d, *J*=7.0Hz, 1H, H4), 5.10(s, 2H, H9), 4.52-4.43(m, 2H, H17), 3.65(m, 1H, H18), 2.50(s, 3H, H7), 1.25(d, *J*=6.0Hz, 3H, H19); ^{13}C NMR δ: 144, 143, 137, 129, 129, 129, 114, 74.4, 58.1, 46.4, 16.3, 14.0; HRMS $[M]^{2+}$ calc. $[C_{16}H_{22}N_2O_2]^{2+}$ 273.1609, found 273.1571.

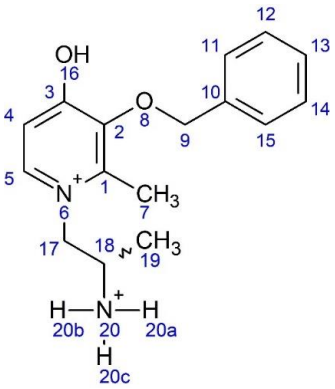

2.3.8. 1-[(2R)-2-ammoniopropyl]-3-(benzyloxy)-4-hydroxy-2-methylpyridinium (MS6B)

Tert-butyl [(2R)-1-[3-(benzyloxy)-2-methyl-4-oxopyridin-1(4H)-yl]propan-2-yl]carbamate (89.5 g, 0.240 mmol) was dissolved in diethyl ether (5.00 mL) and placed in a 50 mL round bottom flask flushed with nitrogen gas and sealed with a septum. Hydrogen chloride in diethyl ether (10.00 mL, 2.00 M) was added to the flask by syringe. After 3 hours, a fine yellow powder formed. The volatile components were removed using a rotary evaporator to give a yellow solid (62.5 mg, 0.228 mmol). Yield 95%; ^{1}H NMR (δ, 500 MHz, DMSO) 8.47 (s, 3H, H20a,b,c), 8.35 (d, 1H, *J*=7.0 Hz, H5), 7.48-7.37(m, 5H, H11,12,13,14,15), 7.20(d, *J*=7.0Hz, 1H, H4), 5.10(s, 2H, H9), 4.52-4.43(m, 2H, H17), 3.65(m, 1H, H18), 2.50(s, 3H, H7), 1.25(d, *J*=6.0Hz, 3H, H19); ^{13}C NMR δ: 144 (1 C, C3), 143 (1C, C5), 137(1 C, C10), 129 (2C, C12, 14), 129 (2C, C11,15), 129(1C, C13), 114 (1C, C4), 74.4(1C, C9), 58.1(1C, C18), 46.4(1C, C17), 16.3 (1C, C19), 14 (1C, C7); HRMS $[M]^{2+}$ calc. $[C_{16}H_{22}N_2O_2]^{2+}$ 273.1609, found 273.1574.

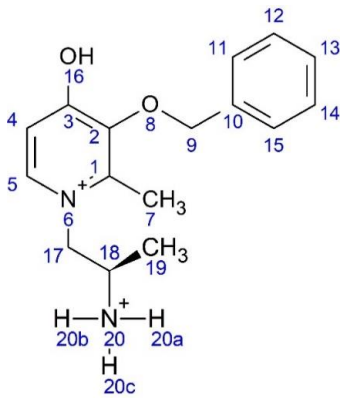

2.3.9. 1-[(2S)-2-ammoniopropyl]-3-(benzyloxy)-4-hydroxy-2-methylpyridinium (MS7B)

Tert-butyl [(2S)-1-[3-(benzyloxy)-2-methyl-4-oxopyridin-1(4H)-yl]propan-2-yl]carbamate (141 mg, 0.379 mmol) was dissolved in diethyl ether (10mL) and placed in a 50mL round bottom flask flushed with nitrogen gas and sealed with a septum. Hydrogen chloride in diethyl ether(10.00 mL, 2.00M) was added to the flask by syringe. After 3 hours, a fine yellow powder had formed. The volatile components were removed using rotary evaporator to give a yellow solid (101 mg, 0.367 mmol). Yield 97%; ^{1}H NMR (δ, 500 MHz, DMSO) 8.47 (s, 3H, H20a,b,c), 8.38 (d, 1H, *J*=7.0 Hz, H5), 7.48-7.37(m, 5H, H11,12,13,14,15), 7.20(d, *J*=6.5Hz, 1H, H4), 5.10(s, 2H, H9), 4.57-4.41(m, 2H, H17), 3.66(m, 1H, H18), 2.5(s, 3H, H7), 1.26(d, *J*=6.5Hz, 3H, H19); ^{13}C NMR δ: 144 (1 C, C3), 143 (1C, C5), 137(1 C, C10), 129 (2C, C12, 14), 129 (2C, C11,15), 129(1C, C13), 114 (1C, C4), 74.3(1C, C9), 58.0 (1C, C18), 46.4(1C, C17), 16.3 (1C, C19), 14.0 (1C, C7); HRMS $[M]^{2+}$ calc. $[C_{16}H_{22}N_2O_2]^{2+}$ 273.1609, found 273.1574.

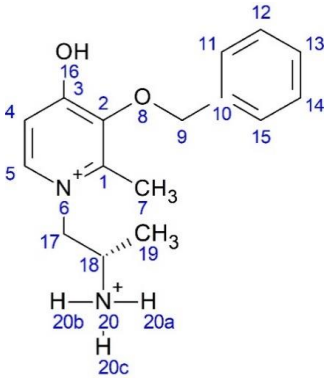

2.3.10. 1-(2-ammoniopropyl)-3,4-dihydroxy-2-methylpyridinium.2HCl (MS5)

1-(2-Ammoniopropyl)-3-(benzyloxy)-4-hydroxy-2-methylpyridinium (70.1 mg, 0.256 mmol) was dissolved in methanol:water (100 mL, 37%) and placed in a 250 mL quick fit conical flask. Aqueous HCl (10.00 mL, 3.00 M) was added followed by palladium on carbon (0.200 g, 5%). The mixture was stirred under an atmosphere of H_2 for 4 hours. The solution was filtered using a Büchner funnel and the filtrate was evaporated using a rotary evaporator and the resulting materials was placed in a freeze drier for 24 hrs to remove all solvent residue to give a purple solid (44.8 mg, 0.2432 mmol). Yield 95%; Optical rotation +2^{o}; ^{1}H

NMR (δ, 500 MHz, DMSO) 8.52 (s, 3H, H13a,b,c), 8.27 (d, 1H, *J*=7.0 Hz, H5), 7.21(d, *J*=7.0Hz, 1H, H4), 4.60-4.48(m, 2H, H10), 3.68(m, 1H, H11), 2.54(s, 3H, H7), 1.28(d, *J*=6.5Hz, 3H, H12); ^{13}C NMR δ: 160, 144, 143, 139, 111, 58.0, 46.4, 16.3, 13.5; HRMS $[M+1]^{2+}$ calc. $[C_9H_{16}N_2O_2]^{2+}$ 183.1139, found 183.1101; FTIR (neat) 3375, 2834, 1635, 1575, 1507, 1328, 1221, 1107, 1029, 910.0, 792.0, 595.0.

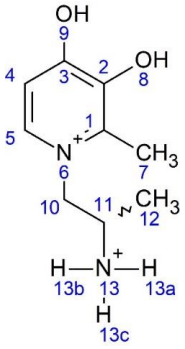

2.3.11. 1-[(2R)-2-ammoniopropyl]-3,4-dihydroxy-2-methylpyridinium.2HCl (MS6)

1-[(2R)-2-ammoniopropyl]-3-(benzyloxy)-4-hydroxy-2-methylpyridinium (62.5 mg, 0.228 mmol) was dissolved in methanol:water (100 mL, 37%) and placed in a 250 mL quick fit conical flask. Aqueous HCl (10.00mL, 3.00M) was added followed by palladium on carbon (0.200 g, 5%). The mixture was stirred under an atmosphere of H_2 for 4 hours. The solution was filtered using a Büchner funnel and the filtrate was evaporated using a rotary evaporator and the resulting materials was placed in a freeze drier for 24 hrs to remove all solvent residue to give a purple solid (40.7 mg, 0.221 mmol). Yield 97%; Optical rotation -22^o; ^{1}H NMR (δ, 500 MHz, DMSO) 8.58 (s, 3H, H13a,b,c), 8.29 (d, 1H, *J*=6.5 Hz, H5), 7.23(d, *J*=6.0Hz, 1H, H4), 4.6-4.49(m, 2H, H10), 3.68(m, 1H, H11), 2.54(s, 3H, H7), 1.29(d, *J*=6.5Hz, 3H, H12); ^{13}C NMR δ: 160 , 144, 143, 139, 111, 58, 46.4, 16.3, 13.5; HRMS $[M+1]^{2+}$ calc. $[C_9H_{16}N_2O_2]^{2+}$ 183.1139, found 183.1122, FTIR (neat) 3375, 2835, 1635, 1575, 1507, 1328, 1222, 1107, 1029, 910.00, 792.0, 597.0.

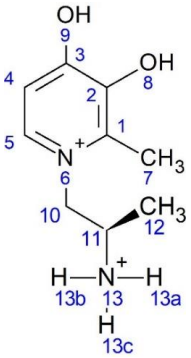

2.3.12. 1-[(2S)-2-ammoniopropyl]-3,4-dihydroxy-2-methylpyridinium.2HCl (MS7)

1-[(2S)-2-ammoniopropyl]-3-(benzyloxy)-4-hydroxy-2-methylpyridinium (101 mg, 0.367 mmol) was dissolved in methanol:water (150 mL, 37%) and placed in a 250mL quick fit conical flask. Aqueous HCl (10.00mL, 3.00M) was added followed by palladium on carbon (0.350 g, 5%). The mixture was stirred under an atmosphere of H_2 for 4 hours. The solution was filtered using a Büchner funnel and the filtrate was evaporated using a rotary evaporator and the resulting materials was placed in a freeze drier for 24 hrs to remove all solvent residue to give a purple solid (65.0 mg, 0.352 mmol). Yield 96%; Optical rotation +22°; ^{1}H NMR (δ, 500 MHz, DMSO) 8.51 (s, 3H, H13a,b,c), 8.28 (d, 1H, *J*=6.5 Hz, H5), 7.22(d, *J*=6.0Hz, 1H, H4), 4.60-4.50(m, 2H, H10), 3.69(m, 1H, H11), 2.54(s, 3H, H7), 1.29(d, *J*=6.5Hz, 3H, H12); ^{13}C NMR δ: 160, 144, 143, 139, 111, 58.0, 46.4, 16.3, 13.5; HRMS $[M+1]^{2+}$ calc. $[C_9H_{16}N_2O_2]^{2+}$ 183.1139, found 183.1138. FTIR (neat) 3375, 2834, 1635, 1575, 1507, 1328, 1221, 1107, 1029, 910.00, 792.0, 597.0.

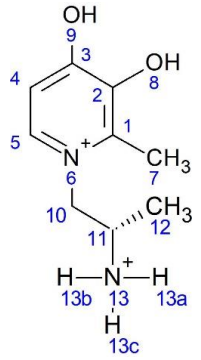

2.3.13. 1-(2-ammonioethyl)-3,4-dihydroxy-2-methylpyridinium.2HCl (MS8)

1-(2-aminoethyl)-3-(benzyloxy)-2-methylpyridin-4(1*H*)-one (83.4 mg, 0.323 mmol) was dissolved in methanol:water (120 mL, 37%) and placed in a 250mL quick fit conical flask. Aqueous HCl (10.00mL, 3.00M) was added followed by palladium on carbon (0.300 g, 5%). The mixture was stirred under an atmosphere of H_2 for 4 hours. The solution was filtered using a Büchner funnel and the filtrate was evaporated using a rotary evaporator and the resulting materials was placed in a freeze drier for 24 hrs to remove all solvent residue to give a bright purple Solid (53.87 mg, 0.3165 mmol). Yield 98%; ^{1}H NMR (δ, 500 MHz, CD_3OD)

8.18 (d, 1H, *J*=7.0 Hz, H5), 7.14(d, *J*=7.0Hz, 1H, H4), 4.69(t, 2H, *J*=7.0Hz, H10), 3.47(t, 2H, *J*=7.5Hz, H11), 2.67(s, 3H, H7); ^{13}C NMR δ: 160.0, 149, 144, 138, 111, 52.5, 38.1, 11.5; HRMS $[M+1]^{2+}$ calc. $[C_8H_{14}N_2O_2]^{2+}$ 169.0983, found 169.0947. FTIR (neat) 3160, 2906, 1629, 1461, 1324, 1254, 1152, 1021, 947.0, 818.0, 759.0, 640.0, 601.0.

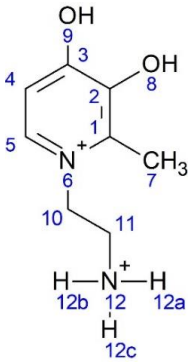

2.3.14. 3,4-dihydroxy-2-methyl-1-(2-methylpropyl)pyridinium.HCl (MS9)

3-(benzyloxy)-2-methyl-1-(2-methylpropyl)pyridin-4(1*H*)-one (198 mg, 0.730 mmol) was dissolved in methanol:water (150 mL, 37%) and placed in a 250mL quick fit conical flask. Aqueous HCl (10.00mL, 3.00M) was added followed by palladium on carbon (0.600 g, 5%). The mixture was stirred under an atmosphere of H_2 for 4 hours. The solution was filtered using a Büchner funnel and the filtrate was evaporated using a rotary evaporator and the resulting materials was placed in a freeze drier for 24 hrs to remove all solvent residue to give a bright purple Solid (125 mg, 0.686 mmol). Yield 94%; ^{1}H NMR (δ, 500 MHz, DMSO) 8.21 (d, 1H, *J*=7.0Hz, H5), 7.36(d, *J*=7.0Hz, 1H, H4), 4.18(d, 2H, *J*=7.5Hz, H10), 2.52(s, 3H, H7), 2.08(m, 1H, H11), 0.88(d, *J*= 6.5Hz, 6H, H12,13); ^{13}C NMR δ: 159, 144, 142, 139, 111, 63.0, 29.0, 19.5, 13.1; HRMS $[M]^{+}$ calc. $[C_{10}H_{16}NO_2]^{+}$ 182.1181, found 182.1174. FTIR (neat) 3343, 2962, 1631, 1495, 1333, 1133, 1032, 792, 594.

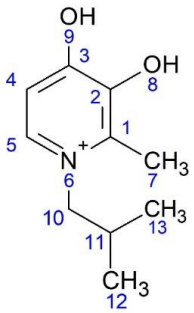

2.3.15. 3[1-(2-ammoniopropyl)-3,4-dihydroxy-2-methylpyridinium]Fe (MS5:Fe)

A methanolic solution of ferric nitrate nonahydrate (1.50 mL, 0.500 mM) was added to a methanolic solution of 1-(2-ammoniopropyl)-3,4-dihydroxy-2-methylpyridinium (1.5 mL, 1.5 mM). The solution was stirred at room temperature for 15 min. Crystals were grown by diffusion of diethyl ether into a methanolic solution in a sealed vessel to give maroon

coloured crystals. HRMS $[M]^+$ calc. $[C_9H_{13}N_2O_2]_2Fe$ 416.1350, found 416.1319 with % abund. *m/z* 416.1319 (6.36), 417.1316 (1.3), 418.1262 (100), 419.1288(23.67) and $[M+1]^+$ calc. $[C_9H_{13}N_2O_2]_3Fe$ 598.2399, found 598.234 with % abund. *m/z* 598.2340 (6.36), 600.2296 (100), 601.2321(34.31) FTIR (neat) 3367, 1604, 1492, 1348, 1279, 825.0, 577.0; UV (10% MeOH in PBS, ε(M^{-1}, cm^{-1})))) 460(4320), 292(27700).

2.3.16. 3[1-[(2R)-2-ammoniopropyl]-3,4-dihydroxy-2-methylpyridinium]Fe (MS6:Fe)

A methanolic solution of ferric nitrate nonahydrate (1.50 mL, 0.500 mM) was added to a methanolic solution of 1-[(2R)-2-ammoniopropyl]-3,4-dihydroxy-2-methylpyridinium (1.5 mL, 1.5 mM). The solution was stirred at room temperature for 15 min. Crystals were grown by diffusion of diethyl ether into a methanolic solution in a sealed vessel to give maroon coloured crystals. HRMS $[M]^+$ calc. $[C_9H_{13}N_2O_2]_2Fe$ 416.1350, found 416.1331 with % abund. *m/z* 416.1403 (6.36), 417.14 (1.3), 418.1336 (100), 419.1356(23.67) and $[M+1]^+$ calc. $[C_9H_{13}N_2O_2]_3Fe$ 598.2399, found 598.2450 with % abund. *m/z* 598.2450 (6.36), 600.2403 (100), 601.2436(34.31) FTIR (neat) 3367, 1604, 1492, 1348, 1279, 825.0, 577.0; UV (10% MeOH in PBS, ε(M^{-1}, cm^{-1})), 460(4308), 292(28044).

2.3.17. 3[1-[(2S)-2-ammoniopropyl]-3,4-dihydroxy-2-methylpyridinium]Fe (MS7:Fe)

A methanolic solution of ferric nitrate nonahydrate (1.50 mL, 0.500 mM) was added to a methanolic solution of 1-[(2S)-2-ammoniopropyl]-3,4-dihydroxy-2-methylpyridinium (1.5 mL, 1.5 mM). The solution was stirred at room temperature for 15 min. Crystals were grown by diffusion of diethyl ether into a methanolic solution in a sealed vessel to give maroon coloured crystals. HRMS $[M]^+$ calc. $[C_9H_{13}N_2O_2]_2Fe$ 416.1350, found 416.1332 with % abund. *m/z* 416.1332 (6.36), 417.1410 (1.3), 418.1289 (100), 419.1314(23.67), 420.1334(3.8) and $[M+1]^+$ calc. $[C_9H_{13}N_2O_2]_3Fe$ 598.2399, found 598.235 with % abund. *m/z* 598.235 (6.36),

600.2318 (100), 601.2362(34.31) FTIR (neat) 3368, 1604, 1491, 1348, 1279, 825.0, 576.0; UV (10% MeOH in PBS, ε(M^{-1}, cm^{-1})), 463(4156), 290.00(27600).

2.3.18. 3[1-(2-ammonioethyl)-3,4-dihydroxy-2-methylpyridinium]Fe (MS8:Fe)

A methanolic solution of ferric nitrate nonahydrate (1.50 mL, 0.500 mM) was added to a methanolic solution of 1-(2-ammonioethyl)-3,4-dihydroxy-2-methylpyridinium (1.5 mL, 1.5 mM). The solution was stirred at room temperature for 15 min. Crystals were grown by diffusion of diethyl ether into a methanolic solution in a sealed vessel to give maroon coloured crystals. HRMS $[M]^+$ calc. $[C_8H_{11}N_2O_2]_2Fe$ 388.1032, found 388.1014 with % abund. *m/z* 388.1014 (6.36), 389.1020 (1.22), 390.0966 (100), 391.0993(21.46), 392.1008(3.31) and $[M+1]^+$ calc. $[C_8H_{11}N_2O_2]_3Fe$ 556.1930, found 556.1800 with % abund. *m/z* 556.1800(6.35), 558.1821 (100), 559.1845(31.02) FTIR (neat) 3365, 1552, 1489, 1345, 1280, 1043, 823.0, 542.0; UV (10% MeOH in PBS, ε(M^{-1}, cm^{-1})), 462(4150), 290(28000).

2.3.19. 3[3,4-dihydroxy-2-methyl-1-(2-methylpropyl)pyridinium]Fe (MS9:Fe)

A methanolic solution of ferric nitrate nonahydrate (1.50 mL, 0.500 mM) was added to a methanolic solution of 3,4-dihydroxy-2-methyl-1-(2-methylpropyl)pyridinium (1.5 mL, 1.5 mM). The solution was stirred at room temperature for 15 min. Crystals were grown by diffusion of diethyl ether into a methanolic solution in a sealed vessel to give maroon coloured crystals. HRMS $[M]^+$ calc. $[C_{10}H_{14}NO_2]_2Fe$ 414.1439, found 414.1269 with % abund. *m/z* 414.1269 (6.36), 415.1316 (1.45), 416.1224 (100), 417.1251(25.12), 418.1280(4.14) and $[M+1]^+$ calc. $[C_{10}H_{14}NO_2]_3Fe$ 595.2543, found 595.2263 with % abund. *m/z* 595.2263(6.34), 597.2243 (100), 598.2267(36.48), 599.2320(8) FTIR (neat) 3366, 2959, 1725, 1607, 1491, 1343, 1261, 825.0, 561.0; UV (10% MeOH in PBS, ε(M^{-1}, cm^{-1})), 463(4180), 286(28200).

2.4. Synthesis and characterization of 8-hydroxyquinoline compounds

2.4.1. 8-Hydroxyquinoline-2-carbaldehyde (MS10A)

2-methylquinolin-8-ol (2.00 g, 12.5 mmol) and selenium dioxide (1.75g, 15.5mmol) were dissolved in dioxane (150 mL) and water (2mL). The mixture was stirred at 80 ^{o}C for 24 hours under nitrogen, cooled to room temperature and filtered. The solvent of the filtrate was evaporated using a rotary evaporator and the crude material was purified using silica gel column chromatography eluting with ethylacetate:n-hexane (5:95).

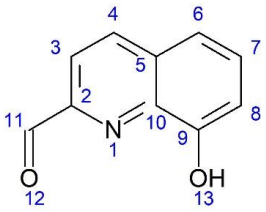

Light yellow solid (1.73 g, 10 mmol). Yield 80%; ^{1}H NMR (δ, 500 MHz, $CDCl_3$) 10.23 (S, 1H, H11), 8.34(d, *J*=8.5Hz, 1H, H4), 8.08(d, *J*=8.5Hz, 1H, H3), 7.63(m, 1H, H7), 7.45(dd, *J*=8.5, 1Hz, 1H, H6), 7.3(dd, *J*=7.5, 1.0 Hz, 1H, H8).

2.4.2. 8-Hydroxyquinoline-5-carbaldehyde (MS13A)

8-Hhydroxyquinoline (30.00 g, 0.210 mol) was dissolved in ethanol (80 mL) and placed in a 250 mL round bottom flask. Aqueous sodium hydroxide (36%) was added until a yellow precipitate started to appear. The mixture was heated with stirring to ~100 ^{o}C until the precipitate disappeared. The temperature was decreased to 50 ^{o}C and chloroform (50 mL) was added slowly with vigorous stirring. The reaction mixture was stirred at reflux for 12 h. After cooling to room temperature, the solvent was removed using a rotary evaporator. Water (100 mL) was added to the residue and the pH adjusted to 5 by using aqueous hydrochloric acid (1 M). A brown/yellow precipitate formed, which was collected by filtration then dissolved in chloroform. The chloroform mixture was filtered and the solvent removed using a rotary evaporator. The crude product was purified by Soxhlet extraction for three days with petroleum spirit (100-200 ^{o}C fraction). The solid material was recrystallised

from absolute ethanol to give white crystals (3.3 g, 18.9 mmol). Yield 9%; ^{1}H NMR (δ, 500 MHz, $CDCl_3$) 10.15 (s, 1H, H11), 9.7(dd, *J*=8.5Hz, 1.5Hz, 1H, H2), 8.88(dd, *J*=4.5, 1.5Hz 1H, H4), 8.02(d, *J*=8.0Hz, 1H, H7), 7.68(m, 1H, H3), 7.3(d, *J*=8.0Hz, 1H, H8).

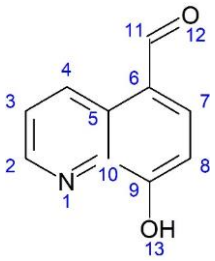

2.4.3. 8-hydroxyquinoline-7-carbaldehyde (MS12A)

This compound was prepared using the same synthetic method as used for 8-hydroxyquinoline-5-carbaldehyde but the crude product was not subjected to Soxhlet extraction. The crude product was purified from its isomer by column chromatography with a gradient of petroleum spirit: ethyl acetate (20:1) and then crystallised from absolute ethanol to give light yellow crystals (1.50 g, 8.40 mmol). Yield 4%; ^{1}H NMR (δ, 500 MHz, $CDCl_3$) 10.37 (s, 1H, H11), 8.96(dd, *J*=4.0, 2Hz, 1H, H2), 8.18(dd, *J*=8.5, 1.5Hz, 1H, H4), 7.76(d, *J*=8.5Hz, 1H, H6), 7.61(m, 1H, H3), 7.39(d, *J*=9.0 Hz, 1H, H7).

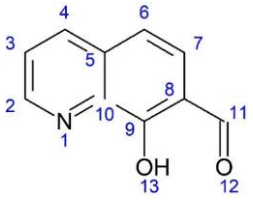

2.4.4. 8-(benzyloxy)quinoline-2-carbaldehyde

8-Hydroxyquinoline-2-carbaldehyde (0.100 g, 0.570 mmol) was dissolved in methanol (10 mL). Aqueous sodium hydroxide (5 mL, 0.1 M) was added dropwise to the stirred methanolic solution. Benzyl bromide (84.0 µL) was added followed by heating to reflux for 18 hours. After 18 hours the solvent volume was reduced using a rotary evaporator. The crude product was dissolved in dichloromethane (20 ml) and the solution transferred to a separating funnel for liquid-liquid extraction. The organic phase was washed using aqueous sodium hydroxide (20ml, 5%). This process was repeated three times, and the collected organic phase was dried using sodium sulfate. The solution was filtered and the

dichloromethane was evaporated using a rotary evaporator to give a yellow solid (1.12 g, 0.430 mmol). Yield 85%; ^{1}H NMR (δ, 500 MHz, $CDCl_3$) 10.3 (s, 1H, H11), 8.30(d, *J*=8.5Hz, 1H, H4), 8.08(d, *J*=8.5Hz, 1H, H3), 7.63-7.16(m, 8H, H6,7,8,16,17,18,19,20), 5.51 (s, 2H, H14).

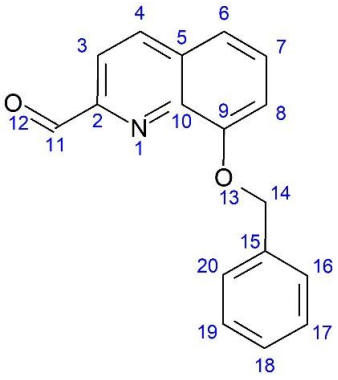

2.4.5. 2-(-2-nitroprop-1-en-1-yl)quinolin-8-ol (MS10B)

8-Hydroxyquinoline-2-carbaldehyde (0.100 g, 0.580 mmol) was added to a single necked round bottom flask and nitroethane (10 ml) and ammonium acetate (0.1 g) were added. The solution was stirred at reflux for 5 hours. The solution was concentrated using a rotary evaporator. The crude product was dissolved in 20mL of dichloromethane and washed three times with brine water. The organic phase was collected and dried using sodium sulfate, filtered, and the solvent was evaporated using a rotary evaporator. The crude compound was purified by silica gel column chromatography with mobile phase dichloromethane: hexane with ratio 75:25. Yellow solid (126.9 mg, 0.550 mmol). Yield 95%; ^{1}H NMR (δ, 500 MHz, $CDCl_3$) 8.26 (d, 1H, *J*=9.0 Hz, H4), 8.14 (s, 1H, H11), 7.58-7.52(m, 2H, H7,3), 7.39(d, 1H, *J*=8.5 Hz, H6), 7.25 (d, 1H, overlapped with $CDCl_3$ peak, H8), 2.82(s, 3H, H13); ^{13}C NMR δ: 137, 130, 129, 125, 118, 111, 14.7.

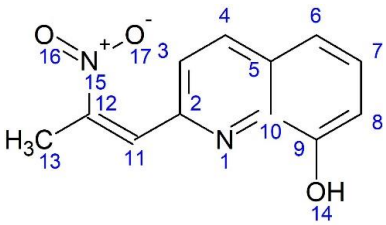

2.4.6. 4-(-2-nitroprop-1-en-1-yl)quinolin-8-ol (MS11B)

8-hydroxyquinoline-4-carbaldehyde (0.100 g, 0.580 mmol) was placed in a single neck round bottom flask and nitroethane (10 ml) and ammonium acetate (0.100 g) was added. The solution was stirred at reflux for 5 hours. After 5 hours, the solution was concentrated by using the rotary evaporator. Then the crude product was dissolved in 20mL of

dichloromethane and washed three times with brine water. The organic phase was collected and dried from water by using sodium sulfate. Finally, dichloromethane was evaporated by rotary evaporator. The crude compound was purified by silica gel column chromatography with mobile phase dichloromethane: hexane with ratio 75:25 respectively. Yellow solid (124 mg, 0.540 mmol). Yield 93%; ^{1}H NMR (δ, 500 MHz, $CDCl_3$) 8.85 (d, 1H, *J*=4.0 Hz, H2), 8.44 (s, 1H, H11), 7.56(m, 1H, H7), 7.37-7.35(m, 2H, H6,3), 7.26 (d, 1H, overlapped with $CDCl_3$ peak, H8), 2.34(s, 3H, H13); ^{13}C NMR δ: 147, 128.9, 128.8, 121, 114, 111, 14.2.

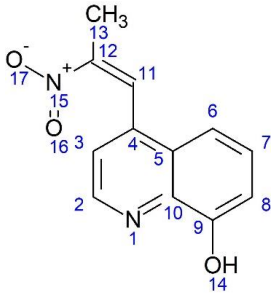

2.4.7. 7-(-2-nitroprop-1-en-1-yl)quinolin-8-ol (MS12B)

8-Hydroxyquinoline-7-carbaldehyde (0.100 g, 0.580 mmol) was added to single neck round bottom flask and nitroethane (10 ml) and ammonium acetate (0.100 g) were added. The solution was stirred at reflux for 5 hours and then the solution was concentrated using a rotary evaporator. The crude product was dissolved in 20mL of dichloromethane and washed three times with brine water. The organic phase was collected, dried using sodium sulfate and filtered. The solvent was evaporated using a rotary evaporator. The crude compound was purified by silica gel column chromatography with mobile phase dichloromethane: hexane with ratio 75:25. Yellow solid (124.18 mg, 0.54 mmol). Yield 94%; ^{1}H NMR (δ, 500 MHz, $CDCl_3$) 8.85 (dd, 1H, *J*=1.5, 4Hz, H2), 8.48 (s, 1H, H11), 8.20(dd, 1H, *J*= 8.0, 1.5 Hz, H4), 7.54(m, 1H, H3), 7.51 (d, 1H, *J*=9.0Hz , H6), 7.40 (d, 1H, *J*=9.0Hz, H7), 2.34(s, 3H, H13); ^{13}C NMR δ: 152, 149, 138, 136, 131, 129, 128, 127, 123, 118, 114, 14.6.

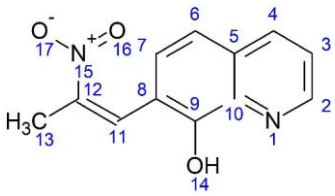

2.4.8. 5-(-2-nitroprop-1-en-1-yl)quinolin-8-ol (MS13B)

8-Hydroxyquinoline-7-carbaldehyde (0.100 g, 0.580 mmol) was added to single neck round bottom flask and nitroethane (10 ml) and ammonium acetate (0.100 g) were added. The solution was stirred at reflux for 5 hours and then the solution was concentrated using a rotary evaporator. The crude product was dissolved in 20mL of dichloromethane and washed three times with brine water. The organic phase was collected, dried using sodium sulfate and filtered. The solvent was evaporated using a rotary evaporator. The crude compound was purified by silica gel column chromatography with mobile phase dichloromethane: hexane with ratio 75:25. Yellow solid (124.2 mg, 0.540 mmol). Yield 94%; ^{1}H NMR (δ, 500 MHz, $CDCl_3$) 8.89 (dd, 1H, *J*=1.5, 4.5Hz, H2), 8.58 (s, 1H, H11), 8.33(dd, 1H, *J*=1.5, 8.5Hz H4), 7.6(m, 1H, H3), 7.55 (d, 1H, *J*=8.0Hz , H7), 7.26 (d, 1H, *J*=8.0Hz, H8), 2.44(s, 3H, H13); ^{13}C NMR δ: 154, 148.4, 148.3, 138, 133, 130, 129.9, 127, 123, 120, 110, 14.4.

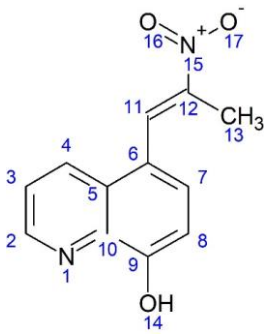

2.4.9. 2-(2-aminopropyl)quinolin-8-ol (MS10)

Anhydrous tetrahydrofuran (10 ml) was transferred into a 100ml three-necked round bottom flask equipped with a magnetic stirring bar, condenser, dropper funnel, rubber septum and nitrogen inlet quick fit on top of the condenser. The round bottom flask was placed on an ice bath followed by addition of $LiAlH_4$ (0.100 g). Separately, 2-(-2-nitroprop-1-en-1-yl)quinolin-8-ol (100 mg, 0.430 mmol) was dissolved in anhydrous tetrahydrofuran (10 ml) and transferred into the dropping funnel and the solution was added was added dropwise over a period of 30 min under a flow of nitrogen and with stirring. An additional 0.100 g of $LiAlH_4$ in tetrahydrofuran (5ml) was added dropwise via the septum. The mixture

was heated at reflux for 4 h with stirring under a nitrogen atmosphere. After cooling to room temperature, the mixture was cooled further in an ice bath and the reaction was quenched by adding hydrated sodium sulfate to the flask until bubbling ceased. A further 0.200g of sodium sulfate was added and the mixture stirred for 1 h at room temperature and then filtered through celite. The solvent was evaporated using a rotary evaporator and the crude product was dissolved in dichloromethane and extracted using 5% aqueous HCl. The aqueous phase was neutralized using aqueous sodium carbonate and transferred to a separating funnel for further liquid-liquid extraction. Aqueous sodium carbonate (20%) was added until pH 11 and then the aqueous phase was further extracted with dichloromethane. The organic phase was collected, dried using anhydrous sodium sulfate, and the solvent was removed using a rotary evaporator to give a brown Solid (18.0 mg, 0.0890 mmol). Yield 20.7 %; ^{1}H NMR (δ, 500 MHz, $CDCl_3$) 8.04 (d, 1H, *J*=8.5Hz, H4), 7.37 (t, 1H, *J*=7.5Hz, H7), 7.27(m, 2H, H6,8), 7.14(d, 1H, *J*=7.5Hz H3), 3.70 (m, 1H, H12), 3.08-3.05 (m, 2H, H11), 1.28(d, 3H, *J*=6.5 Hz, H15); ^{13}C NMR δ: 158, 152, 138, 137, 127.1, 127, 123, 118, 111, 47.2, 46.8, 22.6; HRMS $[M+1]^+$ calc. for $[C_{12}H_{14}N_2O]^+$ 203.1179, found 203.1198; FTIR (neat) 3367, 2925, 1567, 1426, 884.0, 744.0.

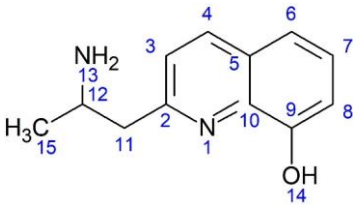

2.4.10. 4-(2-aminopropyl)quinolin-8-ol (MS11)

4-(2-aminopropyl)quinolin-8-ol was prepared using the same procedure as described above for 2-(2-aminopropyl)quinolin-8-ol but 4-(-2-nitroprop-1-en-1-yl)quinolin-8-ol (100 mg, 0.430 mmol) was used as starting material. Brown Solid (15.7 mg, 0.0780 mmol). Yield 18.2 %; ^{1}H NMR (δ, 500 MHz, $CDCl_3$) 8.69 (d, 1H, *J*=4.5Hz, H2), 7.52-7.45 (m, 2H, H6,7), 7.31

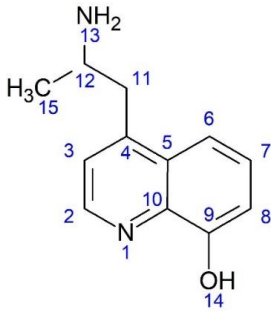

(d, 1H, *J*=4.5Hz, H3), 7.17(dd, 1H, *J*=7.5, 1.5 Hz, H8), 3.4 (m, 1H, H12), 3.17-2.95 (m, 2H, H11), 1.21(d, 3H, *J*=6.5 Hz, H15); ^{13}C NMR δ: 147, 139, 128, 127, 123, 110, 48.0, 43.0, 24.0; HRMS $[M+1]^+$ calc. for $[C_{12}H_{14}N_2O]^+$ 203.1179, found 203.1191; FTIR (neat) 3330, 2932, 1625, 1454, 1371, 1316, 1090, 827.0, 598.0.

2.4.11. 7-(2-aminopropyl)quinolin-8-ol (MS12)

7-(2-aminopropyl)quinolin-8-ol was prepared using the same procedure as described above for 2-(2-aminopropyl)quinolin-8-ol but 7-(-2-nitroprop-1-en-1-yl)quinolin-8-ol (100 mg, 0.430 mmol) was used as starting material. Brown Solid (11.0 mg, 0.0540 mmol). Yield 14.3 %; ^{1}H NMR (δ, 500 MHz, $CDCl_3$) 8.80 (dd, 1H, *J*=1.5, 4.0Hz, H2), 8.12 (dd, 1H, *J*=1.5, 8.0Hz, H6), 7.39 (m, 1H, H3), 7.32(m, 2H, H4,7), 3.4 (m, 1H, H12), 2.99-2.84 (m, 2H, H11), 1.21(d, 3H, *J*=6.0 Hz, H15); ^{13}C NMR δ: 151, 148, 139, 136, 131, 127, 122, 121, 117, 48.0, 41.0, 24.0; HRMS $[M+1]^+$ calc. for $[C_{12}H_{14}N_2O]^+$ 203.1179, found 203.1198; FTIR (neat) 3383, 2815, 1579, 1391, 896.0, 756.0.

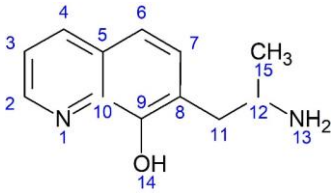

2.4.12. 5-(2-aminopropyl)quinolin-8-ol (MS13)

5-(2-aminopropyl)quinolin-8-ol was prepared using the same procedure as described above for 2-(2-aminopropyl)quinolin-8-ol but 5-(-2-nitroprop-1-en-1-yl)quinolin-8-ol (100 mg, 0.430 mmol) was used as starting material. Brown Solid (17.8 mg, 0.0880 mmol). Yield 20.6 %; ^{1}H NMR (δ, 500 MHz, CDCl3) 8.78 (dd, 1H, *J*=1.5, 4.5Hz, H2), 7.36 (dd, 1H, *J*1= 1Hz, *J*2= 8.5, H4), 7.46 (m, 1H, H3), 7.31(d, 1H, *J*=7.5Hz, H7), 7.13(d, 1H, *J*=7.5Hz, H8), 3.25 (m, 1H, H12), 3.01-2.86 (m, 2H, H11), 1.19(d, 3H, *J*=6.5 Hz, H15); ^{13}C NMR δ: 151, 147, 139, 133, 129, 127, 126, 121, 109,

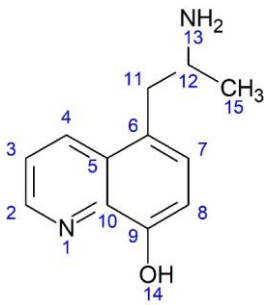

48.1, 42.3, 23.8; HRMS $[M+1]^+$ calc. for $[C_{12}H_{14}N_2O]^+$ 203.1179, found 203.1195; FTIR (neat) 3367, 2957, 1581, 1368, 1258, 1020, 795.0.

2.4.13. 3[2-(2-aminopropyl)quinolin-8-ol]Fe (MS10:Fe)

A methanolic solution of ferric nitrate nonahydrate (1.50 mL, 0.5 mM) was added to a methanolic solution of 2-(2-aminopropyl)quinolin-8-ol (1.50 mL, 1.50 mM). The solution was stirred at ambient temperature for 15 min. The complex was precipitated by diffusion of diethyl ether into the methanolic solution in a sealed vessel. Green colour; HRMS $[M]^+$ calc. $[C_{12}H_{13}N_2O]_2Fe$ 456.1452, found 456.1342with % abund. *m/z* 456.1342 (6.35), 457.1250 (1.77), 458.1343 (100), 459.1374(30.05), 460.14(5.07) and $[M+1]^+$ calc. $[C_{12}H_{13}N_2O]_3Fe$ 658.2553, found 658.2344 with % abund. *m/z* 658.2344(6.33), 659.2500 (2.64), 660.2416(100), 661.2456(43.85), 662.2455(10.32) FTIR (neat) 3404, 2924, 1640, 1343, 1023, 829.0, 592.0; UV (10% MeOH in PBS, ε(M^{-1}, cm^{-1})), 597(2872), 461(3744), 366(4796), 255(69880).

2.4.14. 3[4-(2-aminopropyl)quinolin-8-ol]Fe (MS11:Fe)

A methanolic solution of ferric nitrate nonahydrate (1.50 mL, 0.5 mM) was added to a methanolic solution of 4-(2-aminopropyl)quinolin-8-ol (1.50 mL, 1.50 mM). The solution was stirred at ambient temperature for 15 min. The complex was precipitated by diffusion of diethyl ether into the methanolic solution in a sealed vessel. Green colour; HRMS $[M]^+$ calc. $[C_{12}H_{13}N_2O]_2Fe$ 456.1452, found 456.1318with % abund. *m/z* 456.1318 (6.35), 457.1250 (1.77), 458.1322 (100), 459.1348(30.05), 460.1400(5.07) and $[M+1]^+$ calc. $[C_{12}H_{13}N_2O]_3Fe$ 658.2553, found 658.2326 with % abund. *m/z* 658.2326(6.33), 659.2500 (2.64), 660.2384(100), 661.2417(43.85), 662.2455(10.32) FTIR (neat) 3410, 2927, 1635, 1358,

879.0, 753.0; UV (10% MeOH in PBS, ε(M^{-1}, cm^{-1})), 588(3240), 460(4992), 366(6320), 247(88000).

2.4.15. 3[7-(2-aminopropyl)quinolin-8-ol]Fe (MS12:Fe)

A methanolic solution of ferric nitrate nonahydrate (1.50 mL, 0.5 mM) was added to a methanolic solution of 7-(2-aminopropyl)quinolin-8-ol (1.50 mL, 1.50 mM). The solution was stirred at ambient temperature for 15 min. The complex was precipitated by diffusion of diethyl ether into the methanolic solution in a sealed vessel. Green crystals; HRMS $[M]^+$ calc. $[C_{12}H_{13}N_2O]_2Fe$ 456.1452, found 456.1342with % abund. *m/z* 456.1342 (6.35), 457.1250 (1.77), 458.1343 (100), 459.1374(30.05), 460.1400(5.07) and $[M+1]^+$ calc. $[C_{12}H_{13}N_2O]_3Fe$ 658.2553, found 658.2344 with % abund. *m/z* 658.2344(6.33), 659.2500 (2.64), 660.2416(100), 661.2456(43.85), 662.2455(10.32) FTIR (neat) 3358, 2927, 1633, 1327, 830.00, 592.0; UV (10% MeOH in PBS, ε(M^{-1}, cm^{-1})), 600(2868), 461(3720), 366(4840), 255(69600).

2.4.16. 3[5-(2-aminopropyl)quinolin-8-ol]Fe (MS13:Fe)

A methanolic solution of ferric nitrate nonahydrate (1.50 mL, 0.5 mM) was added to a methanolic solution of 5-(2-aminopropyl)quinolin-8-ol (1.50 mL, 1.50 mM). The solution was stirred at ambient temperature for 15 min. The complex was precipitated by diffusion of diethyl ether into the methanolic solution in a sealed vessel. Green crystals; HRMS $[M]^+$ calc. $[C_{12}H_{13}N_2O]_2Fe$ 456.1452, found 456.1378 with % abund. *m/z* 456.1378 (6.35), 457.1250 (1.77), 458.1373 (100), 459.1404(30.05), 460.1400(5.07) and $[M+1]^+$ calc. $[C_{12}H_{13}N_2O]_3Fe$ 658.2553, found 658.2326 with % abund. *m/z* 658.2326(6.33), 659.25 (2.64), 660.2384(100), 661.2417(43.85), 662.2455(10.32) FTIR (neat) 3388, 2924, 1581, 1364, 1260, 1083, 794.0, 610.00; UV (10% MeOH in PBS, ε(M^{-1}, cm^{-1})), 627(2692), 473(3105), 366(4107), 255(52760).

2.5. Synthesis and characterization of methcathinone compounds

2.5.1. Dimethyl terephthalate (MF2)

Terephthalic acid (18.3 g, 0.0500 mol) was dissolved in methanol (200ml) and placed in a 500ml round bottom flask. Sulfuric acid (5ml) was added dropwise to the solution. The mixture was stirred at reflux for 4 hours. The crude product was cooled down, then neutralized by solid sodium bicarbonate. The methanol was removed by rotary evaporator, followed by adding 20 ml of dichloromethane and 20 ml of water. Then the solution was transferred to separatory funnel for liquid-liquid extraction. The organic phase was collected and dried from water by using sodium sulfate. Then, dichloromethane was evaporated by a rotary evaporator. The crude product was recrystallized by methanol to get pure crystal structure of dimethyl terephthalate. White solid (8.70 g, 0.0450 mol). Yield 90 %; ^{1}H NMR (δ, 500 MHz, DMSO) 8.08 (s, 4H, H2,3,5,6), 3.89 (s, 6H, H9,12).

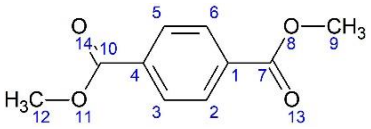

2.5.2. Methyl 4-(3-methoxy-2-methyl-3-oxopropanoyl)benzoate (MF3)

Dimethyl terephthalate (4.80g, 25.0mmol) was dissolved in 25ml of dry xylene then transferred to 50ml two nicked round bottom flask equipped with stirrer bar, a condenser that has nitrogen inlet quick fit on top and dropper funnel. Then sodium hydride (1.20g, 50.00mmol) was added to the round bottom flask. Methyl propanoate (1.55g, 25.0mmol) was dissolved in 5ml of dry xylene and then transferred into the dropper funnel. Methyl propanoate was added dropwise into the round bottom flask solution for one hour under reflux and flush of nitrogen. The reaction was left under reflux for 24 hrs. 5ml of ammonium chloride was added to the cold mixture, followed by adding 6M HCl until the pH= 1. The mixture was

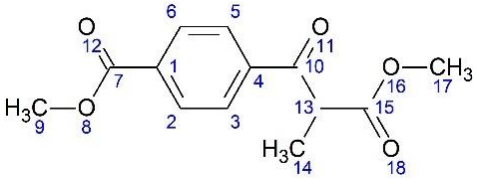

extracted with Ethyl acetate: diethyl ether (1:1, 3x50ml). The combined organic phase was dried with sodium sulfate and concentrated with a rotary evaporator. Yellow oil (3.00 g, 12.0 mmol). Yield 48 %; ^{1}H NMR (δ, 500 MHz, DMSO) 8.08 (m, 4H, H2,3,5,6), 4.70 (m, 1H, H13), 3.88 (s, 6H, H9,17), 1.34(d, 3H, *J*=7.0Hz, H14).

2.5.3. 4-propanoylbenzoic acid (MF4)

Methyl 4-(3-methoxy-2-methyl-3-oxopropanoyl)benzoate (2.00 g, 12.0 mmol) was transferred to 25ml round bottom flask. Aqueous hydrochloric acid (36.0 ml, 1 M) was added, followed by glacial acetic acid (5ml). The mixture was heated at reflux for 24 h. The cooled mixture was extracted with ethyl acetate:diethylether (1:1) three times. The combined organic phases were extracted with 5M NaOH. The aqueous phase was separated and acidified with 1M HCl until pH 1. A white precipitate formed, which was dissolved in the minimum amount of water. The mixture was extracted with ethyl acetate:diethylether (1:1) and the organic phase dried with anhydrous sodium sulfate. The mixture was filtered, and the solvent was evaporated using a rotary evaporator. The crude product was recrystallized from butanone to give a white solid (748 mg, 4.2 mmol). Yield 35 %. ^{1}H NMR (δ, 500 MHz, DMSO) 8.04 (m, 4H, H2,3,5,6), 3.1, 2H, *J*=7Hz, H12), 1.09 (t, 3H, *J*=7.0Hz, H13).

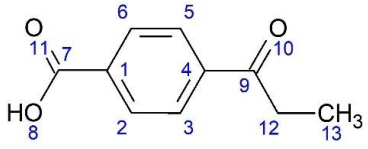

2.5.4. Methyl 4-propanoylbenzoate (MF5)

4-propanoylbenzoic acid (1.32 g, 7.41 mmol), sodium carbonate (1.86 g, 22.2 mmol) and iodomethane (1.30 ml, 22.2 mmol) were dissolved in dimethylformamide (10.0 ml) and stirred for 12 h at room temperature. The mixture was diluted with brine (50 ml) and extracted with diethyl ether (3 x 50ml). The organic phase was washed with water (50 ml) and then dried using anhydrous sodium sulfate. The solvent was evaporated using a rotary

evaporator to give a white solid (0.970 g, 5.00 mmol). Yield 68 %. ^{1}H NMR (δ, 500 MHz, $CDCl_3$) 8.12 (d, 2H, *J*=8.0Hz, H5,3), 8.03 (d, 2H, *J*=8.5Hz, H6,2), 3.96 (s, 3H, H9), 3.05 (q, 2H, *J* = 7.0 Hz, H13), 1.25 (t, 3H, *J*=7.0Hz, H14).

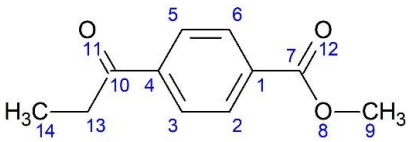

2.5.5. Methyl 4-(2-bromopropanoyl)benzoate (MF6)

Methyl 4-propanoylbenzoate (0.20 g, 1.04 mmol) was dissolved in dichloromethane (20 ml) and transferred into a 50 ml round bottom flask. Bromine (51 µL, 1.00mmol) and a few drops of hydrogen bromide were added dropwise with stirring. The mixture was stirred for 1 h at room temperature. Water (20 ml) was added followed by liquid-liquid extraction. The organic phase was dried with sodium sulfate and the solvent was evaporated using a rotary evaporator to give a yellow/orange oil (260.0 mg, 0.960 mmol). Yield: 92%; ^{1}H NMR (δ, 500 MHz, $CDCl_3$) 8.15-8.06 (m, 4H, H2,3,5,6), 5.28 (m, 1H, H13), 3.95(s, 3H, H9), 1.92 (d, 3H, *J*=6.5Hz, H14).

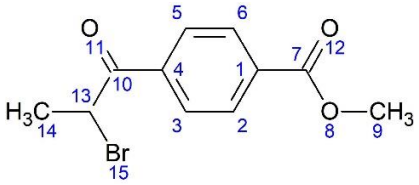

2.5.6. 1-[4-(Methoxycarbonyl)phenyl]-N-methyl-1-oxopropan-2-aminium (MF7)

Methyl 4-(2-bromopropanoyl)benzoate (100 mg, 0.360mmol) was dissolved in DMF (20ml) and 40% methyl amine solution in water (168µL, 0.369mmol) was added dropwise with cooling using an ice bath. The reaction was quenched after 1hr with water (20 ml). The mixture was extracted using diether ether (3 x 30ml). The combined organic phase was dried with sodium sulfate and the solvent evaporated using a rotary evaporator. The crude product was dissolved in anhydrous diethyl ether (10 ml), transferred into one neck round bottom flask equipped with stirrer bar and septum, and 2M HCl in ether (10 mL) was added using a glass syringe. The mixture was stirred for 3 h; and the product was

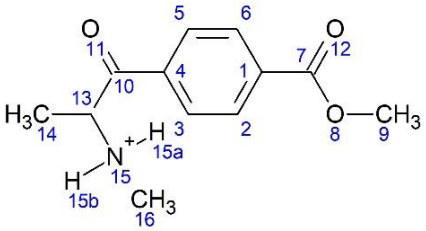

collected by filtration as fine white crystals (260 mg, 0.960 mmol). Yield 94 %; ^{1}H NMR (δ, 500 MHz, DMSO) 9.44 (s, 1H, H15a), 9.09 (s, 1H, H15b), 8.14 (m, 4H, H2,3,5,6), 5.17 (m, 1H, H13), 3.89(s, 3H, H9), 2.62 (s, 3H, H16), 1.45(d, 3H, *J*=7.5Hz, H14).

2.5.7. 1-(4-Carboxyphenyl)-N-methyl-1-oxopropan-2-aminium (MF8)

1-[4-(methoxycarbonyl)phenyl]-N-methyl-1-oxopropan-2-aminium (260.0mg, 0.960 mmol) was dissolved in HCl (2.00M, 10.00ml). The solution was stirred for 24 hours under reflux. The solution was evaporated by using rotary evaporator then left in the freeze drier for 24 hrs to remove all the solvent residues to give a white solid (196 mg, 0.940 mmol). Yield 98 %; ^{1}H NMR (δ, 500 MHz, DMSO) 9.71 (s, 1H, H14a), 9.22 (s, 1H, H14b), 8.13 (m, 4H, H2,3,5,6), 5.21 (m, 1H, H12), 2.60 (s, 3H, H15), 1.46(d, 3H, *J*=7.0Hz, H13).

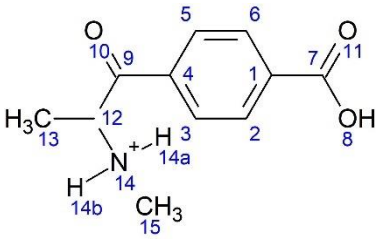

2.5.8. N'-[-(2-Hydroxy-5-nitrophenyl)methylidene]pyridine-4-carbohydrazide (MF9)

2-Hydroxy-5-nitrobenzaldehyde (1.00 g, 0.006 mol) and isonicotinic acid hydrazide (0.820 g, 0.006 mol) were dissolved in ethanol (100ml). The solution was transferred to a round bottom flask equipped with stirrer bar and Dean-Stark apparatus equipped with a condenser. The reaction was stirred at reflux for 2 hours. After the volume of the solution was reduced to about 20 ml, a yellow precipitate formed. The precipitate was collected by filtration and washed with cold ethanol to obtain a yellow solid (1.67 g, 0.00580 mol). Yield 97 %; ^{1}H NMR (δ, 500 MHz, DMSO) 8.81 (m, 2H, H2,6), 8.76 (s, 1H, H11), 8.61 (d, 1H, *J*=2.5Hz, H17), 8.19 (dd, 1H, *J*=9.0, 3.0Hz, H15), 7.85 (d, 2H, 5.5Hz, H3,5), 7.12(d, 1H, *J*=9.0Hz, H14).

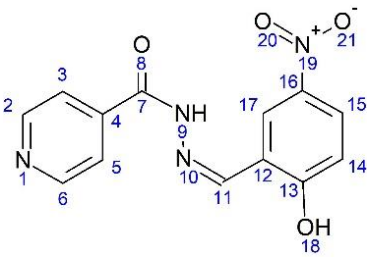

2.5.9. N'-[(5-Amino-2-hydroxyphenyl)methylidene]pyridine-4-carbohydrazide (MF10)

N'-[(2-hydroxy-5-nitrophenyl)methylidene]pyridine-4-carbohydrazide (0.100g, 0.340mmol) was dissolved in absolute ethanol (70ml) in a round bottom flask equipped with stirrer bar and septum. Raney nickel in ethanol (5.00ml) was added and a balloon containing hydrogen gas was connected to the round bottom flask by a syringe with a needle. The reaction stirred overnight under the flush of hydrogen. The reaction mixture was filtered and the filtrate concentrated using a rotary evaporator to give an orange solid (40 mg, 0.156 mmol). Yield 46 %; ^{1}H NMR (δ, 500 MHz, DMSO) 12.1(s, 1H, H18), 9.96 (s, 1H, H9), 8.79 (m, 2H, H2,6), 8.56 (s, 1H, H11), 7.83 (m, 2H, H3,5), 6.83 (s, 1H, H17), 6.67 (d, 1H, *J*=8.5, H14), 6.59 (d, 1H, *J*=8.5Hz, H15).

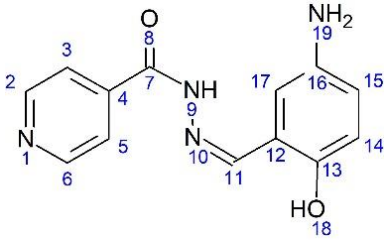

2.5.10. 4-Propanoyl-N-(quinolin-8-yl)benzamide (MF11)

A solution of 4-propanoylbenzoic acid (50.00mg, 0.280mmol), (1-Cyano-2-ethoxy-2-oxoethylidenaminooxy)dimethylamino-morpholino-carbenium hexafluorophosphate (COMU) (0.144g, 0.340mmol) and 10.00ml anhydrous DMF was stirred at room temperature in 2 nicked round bottom flask equipped with stirrer bar, nitrogen inlet quick fit and rubber septum. 100uL of N,N-Diisopropylethylamine was added by syringe into the solution followed by addition quinolin-8-amine (44.4mg, 0.308mmol) under the flush of nitrogen. The solution was stirred for 15 hours at room temperature and under the flush of nitrogen. Then the reaction was quenched by adding 20 ml of water and extracted with ethylacetate (3 x 30ml). The combined organic phase was dried with sodium sulfate. The solvent was evaporated with a rotary evaporator. The crude product was purified by column chromatography (silica gel, ethyl acetate: hexane 1:1) to give a yellow solid (35.0 mg, 0.115

mmol). Yield 41 %; ^{1}H NMR (δ, 500 MHz, DMSO) 10.73(s, 1H, H11), 8.99 (dd, 1H, *J*=2.0, 4.5Hz, H2), 8.72 (dd, 2H, *J*=4.5, 7.5, H3), 8.47 (dd, 1H, *J*=1.5, 8.0Hz, H6), 8.177 (m, 4H, H16,15,18,19), 7.77 (d, 1H, *J*=7Hz, H8), 7.69 (m, 2H, H 4,7), 3.13 (q, 2H, *J* =7.0Hz, H22), 1.12 (t, 3H, *J*=7.0Hz, H23).

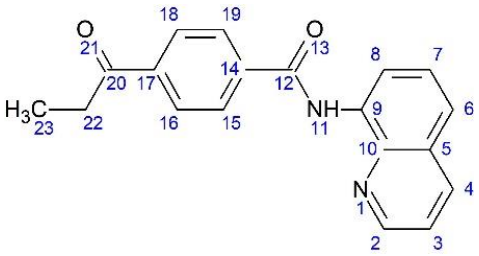

2.6. Antioxidant activity measured by DPPH assay for **MS1-4**

The 1,1-diphenyl-2-picrylhydrazyl (DPPH) assay was used to measure antioxidant activity of **MS1-4** This assay was performed according to a modified published method (Sharma and Bhat, 2009). In brief, stock solutions (10 mM in methanol) of **MS1-4** and a 200 µM methanolic DPPH solution were prepared. A stock solution of ascorbic acid (1 mM in methanol) was used as a control. DPPH (200µM, 50µl) was added to 150µl of sample solutions (ascorbic acid, **MS1-4**) with different concentrations using 96 well microplates. Each of the additions was performed in triplicate. The microplates were wrapped in aluminium foil and kept at 30 °C for 30 minutes in the dark. Spectrophotometric measurements were recorded using a Thermolabsystems Multiskan Ascent spectrophotometer at 520 nm. Measurements were performed, ensuring no exposure to ambient light. Activities were calculated as follows:

DPPH radical scavenging activity (%) = $[(Abs_{control} - Abs_{compound})]/(Abs_{control})] \times 100$

where $Abs_{control}$ is the absorption of DPPH (200µM, 50µL) with 150µL of neat methanol and $Abs_{compound}$ is the absorption of test compounds at different concentrations plus DPPH (200µM, 50µL). The percentage of remaining DPPH radical is calculated using:

DPPH remaining in the reaction (%) = $[(Abs_{compound} - Abs_{blank})/(Abs_{control} - Abs_{blank})] \times 100$

where Abs_{blank} is the absorption of pure methanol. The IC_{50} of ascorbic acid (vitamin C) and **MS1-4** is the samples concentration at which 50% of the DPPH free radical was scavenged.

2.7. Assays to assess interactions with Aβ40

2.7.1. Turbidity assay

A turbidity assay was used to assess the Cu^{2+}-induced aggregation and was performed according to a modified, published method (Chen *et al*., 2009). Aqueous copper(II)sulfate (4 µL, 5 mM) and buffer solution (10 µL, Tris-HCl (200 mM) / NaCl (1.5 M), pH 7.4) were added to aqueous $Aβ_{40}$ (50 µL, 170 µM). The solution was incubated at 37 ºC for 48 hours to prepare the aggregated Cu(II)/$Aβ_{40}$ sample. Then, **MS1-4** (10 µL, 4mM,) were added individually followed by incubation at 37 ºC for 4 hours. Buffer solution (600 µL, Tris-HCl (20 mM), NaCl (150 mM) pH 7.4) was added to dilute the samples. Buffer solution (624 µL and 610 µL, Tris-HCl (20 mM), NaCl (150 mM) pH 7.4) was added to $Aβ_{40}$ and Cu(II)/$Aβ_{40}$ samples, respectively. For each sample, 200 µL was added to a 96 well microplate and performed in triplicate. The UV-visible absorbance was measured at 405 nm.

2.7.2. Concentrations of Aβ40 measured before and after de-aggregation with MS1-4

Six 500 µL vials were labeled as $Aβ_{40}$, Cu(II)/$Aβ_{40}$ and Cu(II)/$Aβ_{40}$/**MS1** (or **MS2, MS3, MS4**). Aqueous $Aβ_{40}$ (50 µL, 170 µM) and buffer solution (50 µL, Tris-HCl (200 mM) / NaCl (1.5 M), pH 7.4) were added to the $Aβ_{40}$ vial. Aqueous copper (II) sulfate (4 µL, 5 mM), buffer solution (46 µL, Tris-HCl (200 mM) / NaCl (1.5 M), pH 7.4) and aqueous $Aβ_{40}$ (50 µL, 170 µM) were added to the Cu (II)/$Aβ_{40}$ vial. Cu (II)/$Aβ_{40}$/**MS1-4** vials were prepared using the same method as for the Cu (II)/$Aβ_{40}$ vial except 36 µL of buffer solution was added. The resultant solutions were incubated at 37 ºC for 48 hours. After 48 hrs, **MS1-4** (10 µL, 4mM) were added to the Cu(II)/$Aβ_{40}$/**MS1-4** vials followed by incubation at 37 ºC for 4 hours.

To a 96 well microplate, 25 µL of solution from each vial was added plus 200 µL of prepared BCA assay reagents. On the same plate, 25 µL of different concentrations of bovine serum albumin plus 200 µL of the reagents were added. Each of the additions was performed in triplicate. The colour change monitored by UV-visible absorbance using a microplate reader at 540 nm.

The concentration of $A\beta_{40}$ was immediately determined with a BCA Protein Assay Kit using bovine serum albumin as a standard.

2.7.3. Mass spectrometric analysis of chelated species

Samples prepared using the procedure outlined in 2.7.1 (before the addition of **MS1-4**) were centrifuged (12000 rpm) for 30 minutes to precipitate any undissolved material. The supernatant was decanted, the pellet was washed with water, centrifuged a second time (12000 rpm) for 30 minutes, and the supernatant decanted. Aqueous solutions of **MS1-4** (5 µL, 4mM) were added followed by incubation at 37 ºC for 4 hours. The pH was adjusted at 7.4 (aq. NaOH (0.5M) or aq. HCl (0.5 M)) and the mixture was centrifuged (12000 rpm) for 30 minutes. Aliquots of the supernatant were examined using ESI-MS.

2.8. Computational studies of **MS1-4**

2.8.1. Docking procedure

In the case of AD, misregulated metal ions bind to the active site of the α-secretase in APP and the non-amyloid pathway is retarded in favour of the amyloid pathway (Figure 2). Aβ may then aggregate in the brain to form plaques, which are implicated in AD progression. **MS1-4** were designed to chelate Zn and Cu ions bounds to APP and prevent Aβ aggregation. For this reason, the E2 domain of APP in complex with Zn/Cu was selected (APP; PDB ID: 3UMI/3UMK; Dahms *et al*., 2012), which was downloaded from the Protein Data Bank

(Berman *et al*., 2000). **MS1-4** were built using Accelrys Draw 4.5. The monomeric structure of the peptide was used for the docking study and was refined (hydrogen atoms were added, the charge of histidine residues was adjusted, and water molecules were not removed) prior to docking studies. Docking was carried out by Discovery Studio 4.5 software (Accelrys, San Diego, CA, USA). The binding site was defined as 15 Å sphere around the zinc and copper metals, and 11 poses were obtained for each compound. A known metal chelator (5-chloro-7-iodoquinolin-8-ol) was docked for comparison. Docking was repeated several times to achieve no visible change in the orientation or the interaction of the ligand in the binding site. The formal and partial charge was set to +2 for copper. From the docking results, possible hydrogen-bonding and non-bonding interactions with the amino acid residues were examined.

2.8.2. ADMET (Absorption, Distribution, Metabolism, Excretion, and Toxicity) Prediction

Many drug failures at the stage of research occur due to undesirable pharmacokinetic factors. Early knowledge of such factors is useful in the drug discovery process. Thus, calculations were performed to predict pharmacokinetics parameters (ADMET parameters) namely, aqueous solubility, Cytochrome P450 2D6 inhibition, intestinal absorption, hepatotoxicity and plasma protein binding, as well as, BBB (blood-brain barrier) permeability to know the ability of the drug to pass through the BBB and chelate the misregulated metals in order to heal AD. These pharmacokinetic parameters were calculated and then evaluated using Discovery Studio 4.5 (Accelrys, San Diego, CA, USA).

2.9. UV-vis study for (**MS5-13**):Fe complexes

Iron nitrate (3mM, 25µl) in 10% Methanol in PBS was added to 150µl of sample solutions (**MS5-13**) with different concentrations (0.25 mM to 3mM) in 10% methanol in PBS using 96

well microplates. Then 125 µL of 10% methanol in PBS was added to each well. Spectral changes were measured as a correlation of ligand-metal binding between 200-800 nm at 25 °C using Agilent Technologies Cary 60 spectrometer (Santa Clara, CA, USA) with 0.1 cm path length quartz cuvette.

2.10. Isothermal titration calorimetry **MS5-13**

Isothermal titration calorimetry (ITC) experiments were carried out at 25 ^{o}C on the Nano-ITC instruments (TA instrument) with 300 rpm. All of the compounds and iron were dissolved in 10% MeOH in PBS with pH= 7.4. In case of (**MS5-9**):Fe complexes, **MS5-9** (0.3mM, 170 µL) were placed in the sample cell and $Fe(NO_3)_3{\cdot}9H_2O$ (3mM, 50 µL) was placed in the syringe, followed by addition of 1.9 µL from burette to the cell every 100 sec. Whereas in case of **MS10-13** complexes, **MS10-13** (3mM, 50 µL) were placed in the syringe and the $Fe(NO_3)_3{\cdot}9H_2O$ (0.15mM, 150 µL) were placed in the sample cell, followed by addition of 1.9 µL of **MS10-13** from burette to the cell every 100 sec. Titration was done in a sequence of 25 injections in both methods. Raw data were processed using Nano analyze software.

2.11. Antioxidant activity measured by DPPH assay for **MS5-13**

The 1,1-diphenyl-2-picrylhydrazyl (DPPH) assay was used to measure antioxidant activity. This assay was performed according to a modified published method (Sharma and Bhat, 2009). In brief, stock solutions (10 mM in methanol) of **MS5-13** and a 200 µM methanolic DPPH solution were prepared. A stock solution of ascorbic acid (1 mM in methanol) was used as a control. DPPH (200µM, 50µl) was added to 150µl of sample solutions (ascorbic acid, **MS5-13**) with different concentrations using 96 well microplates. Each of the additions was performed in triplicate. The microplates were wrapped in aluminium foil and kept at 30 °C for 30 minutes in the dark. Spectrophotometric measurements were recorded using a

Thermolabsystems Multiskan Ascent spectrophotometer at 520 nm. Measurements were performed, ensuring no exposure to ambient light. Activities were calculated as follows:

DPPH radical scavenging activity (%) = $[(Abs_{control} - Abs_{compound})]/(Abs_{control})] \times 100$

where $Abs_{control}$ is the absorption of (200µM, 50µL) DPPH with 150µL of neat methanol and $Abs_{compound}$ is the absorption of test compounds at different concentrations plus DPPH (200µM, 50µL).

2.12. N27 cell culture assay

N27 rat dopaminergic neural cells were obtained from Millipore (product number: SCC048). Glutamax was obtained from Thermo Fisher (product number:61870-036). Foetal calf serum was obtained from Bovogen, Keilor East, Australia. Penicillin/Streptomycin from Thermo Fisher (product number: 15140122). MTT was obtained from Sigma Aldrich (product number: M5655)

2.12.1. Cell culture growth media

All cells were cultured at 37 ^{o}C with 5 % CO_2. N27 cells derived from E12 rat mesencephalic tissue were grown in RPMI 1640 media with Glutamax supplemented by 10% foetal calf serum, penicillin, and streptomycin as described previously by Southon *et al* (Southon *et al*., 2019).

2.12.2. Cell viability assays

A quantitative colorimetric MTT assay was performed to determine the neuroprotective effects of the test compounds on iron mediated cell death.

*Effect of **MS5-13** on N27 cell viability*

The effect of **MS5-13** on the viability of N27 cells was assessed using the colorimetric assay for MTT reduction to determine their direct effect on cell viability and also to determine the optimum concentration of **MS5-13** compounds to be used in subsequent neuroprotection experiments. N27 cells were seeded in triplicate into 96-well plates at a cell density of 20000 cells / well and incubated overnight. Cells were then treated with various concentrations (1 µM, 10 µM, 100 µM and 1000 µM) of **MS5-13**, deferiprone and clioquinol that were first dissolved in DMSO (final DMSO concentration was 0.1%). Vehicle control cells received 0.1% DMSO only.

At the end of the 24 hour treatment periods 16 µL of MTT (5mg/ml in PBS) was added to each well and incubated under an atmosphere of 5% CO_2 at 37°C. After 2 h the supernatant was removed, and the purple formazan product was dissolved in 100 µL DMSO on an orbital shaker for 30 min. The absorbance was read at 595nm using a PowerWave XS microplate spectrophotometer (BioTek Instruments, Winooski, USA). Cell viability was expressed as a percentage of control cells after the background absorbance was subtracted.

Cytotoxicity of iron salts

The effect of iron on the viability of N27 cells was assessed using the colorimetric assay for MTT reduction to determine their direct effect on cell viability and also to determine the optimum concentration of the iron to be used in subsequent neuroprotection experiments. N27 cells were seeded in triplicate into 96-well plates at a cell density of 20000 cells / well and incubated overnight. Cells were then treated with various concentrations (10 µM, 100 µM, 1000 µM and 10000 µM) of different iron salts (ferric ammonium citrate, ferrous ammonium sulphate, ferric citrate hydrate, ferrous sulfate heptahydrate, ferric chloride

hexahydrate and ferric chloride) that were first dissolved in DMSO (final DMSO concentration was 0.1%). Vehicle control cells received 0.1% DMSO only.

At the end of the 24 hour treatment periods 16 µL of MTT (5mg/ml in PBS) was added to each well and incubated under an atmosphere of 5% CO_2 at 37°C. After 2 h the supernatant was removed, and the purple formazan product was dissolved in 100 µL DMSO on an orbital shaker for 30 min. The absorbance was read at 595nm using a PowerWave XS microplate spectrophotometer (BioTek Instruments, Winooski, USA). Cell viability was expressed as a percentage of control cells after the background absorbance was subtracted.

Ferroptosis assay

Ferroptosis is a type of iron-dependent programmed cell death characterised by the accumulation of lipid peroxides, genetically and biochemically distinct from other forms of regulated cell death, such as apoptosis.

The ability of **MS5-13** to slowdown the ferroptosis that is induced by Erastin and RSlL3 was studied by using MTT assay. N27 cells were seeded in triplicate into 96-well plates at a cell density of 20000 cells / well and incubated overnight. Cells were then treated with Erastin (1µM) and RSL3 (0.1µM), followed by addition of deferiprone, clioquinol, **MSX** and **MS5-13** with two different concentrations (10µM and 100µM) that were first dissolved in DMSO (final DMSO concentration was 0.1%). Vehicle control cells received 0.1% DMSO only.

At the end of the 24 hour treatment periods, 16 µL of MTT (5mg/ml in PBS) was added to each well and incubated under an atmosphere of 5% CO2 at 37°C. After 2 h the supernatant was removed, and the purple formazan product was dissolved in 100 µL DMSO on an orbital shaker for 30 min. The absorbance was read at 595nm using a PowerWave XS microplate

spectrophotometer (BioTek Instruments, Winooski, USA). Cell viability was expressed as a percentage of control cells after the background absorbance was subtracted.

Iron toxicity cell rescue assay

The ability of **MS5-13** to rescue N27 cells against iron toxicity was assessed using the colorimetric assay for MTT reduction. N27 cells were seeded in triplicate into 96-well plates at a cell density of 20000 cells / well and incubated overnight. Cells were then treated with two different iron salts: ferrous ammonium sulphate (1mM) and ferric ammonium citrate (1mM) followed by addition of deferiprone, clioquinol, **MSX** and **MS5-13** with two different concentrations (10µM and 100µM) that were first dissolved in DMSO (final DMSO concentration was 0.1%). Vehicle control cells received 0.1% DMSO only.

At the end of the 24 hour treatment periods 16 µL of MTT (5mg/ml in PBS) was added to each well and incubated under an atmosphere of 5% CO_2 at 37°C. After 2 h the supernatant was removed, and the purple formazan product was dissolved in 100 µL DMSO on an orbital shaker for 30 min. The absorbance was read at 595nm using a PowerWave XS microplate spectrophotometer (BioTek Instruments, Winooski, USA). Cell viability was expressed as a percentage of control cells after the background absorbance was subtracted. (Southon *et al*., 2019).

2.13. Statistical analysis

Data were derived in experiments that were conducted at least in triplicate with experiments replicated on at least three occasions. Statistical analyses were performed using the software GraphPad Prism 6.04 (GraphPad Software Inc, San Diego, CA, USA). Data are presented throughout as mean ± standard error of the mean (SEM) and were analysed by one-way analysis of variance (ANOVA) in combination with Fisher's Protected Least

Significant Difference test to detect differences between multiple treatments. $P < 0.05$ was regarded as significant; differences between treatments are indicated in figures as, * $p<0.05$, ** $p<0.01$, *** $p<0.001$ and # $p<0.0001$.

Chapter 3

Results and Discussion

Chapter 3: Results and discussion

3.1. Cyclen-based chelating compounds for Alzheimer's disease*

Although the precise causes of AD are yet to be fully elucidated, metal ions have been implicated in several pathways that may lead to neuronal cell death and AD. Misregulated free metal ions can stimulate the production of extracellular Aβ by inhibiting α-secretase and favouring the amyloid pathway over the non-amyloid pathway. Subsequently, Aβ may aggregate in the brain to form plaques that causes neuronal cell death (Watt *et al*., 2010, Singh *et al*., 2013, Chow *et al*., 2010). Misregulated metal ions can also catalyse the production of ROS that induce oxidative stress in the brain (Guilloreau *et al*., 2007). The metals copper, zinc, and iron have been implicated in this regard and copper, in particular, has been proposed to have a cumulative effect that impairs processes that remove Aβ from the brain (Singh *et al*., 2013).

The development of metal-chelating compounds that also have antioxidant activity has been identified as a promising strategy to treat AD (Leon *et al*., 2013). A number of metal chelators have been investigated as metal ion chelation therapy agents (Cherny *et al*., 2001, Pithadia and Lim, 2012). For example, desferrioxamine is a high affinity chelator of iron (Smith *et al*., 2007) as well as Cu and Zn which has been shown to slow down the development of Alzheimer's disease (Smith *et al*., 2007). Clioquinol is a hydrophobic 8-hydroxyquinoline derivative that readily crosses the BBB and binds Zn and Cu that are coordinated to Aβ. Clioquinol had been shown correcting a defect in copper homeostasis levels in APP2576 transgenic mice by redistributing copper ions in the brain (Cherny *et al*.,

* A significant portion of the work described in this section has been published. See M. El Safadi *et al*, Inorg. Chim. Acta, 467, **2017** 343.

2001) (Moret *et al*., 2006). However, clioquinol and desferrioxamine, whose activity on Aβ-peptide clearance has already been studied *in-vivo* on AD patients, shows some severe side effects. Researchers observed that desferrioxamine and clioquinol had significant neurotoxicity (Fazil *et al*., 2012) (Schimmer *et al*., 2012).

As discussed in Sections 1.2.2 and 1.2.3, macrocyclic polyamine compounds have a strong affinity for metals ions (Rogolino, 2017) and have found applications in diagnostic imaging, as therapeutic agents (Rodríguez-Rodríguez *et al*., 2012), (Delgado *et al*., 2007, Liang and Sadler, 2004)and in targeting Aβ aggregation (Martins *et al*., 2016). These compounds have important physical properties such as low molecular weights, neutral charge, amphiphilic solubility and low toxicities (Rodríguez-Rodríguez *et al*., 2012).

In this work, cyclen-based chelators have been synthesized that bear pendant arms (**MS1-4**, Figure 26). The pendant arms were designed to serve several functions including: (1) to increase ligand affinity by coordinating to the metal, (2) to reduce the oxidative stress caused by particular metals ions, and (3) to increase compound lipophilicity. In compound **MS1**, the phenolic moiety of the pendant 8-hydroxyquinoline group act as an antioxidant (Yoon *et al*., 2006) while the quinolinyl moiety has been shown to decrease levels of Aβ in the brain of AD patients without affecting serum metal ion levels (Zn^{2+} and Cu^{2+}) (Lannfelt *et al*., 2008). The pendant arm of **MS2** bears a 2-(pyridin-2-yl)ethylacetamide group that may also increase lipophilicity and decrease oxidative stress. For comparison, compound **MS3**, which bears a propylpyridin-4-yl pendant arm should increase lipophilicity but have limited effect on oxidative stress. It was predicted that the antioxidant activity of **MS4** would be similar to that of **MS2** but allows the effect of more polar substituents to be examined. The

synthesis of compounds **MS1-4** and some X-ray structural determinations of complexes with Cu^{2+}, Zn^{2+}, and Ni^{2+} are reported in this section.

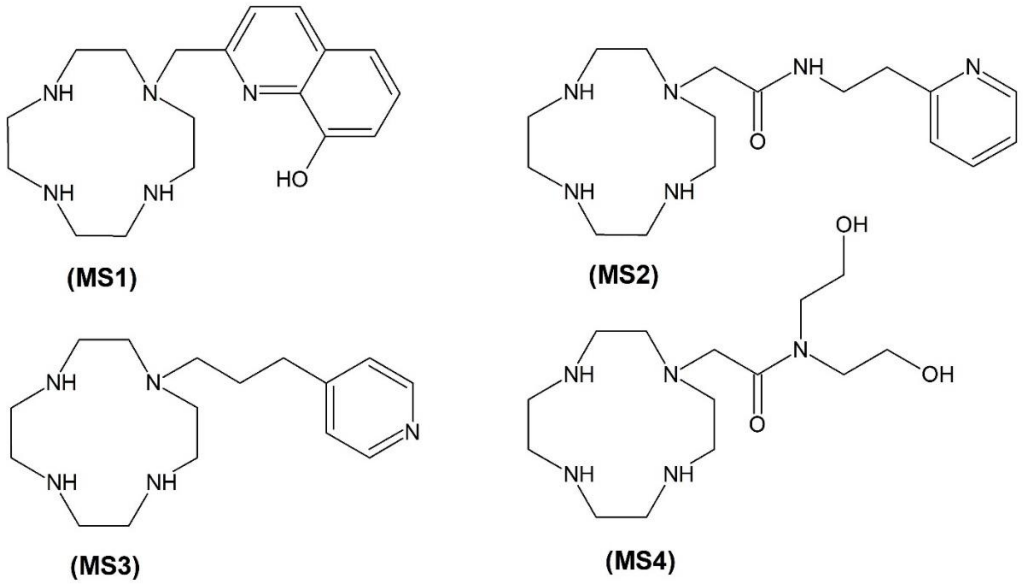

*Figure 26: Structures of compounds **MS1-4**.*

3.1.1. Synthesis of cyclen-based compounds

A key intermediate in the synthesis of **MS1-4** was cyclen. Prior to the attachment of the different pendant arms two methods were investigated to prepare cyclen on gram scales.

Method 1

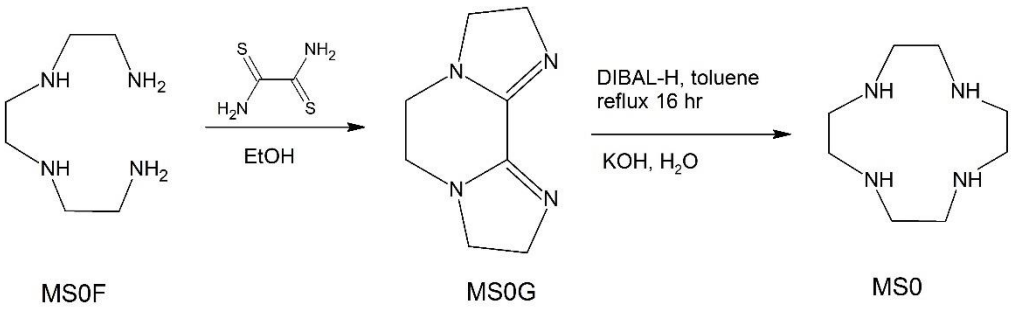

Scheme 1: Cyclen synthesis, Method 1.

Method 1 is shown in scheme 1 and begins with the synthesis of 2,3,5,6,8,9-hexahydrodiimidazo[1,2-a:2',1'-c] pyrazine by reaction of dithiooxamide and triethylenetetramine in ethanol under a nitrogen atmosphere to give 66% yield. This procedure is a modification of the method reported by Weismann and Reed (Weisman and Reed, 1996). A two-carbon, covalent-bond template is introduced by dithiooxamide to convert triethylenetetramine (**MS0F)** to the tricyclic bisamidine. In the second step 2,3,5,6,8,9-hexahydrodiimidazo[1,2-a:2',1'-c] pyrazine (**MS0G)** was reduced to cyclen using di-isobutyl aluminium hydride (DIBAL-H) to give 51% yield. The reaction is a double reductive ring expansion that transforms the two amidine carbons to CH_2CH_2. This reaction was reported by Yamamoto and Maruoka's (Yamamoto and Maruoka, 1981).

Method 2

In Method 2 (Scheme 2) diethylenetriamine (**MS0A**, Scheme 2) was tritosylated to protect the amine functional groups to give 90 % yield. Similarly, alcohol and amine groups in diethanolamine (**MS0B**, Scheme 2) were protected by using toluene-4-sulfonyl chloride with 87% yield. Compounds **MS0C** and **MS0D** were subjected Richman-Atkins cyclisation using caesium carbonate as a base with 71% yield. Compound **MS0E** was then deprotected using hydrobromic acid to give cyclen (**MS0**) in 39% yield (Wilson *et al*., 2007).

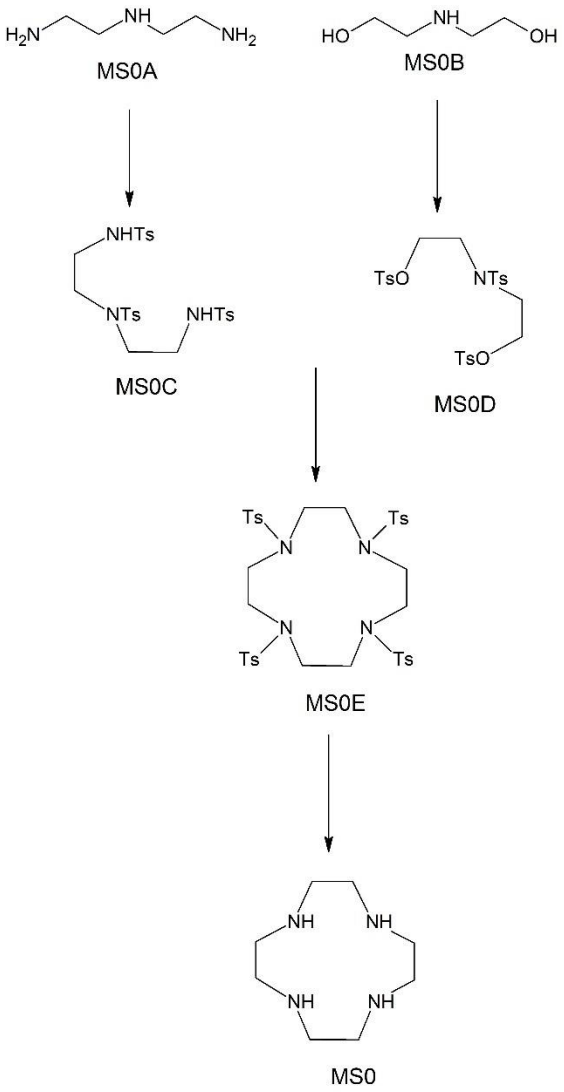

Scheme 2: Cyclen synthesis, Method 2

After successfully synthesising cyclen following both protocols Method 1 was deemed superior because it required fewer synthetic steps and provided cyclen in higher overall yields. Thus, Method 1 was used to prepare the cyclen on gram scales for subsequent synthesis of **MS1-4**. The next step was preparation of the alkyl bromide side-arm groups for **MS1**, **MS2** and **MS4** (Scheme 3 and 4).

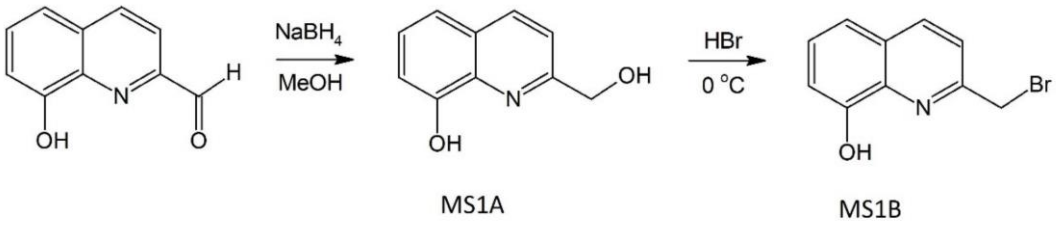

Scheme 3: Synthesis of 2-bromomethyl-8-hydroxyquinoline

2-Bromomethyl-8-hydroxyquinoline (Scheme 3) was synthesized in two steps from 2-formyl-8-hydroxyquinoline by first reducing the aldehyde to the corresponding alcohol (**MS1A)** followed by bromination of the alcohol using hydrobromic acid. 2-Bromo-N-(2-(pyridin-2-yl)ethyl)acetamide (**MS1B)** and bis(2-hydroxyethyl)carbamic bromide were prepared by reacting the commercially available amines with bromoacetyl bromide (Scheme 4).

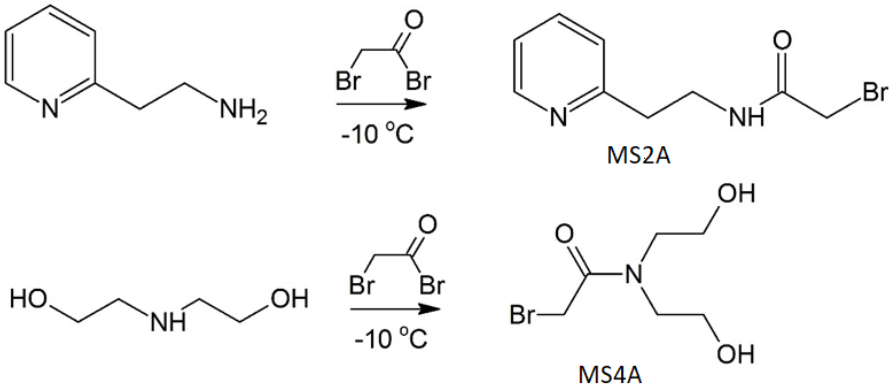

Scheme 4: Synthesis of 2-bromo-N-(2-(pyridin-2-yl)ethyl) acetamide and bis(2-hydroxyethyl) carbamic bromide

Attachment of the pendant arms to cyclen to give **MS1-4** (Figure 26) was achieved by reacting cyclen with the corresponding alkylbromide in a 2:1 (cyclen:RBr) molar ratio (Scheme 5). 2 molar equivalences of cyclen was used to minimise the formation of poly-substituted cyclen products.

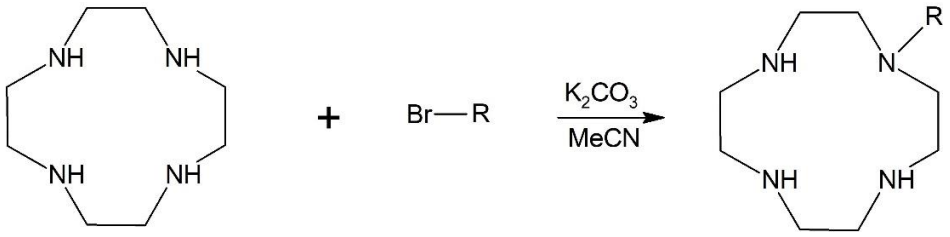

*Scheme 5: Synthesis of **MS1-4** where R = pendant arm*

Using these reaction conditions reasonable yields of **MS1-4** were obtained (60-65%). The monosubstituted cyclen is significantly less reactive than unsubstituted cyclen and so only small amounts of di- and tri- substituted cyclen were obtained. **MS1**, **MS3** and **MS4** are new compounds that have not been previously reported while **MS2** has been reported elsewhere (Du *et al*., 2008).

To be effective chelation therapy agents **MS1-4** must form stable complexes with Cu^{2+}, Zn^{2+} and Ni^{2+}, as these metals are implicated in AD progression. Thus metal (Cu^{2+}, Zn^{2+} and Ni^{2+}) complexes of **MS1-4** were synthesized to gain insights into how **MS1-4** coordinate these biologically important metals. **MS1-4** were reacted with the corresponding metal salts (either sulfate or chloride) in methanol or water. The resultant complexes were readily purified by recrystallization. Copper and nickel complexes of **MS3** (**MS3:**Cu and **MS3:**Ni), the copper complex of MS2 (**MS2**:Cu) and the zinc complex of MS1 (**MS1**:Zn) formed single crystals that were suitable for structure determination by X-ray diffraction. Mass spectra for the complexes of **MS1-4** with Cu^{2+}, Zn^{2+} and Ni^{2+} are collected in Appendix 2 (Figures 111-122).

3.1.2. Single crystal X-ray diffraction studies

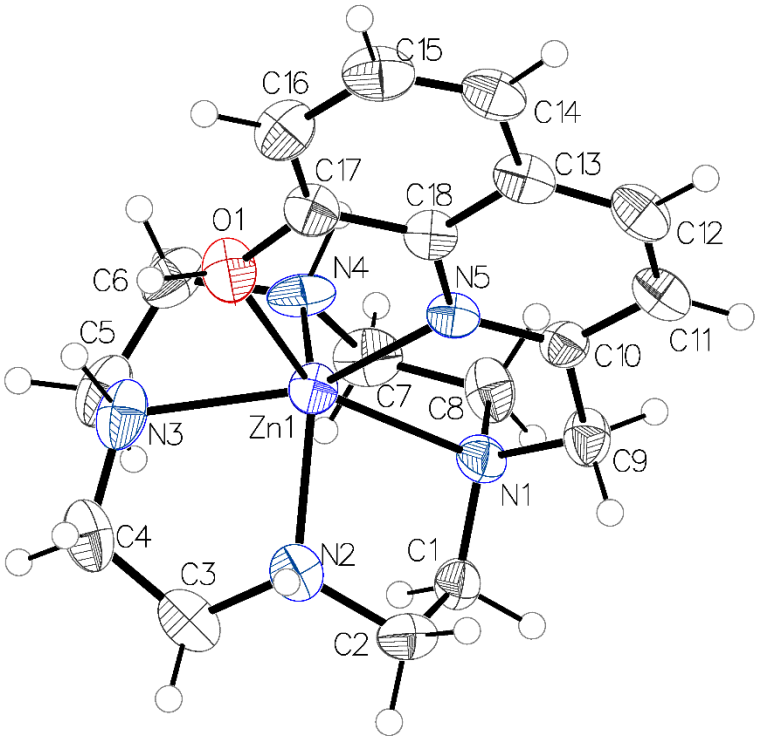

*Figure 27: ORTEP diagram showing the structure of the **MS1**:Zn.*

X-ray crystal structures were obtained for the complexes **MS2**:Cu, **MS3**:Cu, **MS1**:Zn, and **MS3**:Ni. An ORTEP diagram for **MS1**:Zn is shown in Figure 27. Table 1 shows selected bond lengths and angles for **MS1**:Zn, **MS2**:Cu, **MS3**:Cu, and **MS3**:Ni. Other crystal data are collected in the appendix.

*Table 1: Selected bond lengths and angles for **MS1**:Zn, **MS2**:Cu, **MS3**:Cu, and **MS3**:Ni.*

	MS1:Zn	**MS2**:Cu	**MS3**:Cu	**MS3**:Ni
M-N1	2.304 (5)	2.055 (13)	2.047 (4)	2.143 (6)
M-N2	2.120 (5)	2.016 (12)	2.019 (4)	2.044 (7)
M-N3	2.211 (5)	2.024 (13)	2.022 (4)	2.113 (7)
M-N4	2.111 (5)	2.058 (11)	2.020 (4)	2.071 (7)
M-N5	2.094 (4)	-	-	-
M-O	2.340 (4)	2.108 (9)	2.138 (3)	2.099(5)
M-N1-C9	109.4 (3)	112.9 (9)	113.2 (3)	112.6 (5)
N1-C9-C10	112.3 (5)	116.4 (13)	115.3 (5)	118.0 (6)
N1-M-N2	80.26 (17)	85.6 (5)	86.61 (18)	84.9 (3)
N2-M-N3	79.87 (19)	86.6 (5)	85.91 (18)	84.3 (3)
N3-M-N4	80.4 (2)	86.7 (5)	85.99 (18)	81.4 (3)
N4-M-N1	79.78 (18)	86.4 (5)	86.58 (18)	82.0 (3)

In each of the structures, the cyclen macrocycle is bound to the metal centre in the expected tetradentate fashion. In the structures of **MS2**:Cu, **MS3**:Cu and **MS3**:Ni, the pendant arms **of MS2** and **MS3** are not coordinated to the metal centre. In the cases of **MS2**:Cu and **MS3**:Cu, an O atom of the sulfate anions occupies an apical position to give square pyramidal coordination geometry. In the case of **MS3**:Ni, there are two molecules in the asymmetric unit. Each complex has two water molecules coordinated to the Ni centre resulting in a distorted octahedral geometry and no coordination of the accompanying sulfate anions

Unlike the **MS2** and **MS3** complexes, the structure of **MS1**:Zn shows that the remaining two coordination sites of the distorted octahedral geometry are occupied by the donor atoms (N and O) of the 8-hydroxyquinolinyl pendant arm. Thus, this ligand binds in a hexadentate fashion as was envisioned when the ligands were designed. The charge of the **MS1**:Zn cation

is balanced by a tetrahedral $ZnCl_4^{2-}$ anion (not shown). The metal-nitrogen bond distances for **MS1**:Zn (Table 1) are generally longer than the metal-nitrogen distances for the other complexes. Similarly, the N-M-N angles for **MS1**:Zn are smaller than those of the other complexes as are the M-N1-C9 and N1-C9-C10 angles. These geometries allow for accommodation of the bidentate quinolinyl group in the coordination sphere of the metal.

3.1.3. Aβ40 Assays

Aβ40 is a 40 amino acid proteolytic product derived from the amyloid precursor protein (APP) and can be used to study the aggregation behaviour of Aβ *in-vitro*. A turbidimetric assay (Chen *et al*., 2009) was used to investigate the effect of **MS1-4** on the Cu^{2+}-induced aggregation of $A\beta_{40}$. In the assay aggregation of $A\beta_{40}$ is induced by the addition of Cu^{2+} ions and the resulting increase in optical absorbance of the assay mixture, (monitored at 405 nm) can be used to quantify $A\beta_{40}$ aggregation. Upon addition of **MS1-4** disaggregation of $A\beta_{40}$ occurred as shown by a corresponding decrease in optical absorbance of the assay mixture (Figure 28). Disaggregation and dissolution of $A\beta_{40}$ is caused by **MS1-4** binding Cu^{2+} ions. Each chelators was equally effective at decreasing turbidity to levels similar to that of un-aggregated $A\beta_{40}$.

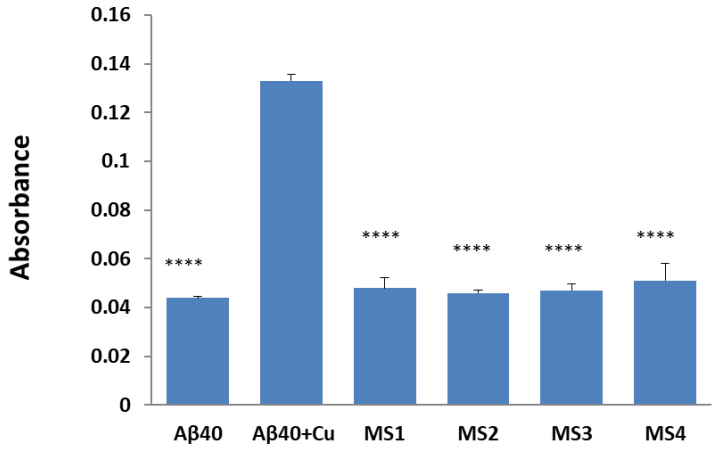

*Figure 28: Optical absorbance at 405 nm for Aв$_{40}$, Aв$_{40}$ + Cu, and Aв$_{40}$ + Cu after incubation for 4 h with **MS1-4**. Different from control (Aв40 + Cu): ****P < 0.0001*

The effect of **MS1-4** on Aβ$_{40}$ aggregation was further evaluated using the BCA protein assay, a biochemical assay for determining the total concentration of protein in a solution using bovine serum albumin as a standard (Smith *et al*., 1985, Stabile *et al*., 2002), which assesses the concentration of Aβ$_{40}$ in solution. After the standard curve of BCA assay was plotted (Figure 64 in appendix), concentrations of different components of Aβ40 in each solution (Aβ40, Aβ40/Cu and Aβ40/Cu/cyclen compounds) (figure 29) were taken from the standard curve.

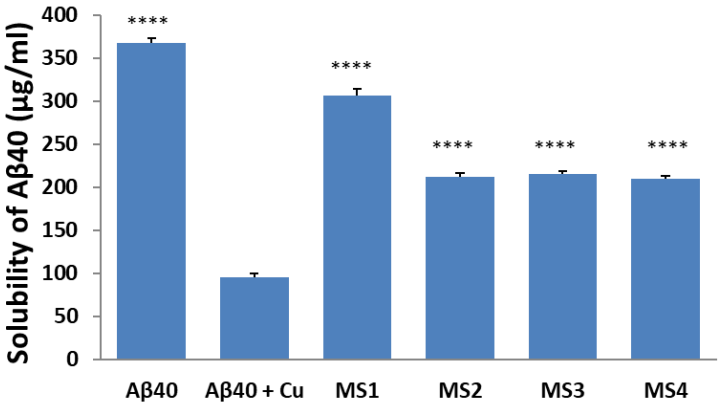

*Figure 29: Solubility data for Aв$_{40}$, Aв$_{40}$+ Cu^{2+} ions, and Aв$_{40}$+ Cu^{2+} after incubation with **MS1-4** for 4h. Different from control (Aв40 + Cu): ****P < 0.0001.*

Figure 29 and Table 13 in the appendix show solubility data for $A\beta_{40}$ before and after treatment with Cu^{2+} ions and then with **MS1-4**. After incubation for 48 hours with Cu^{2+} the solubility of $A\beta_{40}$ decreased by ~75 % due to Cu^{2+}-induced aggregation. Upon addition of **MS1-4** for 4 h, $A\beta_{40}$ solubility increased significantly. The re-solubilisation of the $A\beta_{40}$ is attributed to copper sequestration by **MS1-4** to disassemble the aggregates and thus return the $A\beta_{40}$ to the solution. **MS1** had the greatest effect in this assay and returned $A\beta_{40}$ solubility to ~ 83% of control. **MS2-4** were less active and only restored $A\beta_{40}$ solubility to ~ 60%. The superior activity of **MS1** may be due to its ability to form hexadentate complexes, as opposed to **MS2-4** which can only coordinate Cu in a tetradentate manner. The UV–visible spectrum of **MS1:**Cu (Figure 87 in the appendix) exhibits a maximum absorbance of 646 nm in the visible region, similar to the value of 648 nm reported for a six-coordinate Cu^{II} cyclen complex bearing a picolinate pendant group (Lima *et al*., 2012). Similarly, the complexes bearing the tetradentate ligands **MS2–4** show absorption bands in the range 603–621 nm (Figure 87), indicative of five-coordinate Cu^{II} species (Lima *et al*., 2012).

To confirm that the Cu^{2+} ions responsible for $A\beta_{40}$ aggregation were subsequently chelated upon introduction of the cyclen compounds **MS1-4**, and that unbound $A\beta_{40}$ was returned to the solution, aliquots of the supernatant from centrifuged $A\beta_{40}/Cu^{2+}$/cyclen mixtures were examined using ESI-MS (Table 2 and Figures 65-68 in the appendix). The data obtained from $A\beta_{40}/Cu^{2+}$ samples prior to addition of **MS1-4** contained no signal for $A\beta_{40,}$ indicating that there was no detectable $A\beta_{40}$ in solution. Samples treated with **MS1-4** contained signals for $A\beta_{40}$ species with different degrees of protonation as well as the corresponding cyclen-Cu complex. These data are consistent with the ability of **MS1-4** to sequester Cu^{2+} ions from the assay mixture, resulting in de-aggregation of $A\beta_{40}$ into soluble monomeric species.

*Table 2: ESI-MS data from analysis of the supernatant of centrifuged samples of Aβ40 after de-aggregation using **MS1-4**.*

Chelator	[Aβ40 + 6H]$^{6+}$ (*m/z*) ($C_{194}H_{301}N_{53}O_{58}S$)	[Aβ40 + 5H]$^{5+}$ (*m/z*) ($C_{194}H_{300}N_{53}O_{58}S$)	[Aβ40 + 4H]$^{4+}$ (*m/z*) ($C_{194}H_{299}N_{53}O_{58}S$)	Cu [Cyclen compound] (*m/z*)
MS1	722.5357	866.8405	1083.3023	391.1432 ($CuC_{18}H_{26}ON_5$)
MS2	722.5353	866.8414	1083.3010	397.1767 ($CuC_{17}H_{30}ON_6$)
MS3	722.5346	866.8401	1083.3013	353.1644 ($CuC_{16}H_{28}N_5$)
MS4	722.7002	866.8436	1083.3021	380.1725 ($CuC_{14}H_{31}O_3N_5$)

3.1.4. Antioxidant activity of MS1-4

The antioxidant activities of **MS1-4** were evaluated using the 1,1-diphenyl-2-picrylhydrazyl (DPPH) scavenging assay (Sharma and Bhat, 2009) using ascorbic acid as a reference material. DPPH is a stable free radical that can be scavenged by efficient antioxidants (scheme 6). Thus, the decrease in optical absorbance (at a wavelength corresponding to that of DPPH absorbance) upon introduction of an antioxidant provides a measure of the free radical scavenging activity.

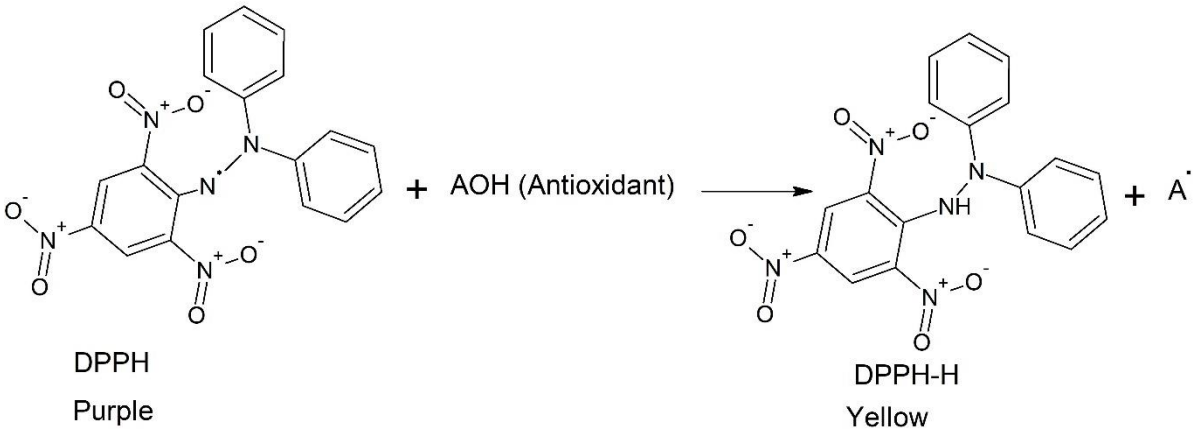

Scheme 6: The DPPH-antioxidant reaction.

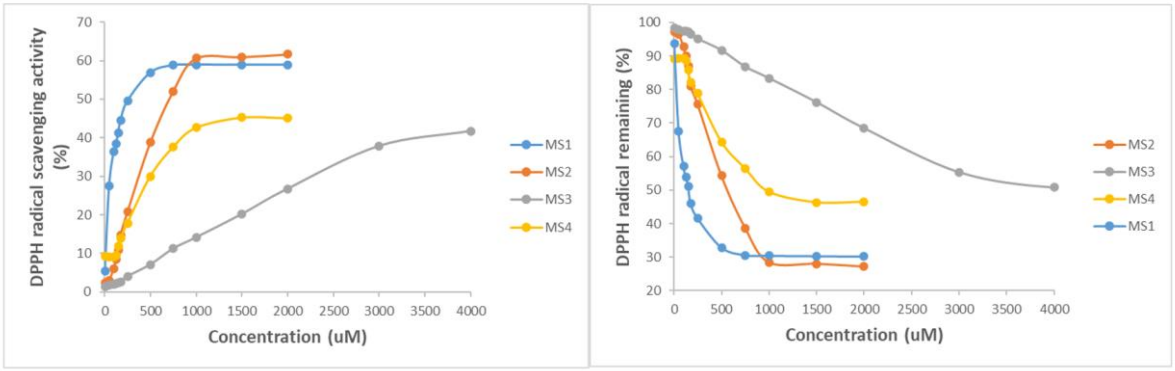

*Figure 30 (Left) graph showing the scavenging activity of the DPPH radical by cyclen compounds and (right) the percentage of DPPH radicals remaining in solution after the reactions with **MS1-4**.*

Figure 30 shows the measured radical scavenging activities (left panel), and the percentages of DPPH radical remaining after reaction (right panel) for **MS1-4** while IC_{50} data are presented in Table 3.

Table 3: IC_{50} data from DPPH assays.

Compound	IC_{50} (µM)
Vit. C	22 ± 3
MS1	71 ± 4
MS2	400 ± 14
MS3	1630 ± 21
MS4	440 ±12

All of the tested compounds exhibit activities lower than that of ascorbic acid. Compound **MS3** shows a very low activity (IC_{50} > 500 µM) whereas **MS1** has a reasonable activity with an IC_{50} value of 71 µM. Compounds **MS2** and **MS4** have modest antioxidant properties (IC50 ~400 µM). These trends are consistent with those that may expected by examination of the molecular structures; ascorbic acid possesses two oxidizable OH functional groups that can donate two protons and thus effectively scavenge the DPPH free radical. On the other hand,

MS1 may donate a single proton from the phenolic OH although the nearby extensive conjugation makes this quite a favourable process. The lack of extended conjugation and readily oxidizable groups in **MS3** is reflected in its low radical scavenging ability.

3.1.5. Computational docking and pharmacokinetic studies

In situations involving aging copper overload, copper may accumulate in the brain capillaries and the BBB (Singh *et al*., 2013) and reduce the level of LRP1 that is responsible for clearing the Aβ. Accumulated free metal ions stimulate the production of extracellular Aβ by binding the active site of α-secretase in APP (Figure 31) through HIS382, HIS432 and HIS436 for zinc and HIS382, HIS432, HIS436 and HIS 313 for copper. In this case, the amyloid production pathway will be enhanced over the non-amyloid pathway (Figure 2), and Aβ can then aggregate in the brain to form plaques, which is the first stage of AD (Singh *et al*., 2013).

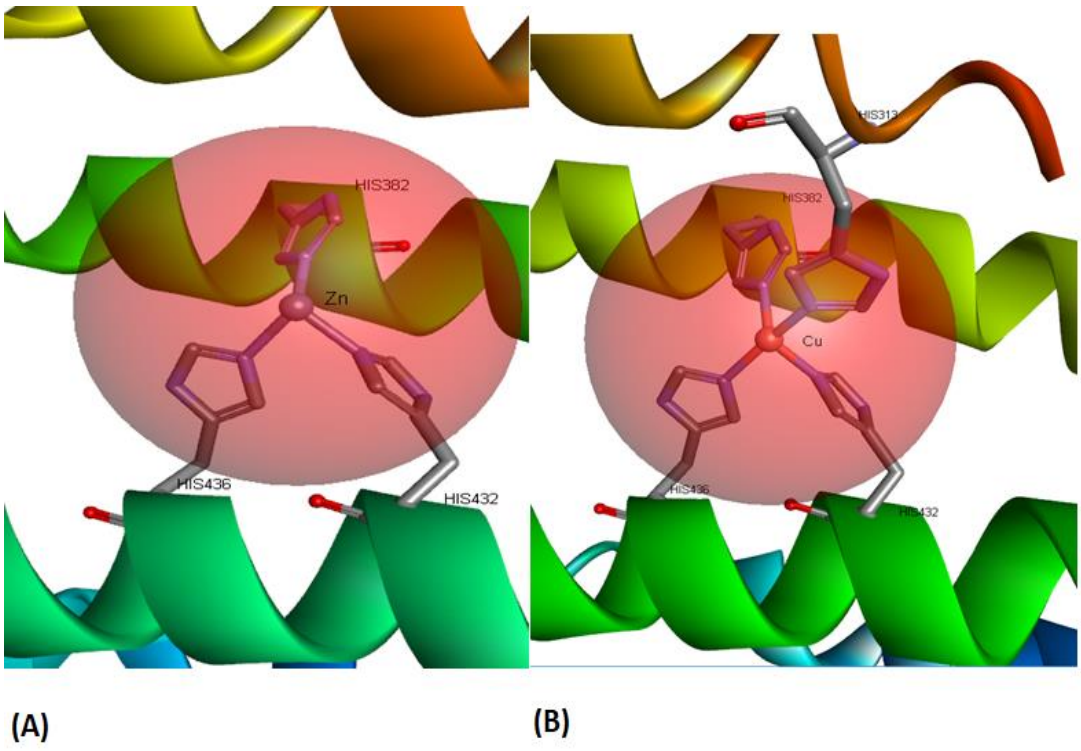

Figure 31: The interaction of APP with Cu^{2+} and Zn^{2+}

Docking studies were used to provide insights into the potential of **MS1-4** to inhibit Aβ production. The E2 domain of the amyloid precursor protein (APP) was selected to model the ability of **MS1-4** to enter the cavity and chelate the Cu^{2+} and Zn^{2+} ions associated with the protein (Baul *et al*., 2015). The binding configurations of Cu^{2+} and Zn^{2+} ions with APP shown in Figure 31 (as well as in Figures 73 and 74 in the appendix) are used as the basis for the calculations.

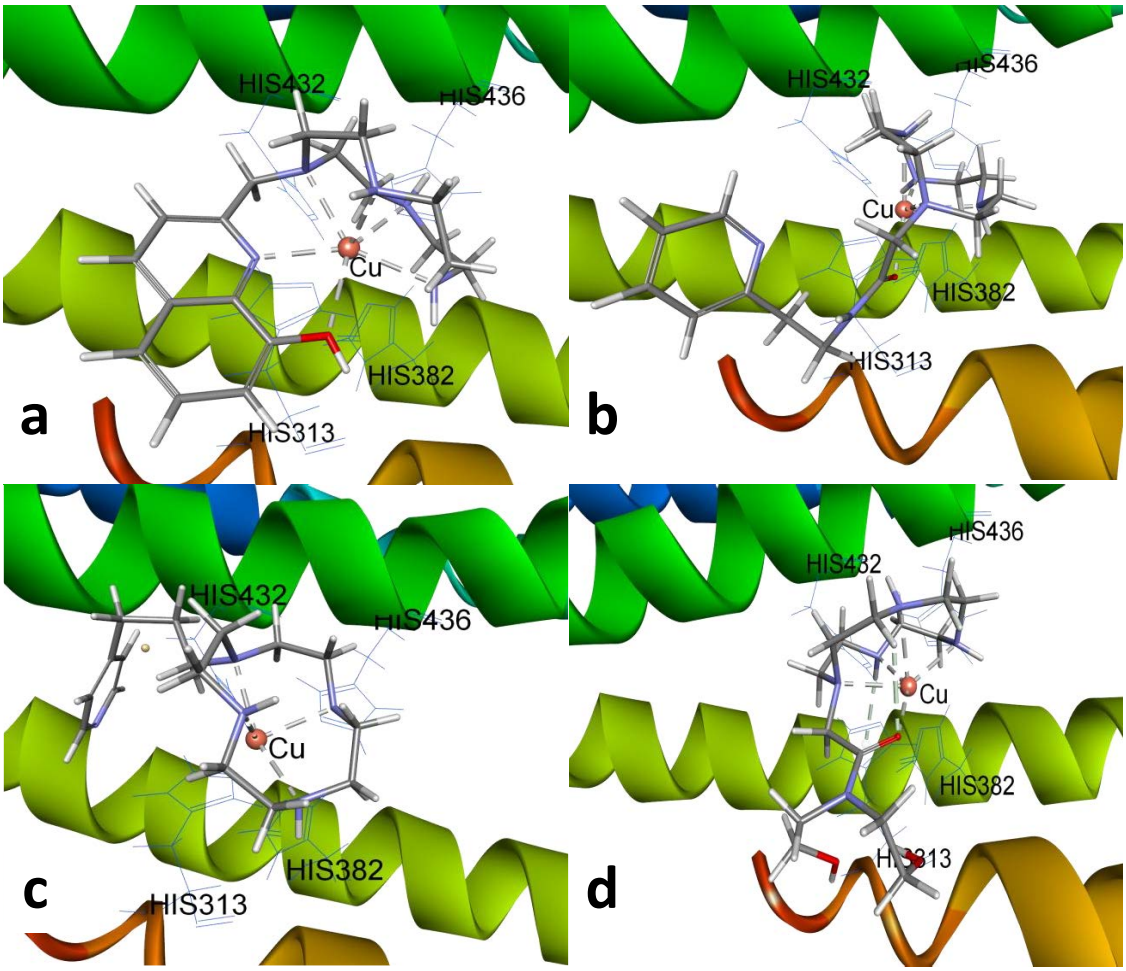

*Figure 32: 3D modelling of the interaction of APP with Cu^{2+} and **MS1** (a), **MS2** (b), **MS3** (c) and **MS4** (d).*

The calculated docking energies (Table 14 in the appendix) are negative for each of the metal-chelator interactions indicating that the chelators are capable of binding the protein-

bound metal ions. In each case, the binding of Zn^{2+} ions was associated with more negative docking energy (i.e. more favorable) than the binding with Cu^{2+} ions. Figure 32 shows the configuration of **MS1-4** chelated to Cu^{2+} ions within the protein where all four nitrogens atoms of the cyclen moiety are bound to the metal ion with N-metal distances ranging from ~2.3-2.5 Å. In the case of **MS1** (Figure 32a), the quinolinyl pendant arm is also bound to the metal centre in a similar fashion to that revealed by the X-ray crystal structure (Figure 27). Metal-oxygen interactions are also evident in the calculated structures of **MS2** and **MS4** with Cu^{2+} (Figure 32b and 32d) and Zn^{2+} (Figure 75 in the appendix), which were not evident in the X-ray structures where the O atoms of sulfate or water occupy the fifth or sixth coordination sites. 2D modelling data of the interaction of APP with Zn^{2+}or Cu^{2+} and **MS1-4** are included in the appendix (Figures 78-85).

For comparison, calculations were performed using clioquinol binding to the same region of the APP protein (Figures 76-77 in the appendix). As expected, docking energies (Table 14 appendix) were negative indicating a favorable interaction of clioquinol with both Cu^{2+} and Zn^{2+} ions. However, the docking energies of **MS1-4** (~-52 to -80 kcal/mol) revealed a significantly stronger interaction with Cu^{2+} and Zn^{2+} ions than those of clioquinol (~-27 and -22 kcal/mol, respectively), which is attributed to the multi-dentate nature of the cyclen groups (plus other O atoms) compared to the bidentate nature of clioquinol.

A bi-plot graph (Figure 86 in the appendix) shows the ADMET_ PSA_2D (polar surface area) versus ADMET_AlogP98 plane (the logarithm of the partition coefficient between n-octanol and water). The ellipses show the regions of well-absorbed compounds by BBB and intestinal membrane. These ellipses were derived from over 800 compounds that are known to pass through BBB after oral administration. The two analogous 95% and 99% confidence

ellipses corresponding to BBB and intestinal absorption. The 95% confidence, ellipse represents the region of chemical space where it may be expected to find well-absorbed compounds (≥90%) 95 out of 100 times, whereas the region of 99% represent the region with excellent absorption. For intestinal absorption, 95% and 99% well-absorbed compounds are expected to be within the ellipses colored in red, green respectively. Whereas for BBB absorption, 95% and 99% well-absorbed compounds are expected to be within the ellipses colored in pink, bright blue respectively. According to this model, in order to have an optimum cell permeability, the following conditions should be met (PSA< 140 $Å^2$ and -2<Alogp98<5) (Egan *et al*, 2002). All the compounds have PSA< 140 $Å^2$ and -2<Alog98<5 except **MS4** (Figure 86 in the appendix and Table 4). compounds **MS1** and **MS3** was found inside the four ellipses (Figure 86 in the appendix), whereas **MS2** was found inside three of them but it was still found in BBB-99 but in case of **MS4** it was found to be outside the 4 ellipses which means all products were satisfied for absorption through BBB and intestine except **MS4**. According to this model, BBB level of a compound penetration varies from 0 to 4 (0: very high, 1: high, 2: medium, 3: low, 4: undefined penetration level). Intestinal absorption level of a compound varies from 0 to 3, (0: good, 1: moderate, 2: low, 3: very low absorption. Table 4 shows that **MS1**, **MS2** and **MS3** have ability to pass through BBB but with low penetrant whereas **MS4** has not showed the ability to pass through BBB.

The aqueous solubility parameter is used to evaluate the solubility in water of the drug-promoted compounds to determine their hydrophilicity and lipophilicity while in the blood stream. It is rated from 1 to 5 corresponding to the predicted solubility based on the drug-likeness similarity (0: extremely low solubility or non-soluble, 1: very low solubility but possible under specific conditions, 2: low solubility, 3: good solubility, 4: optimal solubility, and 5: too soluble). **MS1-4** are having optimal or good aqueous solubility (Table 4).

Furthermore, the products are assessed with respect to cytochrome (CYP2D6) binding, so **MS1-4** are non-inhibitor for CYP2D6 that is one of the important enzymes in drug metabolism. This indicates that **MS1-4** are well-metabolized in the first phase metabolism. Table 4 shows that **MS1**, **MS2** and **MS3** have good intestinal absorption, whereas **MS4** shows very low intestinal absorption.

Table 4: Compliance of 1-4 with the standard range of computational pharmacokinetic parameters (ADMET)

compound	Aqueous solubility level	BBB penetration level	Cytochrome (CYP2D6) binding	Hepato-toxicity	Intestinal Absorption level	Plasma-protein binding (PPB) prediction	A log P98	ADMET PSA 2D
MS1	3 (yes, good)	3 (low penetrant)	False (non-inhibitor)	True (toxic)	0 (good)	False (poorly bounded)	0.69	73.859
MS2	4 (yes, optimal)	3 (low penetrant)	False (non-inhibitor)	False (non-toxic)	0 (good)	False (poorly bounded)	-1.097	83.155
MS3	4 (yes, optimal)	3 (low penetrant)	False (non-inhibitor)	True (toxic)	0 (good)	False (poorly bounded)	0.157	53.044
MS4	5 (too soluble)	4 (undefined penetrant)	False (non-inhibitor)	True (toxic)	3(very low absorption)	False (poorly bounded)	-2.866	104.067

MS1, **MS3** and **MS4** have been predicted to have hepatotoxicity, whereas **MS2** has been predicted to have no toxicity (Table 4). The hepatotoxicity model was derived from over 382 known compounds to exhibit liver toxicity, according to that the model classifies the compounds as true: toxic and false: nontoxic. Finally, **MS1-4** have good bioavailability and show poorly bounded to carrier proteins in the blood according to plasma protein binding prediction (PPB) (Table 4).

3.2. Chelating compounds for Parkinson's disease*

The accumulation of iron in dopaminergic neurons can play a role in oxidizing dopamine into cytotoxic quinone species that cause oxidative stress and progressive dopaminergic neuron degeneration. Iron chelation therapy has been proposed to reduce dopaminergic neurodegeneration (Mounsey and Teismann, 2012). Deferiprone and clioquinol have high selectivity's towards iron, are orally active, and can cross the BBB (Mounsey and Teismann, 2012, Santos *et al*., 2012, Finkelstein *et al*., 2016). While studies into the efficacy of iron chelation therapy are ongoing, there is a concern that removal of iron from all regions of the brain may produce adverse side effects as iron is essential to normal brain function.

The goal of this work was to develop iron chelators that can *preferentially accumulate in the dopaminergic neurons* that are degraded in the early stages of PD. The strategy devised to achieve this was to design metal chelators that are also DAT substrates. DAT is a transport protein expressed in the plasma membrane of dopaminergic neurons that actively transports dopamine and drugs such as amphetamine into dopaminergic neurons. Thus it was hypothesised that introduction of amphetamine-like structures to iron chelators such as deferiprone or 8-hydroxyquinoline may produce novel drug candidates that are both iron chelators and DAT substrates. The structures of the proposed compounds are shown in Figure 33.

* A significant portion of the work described in this section is not able to be published (at the time of submission) due to intellectual property considerations.

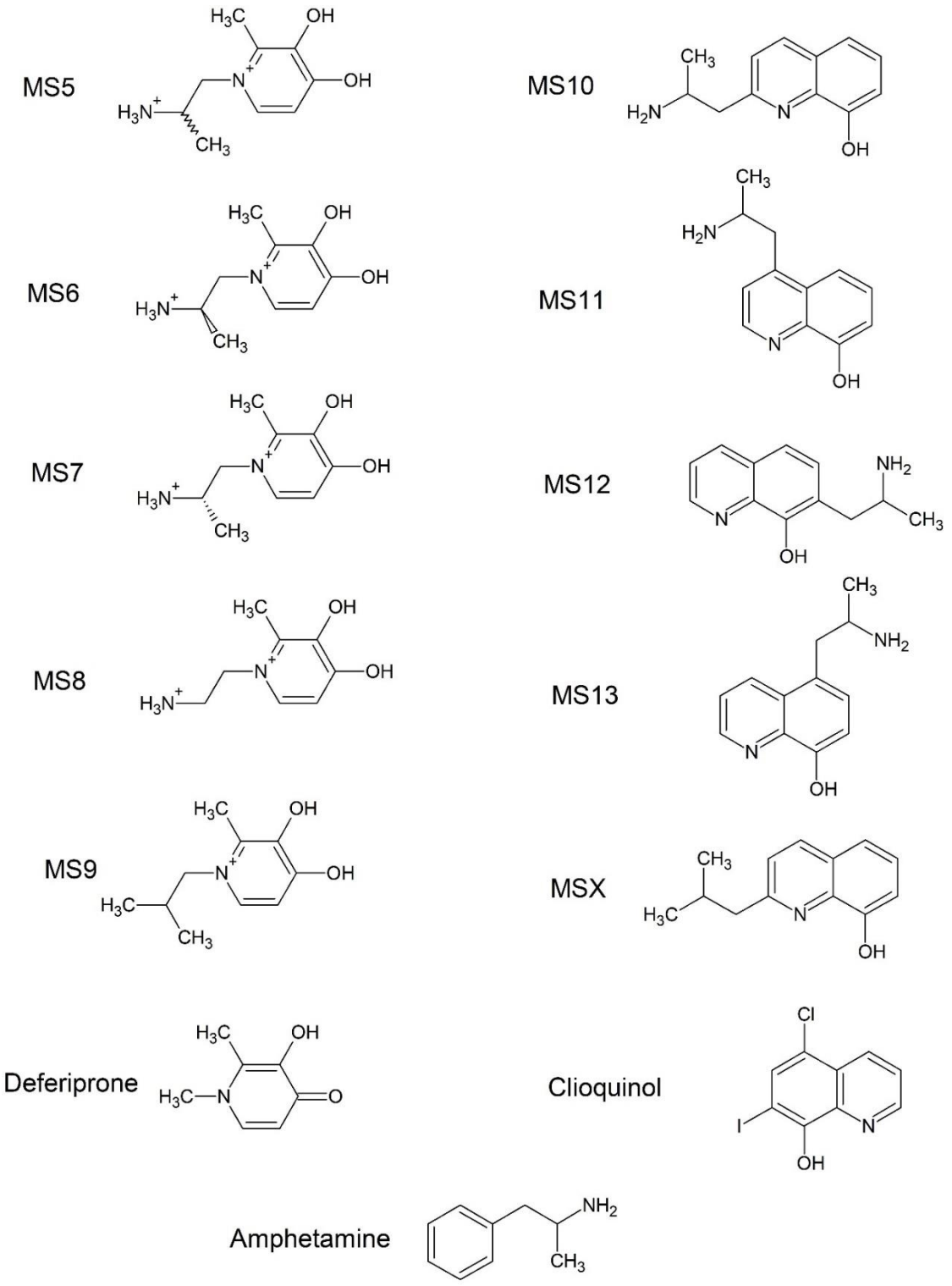

*Figure 33: Chemical structures of deferiprone, clioquinol, amphetamine and the hybrid structures **MSX** and **MS5-13**.*

MS5-9 are deferiprone-based compounds. The *S* enantiomer of amphetamine is the most active DAT substrate (Seddik *et al*., 2013) and so the *S*-isomer of the deferiprone-based

compound was synthesized (**MS7**) together with the *R*- and racemic analogues for comparison (**MS5-6**). **MS8-9** are deferiprone-based compounds that differ from the amphetamine-like structure such that **MS8** has one less carbon atom the chain bearing the amine and **MS9** has the amine replaced with a CH_3 group. **MS8-9** were synthesised to compare the transportation affinity with the deferiprone-based compounds that have an amphetamine-type structure (**MS5-7**). It is hypothesised that **MS8-9** will have inferior transportability compared to **MS5-7**.

Compounds MS**10-13** are 8-hydroxyquinoline-based compounds that have amphetamine-like structures. The amine-bearing chain was located in different positions around the 8-hydroxyquinoline ring to determine if the position affects the transportation affinity of the compounds. **MSX** (prepared in collaboration with UTS student Hannah Kallweit) has no amine group and is therefore hypothesised to have poor transportability.

Iron complexes of **MS5-13** were synthesised and isothermal titration studies were undertaken to examine the affinity of **MS5-13** with iron.

3.2.1. Synthesis and characterisation of deferiprone-based compounds

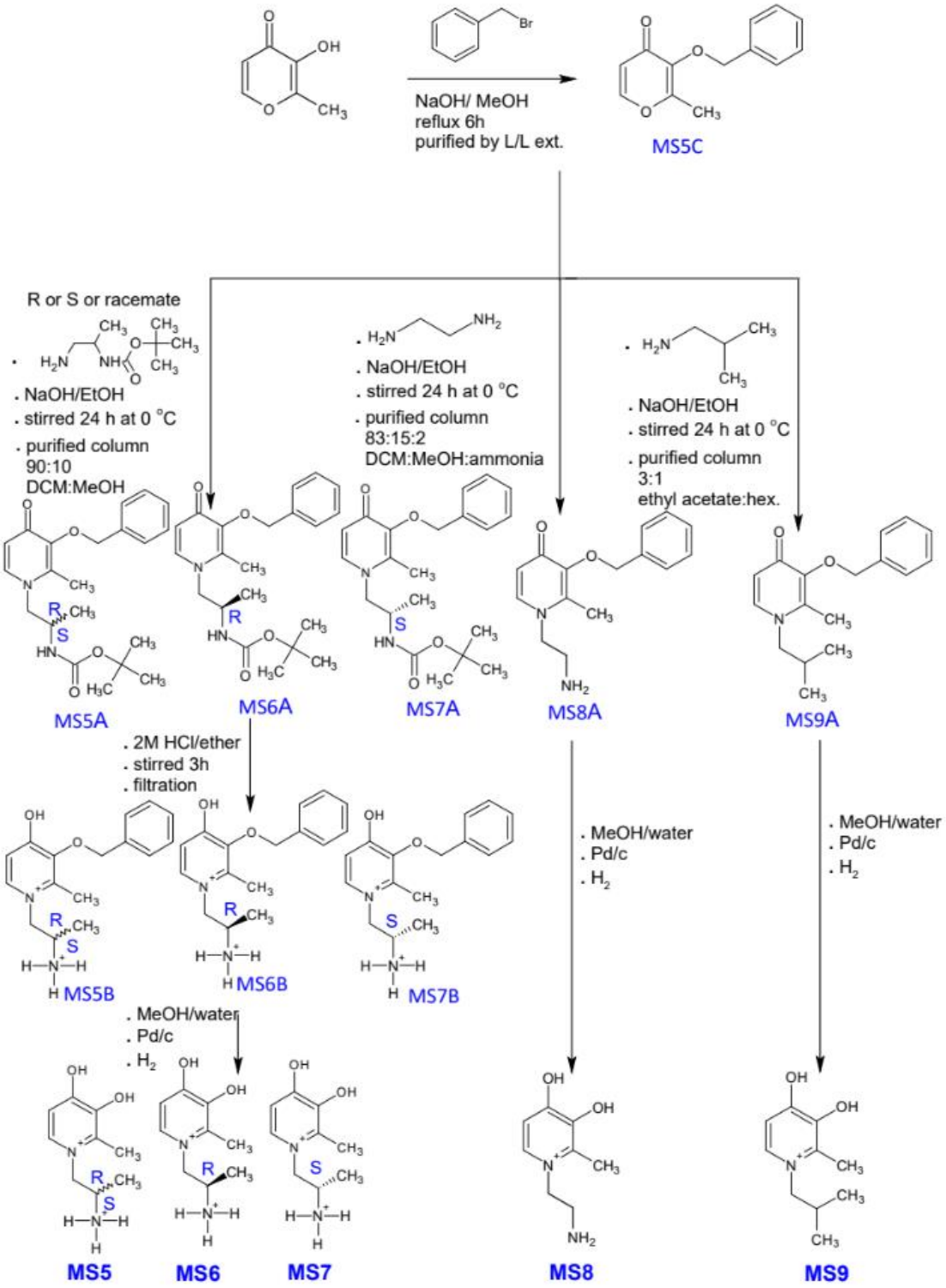

Scheme 7: Synthesis of deferiprone-based compounds

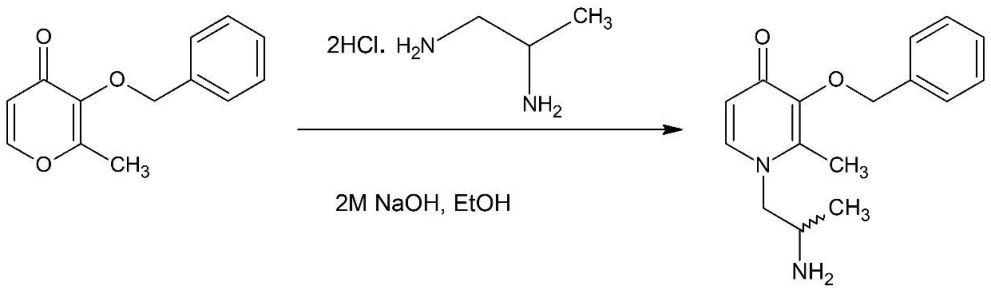

Scheme 8: Preparation of 1-(2-aminopropyl)-3-(benzyloxy)-2-methylpyridin-4(1H)-one

The synthesis of the deferiprone-based compounds was first attempted in a 2-step procedure. Maltol was protected by Williamson ether synthesis using benzyl bromide and sodium hydroxide (Scheme 7) to avoid subsequent interactions of the hydroxy group with amines. Next, (benzyloxy)-2-methyl-4H-pyran-4-one was reacted with alkyl diamine (Scheme 8), which was used in molar excess (five-fold) to minimise the formation of di-substituted products. Two by-products were identified in the crude reaction product by mass spectrometry and NMR spectroscopy (Figure 35 and Figure 88 in the appendix) as [1-(1-aminopropan-2-yl)-3-(benzyloxy)-2-methylpyridin-4(1H)-one] and [1,1'-propane-1,2-diylbis(3-benzyloxy-2-methylpyridin-4(1H)-one)] (Figure 34). The former by-product is an isomer of the desired compound and the latter arises from reaction of the diamine with two -pyran-4-one units. Column chromatography failed to provide pure product, so an alternate synthesis was investigated (Scheme 9).

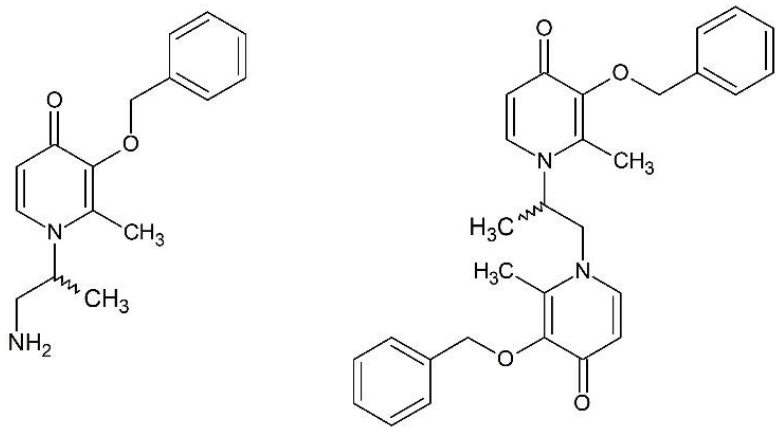

Figure 34: By-products from the synthesis of 1-(2-aminopropyl)-3-(benzyloxy)-2-methylpyridin-4(1H)-one using a diamine.

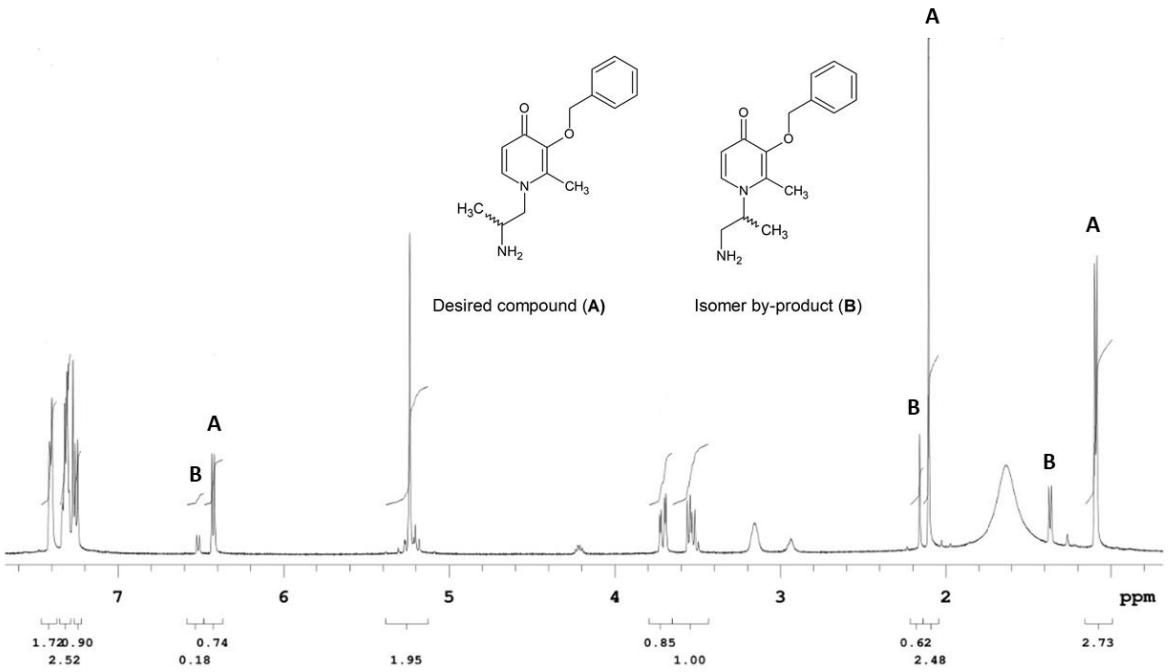

Figure 35: NMR spectrum of by-products from the preparation of 1-(2-aminopropyl)-3-(benzyloxy)-2-methylpyridin-4(1H)-one using the method shown in Scheme 8.

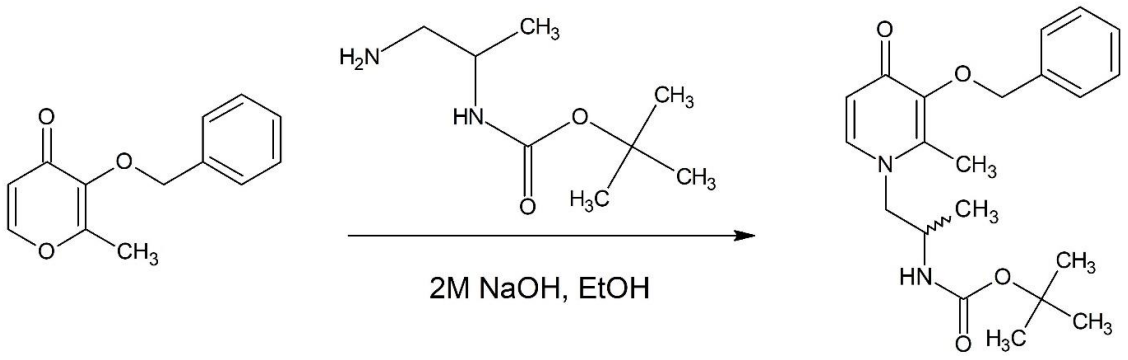

Scheme 9: Preparation of tert-butyl{1-[3-(benzyloxy)-2-methyl-4-oxopyridin-1(4H)-yl]propan-2-yl}carbamate

To prevent by-product formation, the reaction was repeated using tert-butyloxycarbonyl (BOC) protected alkyl diamine (Scheme 9). Ammonolysis of 3-(benzyloxy)-2-methyl-4H-pyran-4-one with racemic BOC-protected alkyl diamine formed tert-butyl{1-[3-(benzyloxy)-2-methyl-4-oxopyridin-1(4H)-yl]propan-2-yl}carbamate. The BOC-protected intermediate was readily purified as no isomers were formed nor any di-substituted amines.

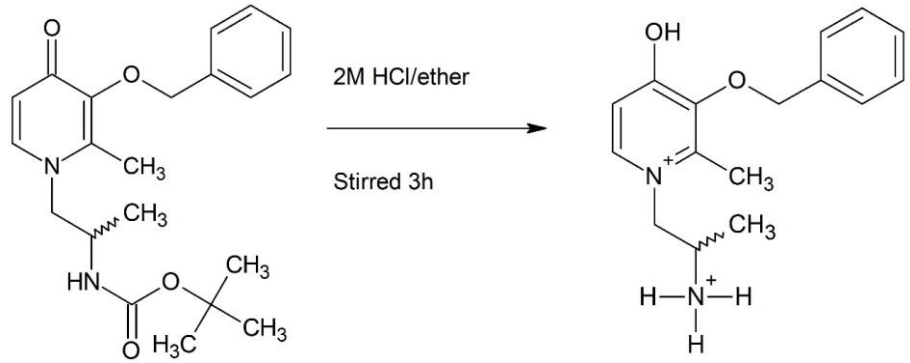

Scheme 10: Preparation of 1-(2-ammoniopropyl)-3-(benzyloxy)-4-hydroxy-2-methylpyridinium

1-(2-Ammoniopropyl)-3-(benzyloxy)-4-hydroxy-2-methylpyridinium was readily synthesised by deprotection of *tert*-butyl{1-[3-(benzyloxy)-2-methyl-4-oxopyridin-1(4H)-yl]propan-2-yl}carbamate using HCl in ether (scheme 10). HCl in ether was found to be superior to aqueous HCl as the product was a fine, fluffy white powder that could be readily collected by filtration, rather than an oily product which formed when using aqueous HCl.

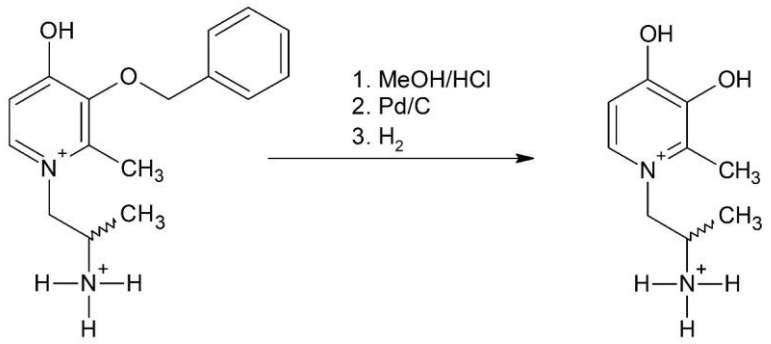

*Scheme 11: 1-(2-ammoniopropyl)-3,4-dihydroxy-2-methylpyridinium (**MS5**)*

MS5 was prepared by removal of the benzyl group of 1-(2-ammoniopropyl)-3-(benzyloxy)-4-hydroxy-2-methylpyridinium using 3M HCl and Pd/C with H_2 (Scheme 11).

MS6-7 were synthesised using the same procedure as **MS5** using by substituting optically active alkyldiamines for the racemic diamine.

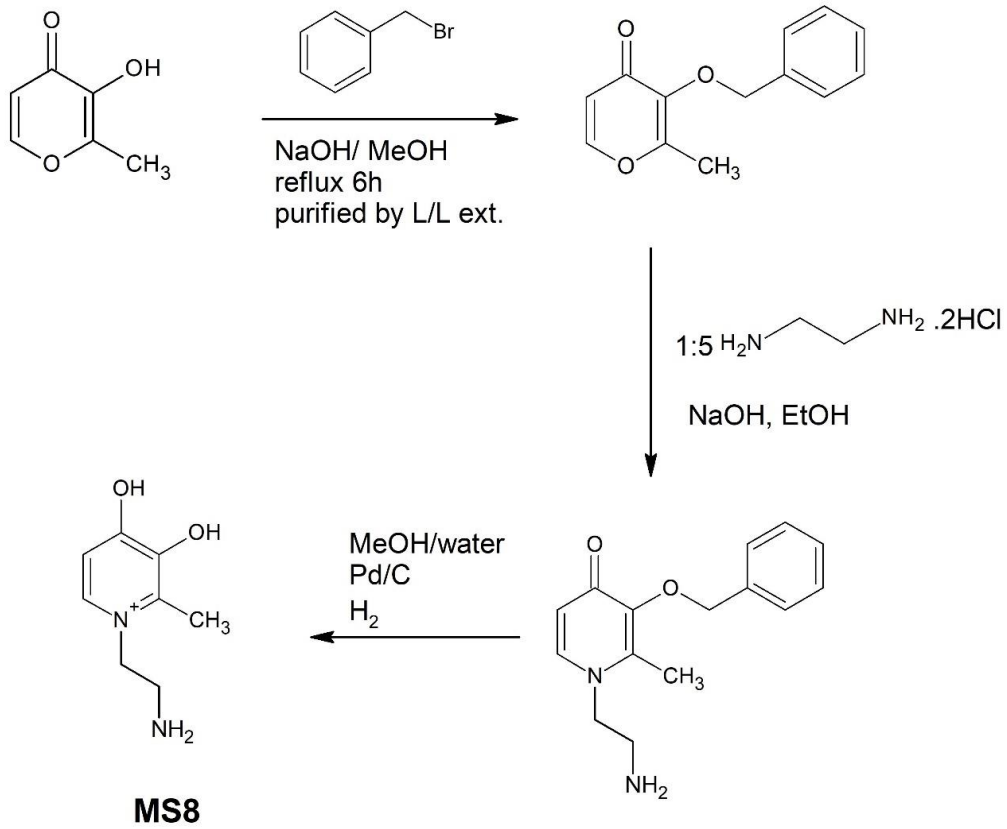

*Scheme 12: Synthetic procedure for the preparation of **MS8***

MS8 was prepared by reacting benzyl-protected maltol with ethylenediamine, which was used in stoichiometric excess (five-fold). Deprotection of the benzyl group using HCl and Pd/C with H_2 afforded **MS8** (Scheme 12 and Figure 36)**. MS9** was prepared similarly by substituting 2-methylpropan-1-amine for ethylenediamine in the second step (Scheme 7).

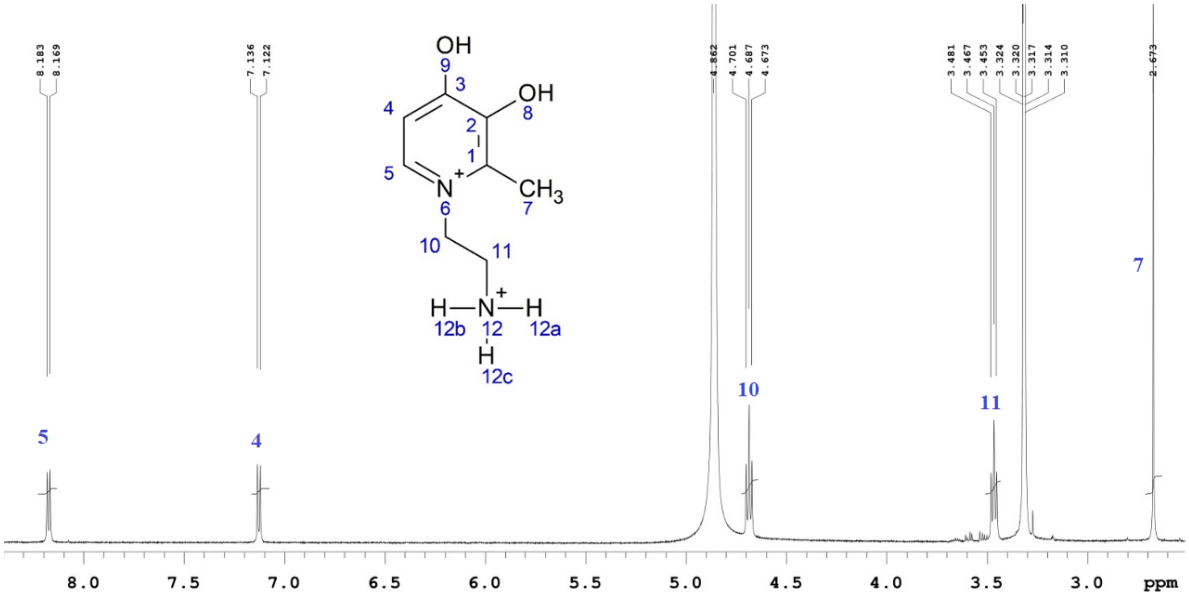

*Figure 36: [1]HNMR for **MS8***

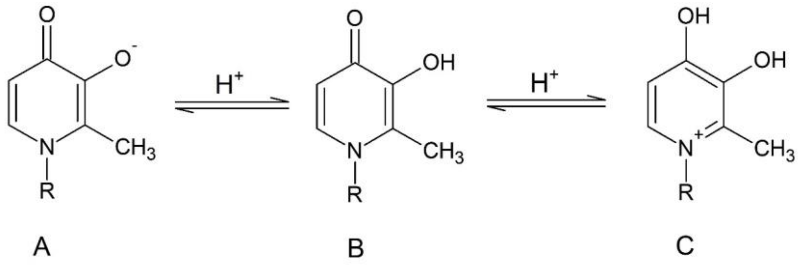

Scheme 13: Protonation/deprotonation of Deferiprone.

Single crystal X-ray crystallography studies of **MS7-9** (Figures 37 and Tables 15-23 in the Appendix) showed the expected structures. Deferiprone-based compounds can be protonated/deprotonated as shown in Scheme 13 depending on the pH (Boroujeni and Gharib, 2016). The acidic conditions used in the final step synthetic step would lead to

products with structures of the type shown in Scheme 13C. This was confirmed by the X-ray analysis as well as ^{13}C NMR spectroscopy, where no signal assigned to a carbonyl peak (expected at ~170 ppm) was observed but a signal assigned to hydroxy group was observed at ~160 ppm.

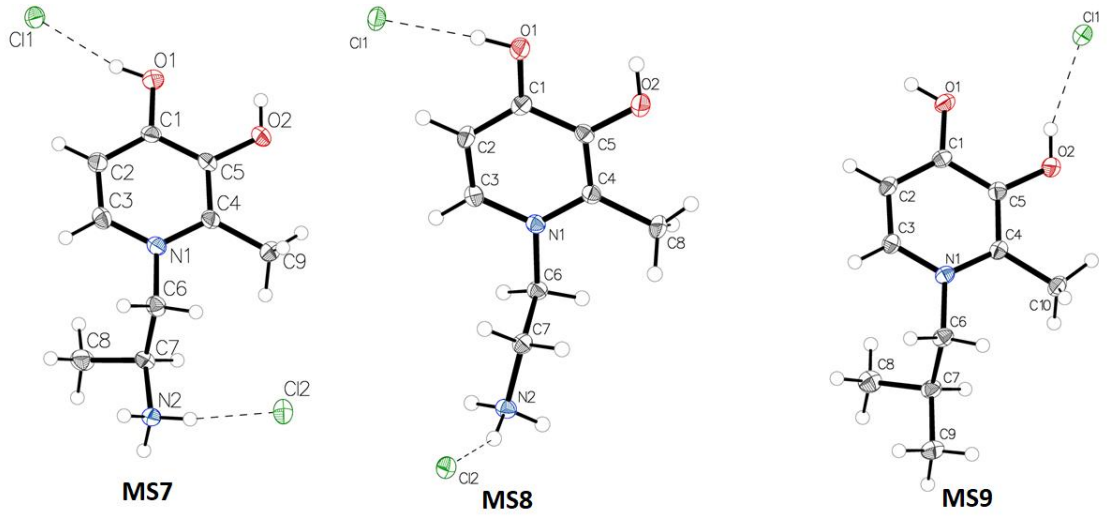

*Figure 37: ORTEP diagrams for **MS7-9***

3.2.2. *Synthesis and characterisation of 8-Hydroxyquinoline-based compounds*

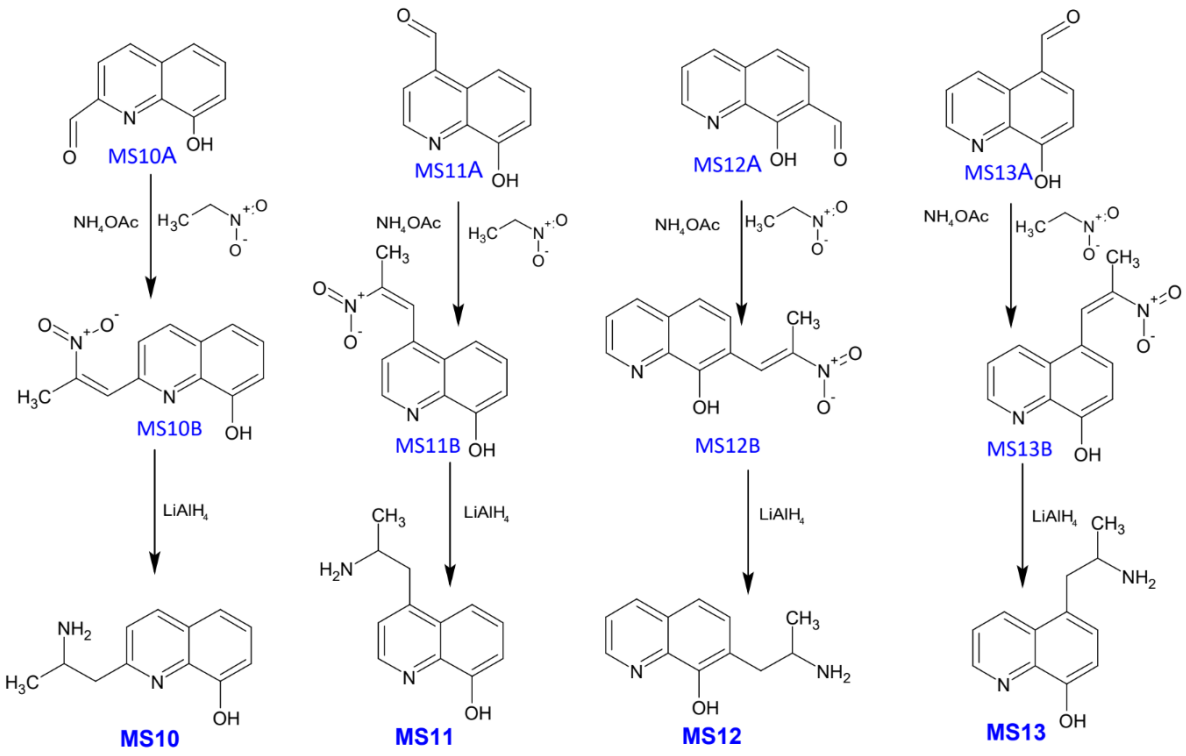

Scheme 14: Synthesis of 8-hydroxyquinoline-based compounds

8-Hydroxyquinoline-2-carbaldehyde was prepared by oxidation of 2-methylquinolin-8-ol using selenium dioxide in dioxane and water (Scheme 15). This procedure is a modification of a previously published synthesis method (Chan *et al*., 2013)

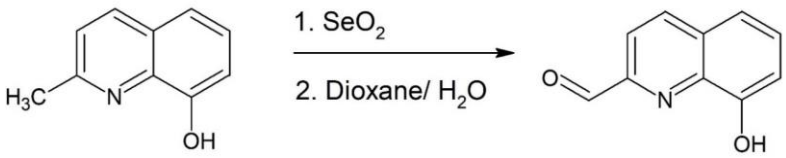

Scheme 15: Preparation of 8-hydroxyquinoline-2-carbaldehyde

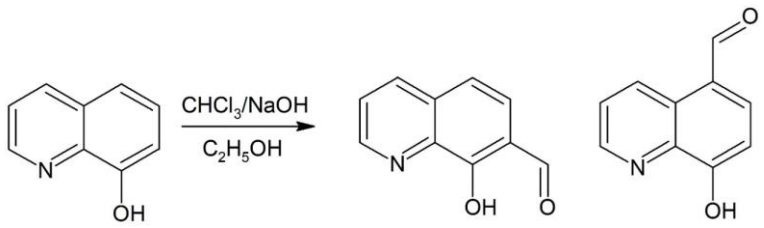

Scheme 16: Preparation of 8-hydroxyquinoline-7-carbaldehyde and 8-hydroxyquinoline-5-carbaldehyde

8-Hydroxyquinoline-7-carbaldehyde and 8-hydroxyquinoline-5-carbaldehyde were prepared according to the modified procedures of Ding *et al.* and Fan *et al.* (Scheme 16) (Ding *et al.*, 2017) (Fan *et al*., 2014). The authors reported contradictory ^{1}H NMR spectra for the two isomers and so single crystal X-ray diffraction studies were undertaken. Single crystals were unable to be obtained for the aldehyde isomers but satisfactory crystals could be grown for the nitroethenyl derivative 5-(-2-nitroprop-1-en-1-yl)quinolin-8-ol (Figure 38).

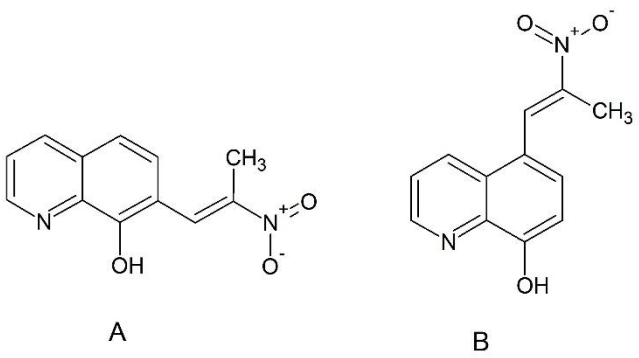

Figure 38: 7-(-2-nitroprop-1-en-1-yl)quinolin-8-ol (A)and 5-(-2-nitroprop-1-en-1-yl)quinolin-8-ol (B).

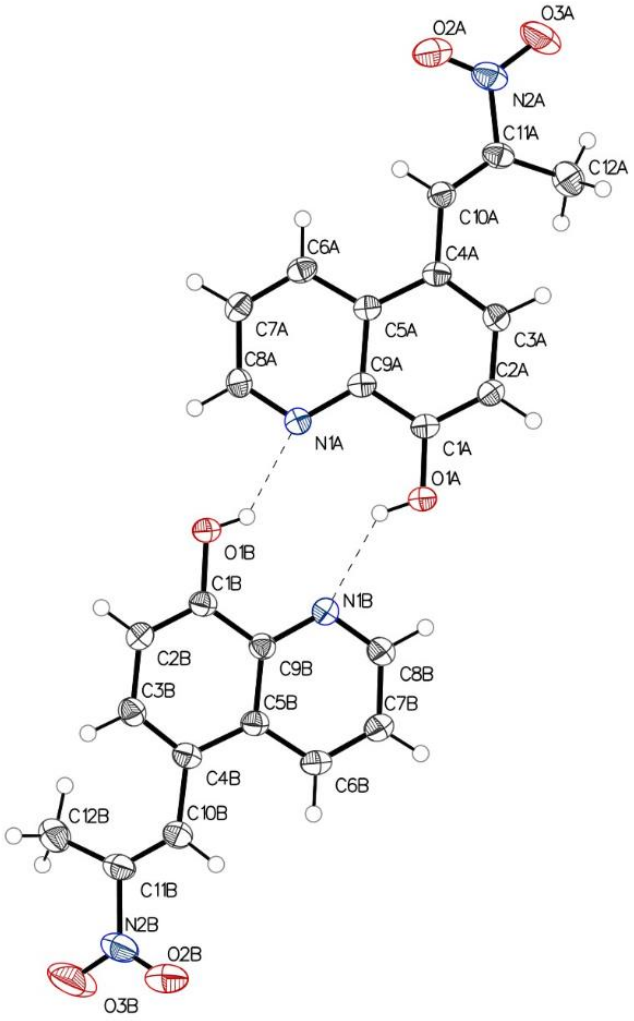

Figure 39: ORTEP diagram of 5-(-2-nitroprop-1-en-1-yl)quinolin-8-ol

The crystallographic analysis of (Figure 39) allowed for unambiguous assignment of the NMR spectra showed that Fan *et al* reported correct spectra for 8-hydroxyquinoline-7-carbaldehyde and 8-hydroxyquinoline-5-carbaldehyde. Figures 40 and 41 show the relevant spectra.

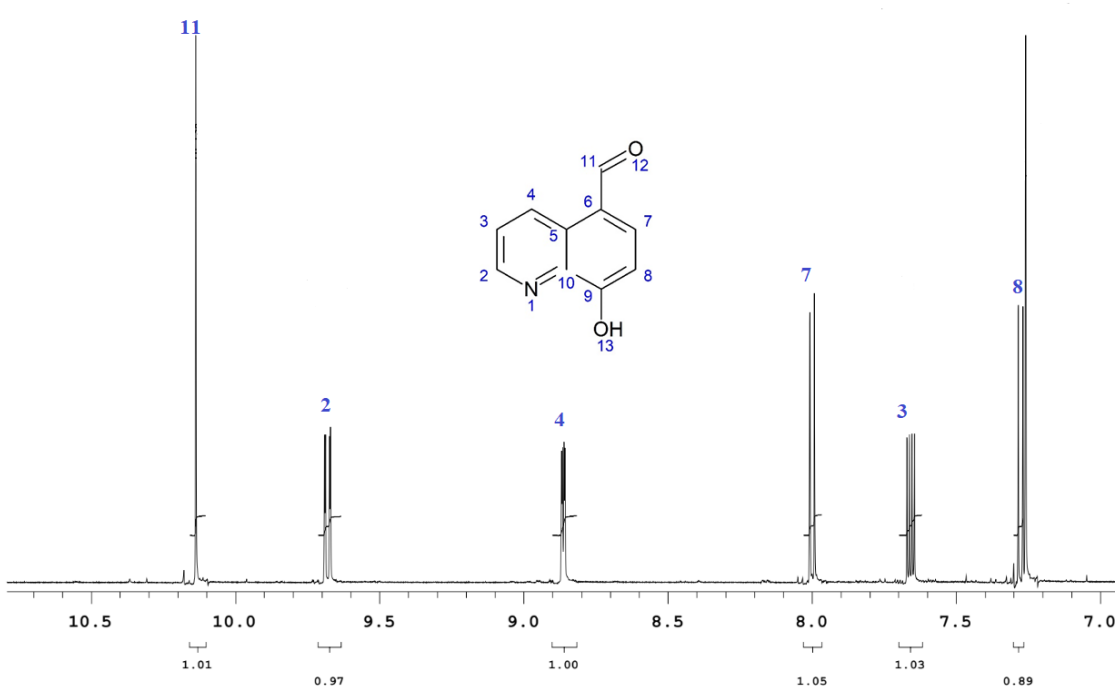

Figure 40: ^{1}H NMR spectrum of 8-hydroxyquinoline-5-carbaldehyde

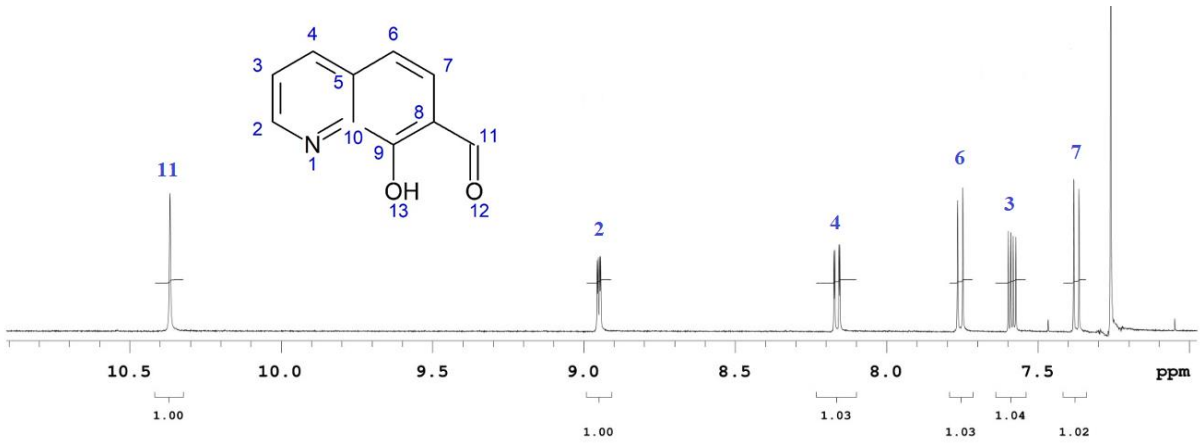

Figure 41: ^{1}H NMR spectrum of 8-hydroxyquinoline-7-carbaldehyde

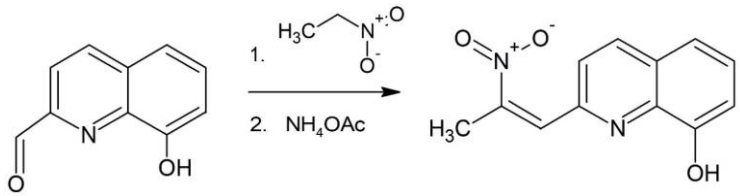

Scheme 17: Preparation of 2-(-2-nitroprop-1-en-1-yl)quinolin-8-ol

2-(-2-Nitroprop-1-en-1-yl)quinolin-8-ol was prepared by the Henry reaction between 8-hydroxyquinoline-2-carbaldehyde and nitroethane in the presence of ammonium acetate (Scheme 17). It is a modification of the procedure of *Liu et al*. (Liu *et al*., 2013). Nitroethane was used as reagent and solvent in this work, which resulted in increased yield compared to the literature method. An X-ray crystal structure confirmed the structure of the compound (Figure 101, tables 24-26 in the appendix).

Similarly, 4-(-2-nitroprop-1-en-1-yl)quinolin-8-ol, 7-(-2-nitroprop-1-en-1-yl)quinolin-8-ol and 5-(-2-nitroprop-1-en-1-yl)quinolin-8-ol were prepared by the Henry reaction. X-ray crystal structures were also obtained for 5-(-2-nitroprop-1-en-1-yl)quinolin-8-ol and 4-(-2-nitroprop-1-en-1-yl)quinolin-8-ol (Figures 102-103, tables 27-32 in the appendix).

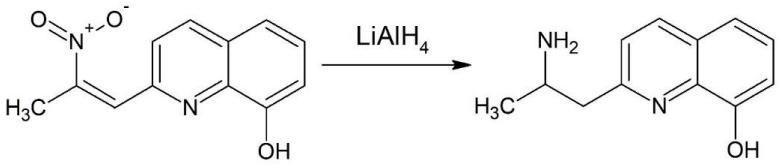

*Scheme 18: Preparation of 2-(2-aminopropyl)quinolin-8-ol (**MS10**)*

MS10 was prepared by reducing the nitropropenyl group to the corresponding aminopropyl group using lithium aluminium hydride (Scheme 18). **MS11**, **MS12** and **MS13** were prepared in a similar fashion (Scheme 14).

The ^{1}H NMR spectra for the crude products of **MS10-13** showed apparent impurities. Upon analysis it was evident that three forms of the compounds were present in the NMR sample: (i) the deprotonated phenoxide (ii) the neutral form (as shown in Scheme 18), and (iii) the doubly protonated salt form (NH^{+} in the ring and NH_3^{+} on the quinolinyl group).

For example, ^{1}H NMR for the crude compound **MS11** (Figure 42) has three peaks for each proton environment (clearly seen between 8.6 and 8.8 ppm in figure 42) arising from the three forms of the compounds. Similar spectra were collected for **MS10**, **MS12** and **MS13**.

Clearly, the degree of protonation of these compounds is highly pH dependent. Adjustment of the pH of a solution of each compound to 10, followed by solvent/solvent extraction allowed pure neutral form of each of the compounds to be isolated (Figure 43).

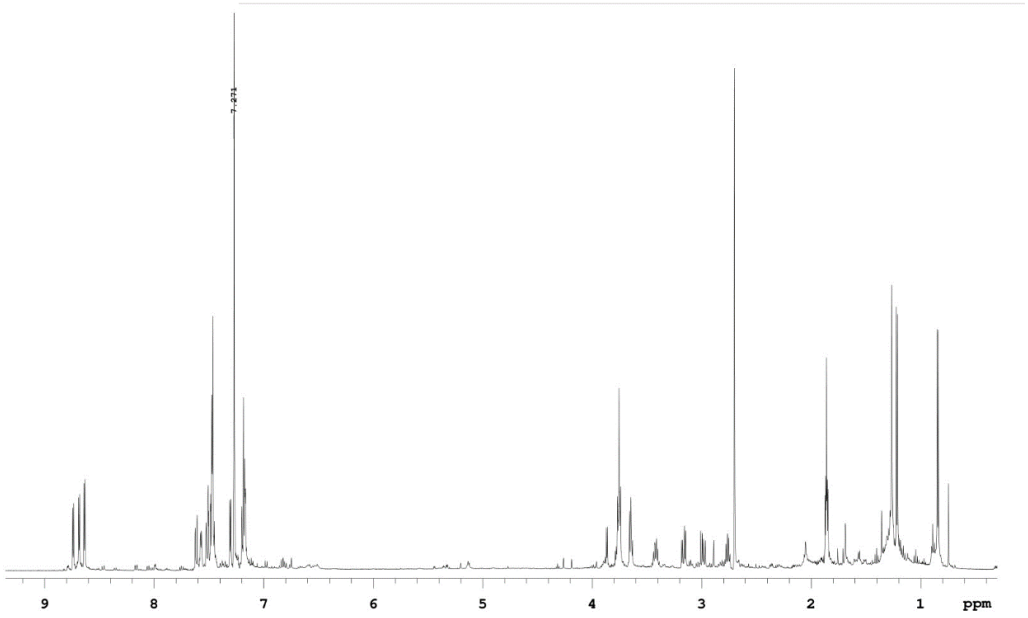

*Figure 42: [1]H NMR spectrum of crude **MS11***

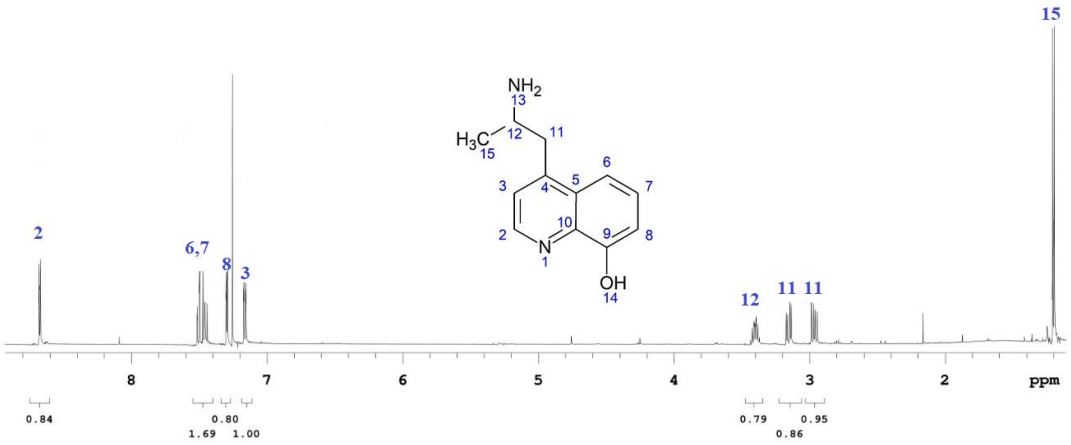

*Figure 43: [1]H NMR spectrum of pure **MS11***

3.2.3. *Iron complexes of deferiprone-based compounds*

The ability of the **MS5-9** to form complexes with iron was investigated. All iron deferiprone-based complexes were prepared by adding iron nitrate to the deferiprone-based

compounds (Scheme 19), and the resulting solutions were analysed by UV-visible spectroscopy and mass spectrometry.

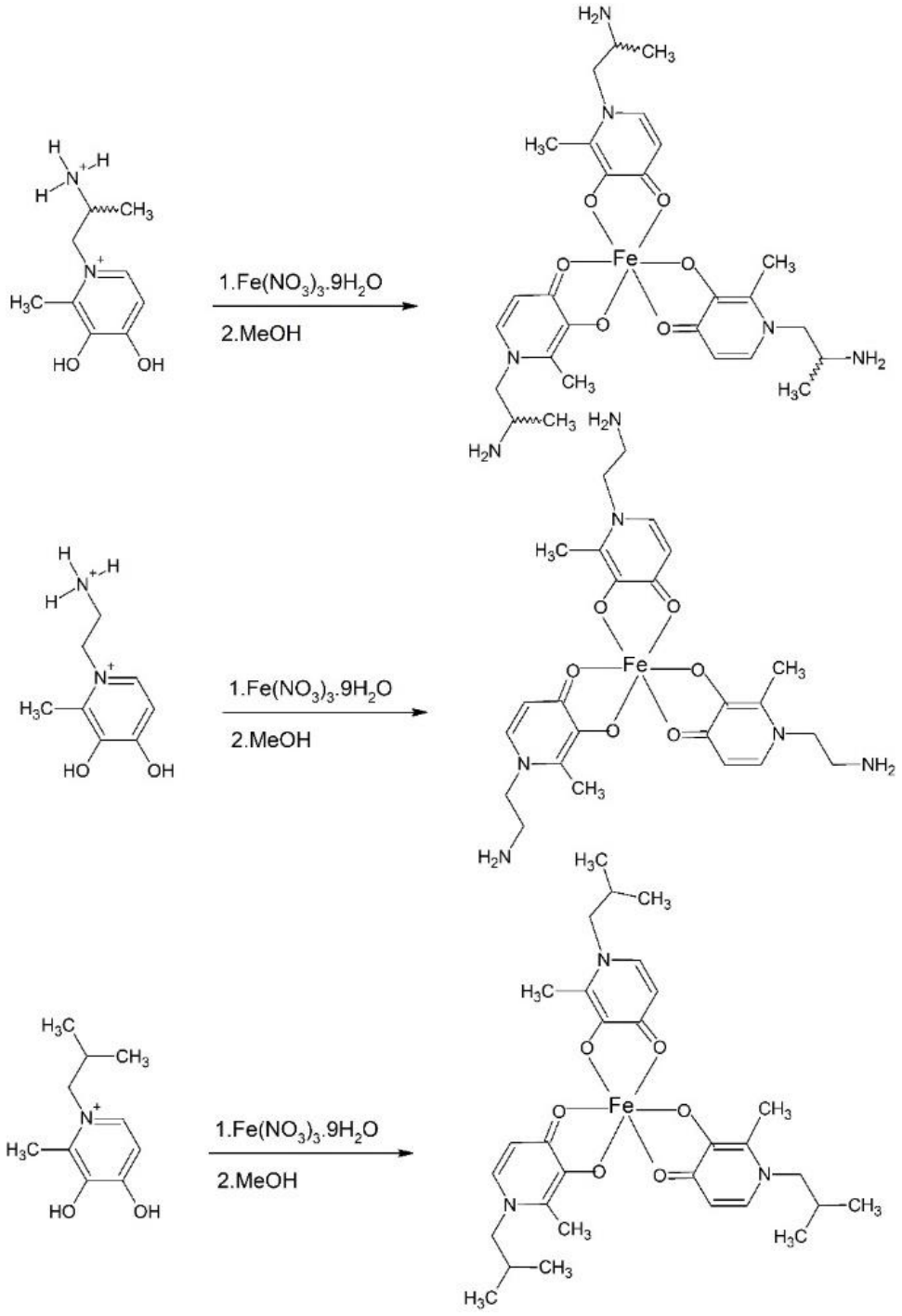

*Scheme 19: Preparation of **(MS5-9)**:Fe complexes*

In the MS study, **MS5-9**:Fe complexes were prepared by adding methanolic solution of iron nitrate to methanolic solution of deferiprone in 3:1 ratio. **MS5-7** displayed similar iron complexation properties. MS analysis (Figure 44) showed peaks with *m/z* vales of 418.12 and 600.23 and were assigned to (**MS5-7**)$_2$:Fe and (**MS5-7**)$_3$:Fe , respectively. Within these complexes the molecular weights of the **MS5-7** were 3.024 less than the parent compounds, indicating the loss of three protons. It can be concluded that the **MS5-7** are in their anionic forms (Scheme 19) within the iron complexes as would be expected.

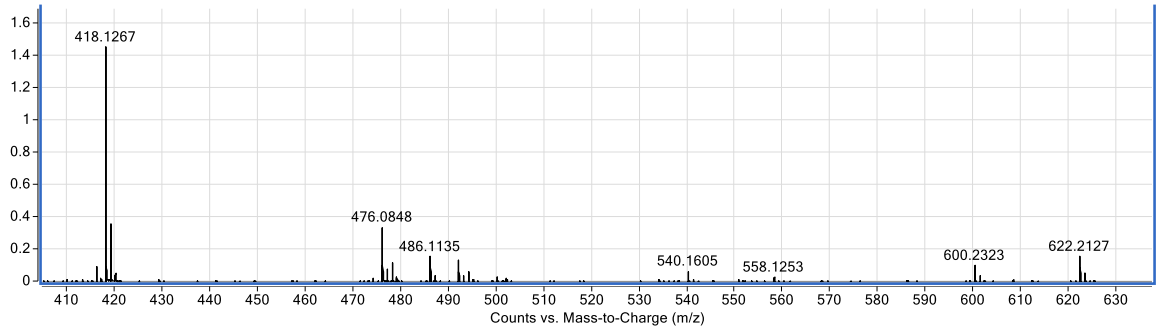

*Figure 44: Mass spectrum of (**MS5-7**):Fe complex*

Similarly for **MS8**:Fe, MS analysis (Figure 89 in the appendix) showed peaks with *m/z* vales of 390.09 and 558.18 and were assigned to (**MS8**)$_2$:Fe and (**MS8**)$_3$:Fe , respectively. Within these complexes the molecular weights of the **MS8** were 3.024 less than the parent compounds, indicating the loss of three protons. It can be concluded that the **MS8** are in their anionic forms (Scheme 19) within the iron complexes as would be expected.

For **MS9**:Fe, MS analysis (Figure 90 in the appendix) showed peaks with *m/z* vales of 416.12 and 597.22 and were assigned to (**MS9**)$_2$:Fe and (**MS9**)$_3$:Fe , respectively. Within these complexes the molecular weights of the **MS9** were 2.024 less than the parent compounds, indicating the loss of two protons. It can be concluded that the **MS9** are in their anionic forms (Scheme 19) within the iron complexes as would be expected.

Iron complexation by **MS5-9** was studied in the UV-Vis as well. In these studies solutions of **MS5-9** and $Fe(NO_3)_3$ were prepared in ratios from 0.5:1 to 6:1 and changes in absorption were followed by UV-visible spectroscopy tested in 10% MeOH in PBS (pH 7.4).

Fe coordination characteristics of **MS5-9** were similar and are discussed together using **MS5** as an example. Figure 45 shows the solution UV/Vis changes that occurred as the **MS5**:Fe ratio was increased from 0.5:1 to 6:1.

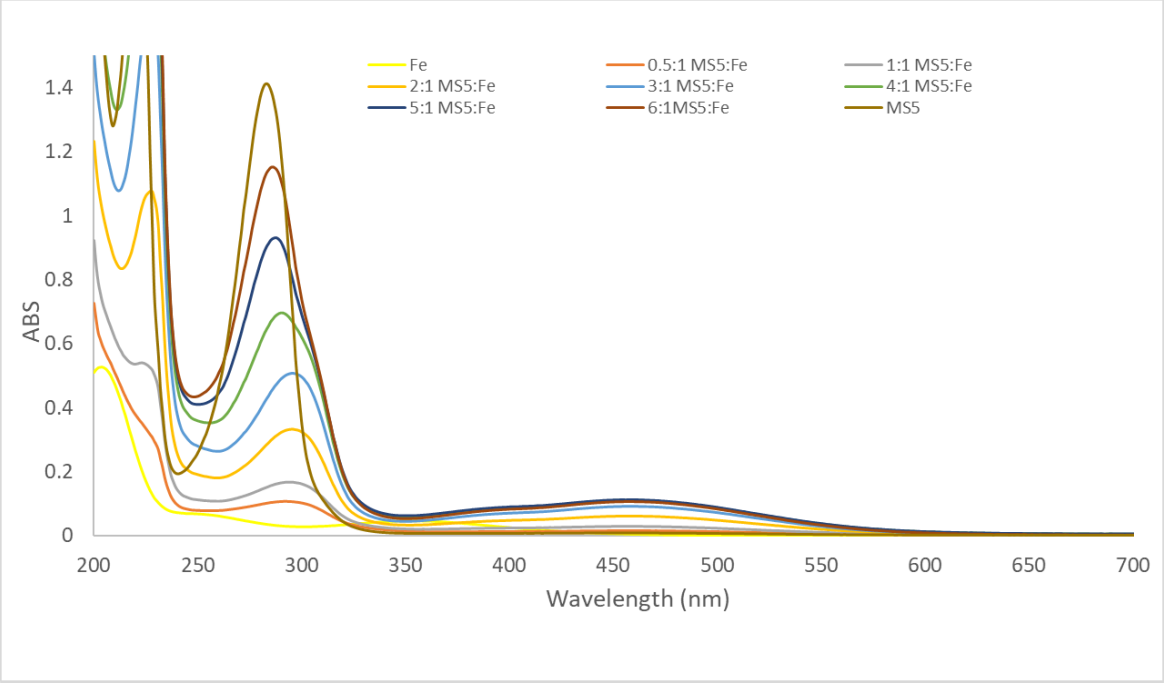

*Figure 45: UV-Vis for **MS5**:Fe complex in 10% MeOH in PBS with **MS5**:Fe ratio from 0.5:1 to 6:1*

In PBS (pH 7.4) with 10% MeOH **MS5**:Fe displayed a new peak at 463 nm (Figure 45), assigned to metal-ligand charge transfer (MLCT). The wavelength of this peak is similar to that reported for a DFP_3:Fe^{III} complex formed under similar conditions.(Sun *et al.*, 2018). The intensity of the MLCT band increased by only a very small amount once a **MS5**:Fe ratio of 3:1 (blue curve in Figure 45) was obtained, indicating that the iron is fully coordinated with three **MS5** ligands i.e. $(\mathbf{MS5})_3$:Fe. As the **MS5**:Fe ratio increased past 3:1, the absorption

band at 300 nm shifted to 283 nm, closer to that of free **MS5** indicating that free **MS5** was in solution after a 3:1 ratio.

The molar absorptivity of (**MS5**)$_3$:Fe was 4320 $M^{-1}cm^{-1}$,which is similar to the published value of $Fe^{III}DFP_3$ 4,600 $M^{-1}cm^{-1}$ (Chan *et al*., 2013, Timoshnikov *et al*., 2014).

As stated previously, **MS6-9** displayed similar behaviour to **MS5** (Figures 91-94 in the Appendix). These studies show that **MS5-9** act as bidentate ligands and formed complexes comprised of 3 ligands / Fe centre.

3.2.4. *Iron complexes of 8-hydroxyquinoline-based compounds*

The ability of the **MS10-13** to form complexes with iron was investigated. All 8-hydroxyquinoline complexes were prepared by adding iron nitrate to 8-hydroxyquinoline-based compounds, and the resulting solutions were analysed by UV-visible spectroscopy and mass spectrometry.

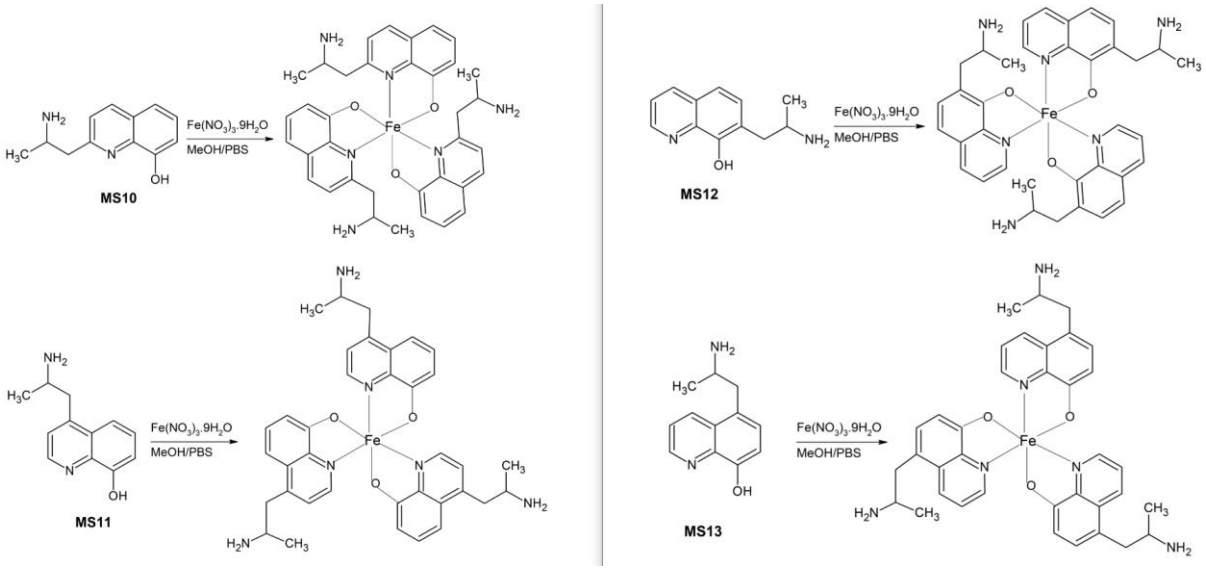

*Scheme 20: Synthesis of **MS(10-13)**:Fe complexes*

MS(10-13):Fe complexes were prepared by adding a methanolic solution of iron nitrate to methanolic solution of deferiprone in 3:1 ratio. **MS10-13** displayed similar iron

complexation properties. MS analysis (Figure 46) showed peaks with *m/z* vales of 458.14 and 600.25 and were assigned to (**MS10-13**)$_2$:Fe and (**MS10-13**)$_3$:Fe, respectively. Within these complexes the molecular weights of the **MS10-13** were ~ 1 less than the parent compounds, indicating the loss of one proton that refers to hydroxy group of the phenol. It can be concluded that the **MS10-13** are in their anionic forms (Scheme 20) within the iron complexes as would be expected.

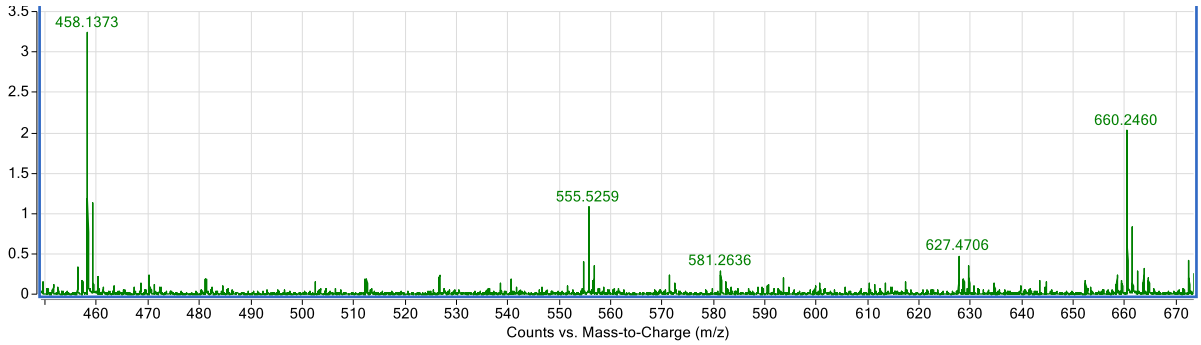

*Figure 46: Mass spectra for **MS10-13**:Fe*

Iron complexation by **MS10-13** was studied in the UV-Vis as well. In these studies solutions of **MS** and $Fe(NO_3)_3$ were prepared in ratios from 0.5:1 to 6:1 and changes in absorption were followed by UV-visible spectroscopy tested in 10% MeOH in PBS (pH 7.4).

Fe coordination characteristics of **MS10-13** were similar and are discussed together using **MS10** as an example. Figure 47 shows the solution UV/Vis changes that occurred as the **MS10**:Fe ratio was increased from 0.5:1 to 6:1.

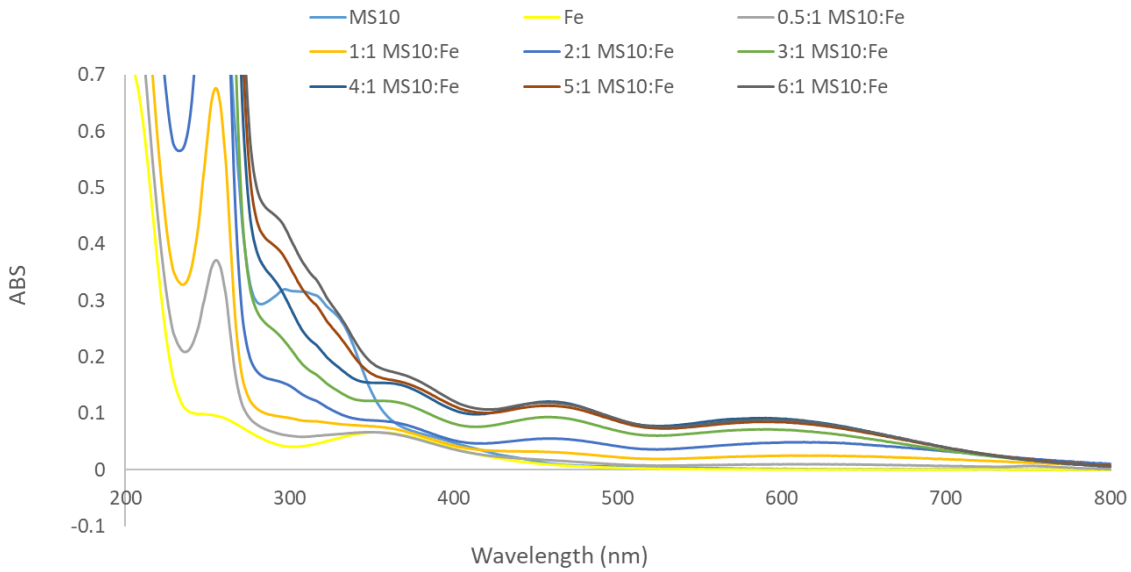

*Figure 47: UV-Vis for (**MS10**):Fe complex in 10% MeOH in PBS with **MS10**:Fe ratio from 0.5:1 to 6:1*

In PBS (pH 7.4) with 10% MeOH, **MS10**:Fe displays new peaks at 590 nm and 461 nm (Figure 47), referring to metal-ligand charge transfer (MLCT), which confirm the formation of **MS10**:Fe complex. The intensity of the MLCT band stops rising when the **MS10**:Fe ratio gets above 3:1 (green curve in figure 47), which indicates that after this point the iron is fully coordinated with three **MS10** ligands i.e. the (**MS10**)$_3$Fe.

Increasing the ligand-iron ratio from 0.5:1 to 6:1, the complex peak was shifted from 624 nm to 590 nm which may indicate the changing of the complex form from **MS10**:Fe to (**MS10**)$_2$:Fe then to (**MS10**)$_3$:Fe

As stated previously **MS11-13** displayed similar behaviour to **MS10** (Figures 95-97 in the appendix). Collectively, these studies show that **MS10-13** act as bidentate ligands and form complexes comprised of 3 ligands / Fe centre.

3.2.5. *Isothermal titration calorimetry (ITC)*

UV-visible spectroscopy indicated that **MS5-13** form complexes with iron. Isothermal titration calorimetry (ITC) was used to measure the affinity constants of each ligand for iron,

as the affinity may be an important determinant of biological activity. ITC was also used to evaluate solution thermodynamic interaction parameters such as stoichiometry of the interaction (n), the association constant (K_a), the free energy (ΔG), enthalpy (ΔH), entropy (ΔS), and heat capacity of binding (ΔC_p).

The ITC apparatus has two cells enclosed in an adiabatic shell. The compounds to be analysed are placed in the sample cell, while the other cell, the reference cell, is used as a monitor and includes the solvent used to dissolve the material (Figure 48) (Pierce *et al*., 1999). Sensitive thermopile/thermocouple circuits detect temperature variations between the reference cell and the sample cell (Holdgate, 2009). Commonly, ITC is used to study the binding between ligands and macromolecules like proteins (Srivastava and Yadav, 2019).

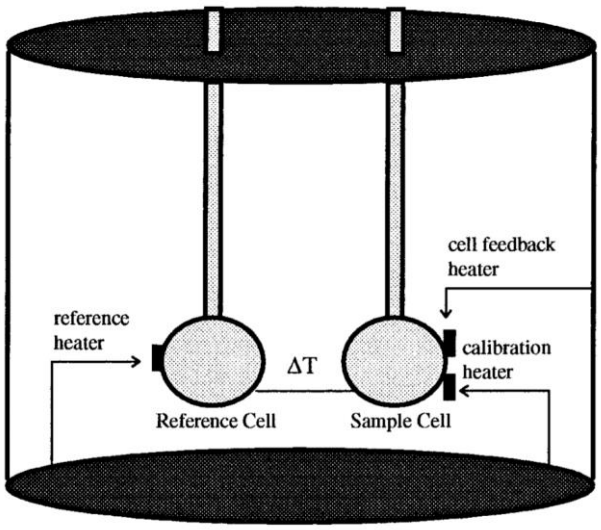

Figure 48: Schematic diagram of an ITC instrument

After initial experiments with various experimental conditions (multiple failed experiments), it was observed that the sensitivity of the ITC instrument decreased as the molecules under investigation become smaller. This phenomenon was described by Ghai *et al*. (Ghai *et al*., 2012), and the choice of experimental conditions is very important. Of particular relevance

are the solvent system (buffer solution), the ratio of the reactants, the iron salt, the time interval of the burette solution addition, and the location of the iron solution (i.e. whether it is in the burette or the sample cell). It is essential to use the same solvent system in both of the sample cell and the reference cell. The solvent system (buffer solution) may affect the affinity constant between the ligand and the metal. For example, the study reported by Robinson *et al*. shows that K_a for TREN/Zn^{2+} is $4x10^4$ M^{-1} in NEM buffer at pH 6.80, whereas it is $1.7x10^6$ M^{-1} in MeOH: NEM buffer at the same pH. (Robinson *et al*., 2016).

After optimising the conditions for **MS5-13**, two methods were chosen: one for quinoline-based compounds (**MS10-13**) and the other for deferiprone-based compounds (**MS5-9**). The two methods are very similar except the iron was titrant in case of **MS5-9** and analyte in case of **MS10-13.** Many experiments were run to use the same method for **MS5-13** but failed to get the right stoichiometric ratios between **MS5-13** and iron. Robinson *et al.* used two different methods to test his compounds as well (i.e. zinc was titrated into N-(2-(1-methylimidazolyl)methyl)iminodiacetic acid (DA2Im), and the other tested compound (8-hydroxyquinoline) was titrated into Zn^{2+}) (Robinson *et al*., 2016). Another example for Jin *et al*. who titrated Cu^{2+} into 8-hydroxyquinoline, whereas titrated histidine into Cu^{2+} (Jin *et al*., 2014).

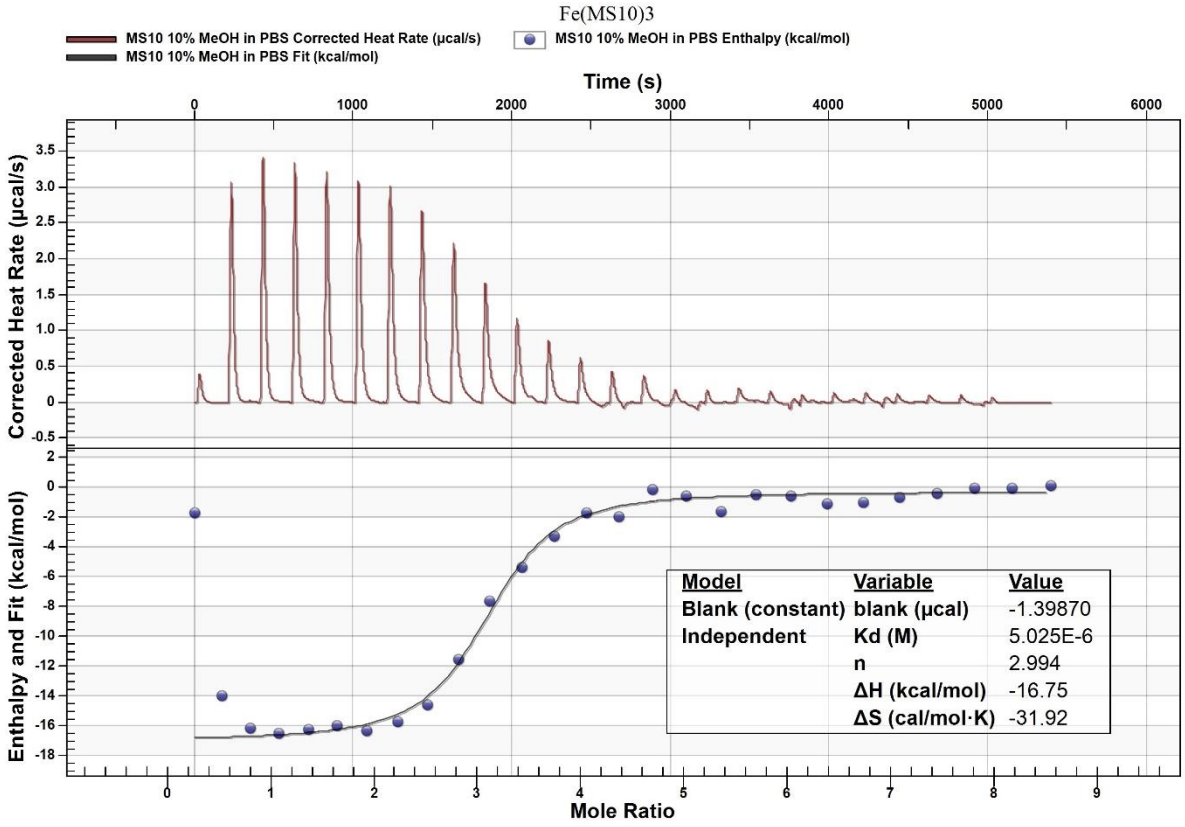

*Figure 49: ITC (**MS10**)$_3$:Fe; **MS10** titrating into iron*

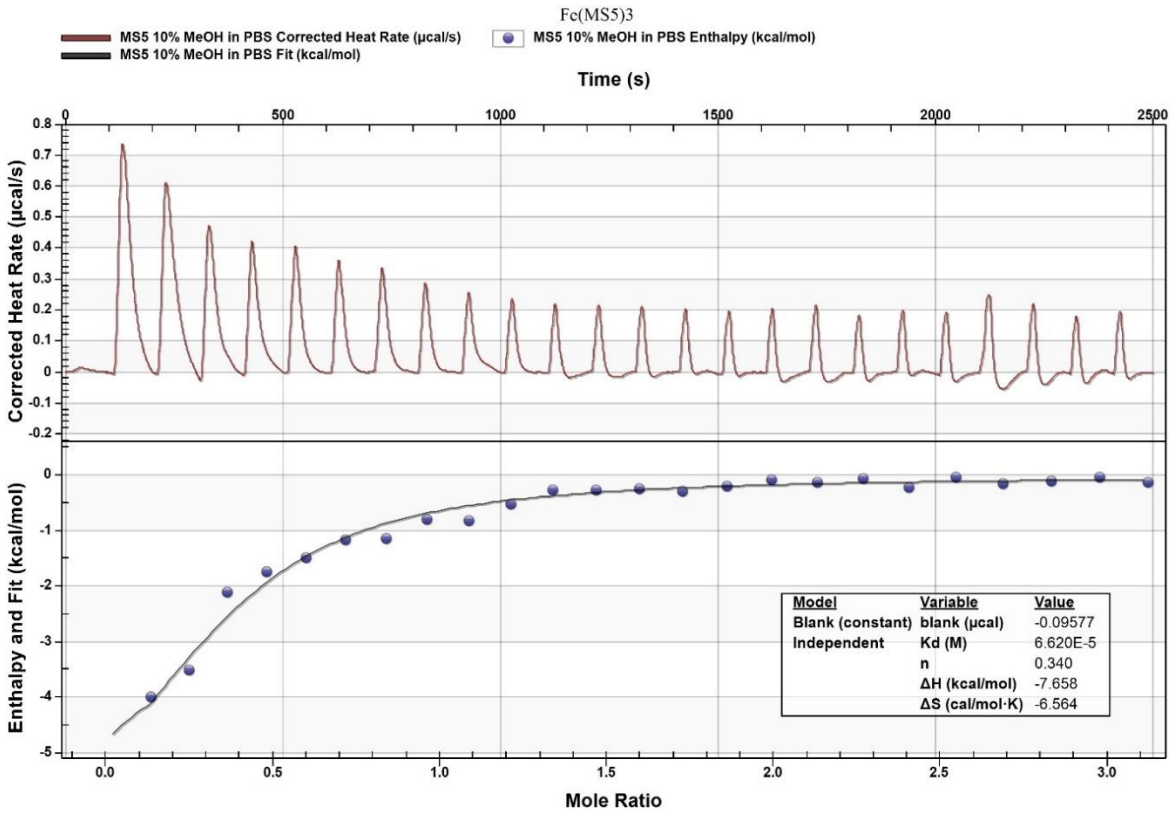

*Figure 50: ITC (**MS5**)$_3$:Fe; Iron titrating into **MS5***

*Table 5: ITC analysis of **MS5-13** reacting with Fe(III)*

	n (**MS**/Fe)	Kd (µM)	Ka=1/Kd (M^{-1})	ΔG_{app} (kcal/mol)	ΔH°_{app} (kcal/mol)	$T\Delta S^{\circ}_{app}$ (kcal/mol)
MS5	2.94	66.2 ± 17.0	1.5 x10^4	-5.70	-7.66 ± 0.817	-1.96
MS6	2.91	62.3 ± 27.5	1.6 x10^4	-5.74	-7.81 ± 2.56	-2.07
MS7	3.03	62.9 ± 25.8	1.5 x 10^4	-5.73	-9.67 ± 1.67	-3.94
MS8	3.01	33.5 ± 21.2	2.9 x 10^4	-6.10	-6.31 ± 1.29	-0.203
MS9	3.03	52.2 ± 23.8	1.9 x 10^4	-5.84	-9.80 ± 1.58	-3.96
MS10	2.99	5.03 ± 1.66	1.9 x 10^5	-7.23	-16.8 ± 0.628	-9.52
MS11	2.63	8.99 ± 2.70	1.1 x 10^5	-6.89	-16.6 ± 1.32	-9.63
MS12	2.67	8.11 ± 2.44	1.2 x 10^5	-6.95	-10.9 ± 0.407	-4.01
MS13	2.93	8.64 ± 2.12	1.2 x 10^5	-6.91	-14.6 ± 1.03	-7.70

The titration of **MS** compounds by $Fe(NO_3)_3$ provides a stoichiometric ratio 0.33 ± 0.1 for **MS5-9** and 2.8 ± 0.2 for **MS10-13** (Figures 49-50, Figures 104-110 in the appendix, and table 5). **MS5-9** have this ratio because iron was titrated into the **MS** compounds (reverse titration) so it ends up with 0.33:1 ratio Fe: **MS**, which is equivalent to a 3:1 ratio **MS**: Fe. Whereas in the case of **MS10-13**, **MS** was titrated into iron, so it ends up with 3:1 ratio **MS**: Fe. These ratios between iron and **MS** confirmed the data that was got in the mass spectra and the UV-Vis study.

The binding constant K_a for (**MS5-9**):Fe is ~1.5 x10^4, whereas it is ~1 x10^5 for (**MS10-13**):Fe. That is, (**MS5-9**):Fe binding constants are an order of magnitude smaller than those of (**MS10-13**):Fe. Thus 8-hydroxyquinoline-based compounds **(MS10-13)** are stronger chelators than deferiprone-based compounds (**MS5-9**).

MS5-13 get the binding isotherms fit well to a one-set-of-sites model (independent-site binding model) which means there is an identical binding site between ligand and metal. (Figures 49-50, Figures 104-110 in the appendix)

MS5-13:Fe complexes have $\Delta H^{\circ} < 0$ so all of the reactions between **MS** compounds and iron are exothermic. $|\Delta H^{\circ}| > |T\Delta S^{\circ}|$ which makes $\Delta G^{\circ} < 0$, thus the reactions are spontaneous and enthalpy driven. Thus, the formation of the coordination bond between the iron and the **MS** compounds is more energetically crucial than the de coordination and the release of water within the solution. In summary, **MS10-13** possess higher binding constant towards iron than those of **MS5-9**, indicating that **MS10-13** are more potent iron chelators.

3.2.6. *Antioxidant activity of MS5-13*

Oxidative damage to dopaminergic neurons is implicated in PD and therapeutic agents with antioxidant activity may offer protection. The antioxidant activity was therefore assessed using the DPPH assay previously described in section 3.1.4, and the results are shown in Figure 51 and Table 6 and 33.

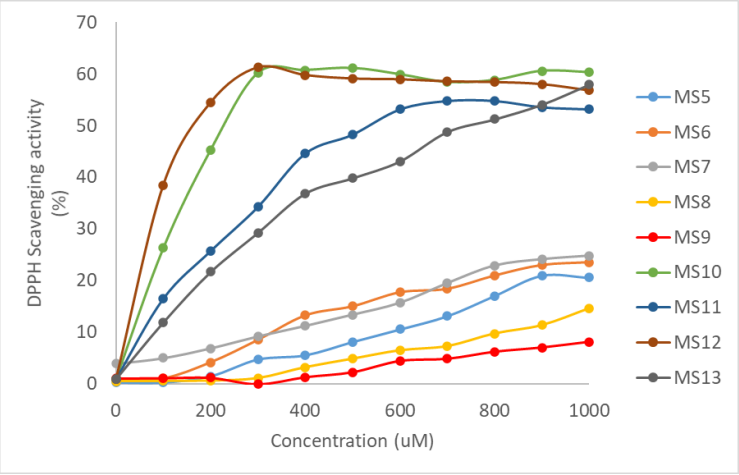

*Figure 51: Scavenging activity of the DPPH radical by **MS5-13** compounds*

*Table 6: Percentage of scavenging activity for **MS5-13** and ascorbic acid compounds at concentrations 100, 300, 500, 700 and 900 µM*

concentration (µM)	100	300	500	700	900
Ascorbic acid	85 (max)				
MS5	0.28	4.74	8.13	13.14	21.00
MS6	1.08	8.53	15.04	18.42	23.03
MS7	5.01	9.21	13.41	19.51	24.11
MS8	0.56	1.13	4.87	7.31	11.38
MS9	1.13	1.14	2.30	4.87	7.04
MS10	26.28	60.16	61.11	58.40	60.56
MS11	16.53	34.28	48.23	54.74	53.52
MS12	38.48	61.24	59.07	58.53	57.99
MS13	11.92	29.26	39.83	48.78	54.06

The antioxidant activities of **MS5-13** were evaluated using the 1,1-diphenyl-2-picrylhydrazyl (DPPH) scavenging assay (Sharma and Bhat, 2009) using ascorbic acid as reference material. DPPH is a stable free radical that can be scavenged by efficient antioxidants (Scheme 6). Thus, the decrease in optical absorbance (at a wavelength corresponding to that of DPPH absorbance) upon introduction of an antioxidant provides a measure of the free radical scavenging activity. The 8-hydroxyquinoline-based compounds **MS10-13** had superior radical scavenging activity compared to those of the deferiprone-based compounds **MS5-9**. These trends are consistent with those that may expected by examination of the molecular structures; ascorbic acid possesses two oxidizable OH functional groups that can donate two protons and thus effectively scavenge the DPPH free radical. On the other hand, **MS10-13** may donate a single proton from the phenolic OH although the nearby extensive conjugation makes this quite a favourable process

Within the 8-hydroxyquinoline-based compounds **MS10** and **MS12** had the greatest anti-oxidant activities. These compounds have the propylamine group *ortho* to the pyridyl N and OH groups, respectively, and suggest a planar structure can enhance the antioxidant activity. On the other hand, the stabilization of phenoxyl radicals by strong hydrogen bonding with an adjacent −OH group and the lack of extended conjugation in **MS5-9** compounds are reflected in its low radical scavenging ability. Deferiprone was discovered not to possess strong antioxidant properties by Ramsaywack *et al*., which confirm the weak antioxidant activity for deferiprone based compounds in DPPH scavenging assay (Ramsaywack *et al*., 2013).

Overall, 8-Hydroxyquinoline-based compounds **MS10-13** had superior radical scavenging activity compared to those of the deferiprone-based compounds **MS5-9**. **MS10-13** might be promising candidates to slow down the oxidative stress that is catalysed by the misregulated iron in the brain.

3.2.7. *Cellular effects of MS5-13*

While the precise causes of PD are yet to be fully elucidated, several lines of evidence suggest that that accumulation of iron within the CNS is an important contributor to disease progression. Within the dopaminergic neural cells excess iron may oxidise dopamine into toxic quinone-species that promote dopaminergic cell death. As shown in sections 3.2.3 to 3.2.6 **MS5-13** possess both iron chelation and antioxidant activity, which suggests that these compounds may be able to prevent iron-induced cell death. To test this directly, iron rescue assays were performed. In these assays, N27 rat dopaminergic neural cells were exposed to excess iron and then treated with **MS5-13** for 24 hours. After the treatment period cell viability was assessed using the MTT colorimetric assays. Viable cells reduce MTT to an

insoluble formazan dye, which has a purple colour (Berridge *et al*., 2005) (Scheme 21). The number of cells can be quantified spectrophotometrically by measuring absorbance at 590 nm. This assay was performed by Dr. Adam Southon at the Florey Institute in Melbourne.

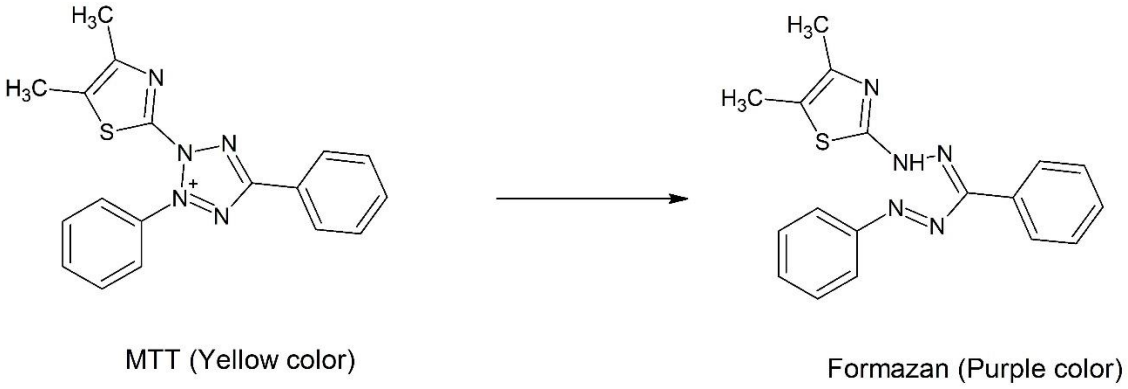

Scheme 21: Reduction of MTT

*The Effect of **MS5-13** on N27 cell viability*

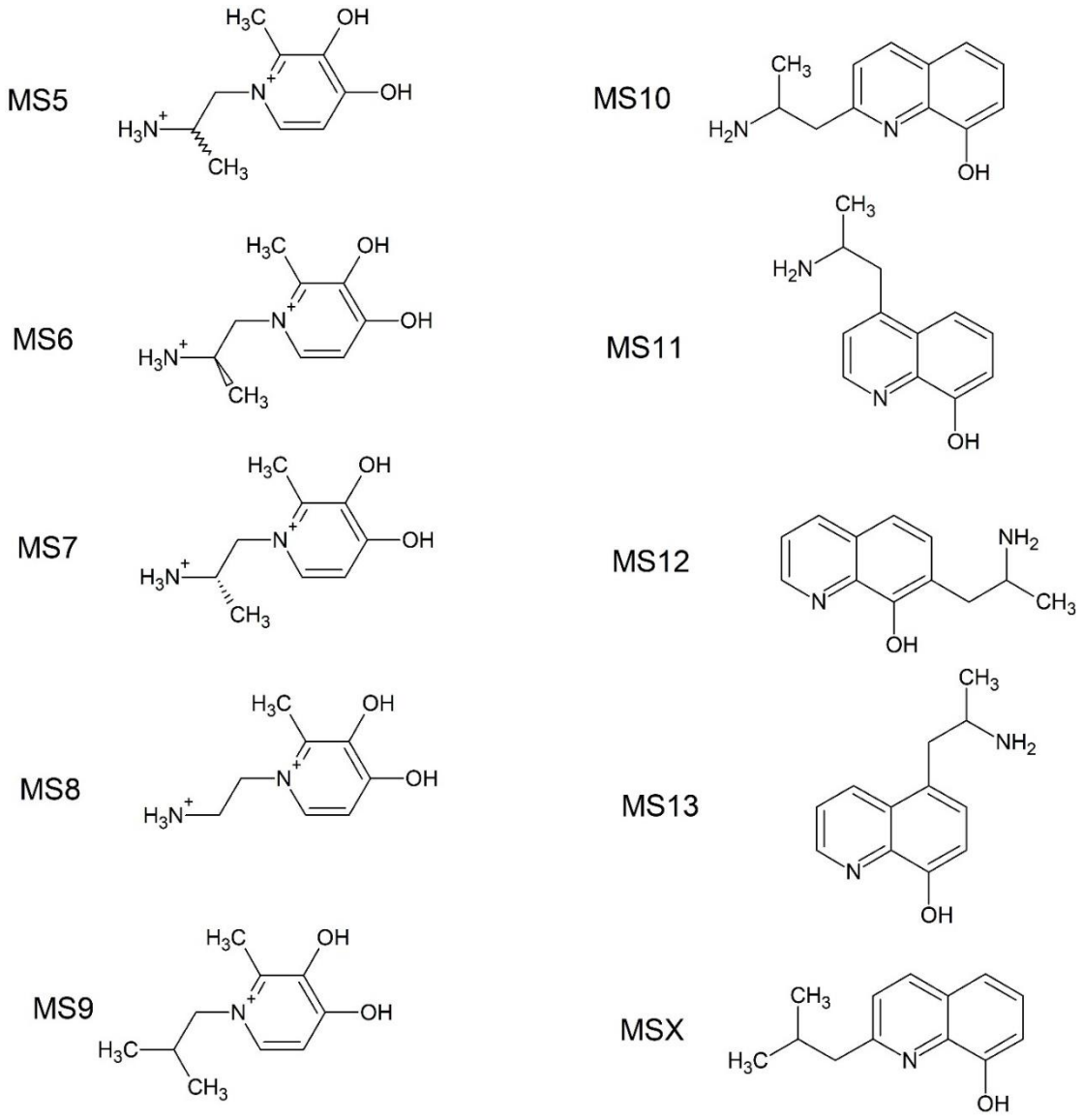

*Figure 52: Chemical structures of **MS5-13** and MSX*

Prior to conducting the iron rescue assays the cytotoxicity of **MS5-13** was assessed against N27 cells. The goal of this assay was to determine the maximum concentration of **MS5-13** that could be used in subsequent iron rescue assays without causing cell death. N27 cells were treated with **MS5-13** at concentrations of 1, 10, 100 and 1000 µM for 24 hours in media containing 10% FBS, and cell viability was assessed using MTT and compared to vehicle only

control. The parent drugs of **MS5-13**, clioquinol (De Clercq) and deferiprone (DFP), were also included in the assay. The results are shown in Figure 53.

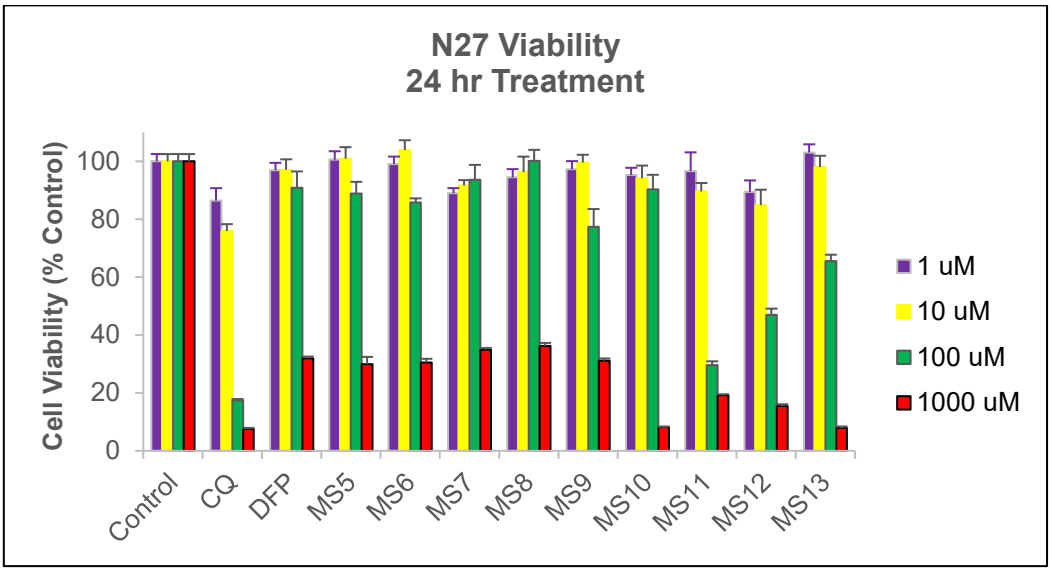

*Figure 53: Effects of **MS5-13** compounds, clioquinol and deferiprone on cell viability of N27 cells*

As shown in Figure 53 the compounds had no effect on N27 viability at the lower concentrations of 1 and 10 µM, while at 1000 µM all test compounds significantly reduced cell viability. At 100 µM the 8-hydroxyquinoline derived compounds were in general more cytotoxic than the deferiprone derivatives. Thus, deferiprone and its analogues **MS5-9** did not significantly alter N27 viability at 100 µM, while clioquinol and its derivatives **MS11-13** had a significant effect on N27 cells at 100 µM, reducing cell viability to 60 – 20 % of control. The exception was **MS10**, which bears a 2-aminopropyl group ortho to the pyridyl nitrogen and had no effect on N27 cells at 100 µM.

Cytotoxicity of iron salts

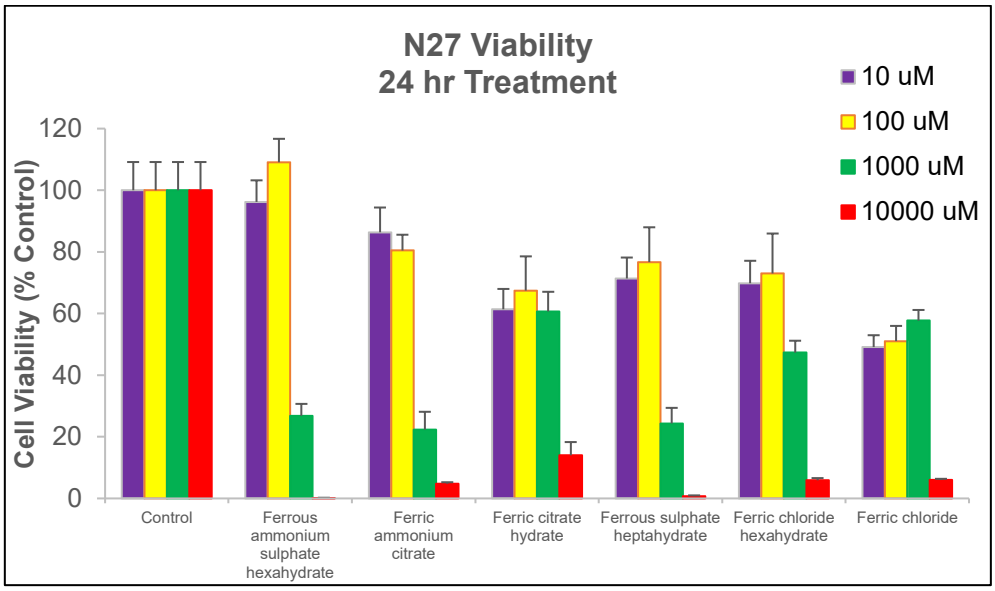

Figure 54: Dose-dependent effect of different Iron salts on cell viability of N27 cells

An important component of neuronal iron rescue assays is the source and concentration of iron, and there is not a clear consensus in the literature. For example Telfer *et al* use 200 µM $FeCl_3$, (Telfer *et al*., 2017), while Das *et al* report using 20 µM of an iron/hydroxyquinoline complex (Das *et al*., 2017). To determine an appropriate iron source for the rescue assays N27 cells were treated for 24 hours with 6 different iron sources (ferrous ammonium sulphate hexahydrate, ferric ammonium citrate, ferric citrate hydrate, ferrous sulphate heptahydrate, ferric chloride hexahydrate and ferric chloride) at concentrations of 10, 100, 1000 and 10,000 µM. As shown in Figure 54 all iron sources produced moderate reductions in N27 cell viability at 10 and 100 µM. At 1000 µM ferrous ammonium sulphate and ferric ammonium citrate were found to be the most toxic iron sources and reduced cell viability to ~25% of control.

Iron toxicity cell rescue assay

Based on the preliminary assessment of the cytotoxicity of **MS5-13** and various iron sources, iron rescue assays were performed using 1000 µM of both ferrous ammonium sulphate and ferric ammonium citrate, and 10 µM and 100 µM of **MS5-13**, **MSX,** deferiprone and clioquinol. To perform the assays, N27 cells were seeded into 96-well plates and then treated with the iron source and iron chelators at the concentrations indicated. After 24 hours cell viability was quantified by MTT and the results are expressed relative to DMSO-treated control. The results are shown in Figures 55 and 56.

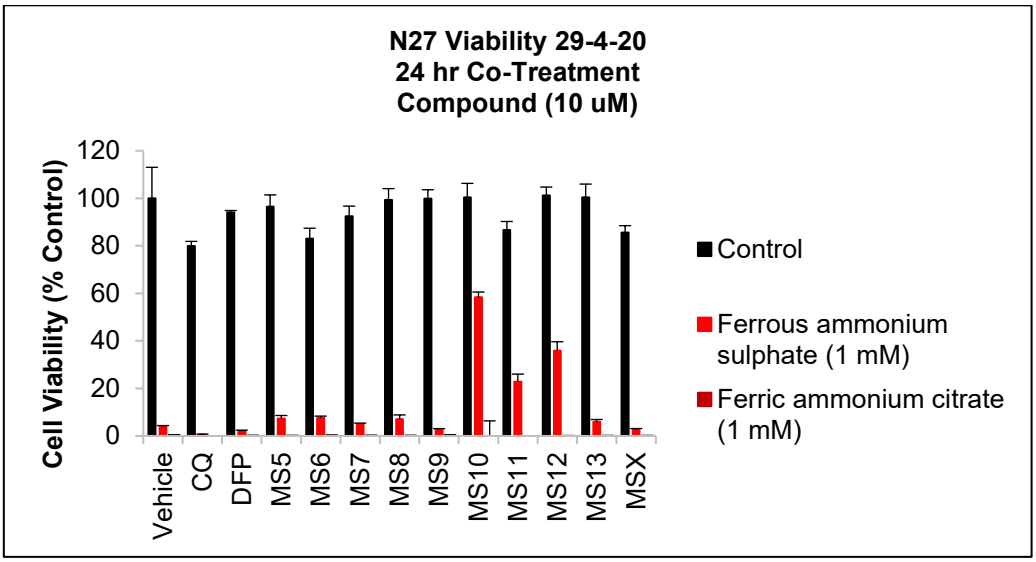

*Figure 55: Effects of **MS5-13, MSX** and known iron chelators clioquinol and deferiprone (10 µM) on the viability of N27 rat dopaminergic neural cells from toxicity induced by ferrous ammonium sulphate and ferric ammonium citrate (1000 µM). Control cells received the chelator (10 µM) only, and results are expresses as a percentage of vehicle-only (DMSO) treated cells. The values shown are the mean ± SD of at least 4 replicates.*

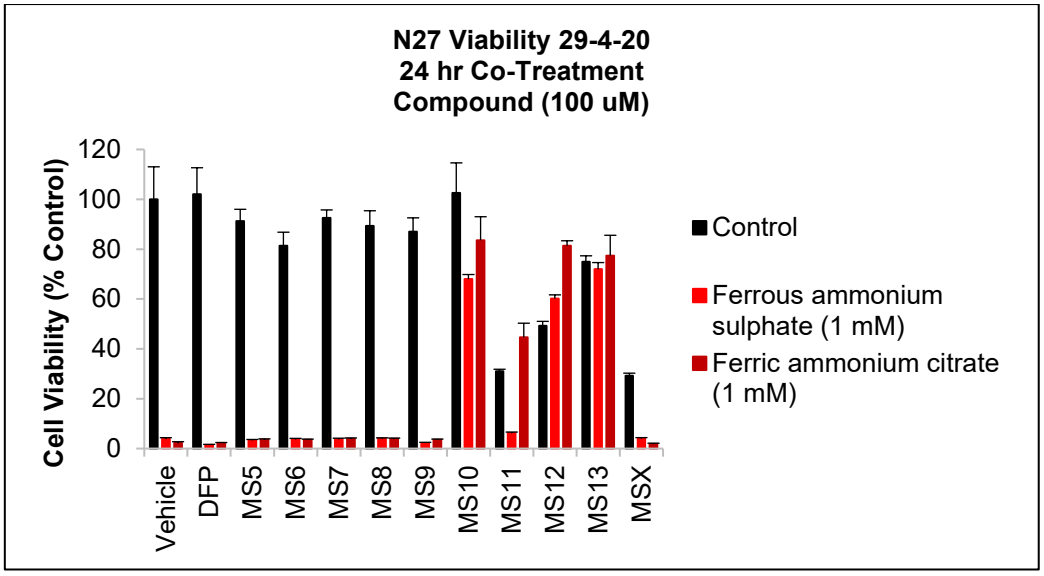

*Figure 56: Effects of **MS5-13, MSX** and known iron chelators clioquinol and deferiprone (100 µM) on the viability of N27 rat dopaminergic neural cells from toxicity induced by ferrous ammonium sulphate and ferric ammonium citrate (1000 µM). Control cells received the chelator (100 µM) only, and results are expresses as a percentage of vehicle-only (DMSO) treated cells. The values shown are the mean ± SD of at least 4 replicates.*

The viability of N27 cells treated with 1000 µM of either iron source was almost fully abolished (see 'vehicle', Figure 55 and 56). At test concentrations of 10 and 100 µM, deferiprone and its derivatives **MS5-9** failed to rescue N27 cells from iron-mediated toxicity. This may be attributed to a number of factors including the poorer chelating ability of **MS5-9** or their weaker antioxidant activities. This data does not allow an unambiguous distinction to be made.

Within the 8-hydroxyquinoline-based compounds, some iron rescue activity was observed. Clioquinol itself failed to protect cells at 10 and 100 µM. At 10 µM **MS10**, **MS11** and **MS12** were able to restore N27 viability to 25 – 60% of vehicle-treated cells, while **MS13** was inactive. Protective effects were only observed with ferrous ammonium sulphate as the iron source. Whilst there is a correlation between the lower antioxidant activity of **MS13**

compared to the others in that series, this does not necessarily imply that this is the reason for the lower rescue activity.

At 100 µM, 8-hydroxyquinoline derivatives **MS10-13** were able to rescue N27 cells from the toxic effects of both iron sources to varying degrees. For example, N27 cells treated with either **MS13** alone, or **MS13** in combination with either iron source were ~80% viable at the end of the treatment period, providing evidence that **MS13** can protect N27 cells from iron-mediated toxicity.

Interestingly, the negative control **MSX,** which lacks the amphetamine-type structure (i.e. no alkylamine group), was the only 8-hydroxyquinoline derivative not to exert protective effects in both concentrations (10 and 100 µM). Whether this lack of activity arises from the inability of **MSX** to be transported by DAT can only be determined through additional experimentation (see Chapter 4).

Importantly, whether the strong chelation affinity, the good antioxidant activity or the structural similarity to amphetamine (or a combination of these factors) enhanced the activity of **MS10-13** cannot be unambiguously deduced from these data.

Ferroptosis assay

Ferroptosis is a type of iron-dependent programmed cell death that is biochemically distinct from other forms of regulated cell death and is characterised by the accumulation of lipid peroxides. Iron chelators and antioxidants can prevent ferroptosis cell death (Yang and Stockwell, 2016) (Zilka *et al*., 2017).

To further assess the ability of **MS5-13** to rescue cells from iron-mediated cell death, ferroptosis-rescue assays were performed. In these assays, N27 cells were co-treated with **MS5-13, MSX** and Erastin (1 µM) or RSL3 (0.1 µM). Erastin and RSL3 induce ferroptosis.

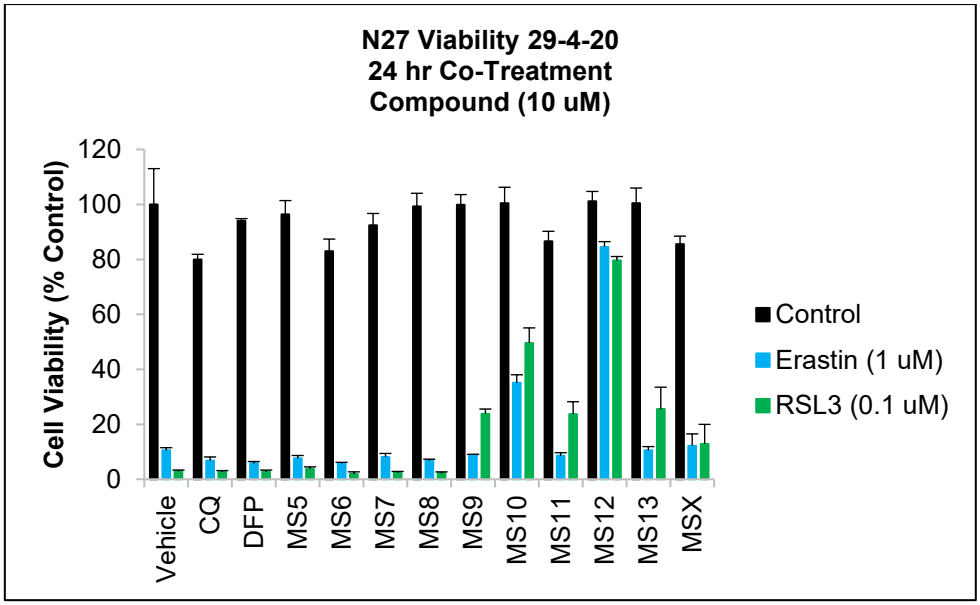

*Figure 57: Effects of **MS5-13, MSX** and known iron chelators clioquinol and deferiprone (10 µM) on the viability of N27 rat dopaminergic neural cells from toxicity induced by Erastin (1µM) and RSL3 (0.1 µM). Control cells received the chelator (10 µM) only, and results are expresses as a percentage of vehicle-only (DMSO) treated cells. The values shown are the mean ± SD of at least 4 replicates.*

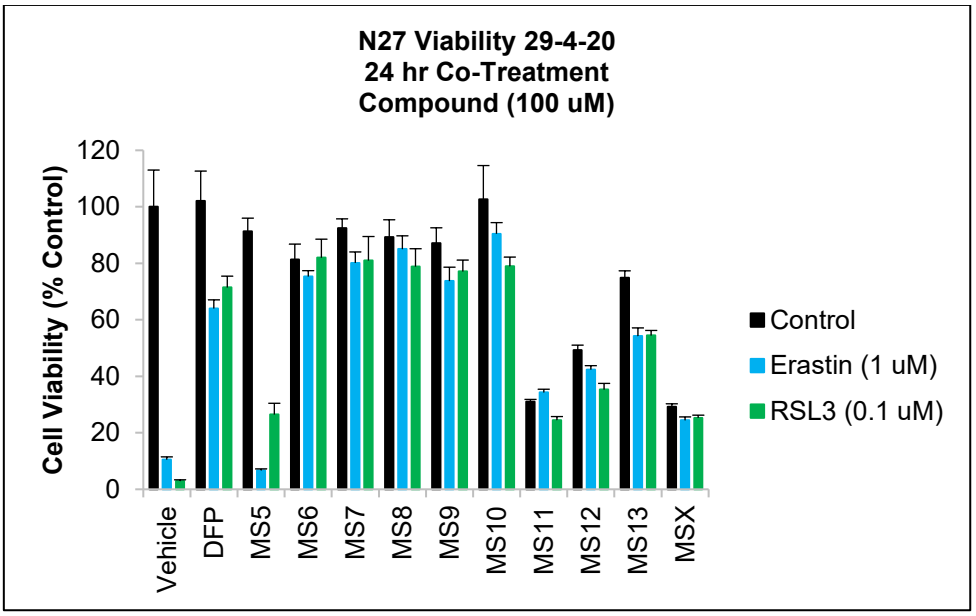

*Figure 58: Effects of **MS5-13, MSX** and deferiprone (100 µM) on the viability of N27 rat dopaminergic neural cells from toxicity induced by Erastin (1µM) and RSL3 (0.1 µM). Control cells received the chelator (100 µM) only, and results are expresses as a percentage of vehicle-only (DMSO) treated cells. The values shown are the mean ± SD of at least 4 replicates.*

Based on the preliminary assessment of the cytotoxicity of **MS5-13** assay, ferroptosis assay was performed using 10 µM and 100 µM of **MS5-13** and **MSX**. To perform the assays N27 cells were seeded into 96-well plates and then treated with the Erastin and RSL3 at the concentrations indicated. After 24 hours cell viability was quantified by MTT, and the results are expressed relative to DMSO-treated control. The results are shown in Figures 57 and 58.

At 10 µM **MS9-13** and **MSX** were able to restore N27 viability to 20-80% of vehicle-treated cells, while CQ, deferiprone and **MS5-8** were inactive. **MS10** and **MS12** were superior in restoring N27 viability (~60 - 80%) and although this is consistent with their stronger antioxidant activities (Section 3.2.6), the mechanism of Erastin-induced ferroptosis involves lipid peroxidation. Thus, a lipophilic antioxidant may be expected to provide protective effects however **MS10** and **MS12** are reasonably polar suggesting that some degree of DAT transport and iron chelation is involved. This conjecture, however, would require further evidence (see Chapter 4). However, these data are very encouraging and demonstrate that this class of compounds and the strategy of amphetamine-like chelators is worthy of further exploration in the future.

When the concentration of **MS** compounds was increased to 100 µM (Figure 58), most of the compounds displayed activity to restore N27 viability (more than 80%). However, these data are not particularly meaningful at such a high concentration and the lower rescue values for **MS11-13** reflects the effects of those compounds on cell viability at this concentration (Figure 53).

3.2.8. *Attempted synthesis of methcathinone-based compounds*

This work was undertaken prior to the investigations into the amphetamine-like 8-hydroxyquinoline and deferiprone-based compounds. The rationale for this work was that methcathinone-like structures could be synthesised that incorporate chelators such as salicylaldehyde isonicotinoyl hydrazone (SIH) and deferoxamine (DFO). The synthesis proved to be challenging and was eventually abandoned in favour of the chelators described above. The synthetic processes used in attempts to prepare methcathinone-based chelators is described here.

A methcathinone analogue bearing a 4-carboxylic acid group was synthesised in seven steps (Scheme 22). The SIH chelator was synthesised in two steps however the final reaction to bind the methcathinone-like moiety with the SIH chelator moiety failed.

First, 1,4-dimethyl terephthalate was prepared from terephthalic acid and methanol in a straightforward fashion (Scheme 22). Methyl 4-(3-methoxy-2-methyl-3-oxopropanoyl)benzoate was synthesised by a Claisen condensation of 1,4-dimethylterephthalate and methyl propanoate(Camps *et al*., 1993).Hydrolysis and decarboxylating methyl 4-(3-methoxy-2-methyl-3-oxopropanoyl)benzoate gave 4-propanoylbenzoic acid (Camps *et al*., 1993), which was then protected (at the carboxylic acid site) using iodomethane. Bromination of the resultant methyl 4-propanoylbenzoate using Br_2, followed by substitution with methylamine gave the primary amine (and subsequently the ammonium salt using HCl in ether). Deprotection of the ester using HCl yielded the free benzoic acid required for the subsequent amidation reaction with the SIH chelator.

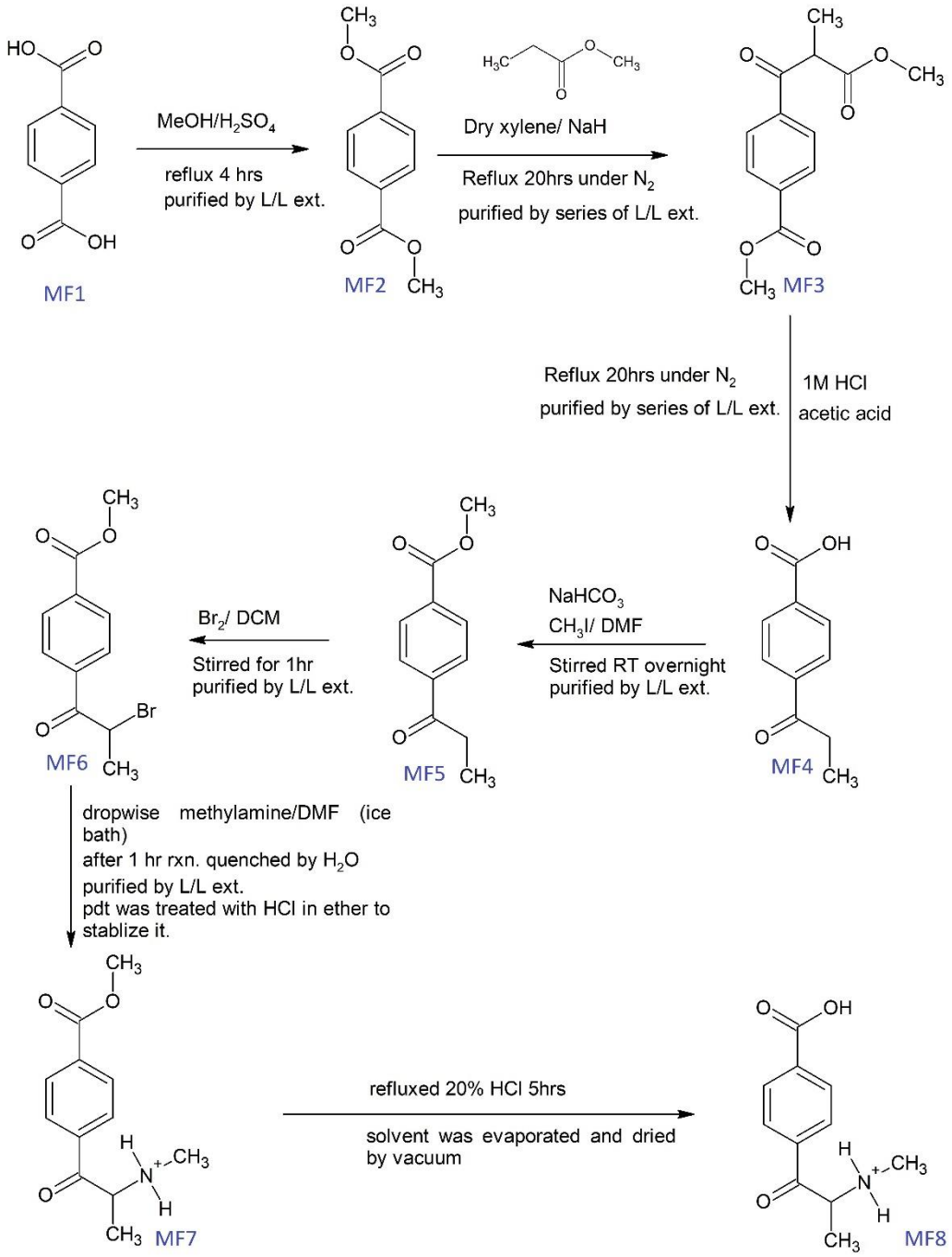

Scheme 22: Synthetic scheme for the preparation of methcathinone-like compounds.

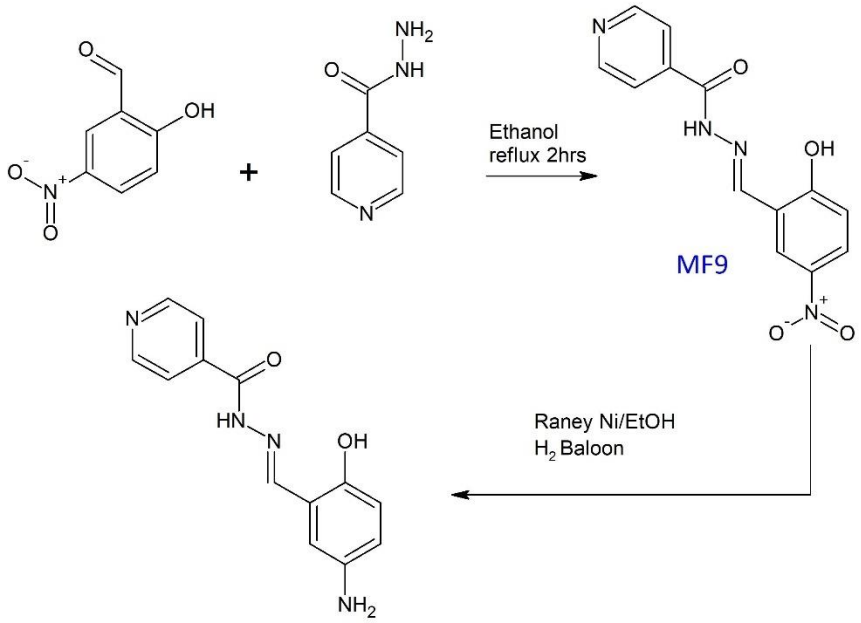

Scheme 23: preparation of SIH chelator

SIH was prepared in two steps (Scheme 23). First, N'-[-(2-hydroxy-5-nitrophenyl)methylidene]pyridine-4-carbohydrazide was prepared by a Schiff base reaction between 2-hydroxy-5-nitrobenzaldehyde and isonicotinic acid hydrazide. Second, the nitro group was reduced using Raney nickel in ethanol and hydrogen gas to form the SIH bearing an amine functional group.

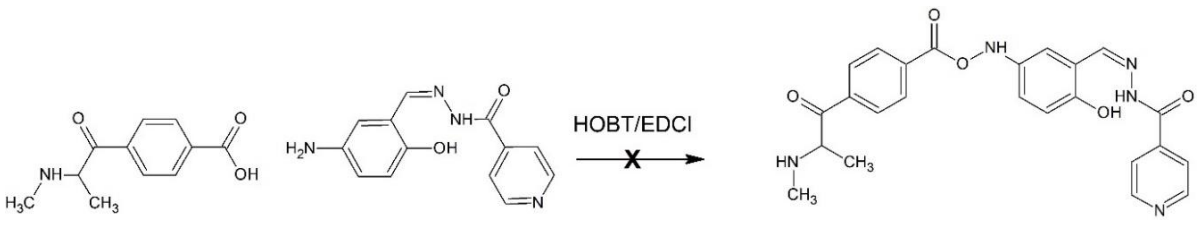

Scheme 24: failure synthesis between 1-(4-carboxyphenyl)-N-methyl-1-oxopropan-2-aminium and SIH.

The final amidation reaction (Scheme 24) failed under multiple reaction conditions. For example, using hydroxybenzotriazole (HOBT), 1-Ethyl-3-(3-

dimethylaminopropyl)carbodiimide (EDCI) and N,N -diisopropylethylamine reagents.

Attempts to solve this problem included:

- Changing amidation reagents (EDCI and HOBT) to (1-cyano-2-ethoxy-2-oxoethylidenaminooxy)dimethylamino-morpholino-carbenium hexafluorophosphate (COMU) (which was reported to give excellent results in the literature for aromatic amidation reactions).
- Using a simple aromatic amine as a test case but with negative results (Scheme 25)

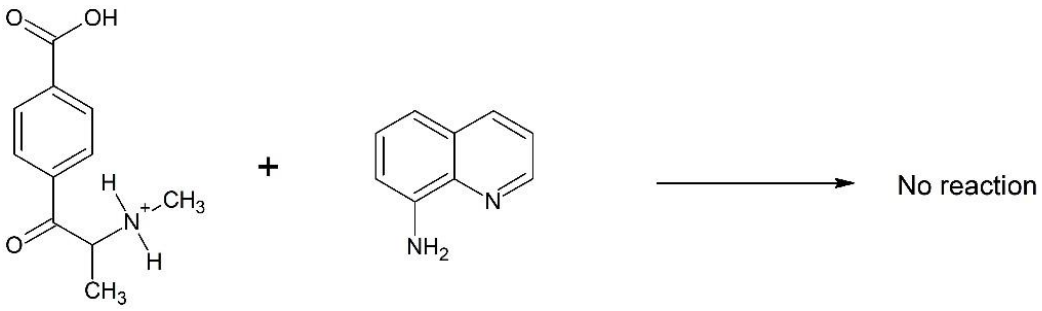

Scheme 25: Unsuccessful reaction of 1-(4-carboxyphenyl)-N-methyl-1-oxopropan-2-aminium with quinolin-8-amine.

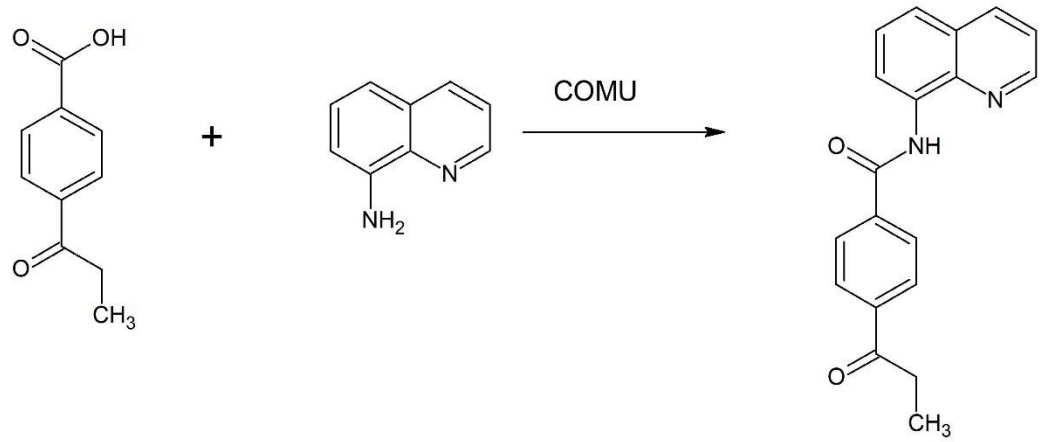

Scheme 26: Preparation of 4-propanoyl-N-(quinolin-8-yl)benzamide

The reaction of 4-propanoylbenzoic acid (Scheme 26) with 8-aminoquinoline (**MF4**) was successful (Figure 59), indicating that the coupling conditions themselves were not the fundamental problem.

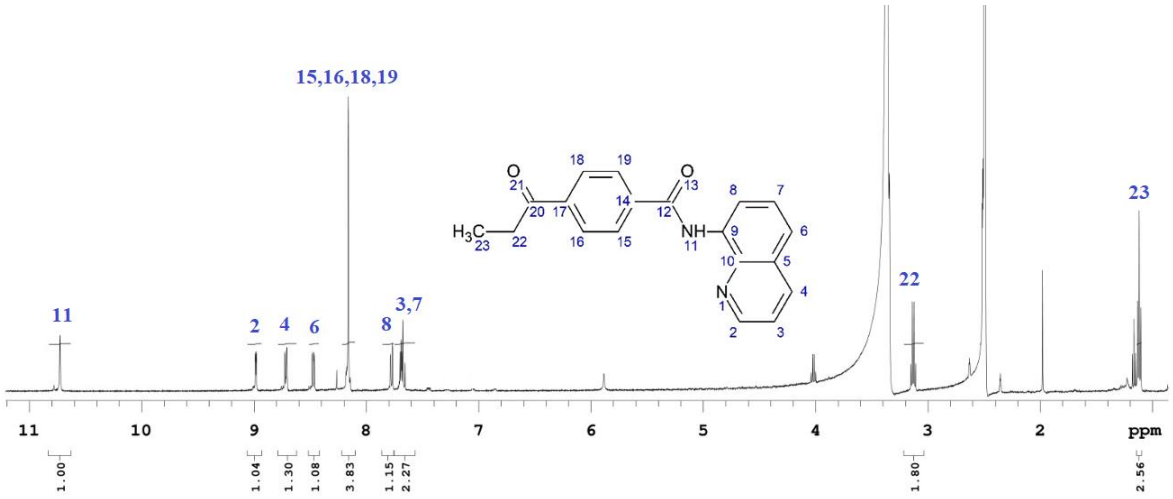

Figure 59: [1]HNMR for 4-propanoyl-N-(quinolin-8-yl)benzamide

Attempts to brominate and substitute 4-propanoyl-N-(quinolin-8-yl)benzamide to prepare 4-(2-aminopropanoyl)-N-(quinolin-8-yl)benzamide (Figure 60) were also unsuccessful even after numerous attempts.

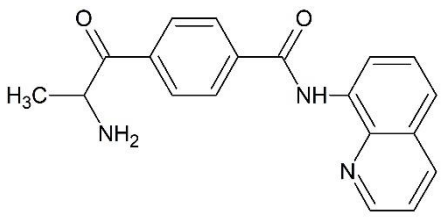

Figure 60: 4-(2-aminopropanoyl)-N-(quinolin-8-yl)benzamide

Because of the significant difficulties in this line of synthesis, the methcathinone-based compounds were abandoned in favour of 8-hydroxyquinoline or deferiprone-based compounds.

Chapter 4

Conclusions and Future Directions

Chapter 4: Conclusions and Future Directions

Many studies show that abnormal metal homeostasis is a significant pathogenic factor in neurodegenerative diseases and several studies have investigated the ability of chelating agents to trap redox-active metals. An effective chelating agent in the context of AD and PD must have relatively low molecular weight and chelation selectivity to prevent depletion of other metal ions while removing pathogen protein metal ions. Antioxidant properties are also desirable.

Overall, the aims of this project were achieved. Novel metal chelators that target misregulated metals for AD and PD were synthesised and characterised and their properties examined.

Compounds based on the cyclen macrocycle that bear pendant arms have been designed, synthesized and characterized. These compounds were designed to chelate copper and zinc ions, which have been implicated in the progression of AD. Each of the compounds has been shown to coordinate Cu^{2+}, Zn^{2+} and Ni^{2+} metal ions in aqueous solution. X-ray crystal structures revealed that **MS1** binds in a hexadentate fashion while **MS2** and **MS3** are tetradentate. Importantly, each of the compounds can remove Cu^{2+} ions from $A\beta_{40}$ to inhibit and reverse aggregation. Of the four chelating compounds, **MS1** was superior in returning aggregated $A\beta_{40}$ to solution compared to **MS2-4**.

Computational studies indicated that **MS1-4** each have favourable interaction energies to bind Cu^{2+} and Zn^{2+} metal ions within the abnormal amyloid precursor protein. In terms of antioxidant properties, **MS1** showed the greatest free radical scavenging activity, although none were greater than Vitamin C.

The cyclen-based chelator **MS1** is a promising candidate drug for AD treatment. It is a multifunctional compound that inhibits plaque formation, decreases brain oxidative stress and may cross the BBB.

It would be useful to focus future research on a cyclen chelator based on 8-hydroxyquinoline analogues as potential AD treatments as this combination showed good copper and zinc chelation as well as antioxidant properties. Additionally, all the synthesised compounds should be tested experimentally in their ability to pass through BBB with possible further investigations *in-vivo.*

Compounds based on 8-hydroxyquinoline and deferiprone that have an amphetamine-like structure have been designed, synthesized and characterized. These compounds were designed to chelate iron, which has been implicated in the progression of Parkinson's disease. **MS5-13** has been shown to coordinate iron ions in aqueous solution. Single crystal X-ray studies revealed the structures of the synthesised compounds and confirmed the presence of two hydroxy groups in **MS5-9** compounds, unlike deferiprone. ITC, MS, and UV-visible spectroscopy studies showed that **MS5-13** chelated iron in a 3:1 ratio and **MS10-13** have stronger binding constants than those of **MS5-9** compounds. In terms of anti-oxidant properties, **MS10-13** showed better free radical scavenging activities than those of **MS5-9** compounds, although none were greater than Vitamin C. Importantly, all the **MS** compounds record good cell viability in ferroptosis assay. In case of the iron toxicity cell rescue assay, **MS10-13** showed very promising results to prevent dopaminergic neuron cell death by chelating toxic iron.

Compounds based on 8-hydroxyquinoline **MS10-13** are potential and highly signicant candidates for Parkinson's disease treatment. These compounds may be transported within

the dopaminergic cells, chelating toxic iron. Simultaneously, **MS10-13** compounds can reduce the iron-induced oxidative stress.

Future studies into PD drug discovery should focus on preparing new bipyridine-based chelators, as bipyridine is expected to be a stronger chelator than 8-hydroxyquinoline (Das *et al*., 2017). This is important as there may be a threshold of chelating strength that, beyond which, the chelators become detrimental to cell health. Since **MS10-13** were able to rescue N27 cells, studies are now focusing on degree to which these compounds are DAT substrates. These studies will provide firm evidence to support the hypothesis that compounds of this nature can act as both chelators and transportable substrates. Further investigations into this class of compound should include *in-vivo* studies as an essential stage in this process.

References

AGNIHOTRI, A. & ARUOMA, O. I. 2020. Alzheimer's disease and Parkinson's disease: a nutritional toxicology perspective of the impact of oxidative stress, mitochondrial dysfunction, nutrigenomics and environmental chemicals. *Journal of the American College of Nutrition,* 39**,** 16-27.

ALAM, M. M., ASIRI, A. M., RAHMAN, M. M. & ISLAM, M. A. 2020. Fabrication of dopamine sensor based on ternary AlMn0.645Cr1.76O7.47 nanoparticles. *Materials Chemistry and Physics,* 244**,** 122740.

ALTAF, M., ISAB, A. A., VANČO, J., DVOŘÁK, Z., TRÁVNÍČEK, Z. & STOECKLI-EVANS, H. 2015. Synthesis, characterization and in vitro cytotoxicity of gold(iii) dialkyl/diaryldithiocarbamato complexes. *RSC Adv.,* 5**,** 81599-81607.

BAUL, T. S. B., KUNDU, S., SINGH, P. & DA SILVA, M. F. C. G. 2015. Insight into inhibition of the human amyloid beta protein precursor (APP: PDB ID 3UMI) using (E)-N-(pyridin-2-ylmethylene) arylamine (LR) models: structure elucidation of a family of ZnX 2-LR complexes. *Dalton Transactions,* 44**,** 2359-2369.

BELAIDI, A. A. & BUSH, A. I. 2016. Iron neurochemistry in Alzheimer's disease and Parkinson's disease: targets for therapeutics. *Journal of neurochemistry,* 139**,** 179-197.

BERMAN, H. M., WESTBROOK, J., FENG, Z., GILLILAND, G., BHAT, T. N., WEISSIG, H., SHINDYALOV, I. N. & BOURNE, P. E. 2000. The Protein Data Bank. *Nucleic Acids Research,* 28**,** 235-242.

BERRIDGE, M. V., HERST, P. M. & TAN, A. S. 2005. Tetrazolium dyes as tools in cell biology: new insights into their cellular reduction. *Biotechnology annual review,* 11**,** 127-152.

BHAT, A. H., DAR, K. B., ANEES, S., ZARGAR, M. A., MASOOD, A., SOFI, M. A. & GANIE, S. A. 2015. Oxidative stress, mitochondrial dysfunction and neurodegenerative diseases; a mechanistic insight. *Biomedicine & Pharmacotherapy,* 74**,** 101-110.

BOROUJENI, H. C. & GHARIB, F. 2016. Thermodynamic investigation on acid-base equilibria of deferiprone and deferasirox at different ionic strengths and various temperatures. *The Journal of Chemical Thermodynamics,* 103**,** 366-373.

BOURASSA, M. W. & MILLER, L. M. 2012. Metal imaging in neurodegenerative diseases. *Metallomics,* 4**,** 721-738.

BREWER, G. J. 2011. Issues raised involving the copper hypotheses in the causation of Alzheimer's disease. *International Journal of Alzheimer's Disease,* 2011.

BRUKER 2001. *SADABS, Bruker AXS Inc.,* Madison, Wisconsin, USA.

BRUKER 2007. *APEX2 and SAINT, Bruker AXS Inc,* Madison, Wisconsin, USA.

BUSH, A. I., PETTINGELL, W., DE PARADIS, M., TANZI, R. E. & WASCO, W. 1994. The amyloid beta-protein precursor and its mammalian homologues. Evidence for a zinc-modulated heparin-binding superfamily. *Journal of Biological Chemistry,* 269**,** 26618-26621.

CAMPS, P., GIÉNEZM, S., FARRÉS, X., MAULEÓN, D. & CARGANICO, G. 1993. Easy and General Method for the Preparation of m-and p-Acylbenzoic Acids: A New Synthesis of rac-Suprofen. *Liebigs Annalen der Chemie,* 1993**,** 641-643.

CHAN, S. H., CHUI, C. H., CHAN, S. W., KOK, S. H. L., CHAN, D., TSOI, M. Y. T., LEUNG, P. H. M., LAM, A. K. Y., CHAN, A. S. C. & LAM, K. H. 2013. Synthesis of 8-hydroxyquinoline derivatives as novel antitumor agents. *ACS medicinal chemistry letters,* 4**,** 170-174.

CHAUHAN, V. & CHAUHAN, A. 2006. Oxidative stress in Alzheimer's disease. *Pathophysiology,* 13**,** 195-208.

CHEN, T., WANG, X., HE, Y., ZHANG, C., WU, Z., LIAO, K., WANG, J. & GUO, Z. 2009. Effects of cyclen and cyclam on zinc(II)- and copper(II)-induced amyloid beta-peptide aggregation and neurotoxicity. *Inorg Chem,* 48**,** 5801-9.

CHERNY, R. A., ATWOOD, C. S., XILINAS, M. E., GRAY, D. N., JONES, W. D., MCLEAN, C. A., BARNHAM, K. J., VOLITAKIS, I., FRASER, F. W. & KIM, Y.-S. 2001. Treatment with a copper-zinc chelator

markedly and rapidly inhibits β-amyloid accumulation in Alzheimer's disease transgenic mice. *Neuron,* 30**,** 665-676.

CHOW, V. W., MATTSON, M. P., WONG, P. C. & GLEICHMANN, M. 2010. An overview of APP processing enzymes and products. *Neuromolecular medicine,* 12**,** 1-12.

CORREIA, H., RAMOS, P., SANTOS, A., PINTO, N. R., MENDES, R., MAGALHÃES, T. & ALMEIDA, A. 2014. A post-mortem study of the anatomical region differences and age-related changes on Ca and Mg levels in the human brain. *Microchemical Journal,* 113**,** 69-76.

COZZI, N. V., BRANDT, S. D., DALEY, P. F., PARTILLA, J. S., ROTHMAN, R. B., TULZER, A., SITTE, H. H. & BAUMANN, M. H. 2013. Pharmacological examination of trifluoromethyl ring-substituted methcathinone analogs. *European Journal of Pharmacology,* 699**,** 180-187.

CRISTÓVÃO, J. S., MOREIRA, G. G., GRABRUCKER, A. M. & GOMES, C. M. 2020. Chapter 9 - Metals and amyloid gain-of-toxic mechanisms in neurodegenerative diseases. *In:* PEY, A. L. (ed.) *Protein Homeostasis Diseases.* Academic Press.

CRONIN, S. J. F., WOOLF, C. J., WEISS, G. & PENNINGER, J. M. 2019. The Role of Iron Regulation in Immunometabolism and Immune-Related Disease. *Frontiers in Molecular Biosciences,* 6.

CURTAIN, C. C., ALI, F., VOLITAKIS, I., CHERNY, R. A., NORTON, R. S., BEYREUTHER, K., BARROW, C. J., MASTERS, C. L., BUSH, A. I. & BARNHAM, K. J. 2001. Alzheimer's disease amyloid-β binds copper and zinc to generate an allosterically ordered membrane-penetrating structure containing superoxide dismutase-like subunits. *Journal of Biological Chemistry,* 276**,** 20466-20473.

DAS, B., KANDEGEDARA, A., XU, L., ANTONIO, T., STEMMLER, T., REITH, M. E. & DUTTA, A. K. 2017. A novel iron (II) preferring dopamine agonist chelator as potential symptomatic and neuroprotective therapeutic agent for Parkinson's disease. *ACS chemical neuroscience,* 8**,** 723-730.

DE CLERCQ, E. 2003. The bicyclam AMD3100 story. *Nature reviews Drug discovery,* 2**,** 581-587.

DE LAU, L. M. & BRETELER, M. M. 2006. Epidemiology of Parkinson's disease. *The Lancet Neurology,* 5**,** 525-535.

DELGADO, R., FELIX, V., LIMA, L. M. P. & PRICE, D. W. 2007. Metal complexes of cyclen and cyclam derivatives useful for medical applications: a discussion based on thermodynamic stability constants and structural data. *Dalton Transactions***,** 2734-2745.

DESIMONE, R. E., BLINN, E. L. & MUCKER, K. F. 1980. Structural aspects of a macrocyclic metal complex containing a copper (II) ion with unusual spectral and kinetic properties. *Inorganic and Nuclear Chemistry Letters,* 16**,** 23-26.

DING, X., ZHANG, F., BAI, Y., ZHAO, J., CHEN, X., GE, M. & SUN, W. 2017. Quinoline-based highly selective and sensitive fluorescent probe specific for Cd2+ detection in mixed aqueous media. *Tetrahedron Letters,* 58**,** 3868-3874.

DU, J., WU, Z.-Y., JIA, M., LI, Y.-Z., WANG, X.-Y. & GUO, Z.-J. 2008. Preparation, Characterisation and DNA Binding Property of a Cu^{II}-Pt^{II} Heterodinuclear Complex Derived from Monosubstituted Cyclen. *Chinese Journal of Inorganic Chemistry,* 24**,** 1669-1674.

EASTON, N., STEWARD, C., MARSHALL, F., FONE, K. & MARSDEN, C. 2007. Effects of amphetamine isomers, methylphenidate and atomoxetine on synaptosomal and synaptic vesicle accumulation and release of dopamine and noradrenaline in vitro in the rat brain. *Neuropharmacology,* 52**,** 405-414.

FABBRI, M., PEREZ-LLORET, S. & RASCOL, O. 2020. Therapeutic strategies for Parkinson's disease: promising agents in early clinical development. *Expert Opinion on Investigational Drugs*.

FAN, L., JIANG, X.-H., WANG, B.-D. & YANG, Z.-Y. 2014. 4-(8'-Hydroxyquinolin-7'-yl)methyleneimino-1-phenyl-2,3-dimethyl-5-pyzole as a fluorescent chemosensor for aluminum ion in acid aqueous medium. *Sensors and Actuators B: Chemical,* 205**,** 249-254.

FAZIL, M., SHADAB, BABOOTA, S., SAHNI, J. K. & ALI, J. 2012. Nanotherapeutics for Alzheimer's disease (AD): past, present and future. *Journal of drug targeting,* 20**,** 97-113.

FEI, H., GRYGORUK, A., BROOKS, E. S., CHEN, A. & KRANTZ, D. E. 2008. Trafficking of vesicular neurotransmitter transporters. *Traffic,* 9**,** 1425-1436.

FINKELSTEIN, D. I., HARE, D. J., BILLINGS, J. L., SEDJAHTERA, A., NURJONO, M., ARTHOFER, E., GEORGE, S., CULVENOR, J. G., BUSH, A. I. & ADLARD, P. A. 2016. Clioquinol Improves Cognitive, Motor Function, and Microanatomy of the Alpha-Synuclein hA53T Transgenic Mice. *ACS Chemical Neuroscience,* 7**,** 119-129.

FLECKENSTEIN, A. E., VOLZ, T. J. & HANSON, G. R. 2009. Psychostimulant-induced alterations in vesicular monoamine transporter-2 function: neurotoxic and therapeutic implications. *Neuropharmacology,* 56**,** 133-138.

GAL, S., FRIDKIN, M., AMIT, T., ZHENG, H. & YOUDIM, M. 2006. M30, a novel multifunctional neuroprotective drug with potent iron chelating and brain selective monoamine oxidase-ab inhibitory activity for Parkinson's disease. *Parkinson's Disease and Related Disorders.* Springer.

GAL, S., ZHENG, H., FRIDKIN, M. & YOUDIM, M. B. 2005. Novel multifunctional neuroprotective iron chelator-monoamine oxidase inhibitor drugs for neurodegenerative diseases. In vivo selective brain monoamine oxidase inhibition and prevention of MPTP-induced striatal dopamine depletion. *Journal of neurochemistry,* 95**,** 79-88.

GHAI, R., FALCONER, R. J. & COLLINS, B. M. 2012. Applications of isothermal titration calorimetry in pure and applied research—survey of the literature from 2010. *Journal of Molecular Recognition,* 25**,** 32-52.

GOEDERT, M. & SPILLANTINI, M. G. 2006. A Century of Alzheimer's Disease. *Science,* 314**,** 777-781.

GOLDBERG, N. R., BEUMING, T., SOYER, O. S., GOLDSTEIN, R. A., WEINSTEIN, H. & JAVITCH, J. A. 2003. Probing conformational changes in neurotransmitter transporters: a structural context. *European Journal of Pharmacology,* 479**,** 3-12.

GREENGARD, P. 2001. The neurobiology of slow synaptic transmission. *Science,* 294**,** 1024-1030.

GUILLOREAU, L., COMBALBERT, S., SOURNIA-SAQUET, A., MAZARGUIL, H. & FALLER, P. 2007. Redox Chemistry of Copper–Amyloid-β: The Generation of Hydroxyl Radical in the Presence of Ascorbate is Linked to Redox-Potentials and Aggregation State. *ChemBioChem,* 8**,** 1317-1325.

HANCOCK, R. D. 1990. Molecular mechanics calculations and metal ion recognition. *Accounts of Chemical Research,* 23**,** 253-257.

HANCOCK, R. D. & MARTELL, A. E. 1989. Ligand design for selective complexation of metal ions in aqueous solution. *Chemical Reviews,* 89**,** 1875-1914.

HANCOCK, R. D., MAUMELA, H. & DE SOUSA, A. S. 1996. Macrocyclic ligands with pendent amide and alcoholic oxygen donor groups. *Coordination chemistry reviews,* 148**,** 315-347.

HEAL, D. J., SMITH, S. L., GOSDEN, J. & NUTT, D. J. 2013. Amphetamine, past and present--a pharmacological and clinical perspective. *Journal of psychopharmacology (Oxford, England),* 27**,** 479-496.

HEIKKILA, R., ORLANSKY, H., MYTILINEOU, C. & COHEN, G. 1975. Amphetamine: evaluation of d-and l-isomers as releasing agents and uptake inhibitors for 3H-dopamine and 3H-norepinephrine in slices of rat neostriatum and cerebral cortex. *Journal of Pharmacology and Experimental Therapeutics,* 194**,** 47-56.

HILBER, B., SCHOLZE, P., DOROSTKAR, M. M., SANDTNER, W., HOLY, M., BOEHM, S., SINGER, E. A. & SITTE, H. H. 2005. Serotonin-transporter mediated efflux: A pharmacological analysis of amphetamines and non-amphetamines. *Neuropharmacology,* 49**,** 811-819.

HOLDGATE, G. 2009. Isothermal titration calorimetry and differential scanning calorimetry. *Methods Mol Biol,* 572**,** 101-33.

JIN, L., SAKIYAN, I., GONZALES, N. S., LANE, D. & CHERALA, S. 2014. Synthesis, characterization and Cu2+ binding studies of l-histidine ester of 8-hydroxyquinoline. *Inorganica Chimica Acta,* 423**,** 72-78.

KEBERLE, H. 1964. The biochemistry of desferrioxamine and its relation to iron metabolism. *Annals of the New York Academy of Sciences,* 119**,** 758-768.

KEPP, K. P. 2012. Bioinorganic chemistry of Alzheimer's disease. *Chemical reviews,* 112**,** 5193-5239.

KHANDHAR, S. M. & MARKS, W. J. 2007. Epidemiology of Parkinson's disease. *Disease-a-month,* 53**,** 200-205.

KIMURA, E. 1992. Macrocyclic polyamines with intelligent functions. *Tetrahedron (Oxford. Print),* 48**,** 6175-6217.

LANNFELT, L., BLENNOW, K., ZETTERBERG, H., BATSMAN, S., AMES, D., HARRISON, J., MASTERS, C. L., TARGUM, S., BUSH, A. I. & MURDOCH, R. 2008. Safety, efficacy, and biomarker findings of PBT2 in targeting Aβ as a modifying therapy for Alzheimer's disease: a phase IIa, double-blind, randomised, placebo-controlled trial. *The Lancet Neurology,* 7**,** 779-786.

LEE, S., ZHENG, X., KRISHNAMOORTHY, J., SAVELIEFF, M. G., PARK, H. M., BRENDER, J. R., KIM, J. H., DERRICK, J. S., KOCHI, A. & LEE, H. J. 2014. Rational design of a structural framework with potential use to develop chemical reagents that target and modulate multiple facets of Alzheimer's disease. *Journal of the American Chemical Society,* 136**,** 299-310.

LEON, R., GARCIA, A. G. & MARCO-CONTELLES, J. 2013. Recent advances in the multitarget-directed ligands approach for the treatment of Alzheimer's disease. *Med Res Rev,* 33**,** 139-89.

LIANG, X. & SADLER, P. J. 2004. Cyclam complexes and their applications in medicine. *Chemical Society Reviews,* 33**,** 246-266.

LIMA, L. M., ESTEBAN-GÓMEZ, D., DELGADO, R., PLATAS-IGLESIAS, C. & TRIPIER, R. L. 2012. Monopicolinate cyclen and cyclam derivatives for stable copper (II) complexation. *Inorganic chemistry,* 51**,** 6916-6927.

LINERT, W. & JAMESON, G. 2000. Redox reactions of neurotransmitters possibly involved in the progression of Parkinson's Disease. *Journal of inorganic biochemistry,* 79**,** 319-326.

LIU, G., LIU, X., CAI, Z., JIAO, G., XU, G. & TANG, W. 2013. Design of Phosphorus Ligands with Deep Chiral Pockets: Practical Synthesis of Chiral β-Arylamines by Asymmetric Hydrogenation. *Angewandte Chemie International Edition,* 52**,** 4235-4238.

MAINES, M. D. 1988. Heme oxygenase: function, multiplicity, regulatory mechanisms, and clinical applications. *The FASEB Journal,* 2**,** 2557-2568.

MARKESBERY, W. R. 1997. Oxidative stress hypothesis in Alzheimer's disease. *Free Radical Biology and Medicine,* 23**,** 134-147.

MARTINS, A. F., OLIVEIRA, A. C., MORFIN, J.-F., LAURENTS, D. V., TÓTH, É. & GERALDES, C. F. 2016. Associating a negatively charged GdDOTA-derivative to the Pittsburgh compound B for targeting Aβ amyloid aggregates. *JBIC Journal of Biological Inorganic Chemistry,* 21**,** 83-99.

MASTERS, C. L., CAPPAI, R., BARNHAM, K. J. & VILLEMAGNE, V. L. 2006. Molecular mechanisms for Alzheimer's disease: implications for neuroimaging and therapeutics. *Journal of neurochemistry,* 97**,** 1700-1725.

MCKIE, A. T., BARROW, D., LATUNDE-DADA, G. O., ROLFS, A., SAGER, G., MUDALY, E., MUDALY, M., RICHARDSON, C., BARLOW, D., BOMFORD, A., PETERS, T. J., RAJA, K. B., SHIRALI, S., HEDIGER, M. A., FARZANEH, F. & SIMPSON, R. J. 2001. An Iron-Regulated Ferric Reductase Associated with the Absorption of Dietary Iron. *Science,* 291**,** 1755-1759.

MONACELLI, F., ACQUARONE, E., GIANNOTTI, C., BORGHI, R. & NENCIONI, A. 2017. Vitamin C, Aging and Alzheimer's Disease. *Nutrients,* 9**,** 670.

MONTAGUE, P. R. & BERNS, G. S. 2002. Neural economics and the biological substrates of valuation. *Neuron,* 36**,** 265-284.

MORET, V., LARAS, Y., PIETRANCOSTA, N., GARINO, C., QUÉLÉVER, G., ROLLAND, A., MALLET, B., NORREEL, J.-C. & KRAUS, J.-L. 2006. 1, 1'-Xylyl bis-1, 4, 8, 11-tetraaza cyclotetradecane: a new potential copper chelator agent for neuroprotection in Alzheimer's disease. Its comparative effects with clioquinol on rat brain copper distribution. *Bioorganic & medicinal chemistry letters,* 16**,** 3298-3301.

MORRIS, M. C., BECKETT, L. A., SCHERR, P. A., HEBERT, L., BENNETT, D. A., FIELD, T. S. & EVANS, D. A. 1998. Vitamin E and vitamin C supplement use and risk of incident Alzheimer disease. *Alzheimer disease and associated disorders*.

MOUNSEY, R. B. & TEISMANN, P. 2012. Chelators in the treatment of iron accumulation in Parkinson's disease. *International journal of cell biology,* 2012.

MUCKENTHALER, M. U., RIVELLA, S., HENTZE, M. W. & GALY, B. 2017. A red carpet for iron metabolism. *Cell,* 168**,** 344-361.

NETZER, W. 2013. Copper may play a role in Alzheimer's disease. *PNAS,* 110**,** 5.

NUÑEZ, M. T. & CHANA-CUEVAS, P. 2018. New Perspectives in Iron Chelation Therapy for the Treatment of Neurodegenerative Diseases. *Pharmaceuticals (Basel, Switzerland),* 11.

OLEX, A. 2009. Complete Structure Solution, Refinement and Analysis Program: OV Dolomanov, LJ Bourhis, RJ Gildea, JAK Howard, H. Puschmann. *J. Appl. Crystallogr,* 42**,** 339-341.

OSREDKAR, J. & SUSTAR, N. 2011. Copper and zinc, biological role and significance of copper/zinc imbalance. *J Clinic Toxicol S,* 3**,** 0495.

PAVULURU, N. & LUO, X. 2019. The investigation of metal-ion coordination to amyloid-beta and potential chelation materials for the treatment of Alzheimer's disease. *PeerJ Preprints*.

PERLUIGI, M., JOSHI, G., SULTANA, R., CALABRESE, V., DE MARCO, C., COCCIA, R. & BUTTERFIELD, D. 2006. In vivo protection by the xanthate tricyclodecan-9-yl-xanthogenate against amyloid β-peptide (1–42)-induced oxidative stress. *Neuroscience,* 138**,** 1161-1170.

PIERCE, M. M., RAMAN, C. S. & NALL, B. T. 1999. Isothermal Titration Calorimetry of Protein–Protein Interactions. *Methods,* 19**,** 213-221.

PITHADIA, A. S. & LIM, M. H. 2012. Metal-associated amyloid-beta species in Alzheimer's disease. *Curr Opin Chem Biol,* 16**,** 67-73.

RAMAMOORTHY, S., SHIPPENBERG, T. S. & JAYANTHI, L. D. 2011. Regulation of monoamine transporters: Role of transporter phosphorylation. *Pharmacology & therapeutics,* 129**,** 220-238.

RAMSAYWACK, S., VOGELS, C. M., RICKER, S. L., WESTCOTT, S. A. & BARCLAY, L. R. C. 2013. Pyridinones Are Not Antioxidants As Shown by Kinetics of Free Radical Autoxidation, but They Prevent Radical Oxidations Catalyzed by Toxic Heavy Metals. *Chemical Research in Toxicology,* 26**,** 399-409.

RIEDERER, P., RAUSCH, W., SCHMIDT, B., KRUZIK, P., KONRADI, C., SOFIĆ, E., DANIELCZYK, W., FISCHER, M. & OGRIS, E. 1988. Biochemical fundamentals of Parkinson's disease. *The Mount Sinai journal of medicine, New York,* 55**,** 21.

ROBINSON, S. G., BURNS, P. T., MICELI, A. M., GRICE, K. A., KARVER, C. E. & JIN, L. 2016. Calorimetric studies of the interactions of metalloenzyme active site mimetics with zinc-binding inhibitors. *Dalton Transactions,* 45**,** 11817-11829.

RODRÍGUEZ-RODRÍGUEZ, C., SANCHEZ DE GROOT, N., RIMOLA, A., ALVAREZ-LARENA, A., LLOVERAS, V., VIDAL-GANCEDO, J., VENTURA, S., VENDRELL, J., SODUPE, M. & GONZÁLEZ-DUARTE, P. 2009. Design, selection, and characterization of thioflavin-based intercalation compounds with metal chelating properties for application in Alzheimer's disease. *Journal of the American Chemical Society,* 131**,** 1436-1451.

RODRÍGUEZ-RODRÍGUEZ, C., TELPOUKHOVSKAIA, M. & ORVIG, C. 2012. The art of building multifunctional metal-binding agents from basic molecular scaffolds for the potential application in neurodegenerative diseases. *Coordination Chemistry Reviews,* 256**,** 2308-2332.

ROSSI, L., LOMBARDO, M. F., CIRIOLO, M. R. & ROTILIO, G. 2004. Mitochondrial dysfunction in neurodegenerative diseases associated with copper imbalance. *Neurochemical research,* 29**,** 493-504.

ROTHMAN, R. B. & BAUMANN, M. H. 2003. Monoamine transporters and psychostimulant drugs. *European Journal of Pharmacology,* 479**,** 23-40.

RUSCONI, S., SCOZZAFAVA, A., MASTROLORENZO, A. & SUPURAN, C. T. 2004. New advances in HIV entry inhibitors development. *Current Drug Targets-Infectious Disorders,* 4**,** 339-355.

SALAMONE, J. D., CORREA, M., FARRAR, A. M., NUNES, E. J. & PARDO, M. 2009. Dopamine, behavioral economics, and effort. *Frontiers in behavioral neuroscience,* 3**,** 13.

SAMPSON, E. L., JENAGARATNAM, L. & MCSHANE, R. 2014. Metal protein attenuating compounds for the treatment of Alzheimer's dementia. *Cochrane Database of Systematic Reviews*.

SANTOS, M. A., MARQUES, S. M. & CHAVES, S. 2012. Hydroxypyridinones as "privileged" chelating structures for the design of medicinal drugs. *Coordination Chemistry Reviews,* 256**,** 240-259.

SCHEIBER, I. F., MERCER, J. F. B. & DRINGEN, R. 2014. Metabolism and functions of copper in brain. *Progress in Neurobiology,* 116**,** 33-57.

SCHIMMER, A. D., JITKOVA, Y., GRONDA, M., WANG, Z., BRANDWEIN, J., CHEN, C., GUPTA, V., SCHUH, A., YEE, K. & CHEN, J. 2012. A phase I study of the metal ionophore clioquinol in patients with advanced hematologic malignancies. *Clinical Lymphoma Myeloma and Leukemia,* 12**,** 330-336.

SCHMITT, K. C., ROTHMAN, R. B. & REITH, M. E. A. 2013. Nonclassical Pharmacology of the Dopamine Transporter: Atypical Inhibitors, Allosteric Modulators, and Partial Substrates. *Journal of Pharmacology and Experimental Therapeutics,* 346**,** 2-10.

SEDDIK, A., HOLY, M., WEISSENSTEINER, R., ZDRAZIL, B., SITTE, H. H. & ECKER, G. F. 2013. Probing the selectivity of monoamine transporter substrates by means of molecular modeling. *Molecular informatics,* 32**,** 409.

SEIDEL, S., SINGER, E. A., JUST, H., FARHAN, H., SCHOLZE, P., KUDLACEK, O., HOLY, M., KOPPATZ, K., KRIVANEK, P., FREISSMUTH, M. & SITTE, H. H. 2005. Amphetamines take two to tango: an oligomer-based counter-transport model of neurotransmitter transport explores the amphetamine action. *Molecular Pharmacology,* 67**,** 140-151.

SHARMA, O. P. & BHAT, T. K. 2009. DPPH antioxidant assay revisited. *Food Chemistry,* 113**,** 1202-1205.

SHELDRICK, G. 2008. A short history of SHELX. *Acta Crystallographica Section A,* 64**,** 112-122.

SHI, L., QUICK, M., ZHAO, Y., WEINSTEIN, H. & JAVITCH, J. A. 2008. The Mechanism of a Neurotransmitter:Sodium Symporter—Inward Release of Na+ and Substrate Is Triggered by Substrate in a Second Binding Site. *Molecular Cell,* 30**,** 667-677.

SHISHODIA, S., SETHI, G. & AGGARWAL, B. B. 2005. Curcumin: getting back to the roots. *Annals of the New York Academy of Sciences,* 1056**,** 206-217.

SINGH, I., SAGARE, A. P., COMA, M., PERLMUTTER, D., GELEIN, R., BELL, R. D., DEANE, R. J., ZHONG, E., PARISI, M. & CISZEWSKI, J. 2013. Low levels of copper disrupt brain amyloid-β homeostasis by altering its production and clearance. *Proceedings of the National Academy of Sciences,* 110**,** 14771-14776.

SINGH, Y. P., PANDEY, A., VISHWAKARMA, S. & MODI, G. 2019. A review on iron chelators as potential therapeutic agents for the treatment of Alzheimer's and Parkinson's diseases. *Molecular diversity,* 23**,** 509-526.

SITTE, H. H. & FREISSMUTH, M. 2010. The reverse operation of Na+/Cl−-coupled neurotransmitter transporters–why amphetamines take two to tango. *Journal of neurochemistry,* 112**,** 340-355.

SMITH, D. G., CAPPAI, R. & BARNHAM, K. J. 2007. The redox chemistry of the Alzheimer's disease amyloid β peptide. *Biochimica et Biophysica Acta (BBA)-Biomembranes,* 1768**,** 1976-1990.

SMITH, J., XIONG, S., MARKESBERY, W. & LOVELL, M. 2006. Altered expression of zinc transporters-4 and-6 in mild cognitive impairment, early and late Alzheimer's disease brain. *Neuroscience,* 140**,** 879-888.

SMITH, P. K., KROHN, R. I., HERMANSON, G. T., MALLIA, A. K., GARTNER, F. H., PROVENZANO, M. D., FUJIMOTO, E. K., GOEKE, N. M., OLSON, B. J. & KLENK, D. C. 1985. Measurement of protein using bicinchoninic acid. *Analytical Biochemistry,* 150**,** 76-85.

SONNE, J. & BEATO, M. R. 2018. Neuroanatomy, substantia nigra. *StatPearls [Internet]*.

SOUTHON, A. A., SZOSTAK, K., ACEVEDO, K. M., DENT, K. A., VOLITAKIS, I., BELAIDI, A. A., BARNHAM, K. J., CROUCH, P. J., AYTON, S. & DONNELLY, P. S. 2019. CuII (atsm) inhibits ferroptosis: implications for treatment of neurodegenerative disease. *British journal of pharmacology*.

SRIVASTAVA, V. K. & YADAV, R. 2019. Chapter 9 - Isothermal titration calorimetry. *In:* MISRA, G. (ed.) *Data Processing Handbook for Complex Biological Data Sources.* Academic Press.

STABILE, L. P., DAVIS, A. L. G., GUBISH, C. T., HOPKINS, T. M., LUKETICH, J. D., CHRISTIE, N., FINKELSTEIN, S. & SIEGFRIED, J. M. 2002. Human Non-Small Cell Lung Tumors and Cells Derived from Normal Lung Express Both Estrogen Receptor α and β and Show Biological Responses to Estrogen. *Cancer Research,* 62**,** 2141-2150.

SUN, Y., PHAM, A. N. & WAITE, T. D. 2018. Mechanism underlying the effectiveness of deferiprone in alleviating Parkinson's disease symptoms. *ACS chemical neuroscience,* 9**,** 1118-1127.

TABNER, B. J., MAYES, J. & ALLSOP, D. 2011. Hypothesis: soluble Aβ oligomers in association with redox-active metal ions are the optimal generators of reactive oxygen species in Alzheimer's disease. *International Journal of Alzheimer's Disease,* 2011.

TELFER, T. J., LIDDELL, J. R., DUNCAN, C., WHITE, A. R. & CODD, R. 2017. Adamantyl- and other polycyclic cage-based conjugates of desferrioxamine B (DFOB) for treating iron-mediated toxicity in cell models of Parkinson's disease. *Bioorganic & Medicinal Chemistry Letters,* 27**,** 1698-1704.

TIMOSHNIKOV, V., KLIMENTIEV, V., POLYAKOV, N. & KONTOGHIORGHES, G. 2014. Photoinduced transformation of iron chelator deferiprone: Possible implications in drug metabolism and toxicity. *Journal of Photochemistry and Photobiology A: Chemistry,* 289**,** 14-21.

TRAMUTOLA, A., LANZILLOTTA, C., PERLUIGI, M. & BUTTERFIELD, D. A. 2017. Oxidative stress, protein modification and Alzheimer disease. *Brain research bulletin,* 133**,** 88-96.

TRIST, B. G., HARE, D. J. & DOUBLE, K. L. 2019. Oxidative stress in the aging substantia nigra and the etiology of Parkinson's disease. *Aging cell,* 18**,** e13031.

TYSNES, O.-B. & STORSTEIN, A. 2017. Epidemiology of Parkinson's disease. *Journal of Neural Transmission,* 124**,** 901-905.

TYSZKA-CZOCHARA, M., GRZYWACZ, A., GDULA-ARGASIŃSKA, J., LIBROWSKI, T., WILIŃSKI, B. & OPOKA, W. 2014. The role of zinc in the pathogenesis and treatment of central nervous system (CNS) diseases. Implications of zinc homeostasis for proper CNS function. *Acta Pol Pharm,* 71**,** 369-77.

WARD, R. J., DEXTER, D. T. & CRICHTON, R. R. 2012. Chelating Agents for Neurodegenerative Diseases. *Current Medicinal Chemistry,* 19**,** 2760-2772.

WARD, R. J., ZUCCA, F. A., DUYN, J. H., CRICHTON, R. R. & ZECCA, L. 2014. The role of iron in brain ageing and neurodegenerative disorders. *The Lancet Neurology,* 13**,** 1045-1060.

WATT, N. T., WHITEHOUSE, I. J. & HOOPER, N. M. 2010. The role of zinc in Alzheimer's disease. *International Journal of Alzheimer's Disease,* 2011.

WEISMAN, G. R. & REED, D. P. 1996. A New Synthesis of Cyclen (1,4,7,10-Tetraazacyclododecane). *The Journal of Organic Chemistry,* 61**,** 5186-5187.

WHITE, A. 2014. Metals on our mind. *the scientist magazine,* 1**,** 7.

WICHUR, T., WIĘCKOWSKA, A., WIĘCKOWSKI, K., GODYŃ, J., JOŃCZYK, J., VALDIVIESO, Á. D. R., PANEK, D., PASIEKA, A., SABATÉ, R., KNEZ, D., GOBEC, S. & MALAWSKA, B. 2020. 1-Benzylpyrrolidine-3-amine-based BuChE inhibitors with anti-aggregating, antioxidant and metal-chelating properties as multifunctional agents against Alzheimer's disease. *European Journal of Medicinal Chemistry,* 187**,** 111916.

WILSON, J. M., GIORDANI, F., FARRUGIA, L. J., BARRETT, M. P., ROBINS, D. J. & SUTHERLAND, A. 2007. Synthesis, characterisation and anti-protozoal activity of carbamate-derived polyazamacrocycles. *Organic & biomolecular chemistry,* 5**,** 3651-3656.

WIPPOLD, F., CAIRNS, N., VO, K., HOLTZMAN, D. & MORRIS, J. 2008. Neuropathology for the neuroradiologist: plaques and tangles. *American Journal of Neuroradiology,* 29**,** 18-22.

YAMAMOTO, H. & MARUOKA, K. 1981. Regioselective carbonyl amination using diisobutylaluminum hydride. *Journal of the American Chemical Society,* 103**,** 4186-4194.

YANATORI, I., RICHARDSON, D. R., IMADA, K. & KISHI, F. 2016. Iron export through the transporter ferroportin 1 is modulated by the iron chaperone PCBP2. *Journal of Biological Chemistry,* 291**,** 17303-17318.

YANG, W. S. & STOCKWELL, B. R. 2016. Ferroptosis: Death by Lipid Peroxidation. *Trends in cell biology,* 26**,** 165-176.

YANG, Z., SONG, Q., CAO, Z., YU, G., LIU, Z., TAN, Z. & DENG, Y. 2020. Design, synthesis and evaluation of flurbiprofen-clioquinol hybrids as multitarget-directed ligands against Alzheimer's disease. *Bioorganic & Medicinal Chemistry,* 28**,** 115374.

YOON, I., LEE, K. H. & CHO, J. 2004. Gossypin protects primary cultured rat cortical cells from oxidative stress-and β-amyloid-lnduced toxicity. *Archives of pharmacal research,* 27**,** 454-459.

YOON, M.-A., JEONG, T.-S., PARK, D.-S., XU, M.-Z., OH, H.-W., SONG, K.-B., LEE, W. S. & PARK, H.-Y. 2006. Antioxidant effects of quinoline alkaloids and 2, 4-di-tert-butylphenol isolated from Scolopendra subspinipes. *Biological and Pharmaceutical Bulletin,* 29**,** 735-739.

YOUDIM, M., FRIDKIN, M. & ZHENG, H. 2004. Novel bifunctional drugs targeting monoamine oxidase inhibition and iron chelation as an approach to neuroprotection in Parkinson's disease and other neurodegenerative diseases. *Journal of neural transmission,* 111**,** 1455-1471.

ZANDI, P. P., ANTHONY, J. C., KHACHATURIAN, A. S., STONE, S. V., GUSTAFSON, D., TSCHANZ, J. T., NORTON, M. C., WELSH-BOHMER, K. A. & BREITNER, J. C. 2004. Reduced risk of Alzheimer disease in users of antioxidant vitamin supplements: the Cache County Study. *Archives of neurology,* 61**,** 82-88.

ZATTA, P., TOGNON, G. & CARAMPIN, P. 2003. Melatonin prevents free radical formation due to the interaction between β-amyloid peptides and metal ions [Al (III), Zn (II), Cu (II), Mn (II), Fe (II)]. *Journal of pineal research,* 35**,** 98-103.

ZHANG, L.-H., WANG, X., STOLTENBERG, M., DANSCHER, G., HUANG, L. & WANG, Z.-Y. 2008. Abundant expression of zinc transporters in the amyloid plaques of Alzheimer's disease brain. *Brain research bulletin,* 77**,** 55-60.

ZHENG, H., WEINER, L. M., BAR-AM, O., EPSZTEJN, S., CABANTCHIK, Z. I., WARSHAWSKY, A., YOUDIM, M. B. H. & FRIDKIN, M. 2005. Design, synthesis, and evaluation of novel bifunctional iron-chelators as potential agents for neuroprotection in Alzheimer's, Parkinson's, and other neurodegenerative diseases. *Bioorganic & Medicinal Chemistry,* 13**,** 773-783.

ZHENG, W. & MONNOT, A. D. 2012. Regulation of brain iron and copper homeostasis by brain barrier systems: implication in neurodegenerative diseases. *Pharmacology & therapeutics,* 133**,** 177-188.

ZILKA, O., SHAH, R., LI, B., FRIEDMANN ANGELI, J. P., GRIESSER, M., CONRAD, M. & PRATT, D. A. 2017. On the Mechanism of Cytoprotection by Ferrostatin-1 and Liproxstatin-1 and the Role of Lipid Peroxidation in Ferroptotic Cell Death. *ACS central science,* 3**,** 232-243.

ZUCCA, F. A., SEGURA-AGUILAR, J., FERRARI, E., MUÑOZ, P., PARIS, I., SULZER, D., SARNA, T., CASELLA, L. & ZECCA, L. 2017. Interactions of iron, dopamine and neuromelanin pathways in brain aging and Parkinson's disease. *Progress in neurobiology,* 155**,** 96-119.

Appendix 1

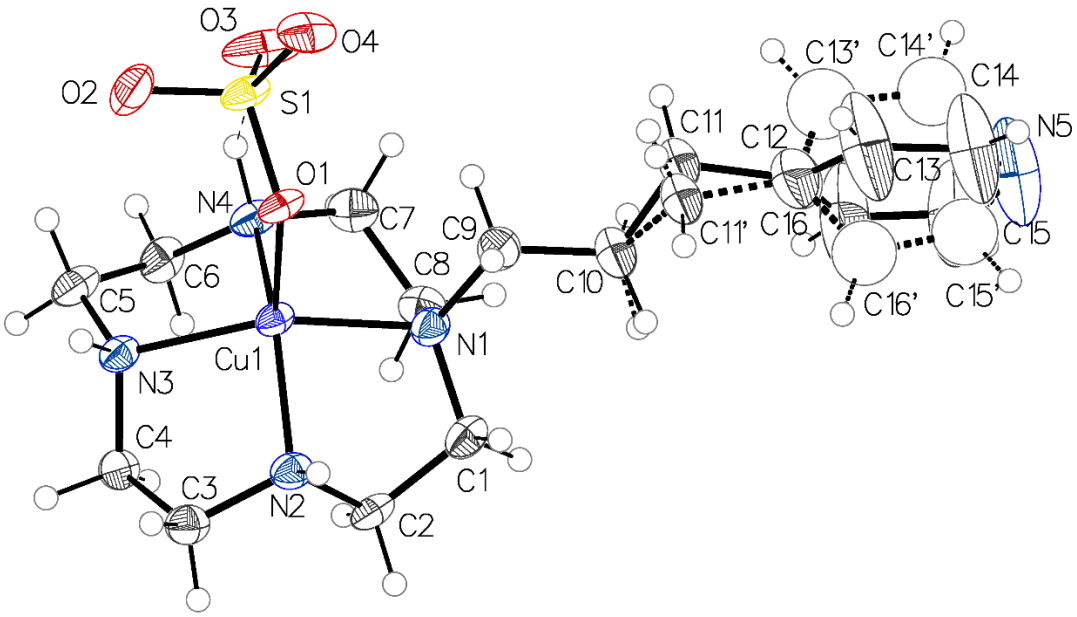

*Figure 61: ORTEP plot of **MS3**:Cu*

*Table 7: Bond lengths and angles for **MS3**:Cu.*

Cu1—O1	2.138 (3)	N5—C14'	1.243 (16)
Cu1—N1	2.047 (4)	N5—C15'	1.250 (16)
Cu1—N2	2.019 (4)	C1—C2	1.513 (7)
Cu1—N3	2.022 (4)	C3—C4	1.515 (8)
Cu1—N4	2.020 (4)	C5—C6	1.521 (8)
S1—O1	1.498 (4)	C7—C8	1.522 (8)
S1—O2	1.475 (5)	C9—C10	1.519 (8)
S1—O3	1.467 (4)	C10—C11	1.520 (11)
S1—O4	1.470 (5)	C10—C11'	1.565 (12)
N1—C1	1.493 (7)	C11—C12	1.496 (13)
N1—C8	1.487 (7)	C12—C13	1.34 (4)
N1—C9	1.488 (6)	C12—C16	1.14 (4)
N2—C2	1.473 (7)	C12—C11'	1.564 (13)
N2—C3	1.484 (7)	C12—C13'	1.448 (15)
N3—C4	1.493 (6)	C12—C16'	1.279 (13)
N3—C5	1.482 (7)	C13—C14	1.32 (5)
N4—C6	1.471 (7)	C15—H15	0.9500
N4—C7	1.469 (7)	C15—C16	1.43 (5)
N5—C14	1.17 (4)	C13'—C14'	1.389 (16)
N5—C15	1.53 (4)	C15'—C16'	1.360 (17)
N1—Cu1—O1	101.85 (15)	C7—N4—C6	115.9 (4)
N2—Cu1—O1	113.53 (16)	C14—N5—C15	102 (3)
N2—Cu1—N1	86.61 (18)	C14'—N5—C15'	115.1 (12)
N2—Cu1—N3	85.91 (18)	N1—C1—C2	109.4 (4)
N2—Cu1—N4	147.45 (17)	N2—C2—C1	108.2 (4)
N3—Cu1—O1	104.77 (15)	N2—C3—C4	110.3 (4)
N3—Cu1—N1	153.16 (17)	N3—C4—C3	107.3 (4)
N4—Cu1—O1	99.02 (15)	N3—C5—C6	109.5 (5)
N4—Cu1—N1	86.58 (18)	N4—C6—C5	108.2 (4)
N4—Cu1—N3	85.99 (18)	N4—C7—C8	109.9 (4)
O2—S1—O1	108.3 (2)	N1—C8—C7	110.5 (4)
O3—S1—O1	109.0 (2)	N1—C9—C10	115.3 (5)
O3—S1—O2	110.1 (3)	C9—C10—C11	112.5 (6)
O3—S1—O4	109.8 (3)	C9—C10—C11'	109.1 (6)
O4—S1—O1	109.2 (2)	C12—C11—C10	114.6 (9)
O4—S1—O2	110.4 (3)	C13—C12—C11'	111.3 (17)
S1—O1—Cu1	127.9 (2)	C16—C12—C13	123 (3)
C1—N1—Cu1	106.3 (3)	C16—C12—C11'	125 (2)
C8—N1—Cu1	101.6 (3)	C13'—C12—C11	118.7 (9)
C8—N1—C1	111.9 (4)	C16'—C12—C11	128.9 (11)
C8—N1—C9	113.2 (4)	C16'—C12—C13'	111.4 (10)
C9—N1—Cu1	113.2 (3)	C14—C13—C12	113 (3)
C9—N1—C1	110.2 (4)	N5—C14—C13	140 (4)
C2—N2—Cu1	102.1 (3)	C16—C15—N5	120 (3)
C2—N2—C3	114.0 (4)	C12—C16—C15	120 (4)
C3—N2—Cu1	108.4 (3)	C12—C11'—C10	108.4 (8)
C4—N3—Cu1	103.6 (3)	C14'—C13'—C12	116.8 (12)
C5—N3—Cu1	108.3 (3)	N5—C14'—C13'	126.3 (15)
C5—N3—C4	113.9 (4)	N5—C15'—C16'	123.5 (15)
C6—N4—Cu1	105.3 (3)	C12—C16'—C15'	125.4 (14)
C7—N4—Cu1	109.2 (3)		

*Table 8: Crystallographic data for **MS3**:Cu.*

Crystal data	
Chemical formula	$C_{16}H_{29}CuN_5O_4S·2.5(CH_4O)·0.25(CHO)$
M_r	538.40
Crystal system, space group	Monoclinic, $P2_1/c$
Temperature (K)	149
a, b, c (Å)	16.686 (2), 11.6445 (16), 16.735 (2)
β (°)	114.933 (8)
V (Å^3)	2948.6 (7)
Z	4
Radiation type	Mo $K\alpha$
μ (mm^{-1})	0.85
Crystal size (mm)	0.27 × 0.26 × 0.04
Data collection	
Diffractometer	Bruker *APEX*-II CCD
Absorption correction	Multi-scan *SADABS2014*/5 (Bruker,2014/5) was used for absorption correction. wR2(int) was 0.1271 before and 0.0647 after correction. The Ratio of minimum to maximum transmission is 0.7830. The λ/2 correction factor is 0.00150.
T_{min}, T_{max}	0.584, 0.746
No. of measured, independent and observed [$I > 2\sigma(I)$] reflections	21577, 6367, 3650
R_{int}	0.110
$(\sin \theta/\lambda)_{max}$ (Å^{-1})	0.638
Refinement	
$R[F^2 > 2\sigma(F^2)]$, $wR(F^2)$, S	0.073, 0.223, 1.02
No. of reflections	6367
No. of parameters	336
No. of restraints	51
H-atom treatment	H-atom parameters constrained
$\Delta\rangle_{max}$, $\Delta\rangle_{min}$ (e Å^{-3})	1.21, -0.55

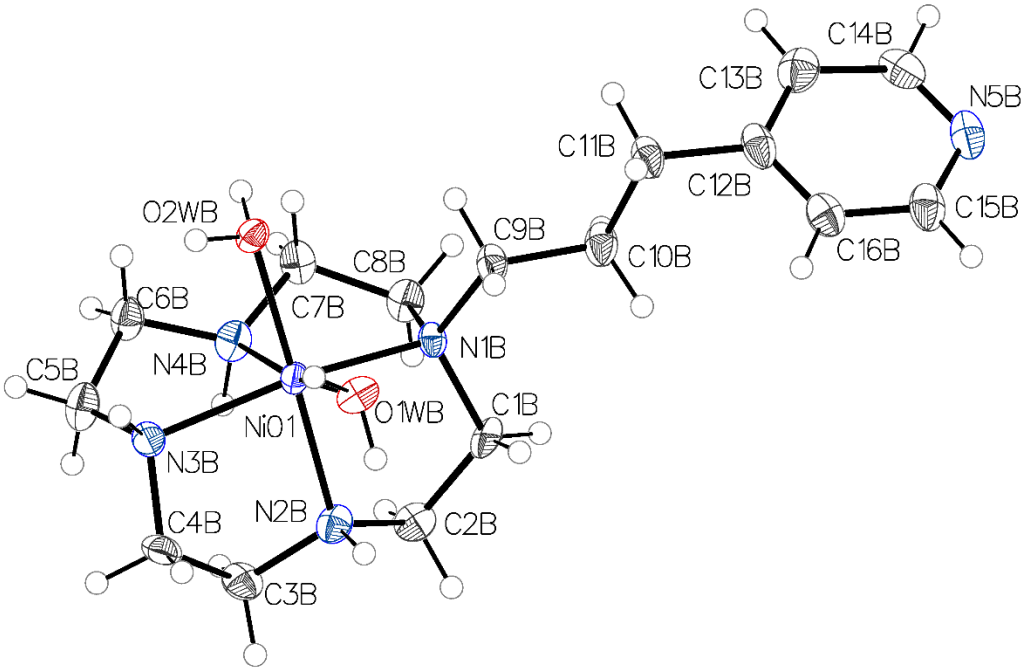

*Figure 62: ORTEP plot of **MS3**:Ni*

*Table 9: Bond lengths and angles for **MS3**:Ni*

Ni01—N1B	2.143 (6)	N4B—C7B	1.441 (10)
Ni01—N2B	2.044 (7)	N5B—C14B	1.325 (14)
Ni01—N3B	2.113 (7)	N5B—C15B	1.338 (12)
Ni01—N4B	2.071 (7)	C1B—C2B	1.504 (11)
Ni01—O1WB	2.089 (5)	C3B—C4B	1.526 (12)
Ni01—O2WB	2.110 (5)	C5B—C6B	1.510 (12)
N1B—C1B	1.481 (10)	C7B—C8B	1.512 (11)
N1B—C8B	1.490 (10)	C9B—C10B	1.534 (12)
N1B—C9B	1.476 (11)	C10B—C11B	1.530 (11)
N2B—C2B	1.480 (10)	C11B—C12B	1.499 (13)
N2B—C3B	1.472 (11)	C12B—C13B	1.388 (14)
N3B—C4B	1.474 (10)	C12B—C16B	1.377 (13)
N3B—C5B	1.479 (11)	C13B—C14B	1.385 (13)
N4B—C6B	1.456 (10)	C15B—C16B	1.380 (12)
Ni01—N1B	2.143 (6)	N4B—C7B	1.441 (10)
Ni01—N2B	2.044 (7)	N5B—C14B	1.325 (14)
Ni01—N3B	2.113 (7)	N5B—C15B	1.338 (12)
Ni01—N4B	2.071 (7)	C1B—C2B	1.504 (11)
Ni01—O1WB	2.089 (5)	C3B—C4B	1.526 (12)
Ni01—O2WB	2.110 (5)	C5B—C6B	1.510 (12)
N1B—C1B	1.481 (10)	C7B—C8B	1.512 (11)
N1B—C8B	1.490 (10)	C9B—C10B	1.534 (12)
N1B—C9B	1.476 (11)	C10B—C11B	1.530 (11)
N2B—C2B	1.480 (10)	C11B—C12B	1.499 (13)
N2B—C3B	1.472 (11)	C12B—C13B	1.388 (14)
N3B—C4B	1.474 (10)	C12B—C16B	1.377 (13)
N3B—C5B	1.479 (11)	C13B—C14B	1.385 (13)
N4B—C6B	1.456 (10)	C15B—C16B	1.380 (12)
N2B—Ni01—N1B	84.9 (3)	C4B—N3B—Ni01	105.9 (5)
N2B—Ni01—N3B	84.3 (3)	C4B—N3B—C5B	111.4 (7)
N2B—Ni01—N4B	98.7 (3)	C5B—N3B—Ni01	109.2 (5)
N2B—Ni01—O1WB	88.5 (2)	C6B—N4B—Ni01	105.5 (5)
N2B—Ni01—O2WB	169.9 (2)	C7B—N4B—Ni01	104.6 (5)
N3B—Ni01—N1B	158.5 (2)	C7B—N4B—C6B	119.0 (6)
N4B—Ni01—N1B	82.0 (3)	C14B—N5B—C15B	115.0 (8)
N4B—Ni01—N3B	81.4 (3)	N1B—C1B—C2B	110.9 (6)
N4B—Ni01—O1WB	172.4 (3)	N2B—C2B—C1B	108.0 (6)
N4B—Ni01—O2WB	90.5 (2)	N2B—C3B—C4B	107.2 (6)
O1WB—Ni01—N1B	96.3 (2)	N3B—C4B—C3B	110.4 (7)
O1WB—Ni01—N3B	101.9 (2)	N3B—C5B—C6B	111.5 (7)
O1WB—Ni01—O2WB	82.5 (2)	N4B—C6B—C5B	108.0 (7)
O2WB—Ni01—N1B	100.5 (2)	N4B—C7B—C8B	108.3 (7)
O2WB—Ni01—N3B	93.1 (2)	N1B—C8B—C7B	109.9 (6)
C1B—N1B—Ni01	103.4 (5)	N1B—C9B—C10B	118.0 (6)
C1B—N1B—C8B	111.6 (6)	C11B—C10B—C9B	110.4 (6)
C8B—N1B—Ni01	107.6 (5)	C12B—C11B—C10B	112.5 (7)
C9B—N1B—Ni01	112.6 (5)	C13B—C12B—C11B	122.8 (9)
C9B—N1B—C1B	111.4 (6)	C16B—C12B—C11B	119.9 (9)
C9B—N1B—C8B	110.0 (7)	C16B—C12B—C13B	117.3 (9)
C2B—N2B—Ni01	107.7 (5)	C14B—C13B—C12B	118.2 (9)
C2B—N2B—H2B	107.8	N5B—C14B—C13B	125.6 (9)
C3B—N2B—Ni01	108.3 (5)	N5B—C15B—C16B	124.1 (9)
C3B—N2B—C2B	117.1 (6)	C12B—C16B—C15B	119.8 (9)

*Table 10: Crystallographic data for **MS3**:Ni.*

Crystal data	
Chemical formula	$2(C_{16}H_{33}N_5NiO_2)\cdot 2(O_4S)\cdot 3.25(O)\cdot 5.25(H_2O)\cdot 0.5(CH_4O)$
M_r	1127.09
Crystal system, space group	Orthorhombic, *Pna*2$_1$
Temperature (K)	150
a, *b*, *c* (Å)	17.3451 (12), 12.3892 (10), 25.8267 (19)
V (Å^3)	5549.9 (7)
Z	4
Radiation type	Mo *K*α
μ (mm^{-1})	0.83
Crystal size (mm)	0.12 × 0.06 × 0.04
Data collection	
Diffractometer	Bruker *APEX*-II CCD
Absorption correction	Multi-scan *SADABS2014*/5 (Bruker,2014/5) was used for absorption correction. wR2 (int) was 0.1436 before and 0.0665 after correction. The Ratio of minimum to maximum transmission is 0.8672. The λ/2 correction factor is 0.00150.
T_{min}, T_{max}	0.647, 0.746
No. of measured, independent and observed [$I > 2\sigma(I)$] reflections	66752, 12112, 9682
R_{int}	0.086
$(\sin\theta/\lambda)_{max}$ (Å^{-1})	0.640
Refinement	
$R[F^2 > 2\sigma(F^2)]$, $wR(F^2)$, *S*	0.061, 0.177, 1.04
No. of reflections	12112
No. of parameters	671
No. of restraints	7
H-atom treatment	H atoms treated by a mixture of independent and constrained refinement
$\Delta\rangle_{max}$, $\Delta\rangle_{min}$ (e Å^{-3})	1.22, -0.65
Absolute structure	Flack x determined using 3900 quotients [(I+)-(I-)]/[(I+)+(I-)] (Parsons, Flack and Wagner, Acta Cryst. B69 (2013) 249-259).
Absolute structure parameter	0.354 (10)

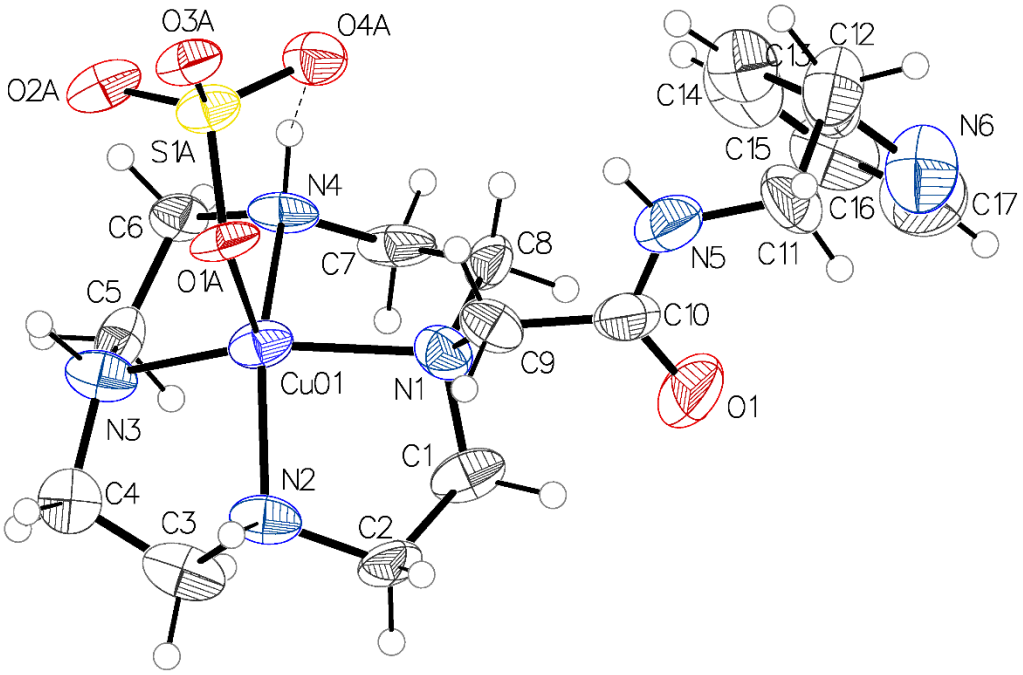

*Figure 63: ORTEP plot of **MS2**:Cu*

*Table 11: Bond lengths and angles for **MS2**:Cu.*

Cu01—N1	2.055 (13)	N6—C13	1.36 (2)
Cu01—N2	2.016 (12)	N6—C17	1.35 (3)
Cu01—N3	2.024 (13)	C1—C2	1.531 (19)
Cu01—N4	2.058 (11)	C3—C4	1.51 (2)
Cu01—O1A	2.108 (9)	C5—C6	1.529 (19)
O1—C10	1.223 (18)	C7—C8	1.55 (2)
N1—C1	1.494 (18)	C9—C10	1.53 (2)
N1—C8	1.500 (18)	C11—C12	1.57 (2)
N1—C9	1.502 (19)	C12—C13	1.50 (2)
N2—C2	1.485 (19)	C13—C14	1.35 (2)
N2—C3	1.53 (2)	C14—C15	1.38 (2)
N3—C4	1.465 (18)	C15—C16	1.37 (3)
N3—C5	1.484 (18)	C16—C17	1.39 (3)
N4—C6	1.464 (19)	S1A—O1A	1.506 (9)
N4—C7	1.469 (18)	S1A—O2A	1.507 (12)
N5—C10	1.298 (19)	S1A—O3A	1.461 (10)
N5—C11	1.43 (2)	S1A—O4A	1.470 (10)
N1—Cu01—N4	86.4 (5)	N2—C2—C1	110.3 (12)
N1—Cu01—O1A	100.7 (5)	C4—C3—N2	108.4 (13)
N2—Cu01—N1	85.6 (5)	N3—C4—C3	107.6 (13)
N2—Cu01—N3	86.6 (5)	N3—C5—C6	108.1 (12)
N2—Cu01—N4	147.4 (5)	N4—C6—C5	112.4 (12)
N2—Cu01—O1A	111.9 (4)	N4—C7—C8	107.0 (12)
N3—Cu01—N1	153.4 (5)	N1—C8—C7	109.5 (12)
N3—Cu01—N4	86.7 (5)	N1—C9—C10	116.4 (13)
N3—Cu01—O1A	105.8 (5)	O1—C10—N5	123.1 (18)
N4—Cu01—O1A	100.6 (4)	O1—C10—C9	120.1 (17)
C1—N1—Cu01	102.3 (9)	N5—C10—C9	116.6 (15)
C1—N1—C8	110.4 (11)	N5—C11—C12	111.1 (16)
C1—N1—C9	114.8 (13)	C13—C12—C11	113.1 (15)
C8—N1—Cu01	106.5 (10)	N6—C13—C12	116.5 (18)
C8—N1—C9	109.5 (11)	C14—C13—N6	119.4 (19)
C9—N1—Cu01	112.9 (9)	C14—C13—C12	124.0 (18)
C2—N2—Cu01	109.9 (9)	C13—C14—C15	122 (2)
C2—N2—C3	113.9 (13)	C16—C15—C14	117 (2)
C3—N2—Cu01	102.3 (10)	C15—C16—C17	121 (2)
C4—N3—Cu01	109.0 (10)	N6—C17—C16	119 (2)
C4—N3—C5	114.9 (12)	O1A—S1A—O2A	107.6 (6)
C5—N3—Cu01	103.5 (9)	O3A—S1A—O1A	108.4 (6)
C6—N4—Cu01	106.5 (8)	O3A—S1A—O2A	112.3 (6)
C6—N4—C7	115.3 (13)	O3A—S1A—O4A	112.2 (6)
C7—N4—Cu01	102.6 (9)	O4A—S1A—O1A	107.8 (6)
C10—N5—C11	125.6 (15)	O4A—S1A—O2A	108.3 (7)
C17—N6—C13	121 (2)	S1A—O1A—Cu01	121.2 (6)
N1—C1—C2	109.2 (12)		

*Table 12: Crystallographic data for **MS2**:Cu*

Crystal data	
Chemical formula	$C_{17}H_{30}CuN_6O_5S\cdot 1.67(C_{0.75}O_{0.75})$
M_r	529.08
Crystal system, space group	Monoclinic, $P2_1/c$
Temperature (K)	150
a, b, c (Å)	12.906 (5), 16.760 (6), 11.940 (4)
β (°)	98.14 (3)
V (Å^3)	2556.7 (16)
Z	4
Radiation type	Mo $K\alpha$
μ (mm^{-1})	0.98
Crystal size (mm)	0.26 × 0.09 × 0.04
Data collection	
Diffractometer	Bruker *APEX*-II CCD
Absorption correction	Multi-scan *SADABS2014*/5 (Bruker,2014/5) was used for absorption correction. wR2(int) was 0.1444 before and 0.0650 after correction. The Ratio of minimum to maximum transmission is 0.6503. The λ/2 correction factor is 0.00150.
T_{min}, T_{max}	0.485, 0.746
No. of measured, independent and observed [$I > 2\sigma(I)$] reflections	14242, 5501, 1355
R_{int}	0.481
$(\sin\theta/\lambda)_{max}$ (Å^{-1})	0.640
Refinement	
$R[F^2 > 2\sigma(F^2)]$, $wR(F^2)$, S	0.128, 0.375, 0.94
No. of reflections	5501
No. of parameters	291
H-atom treatment	H-atom parameters constrained
$\Delta\rangle_{max}$, $\Delta\rangle_{min}$ (e Å^{-3})	0.92, -0.72

*Table 13: Experimental data for BCA assay of $A\beta_{40}$ treated with **MS1-4**.*

Sample	Absorbance at 540 nm	Concentration of soluble $A\beta_{40}$ (µg/ml)
Aβ40	0.829 ± 0.005	368 ± 6
Aβ40+Cu^{2+}	0.283 ± 0.02	95 ± 5
Aβ40+Cu^{2+} + **MS1**	0.706 ± 0.02	307 ± 9
Aβ40+Cu^{2+} + **MS2**	0.517 ± 0.01	212 ± 5
Aβ40+Cu^{2+} + **MS3**	0.524 ± 0.008	216 ± 4
Aβ40+Cu^{2+} + **MS4**	0.513 ± 0.006	210 ± 3

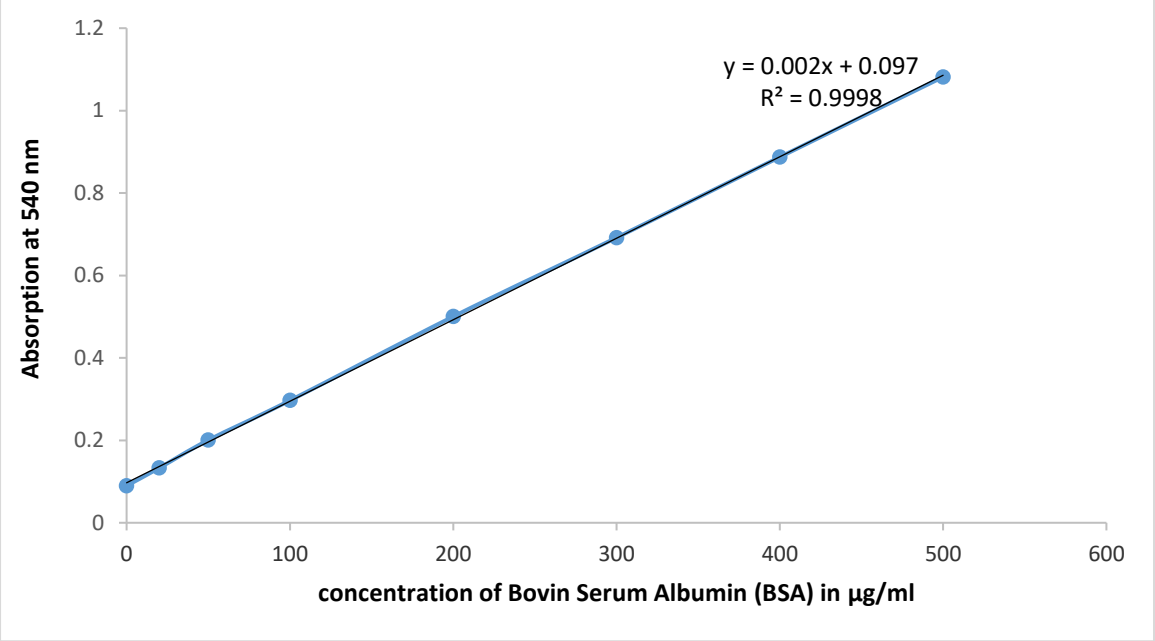

Figure 64: BCA assay standard curve

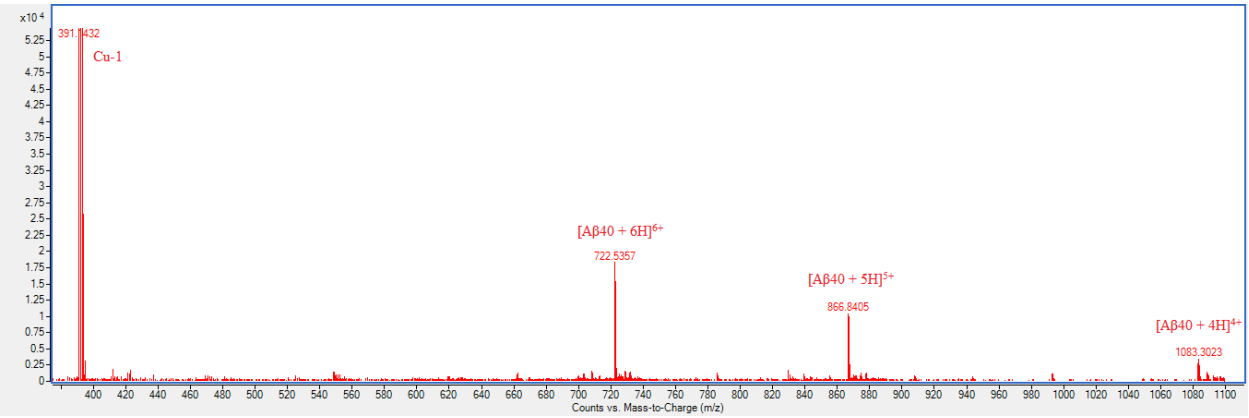

*Figure 65: Mass spectrum showing Aв$_{40}$ and **MS1**:Cu species.*

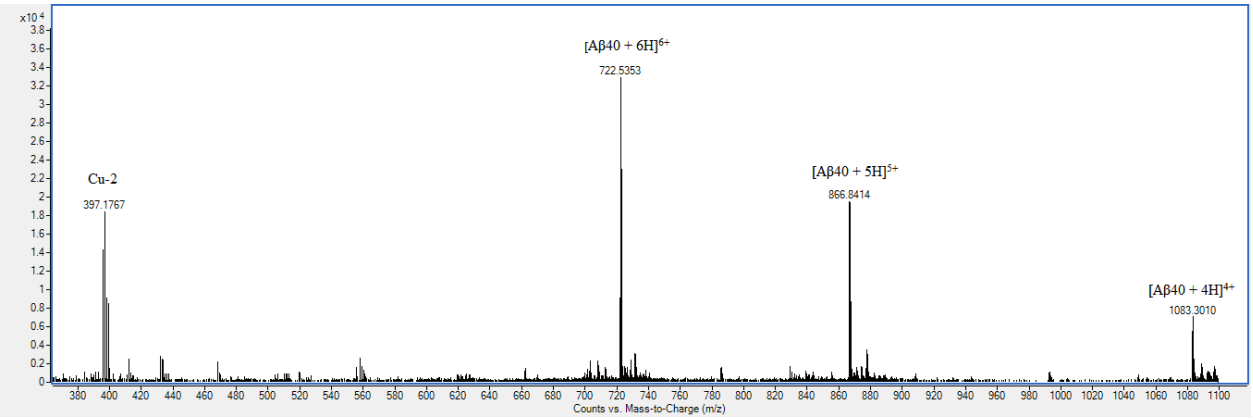

*Figure 66: Mass spectrum showing Aв$_{40}$ and **MS2**:Cu species.*

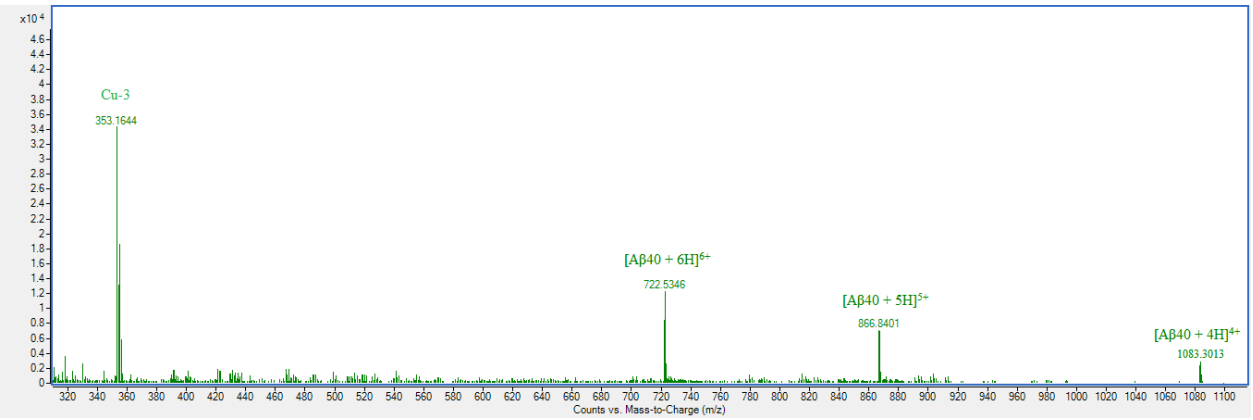

*Figure 67: Mass spectrum showing Aв$_{40}$ and **MS3**:Cu species.*

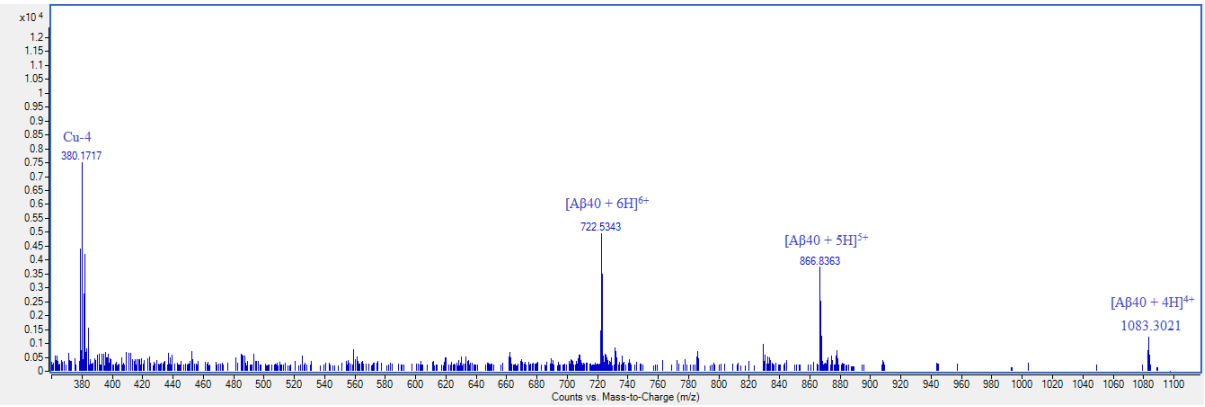

*Figure 68: Mass spectrum showing Aβ$_{40}$ and **MS4**:Cu species.*

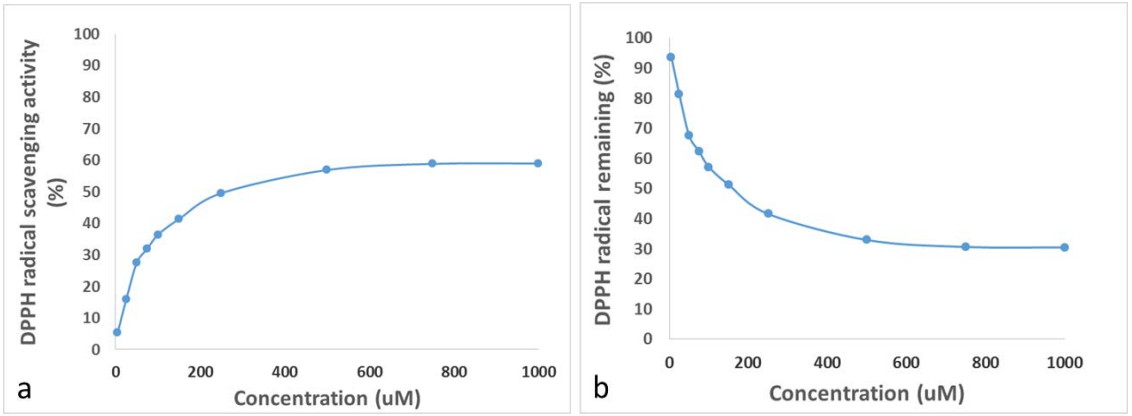

*Figure 69: (a) scavenging activity of DPPH radical by **MS1** (b) DPPH radical remaining in the solution by the reaction with **MS1**.*

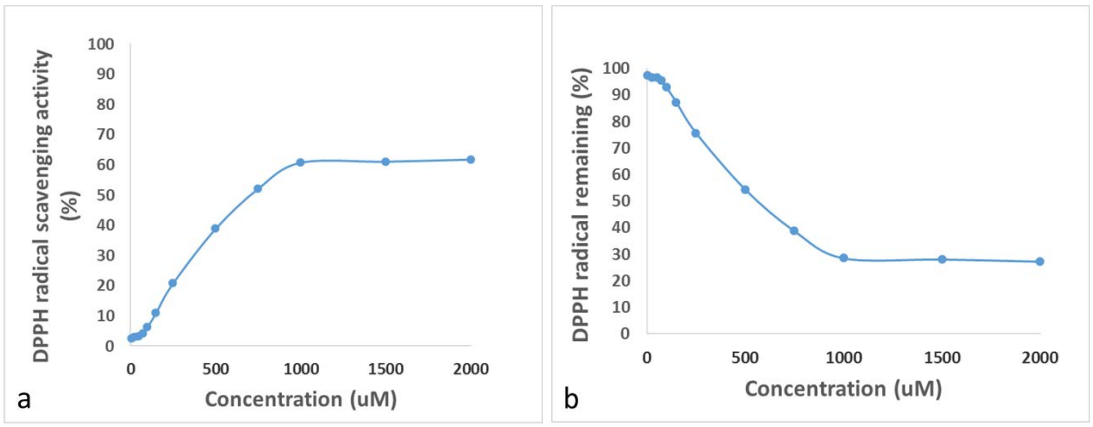

*Figure 70: (a) scavenging of DPPH radical by **MS2** (b) DPPH radical remaining in the solution by the reaction with **MS2**.*

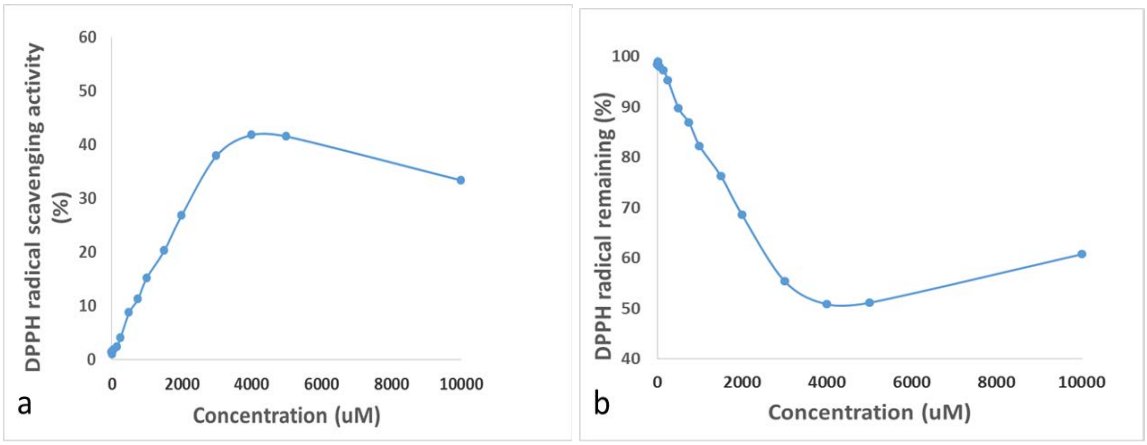

*Figure 71(a) scavenging activity of DPPH radical by **MS3** (b) DPPH radical remaining in the solution by the reaction with **MS3***

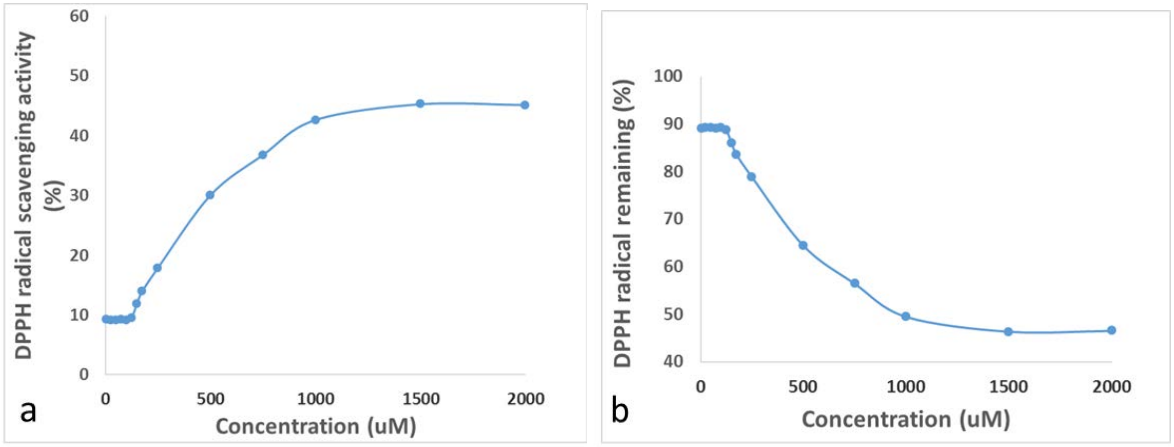

*Figure 72**:** (a) scavenging activity of DPPH radical by **MS4** (b) DPPH radical remaining in the solution by the reaction with **MS4**.*

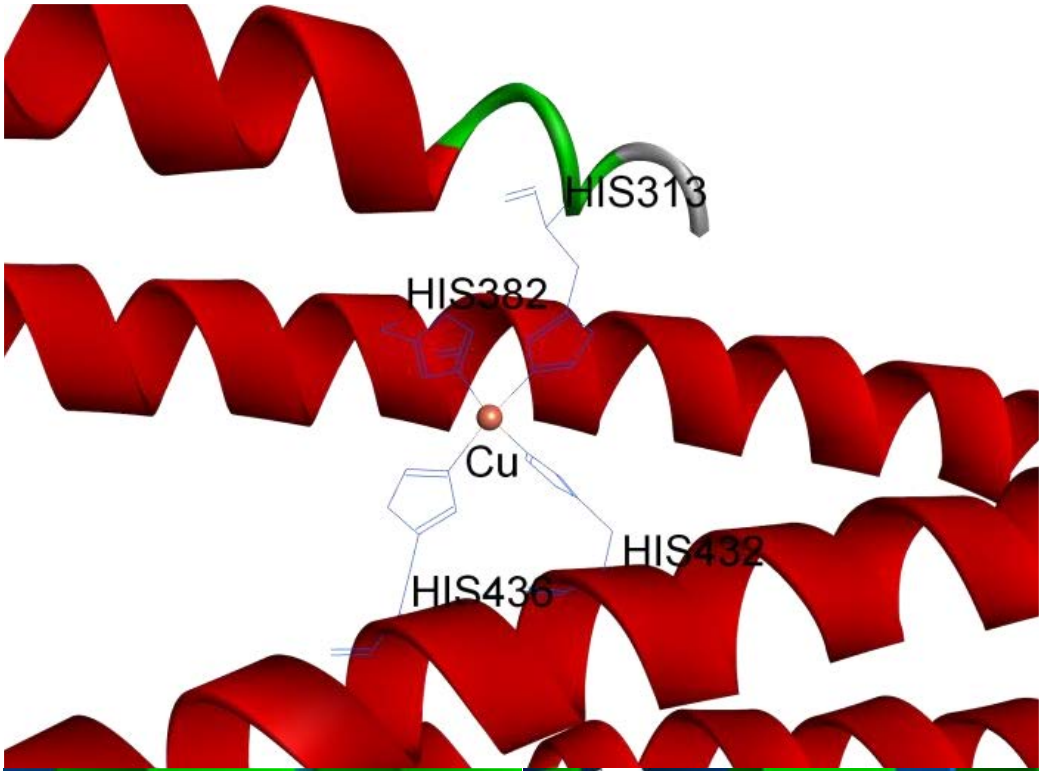

Figure 73: 3D modelling of the interaction of APP with Cu^{2+}.

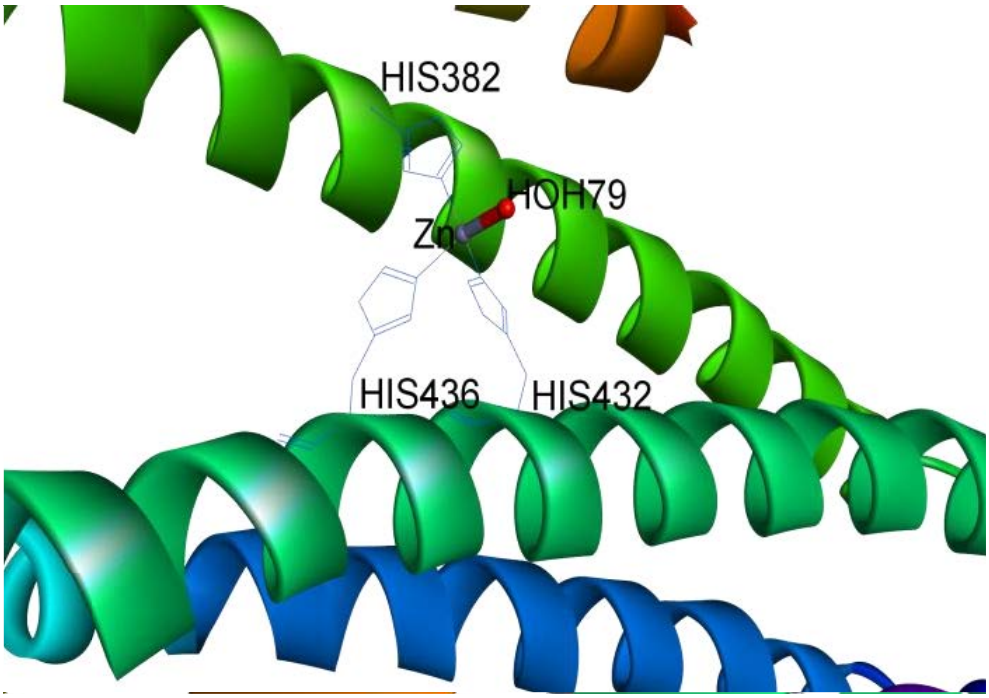

Figure 74: 3D modelling of the interaction of APP with Zn^{2+}.

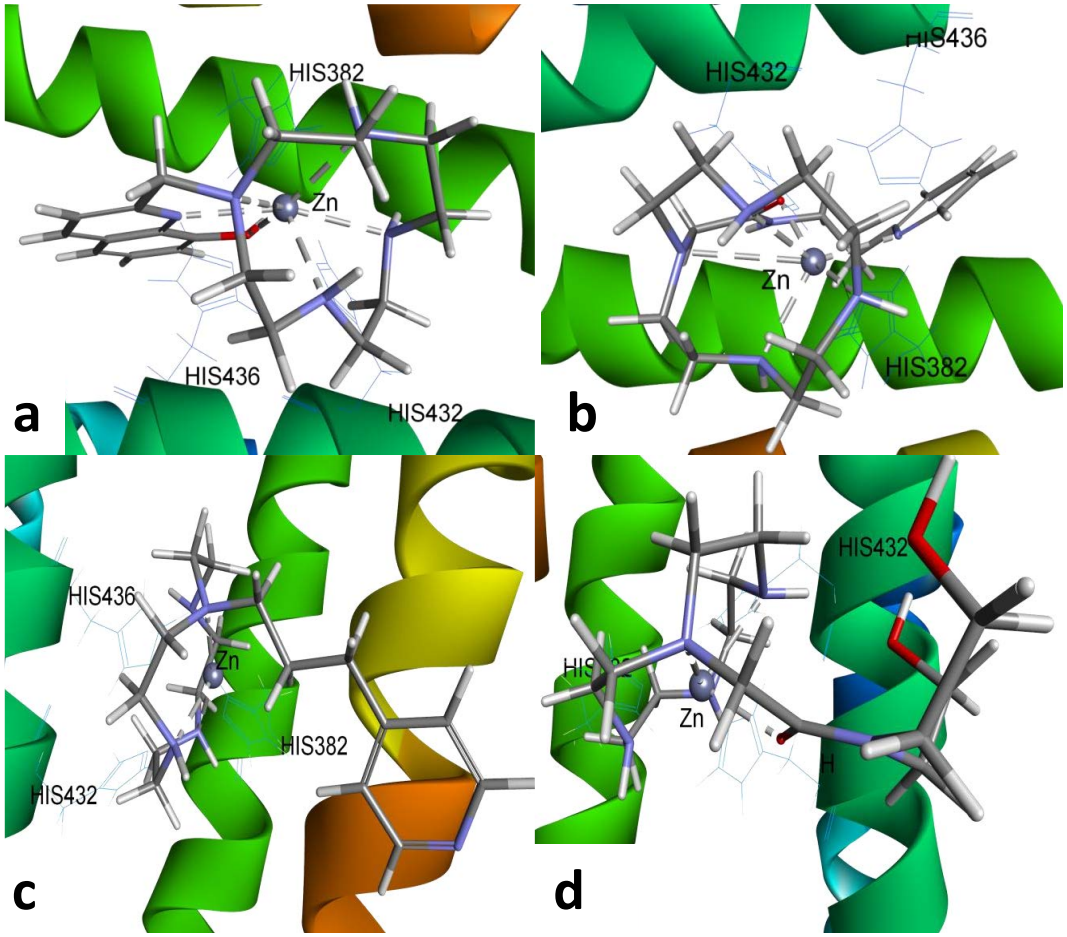

*Figure 75: 3D modelling of the interaction of APP with Zn^{2+} and **MS1** (a), **MS2** (b), **MS3**(c) and **MS4**(d).*

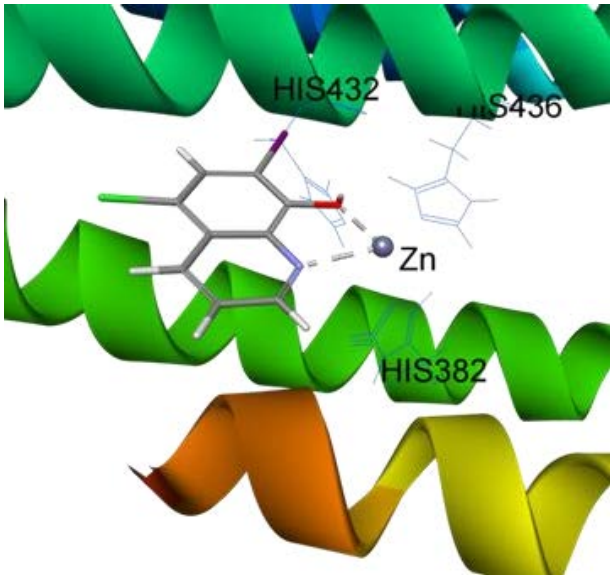

Figure 76: 3D modelling of the interaction of APP with Zn^{2+} and clioquinol

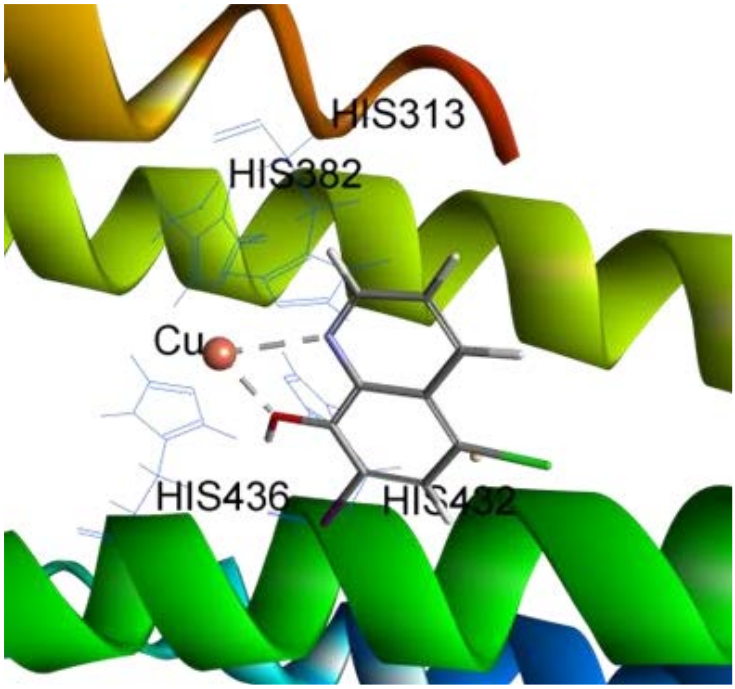

Figure 77: 3D modelling of the interaction of APP with Cu^{2+} and clioquinol

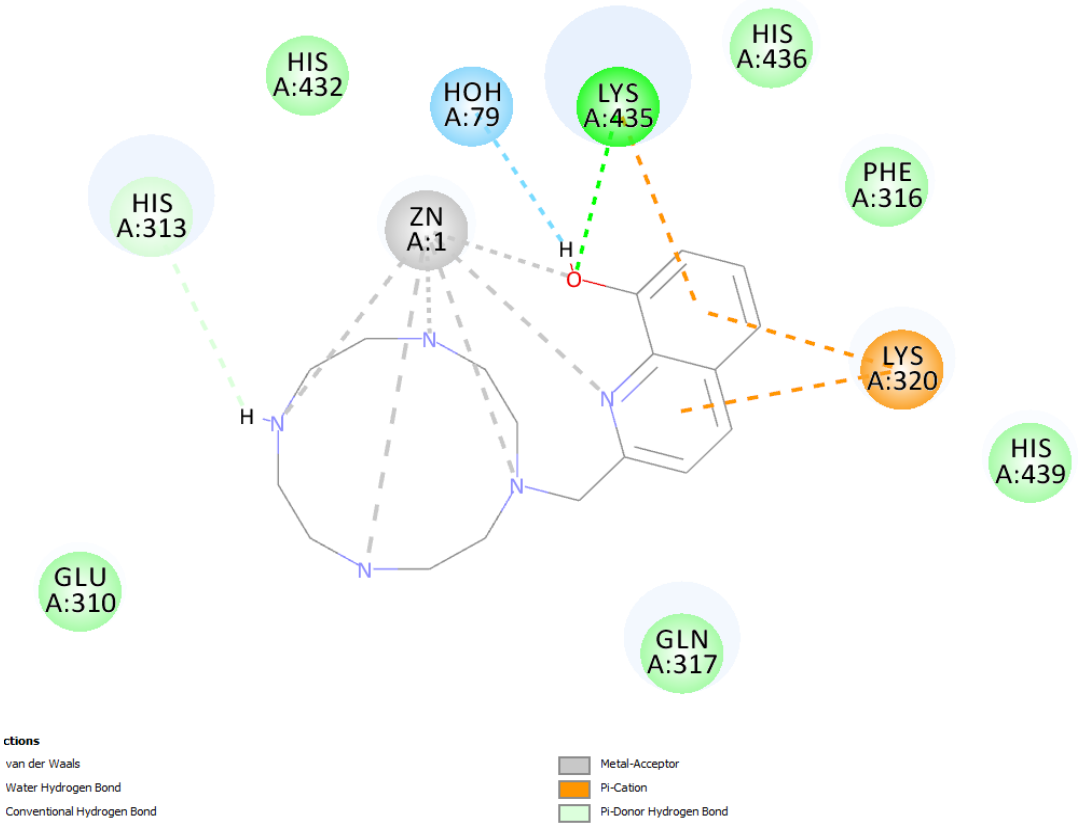

*Figure 78: : 2D modelling of the interaction of APP with Zn^{2+} and **MS1***

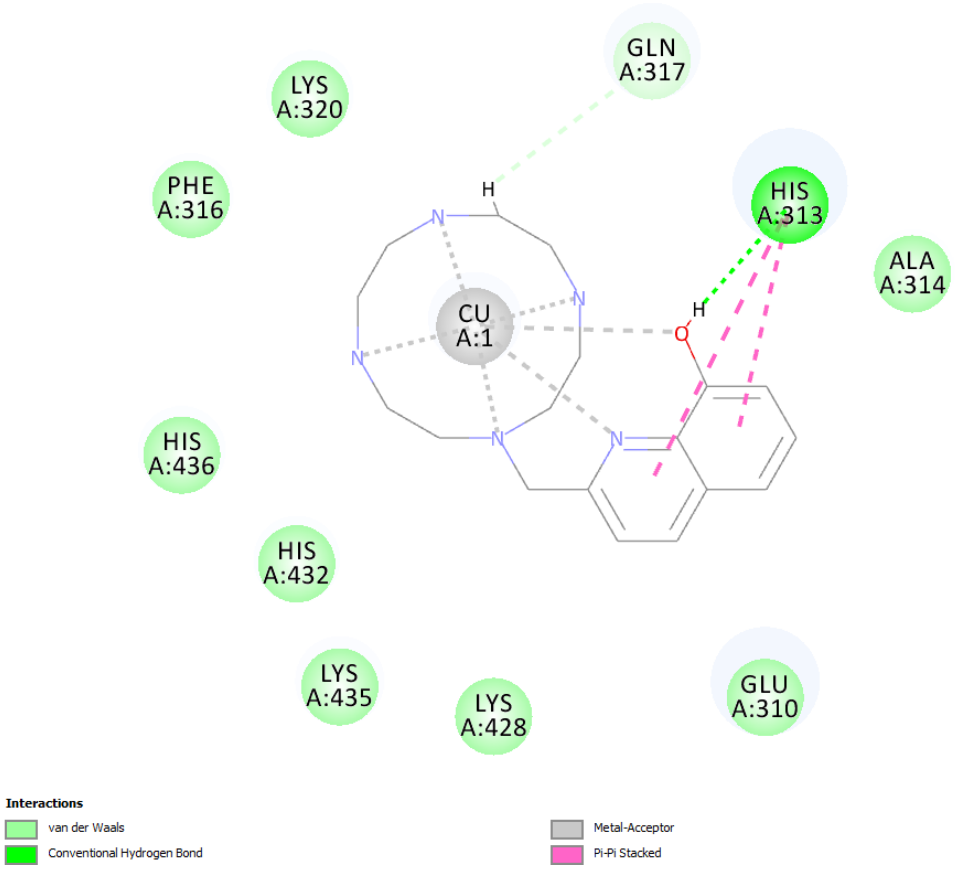

*Figure 79: 2D modelling of the interaction of APP with Cu^{2+} and **MS1***

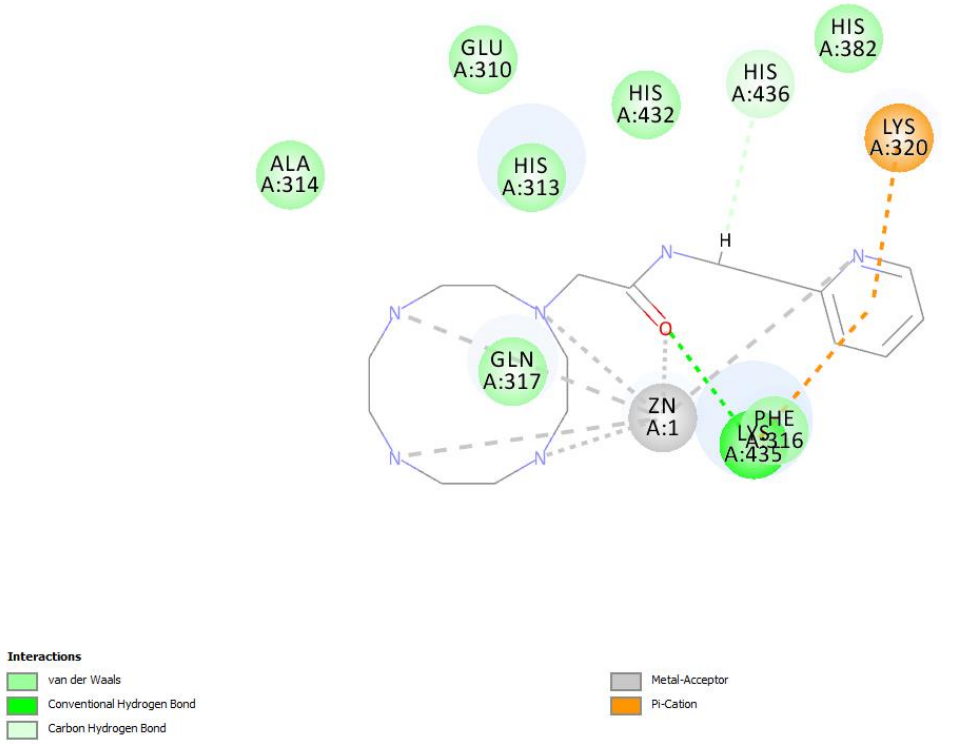

*Figure 80: 2D modelling of the interaction of APP with Zn^{2+} and **MS2***

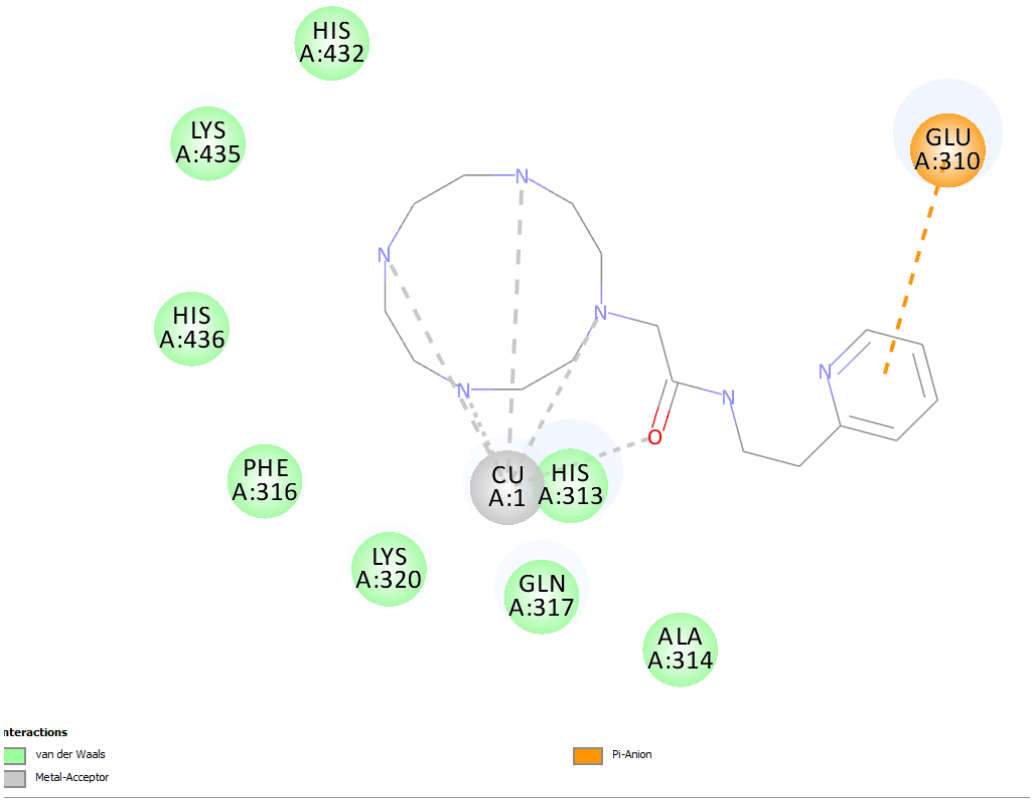

*Figure 81: 2D modelling of the interaction of APP with Cu^{2+} and **MS3***

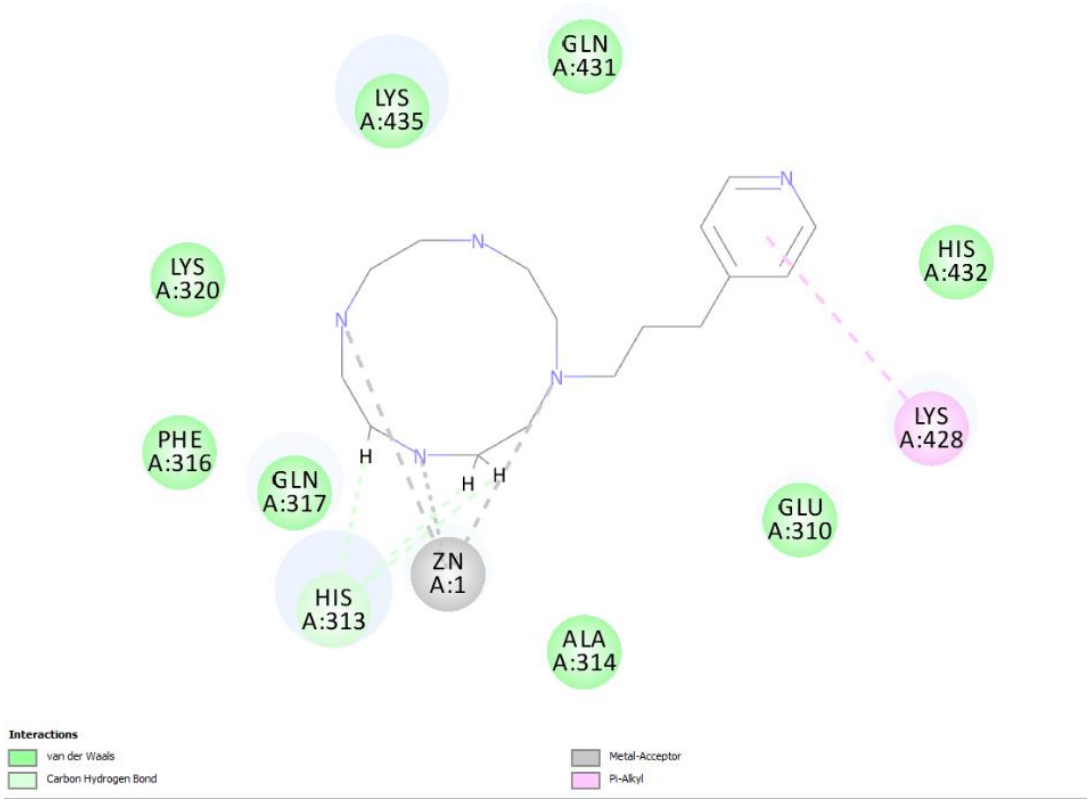

*Figure 82: 2D modelling of the interaction of APP with Zn^{2+} and **MS3***

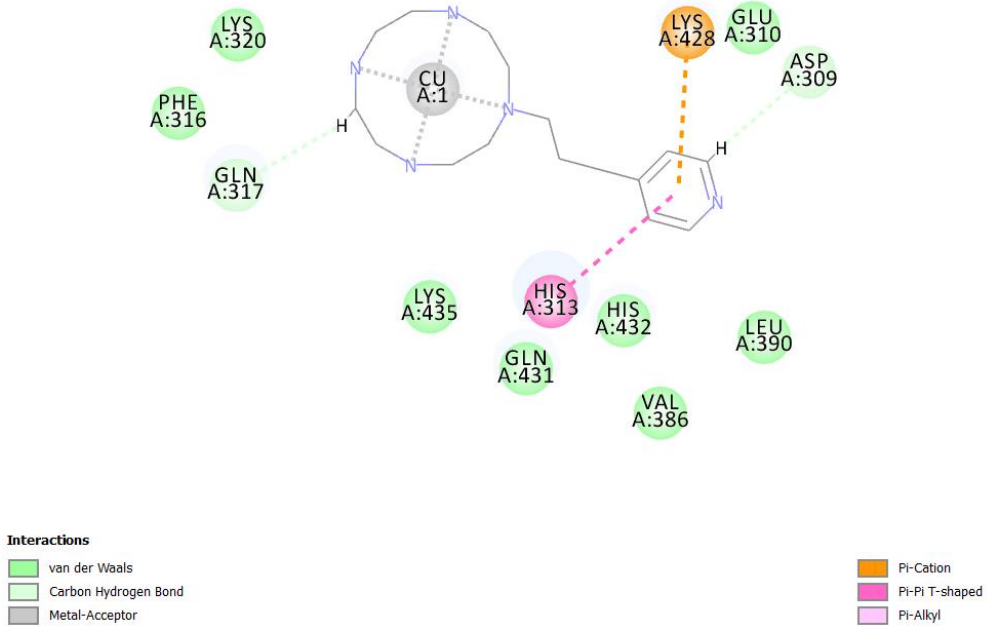

*Figure 83: 2D modelling of the interaction of APP with Cu^{2+} and **MS3***

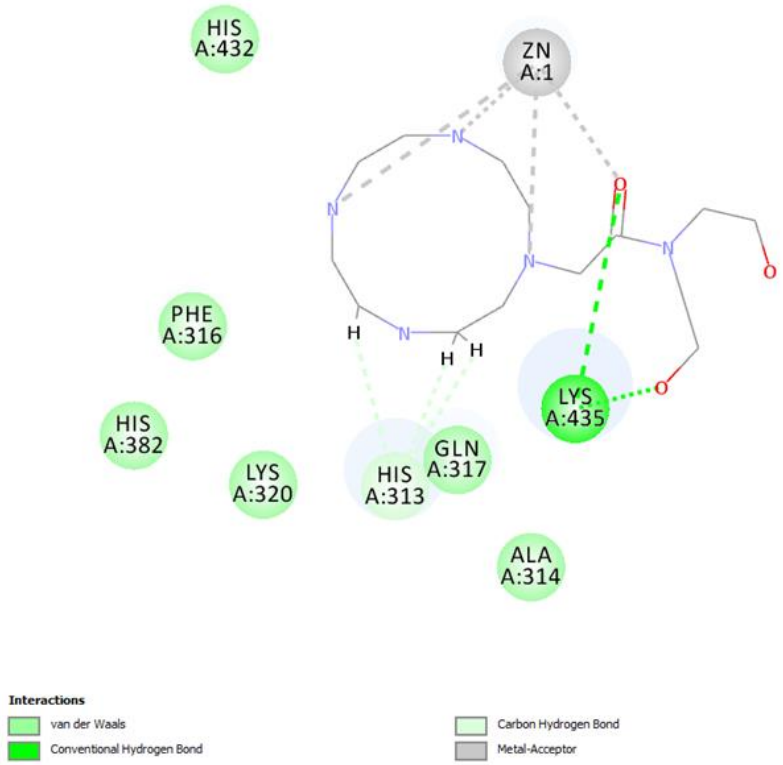

*Figure 84: 2D modelling of the interaction of APP with Zn^{2+} and **MS4***

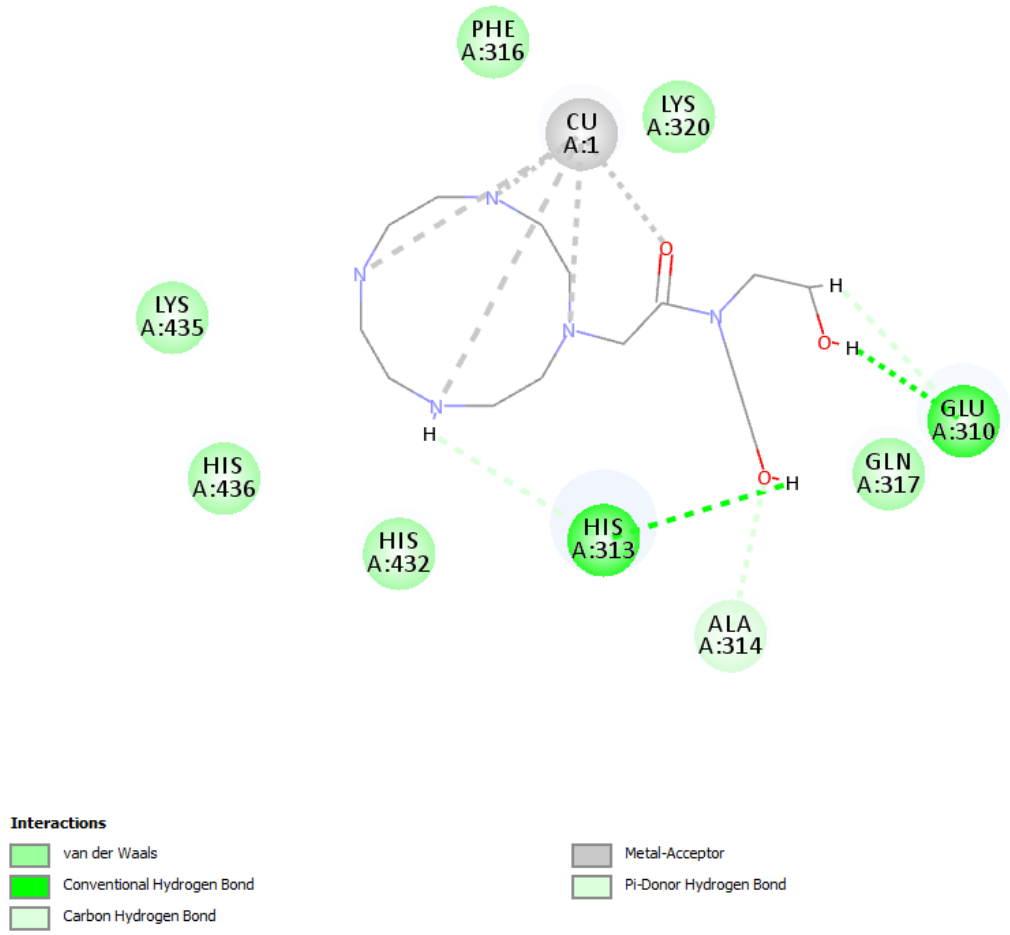

*Figure 85: 2D modelling of the interaction of APP with Cu^{2+} and **MS4***

Table 14: Selected calculated bond distances and CDOCKER energies for the interaction of ***MS1-4*** *with APP-bound metals*

Complex	CDOCKER energy (kcal/mol)		Distance (Å)
MS1:Zn	-65.23	Zn-N(cyclen)	2.26-2.72
		Zn-N(quinoline)	2.48
		Zn-O(quinoline)	2.26
MS1:Cu	-60.6157	Cu-N(cyclen):	2.34-2.45
		Cu-N(quinoline)	2.34
		Cu-O(quinoline):	2.51
MS2:Zn	-80.4224	Zn-N(cyclen)	2.36-3.12;
		Zn-O(carbonyl)	2.07
		Zn-N(pyridine)	2.37
MS2:Cu	-67.2698	Cu-N(cyclen)	2.37-2.5
		Cu-O(carbonyl)	2.26
MS3:Zn	-58.5742	Zn-N(cyclen)	2.12-2.22
MS3:Cu	-51.5976	Cu-N(cyclen)	2.32-2.44
MS4:Zn	-81.1692	Zn-N(cyclen)	2.11-2.28;
		Zn-O(carbonyl)	2.12
MS4:Cu	-65.534	Cu-N(cyclen)	2.34-2.49
		Cu-O(carbonyl)	2.29
Zn-Clioquinol	-26.5729	Zn-N	2.28
		Zn-O	2.27
Cu-Clioquinol	-21.8458	Cu-N	2.54
		Cu-O	2.29

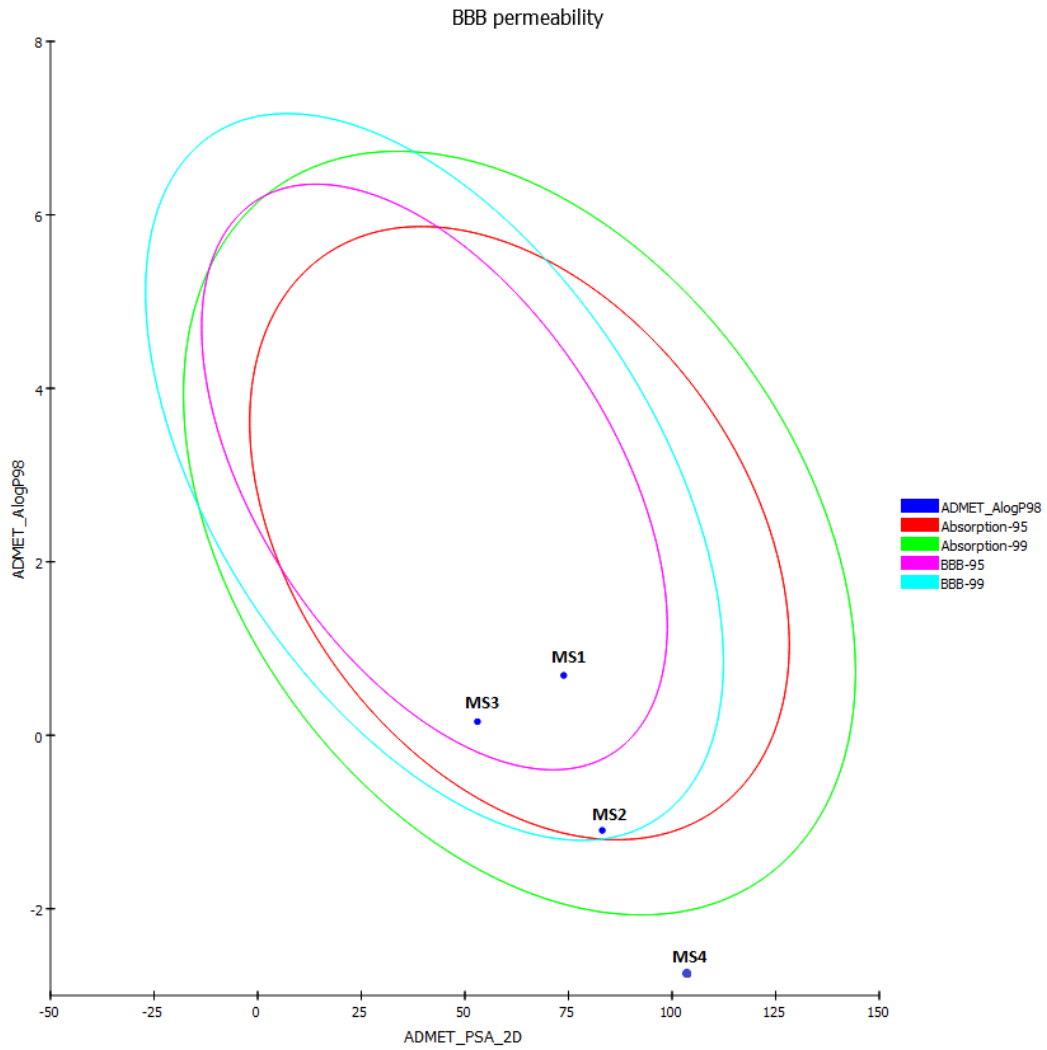

*Figure 86: Plot of PSA versus log P for **MS1-4** showing the 95% and 99% confidence limit ellipses corresponding to the blood–brain barrier and intestinal absorption models. The ellipses show the regions of well-absorbed compounds by BBB and intestinal membrane.*

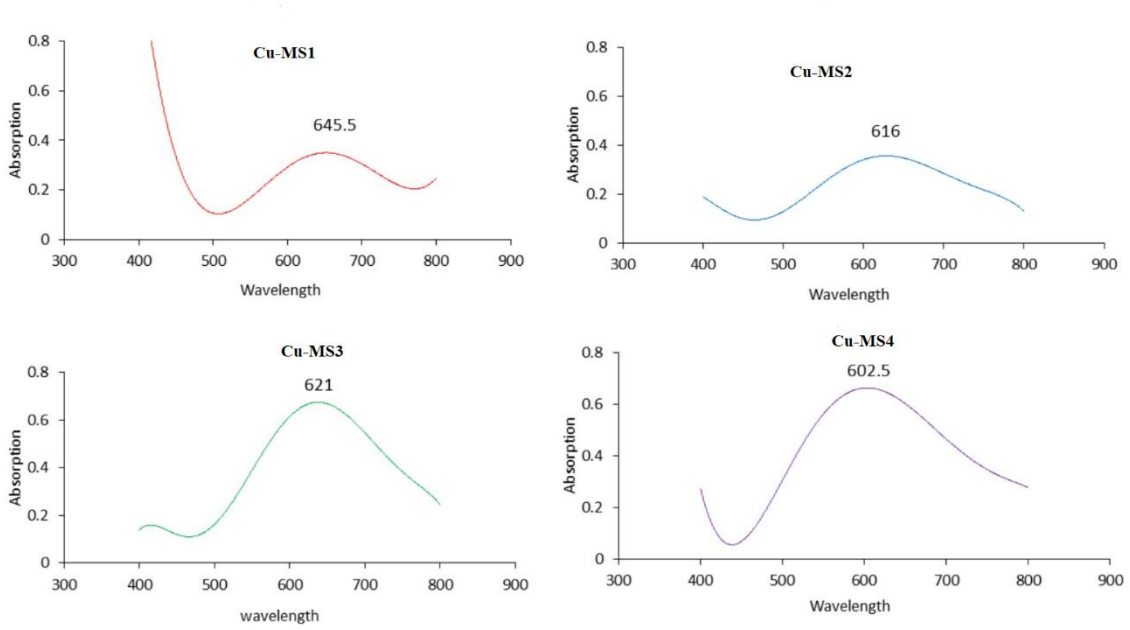

*Figure 87: UV-visible spectra for (**MS1-4):Cu** in the region 400 – 800 nm.*

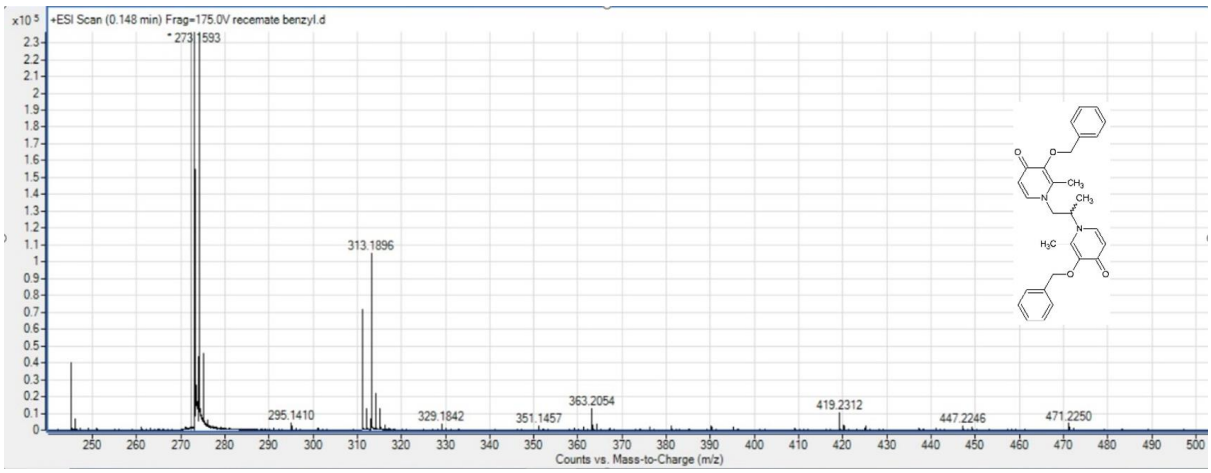

Figure 88: MS spectrum of by-products from the Preparation of 1-(2-aminopropyl)-3-(benzyloxy)-2-methylpyridin-4(1H)-one

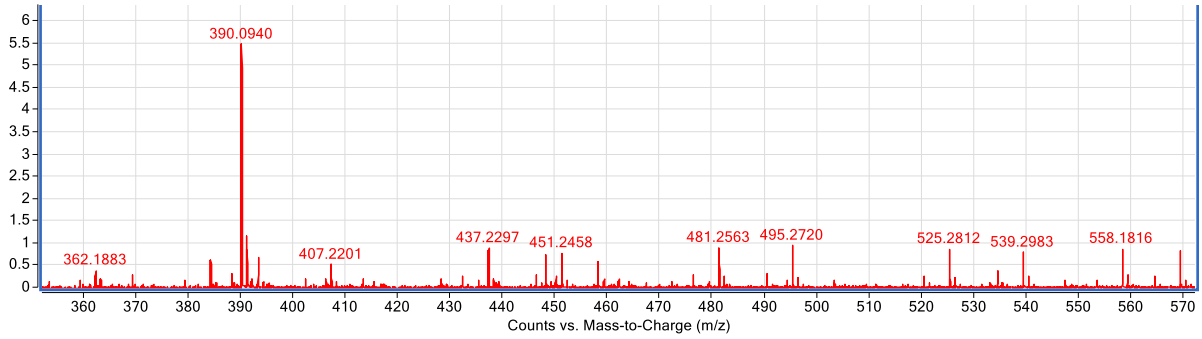

*Figure 89: mass spec. for **MS8**:Fe complex*

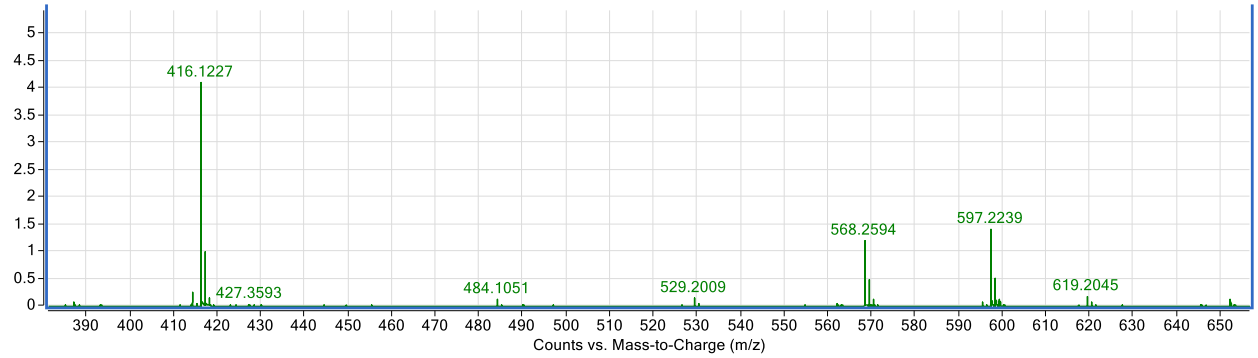

*Figure 90: Mass spec. for **MS9**:Fe complex*

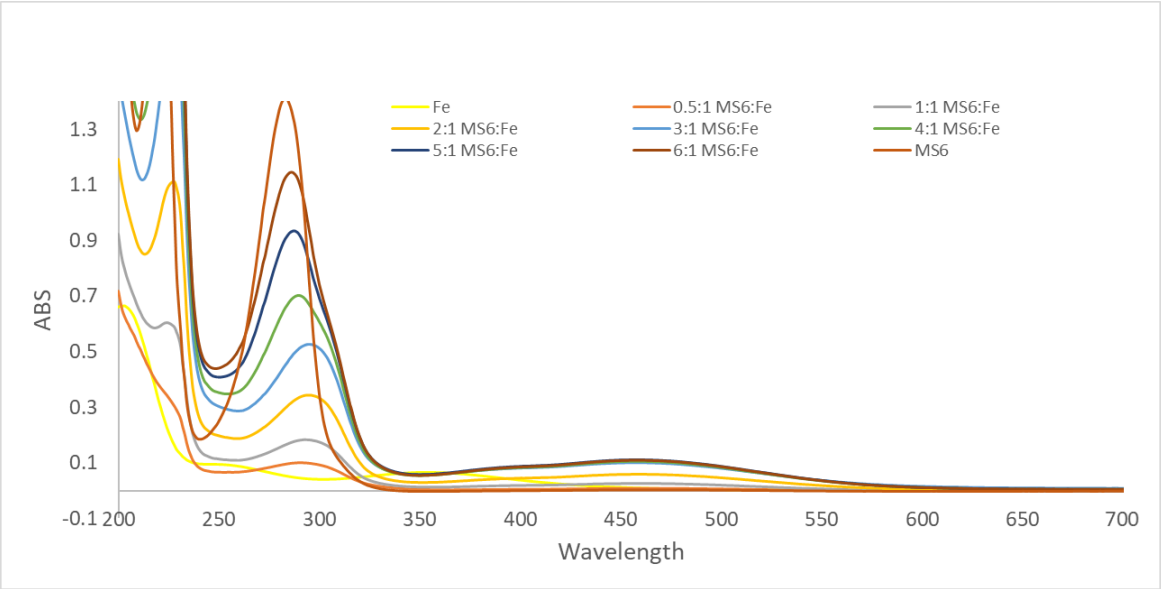

*Figure 91: UV-Vis for **MS6:**Fe complex in 10% MeOH in PBS with **MS6**:Fe ratio from 0.5:1 to 6:1*

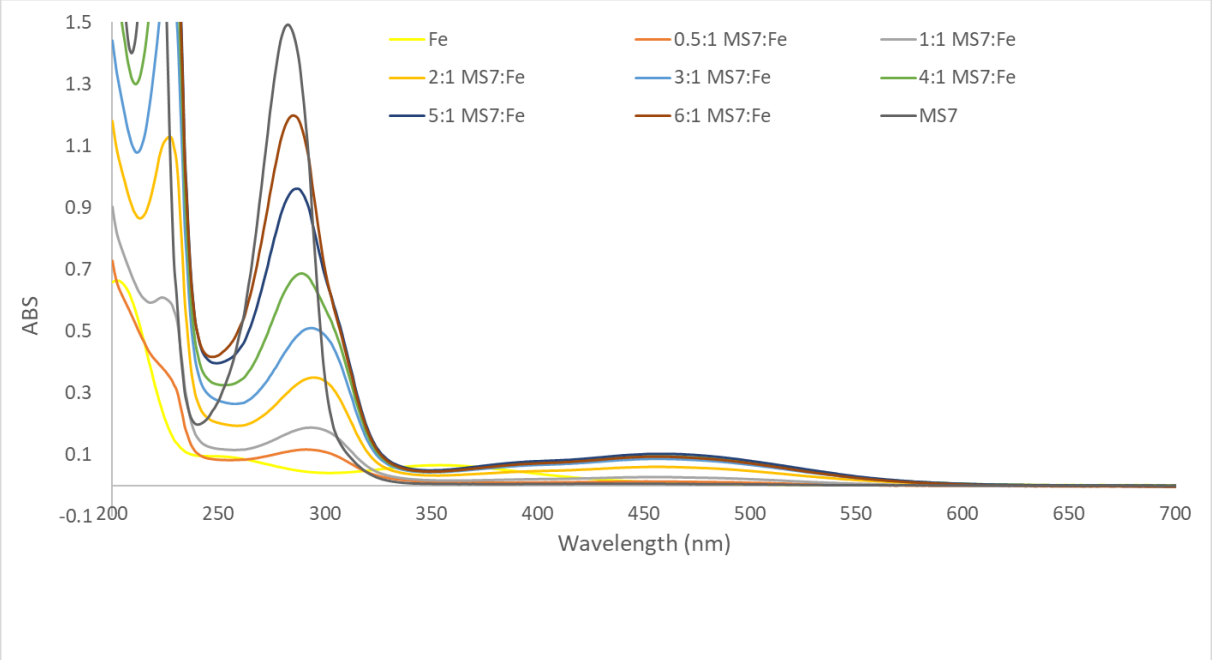

*Figure 92: UV-Vis for **MS7**:Fe complex in 10% MeOH in PBS with **MS7**:Fe ratio from 0.5:1 to 6:1*

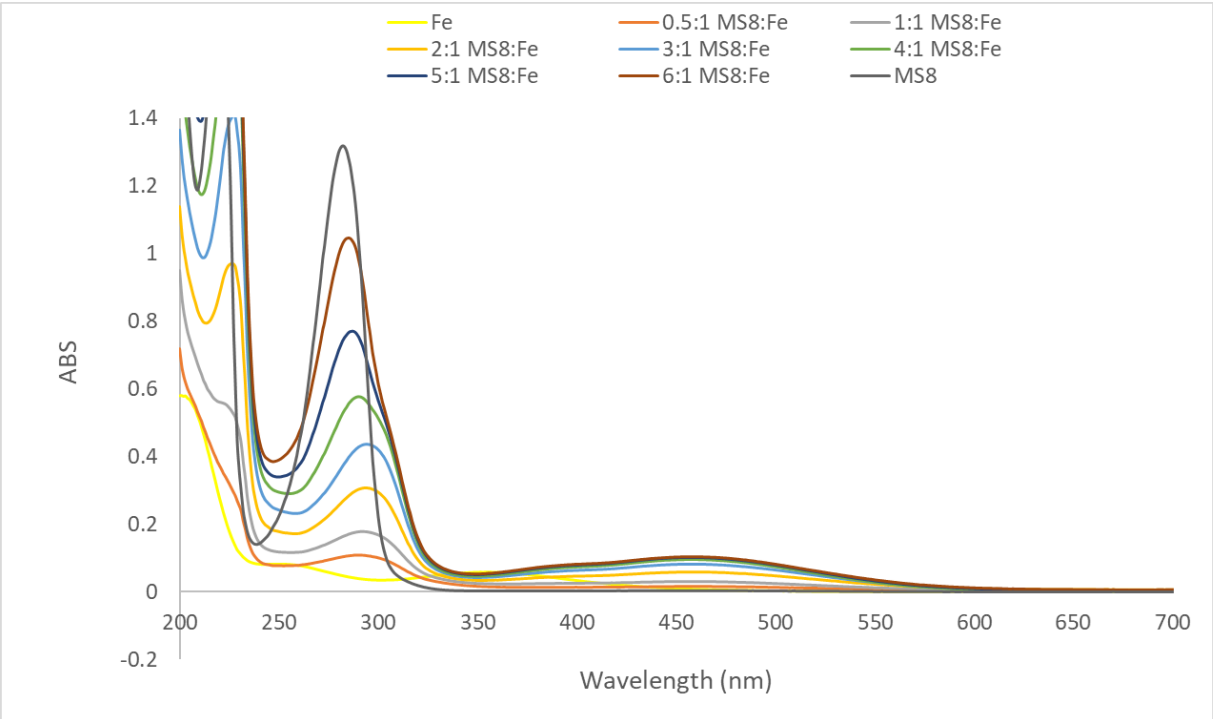

*Figure 93: UV-Vis for **MS8:**Fe complex in 10% MeOH in PBS with **MS8**:Fe ratio from 0.5:1 to 6:1*

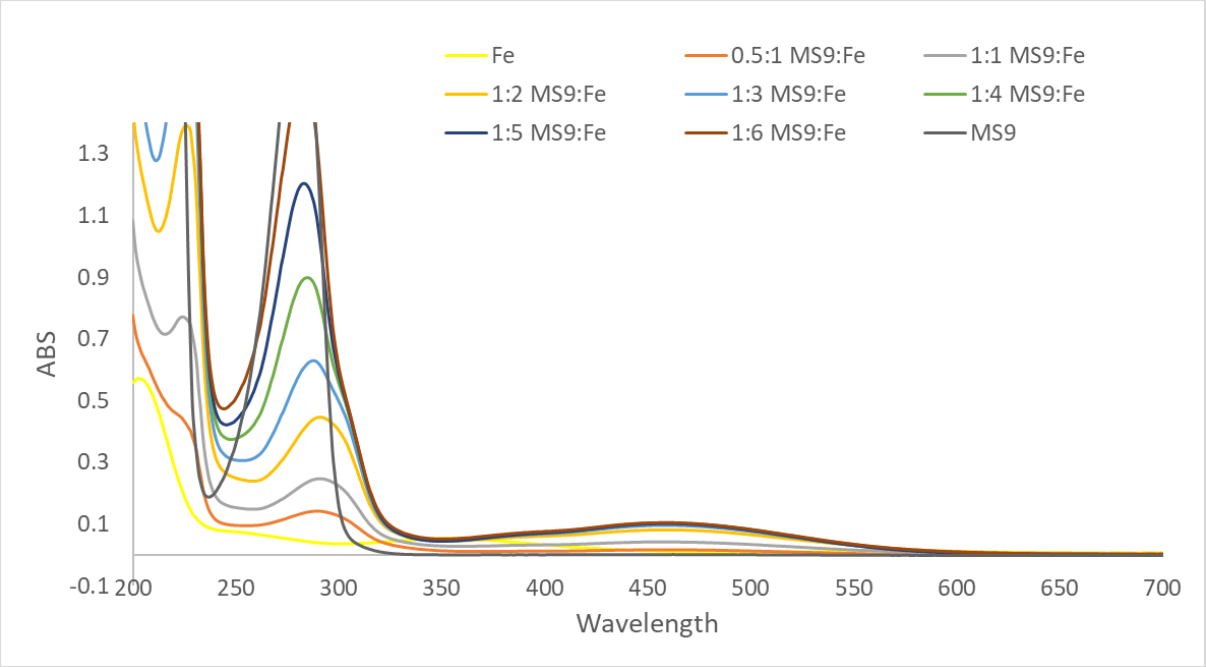

*Figure 94: UV-Vis for **MS9:**Fe complex in 10% MeOH in PBS with **MS9**:Fe ratio from 0.5:1 to 6:1*

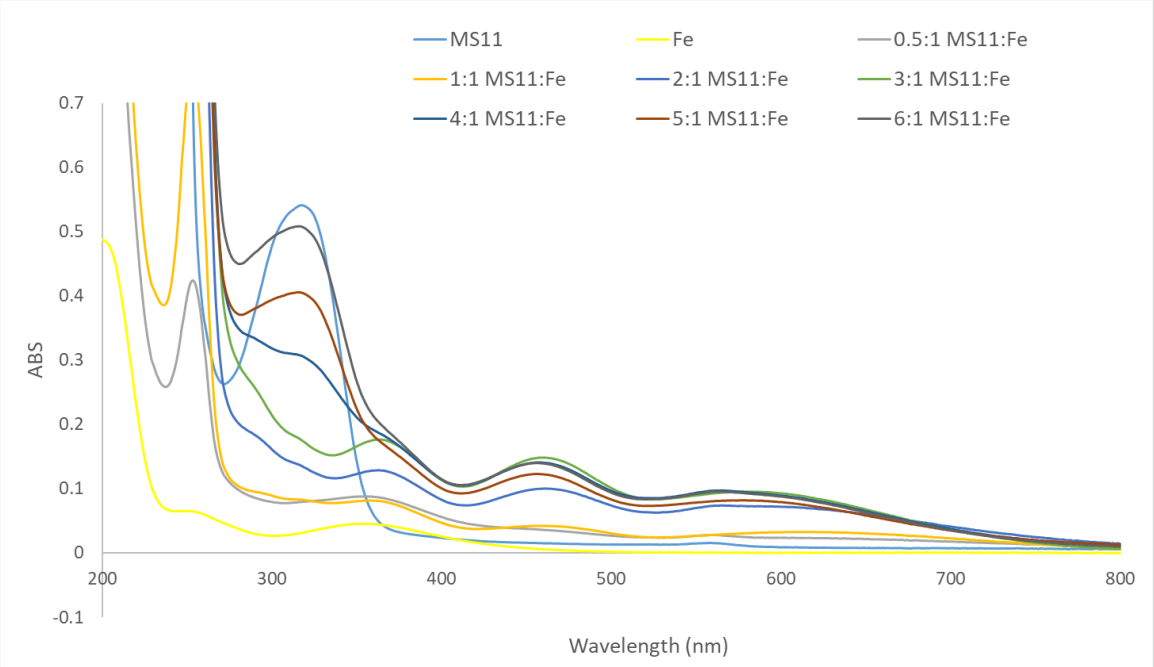

*Figure 95: UV-Vis for **MS11:**Fe complex in 10% MeOH in PBS with **MS11**:Fe ratio from 0.5:1 to 6:1*

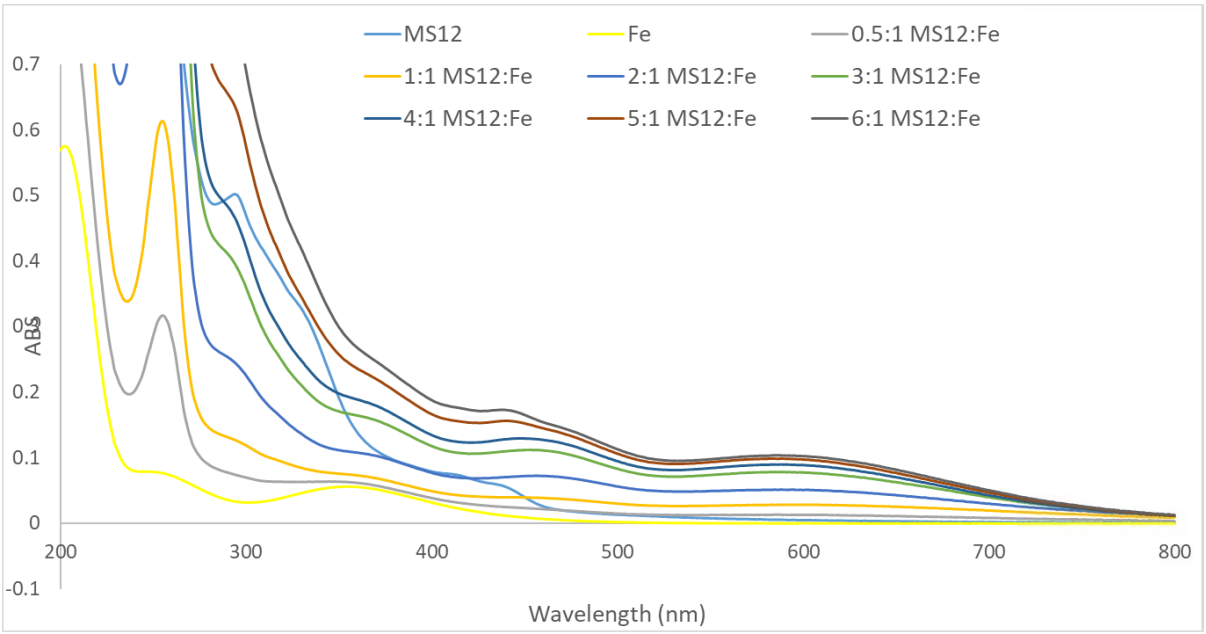

*Figure 96: UV-Vis for **MS12:**Fe complex in 10% MeOH in PBS with MS12:Fe ratio from 0.5:1 to 6:1*

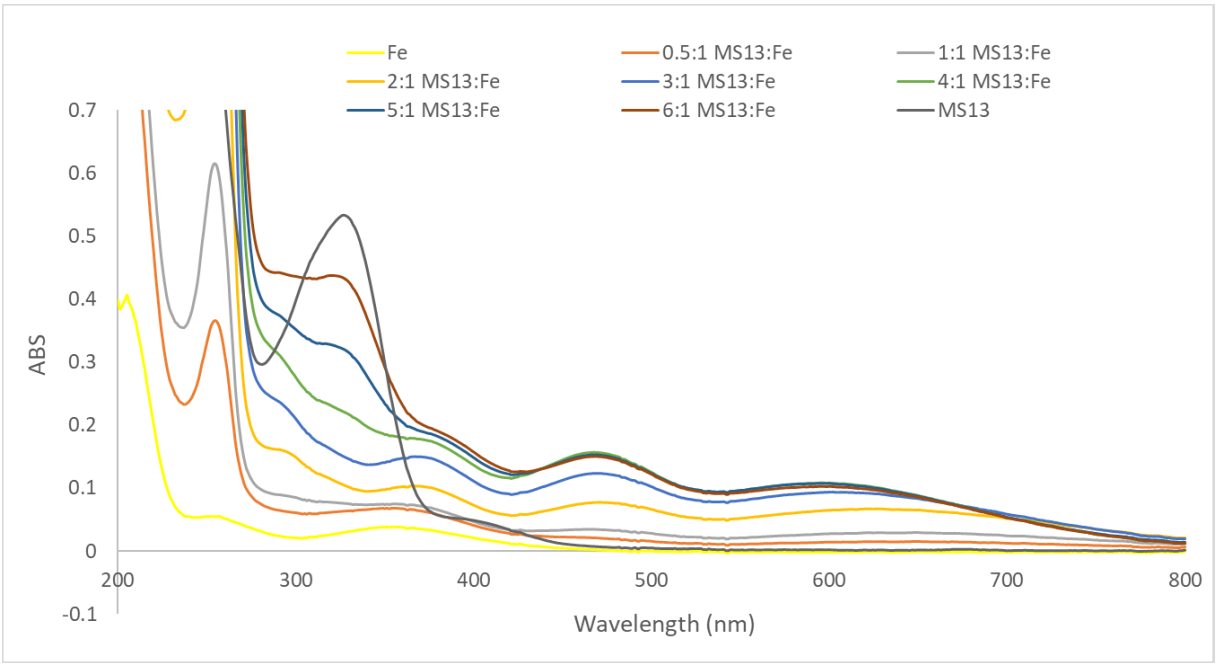

*Figure 97: UV-Vis for **MS13:**Fe complex in 10% MeOH in PBS with **MS13**:Fe ratio from 0.5:1 to 6:1*

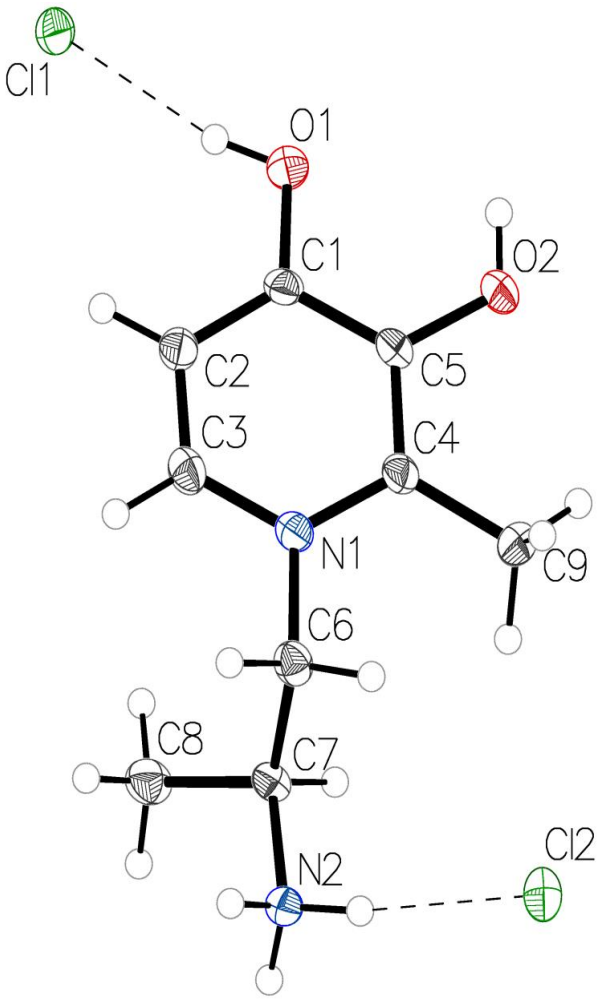

*Figure 98: ORTEP diagram for **MS7***

*Table 15: Crystallographic data for **MS7**.*

Crystal data	
Chemical formula	$2(Cl)\cdot C_9H_{16}N_2O_2$
M_r	255.14
Crystal system, space group	Monoclinic, $P2_1$
Temperature (K)	150
a, b, c (Å)	6.357 (9), 9.124 (12), 10.724 (17)
β (°)	96.25 (3)
V (Å^3)	618.3 (15)
Z	2
Radiation type	Mo $K\alpha$
μ (mm^{-1})	0.51
Crystal size (mm)	× ×
Data collection	
Diffractometer	Bruker *APEX*-II CCD
Absorption correction	Multi-scan *SADABS2016*/2 (Bruker,2016/2) was used for absorption correction. wR2(int) was 0.1196 before and 0.0645 after correction. The Ratio of minimum to maximum transmission is 0.7787. The λ/2 correction factor is Not present.
T_{min}, T_{max}	0.581, 0.746
No. of measured, independent and observed [$I > 2\sigma(I)$] reflections	12277, 2845, 2331
R_{int}	0.072
$(\sin \theta/\lambda)_{max}$ (Å^{-1})	0.651
Refinement	
$R[F^2 > 2\sigma(F^2)]$, $wR(F^2)$, S	0.035, 0.068, 1.02
No. of reflections	2845
No. of parameters	147
No. of restraints	1
H-atom treatment	H atoms treated by a mixture of independent and constrained refinement
$\Delta\rho_{max}$, $\Delta\rho_{min}$ (e Å^{-3})	0.26, −0.26
Absolute structure	Flack x determined using 922 quotients [(I+)-(I-)]/[(I+)+(I-)] (Parsons, Flack and Wagner, Acta Cryst. B69 (2013) 249-259).
Absolute structure parameter	0.03 (5)

*Table 16: Bond lengths and angles for **MS7**.*

O1—C1	1.350 (4)	C3—H3	0.9500
O1—H1	0.85 (5)	C4—C5	1.392 (4)
O2—C5	1.354 (4)	C4—C9	1.487 (5)
O2—H2	0.82 (5)	C6—H6A	0.9900
N1—C3	1.354 (4)	C6—H6B	0.9900
N1—C4	1.374 (4)	C6—C7	1.539 (5)
N1—C6	1.486 (4)	C7—H7	1.0000
N2—H2A	0.9100	C7—C8	1.514 (5)
N2—H2B	0.9100	C8—H8A	0.9800
N2—H2C	0.9100	C8—H8B	0.9800
N2—C7	1.499 (4)	C8—H8C	0.9800
C1—C2	1.388 (5)	C9—H9A	0.9800
C1—C5	1.393 (4)	C9—H9B	0.9800
C2—H2D	0.9500	C9—H9C	0.9800
C2—C3	1.370 (5)		
C1—O1—H1	108 (3)	C4—C5—C1	120.7 (3)
C5—O2—H2	118 (4)	N1—C6—H6A	109.0
C3—N1—C4	121.5 (3)	N1—C6—H6B	109.0
C3—N1—C6	117.3 (3)	N1—C6—C7	112.9 (3)
C4—N1—C6	121.1 (3)	H6A—C6—H6B	107.8
H2A—N2—H2B	109.5	C7—C6—H6A	109.0
H2A—N2—H2C	109.5	C7—C6—H6B	109.0
H2B—N2—H2C	109.5	N2—C7—C6	105.8 (3)
C7—N2—H2A	109.5	N2—C7—H7	109.2
C7—N2—H2B	109.5	N2—C7—C8	109.1 (3)
C7—N2—H2C	109.5	C6—C7—H7	109.2
O1—C1—C2	124.2 (3)	C8—C7—C6	114.3 (3)
O1—C1—C5	115.9 (3)	C8—C7—H7	109.2
C2—C1—C5	119.8 (3)	C7—C8—H8A	109.5
C1—C2—H2D	120.8	C7—C8—H8B	109.5
C3—C2—C1	118.3 (3)	C7—C8—H8C	109.5
C3—C2—H2D	120.8	H8A—C8—H8B	109.5
N1—C3—C2	121.8 (3)	H8A—C8—H8C	109.5
N1—C3—H3	119.1	H8B—C8—H8C	109.5
C2—C3—H3	119.1	C4—C9—H9A	109.5
N1—C4—C5	117.8 (3)	C4—C9—H9B	109.5
N1—C4—C9	120.8 (3)	C4—C9—H9C	109.5

C5—C4—C9	121.4 (3)	H9A—C9—H9B	109.5
O2—C5—C1	122.3 (3)	H9A—C9—H9C	109.5
O2—C5—C4	117.0 (3)	H9B—C9—H9C	109.5
O1—C1—C2—C3	179.2 (3)	C3—N1—C4—C9	-178.1 (3)
O1—C1—C5—O2	0.6 (5)	C3—N1—C6—C7	85.2 (3)
O1—C1—C5—C4	-177.5 (3)	C4—N1—C3—C2	0.6 (4)
N1—C4—C5—O2	179.4 (3)	C4—N1—C6—C7	-95.4 (4)
N1—C4—C5—C1	-2.4 (4)	C5—C1—C2—C3	-0.1 (4)
N1—C6—C7—N2	175.1 (2)	C6—N1—C3—C2	180.0 (3)
N1—C6—C7—C8	-64.9 (4)	C6—N1—C4—C5	-178.2 (3)
C1—C2—C3—N1	-1.1 (4)	C6—N1—C4—C9	2.6 (4)
C2—C1—C5—O2	180.0 (3)	C9—C4—C5—O2	-1.3 (4)
C2—C1—C5—C4	1.9 (5)	C9—C4—C5—C1	176.9 (3)
C3—N1—C4—C5	1.2 (4)		

*Table 17: Selected hydrogen-bond parameters for **MS7**; Symmetry code(s): (i) -x+2, y-1/2, -z; (ii) -x+1, y-1/2, -z+1; (iii) x, y-1, z; (iv) x+1, y, z; (v) -x, y+1/2, -z+1.*

D—H···*A*	*D*—H (Å)	H···*A* (Å)	*D*···*A* (Å)	*D*—H···*A* (°)
N2—H2A···Cl2^{i}	0.91	2.19	3.096 (4)	172.2
N2—H2B···Cl1^{ii}	0.91	2.31	3.205 (5)	170.0
N2—H2C···Cl2	0.91	2.18	3.082 (4)	172.7
C8—H8C···O2^{iii}	0.98	3.00	3.400 (6)	106.1
C9—H9A···O1^{iv}	0.98	2.62	3.502 (6)	150.1
C9—H9B···O2	0.98	2.36	2.782 (5)	105.4
O2—H2···Cl1^{v}	0.82 (5)	2.31 (5)	3.109 (4)	165 (5)
O2—H2···O1	0.82 (5)	2.42 (5)	2.707 (4)	102 (4)
O1—H1···Cl1	0.85 (5)	2.09 (5)	2.935 (4)	169 (4)

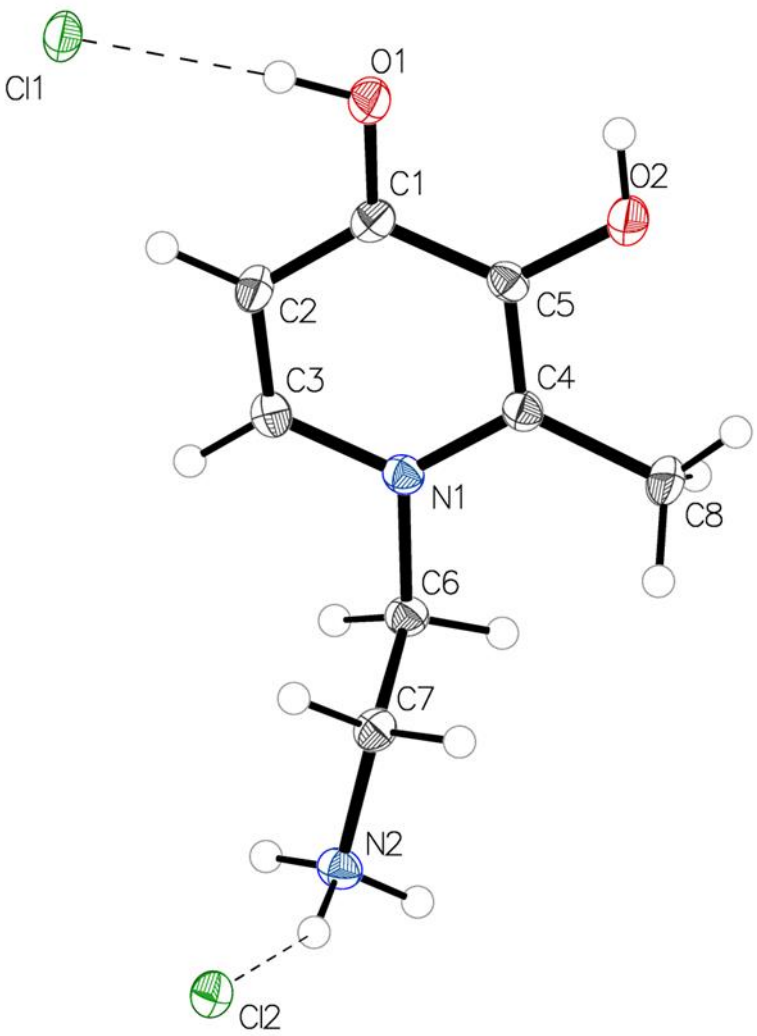

*Figure 99: ORTEP diagram **MS8***

*Table 18: Crystallographic data for **MS8**.*

Crystal data	
Chemical formula	$2(Cl)\cdot C_8H_{14}N_2O_2$
M_r	241.11
Crystal system, space group	Monoclinic, $P2_1/n$
Temperature (K)	150
a, b, c (Å)	4.5926 (6), 14.7686 (18), 15.2875 (19)
β (°)	92.698 (4)
V (Å^3)	1035.7 (2)
Z	4
Radiation type	Mo $K\alpha$
μ (mm^{-1})	0.60
Crystal size (mm)	× ×
Data collection	
Diffractometer	Bruker *APEX*-II CCD
Absorption correction	Multi-scan *SADABS2016*/2 (Bruker,2016/2) was used for absorption correction. wR2 (int() was 0.1417 before and 0.0922 after correction. The Ratio of minimum to maximum transmission is 0.6552. The λ/2 correction factor is Not present.
T_{min}, T_{max}	0.489, 0.746
No. of measured, independent and observed [$I > 2\sigma(I)$] reflections	17507, 2378, 1888
R_{int}	0.093
$(\sin \theta/\lambda)_{max}$ (Å^{-1})	0.651
Refinement	
$R[F^2 > 2\sigma(F^2)]$, $wR(F^2)$, S	0.040, 0.085, 1.06
No. of reflections	2378
No. of parameters	137
H-atom treatment	H atoms treated by a mixture of independent and constrained refinement
$\Delta\rho_{max}$, $\Delta\rho_{min}$ (e Å^{-3})	0.31, −0.33

*Table 19: Bond lengths and angles for **MS8**.*

O1—C1	1.324 (3)	C2—H2D	0.9500
O1—H1	0.89 (3)	C2—C3	1.357 (3)
O2—C5	1.357 (3)	C3—H3	0.9500
O2—H2	0.87 (4)	C4—C5	1.385 (3)
N1—C3	1.365 (3)	C4—C8	1.494 (3)
N1—C4	1.361 (3)	C6—H6A	0.9900
N1—C6	1.477 (3)	C6—H6B	0.9900
N2—H2A	0.9100	C6—C7	1.523 (3)
N2—H2B	0.9100	C7—H7A	0.9900
N2—H2C	0.9100	C7—H7B	0.9900
N2—C7	1.479 (3)	C8—H8A	0.9800
C1—C2	1.387 (3)	C8—H8B	0.9800
C1—C5	1.397 (3)	C8—H8C	0.9800
C1—O1—H1	110 (2)	C5—C4—C8	121.5 (2)
C5—O2—H2	116 (3)	O2—C5—C1	121.7 (2)
C3—N1—C6	116.03 (18)	O2—C5—C4	117.55 (19)
C4—N1—C3	121.36 (19)	C4—C5—C1	120.7 (2)
C4—N1—C6	122.47 (18)	N1—C6—H6A	109.9
H2A—N2—H2B	109.5	N1—C6—H6B	109.9
H2A—N2—H2C	109.5	N1—C6—C7	108.70 (17)
H2B—N2—H2C	109.5	H6A—C6—H6B	108.3
C7—N2—H2A	109.5	C7—C6—H6A	109.9
C7—N2—H2B	109.5	C7—C6—H6B	109.9
C7—N2—H2C	109.5	N2—C7—C6	111.27 (17)
O1—C1—C2	125.0 (2)	N2—C7—H7A	109.4
O1—C1—C5	116.2 (2)	N2—C7—H7B	109.4
C2—C1—C5	118.8 (2)	C6—C7—H7A	109.4
C1—C2—H2D	120.2	C6—C7—H7B	109.4
C3—C2—C1	119.6 (2)	H7A—C7—H7B	108.0
C3—C2—H2D	120.2	C4—C8—H8A	109.5
N1—C3—H3	119.5	C4—C8—H8B	109.5
C2—C3—N1	121.0 (2)	C4—C8—H8C	109.5
C2—C3—H3	119.5	H8A—C8—H8B	109.5
N1—C4—C5	118.47 (19)	H8A—C8—H8C	109.5
N1—C4—C8	120.0 (2)	H8B—C8—H8C	109.5
O1—C1—C2—C3	-177.9 (2)	C3—N1—C4—C8	178.8 (2)

O1—C1—C5—O2	-0.1 (3)	C3—N1—C6—C7	-82.9 (2)
O1—C1—C5—C4	177.0 (2)	C4—N1—C3—C2	-0.2 (3)
N1—C4—C5—O2	179.29 (18)	C4—N1—C6—C7	92.9 (2)
N1—C4—C5—C1	2.1 (3)	C5—C1—C2—C3	1.7 (3)
N1—C6—C7—N2	165.16 (16)	C6—N1—C3—C2	175.6 (2)
C1—C2—C3—N1	-0.3 (3)	C6—N1—C4—C5	-176.24 (19)
C2—C1—C5—O2	-179.7 (2)	C6—N1—C4—C8	3.2 (3)
C2—C1—C5—C4	-2.6 (3)	C8—C4—C5—O2	-0.1 (3)
C3—N1—C4—C5	-0.6 (3)	C8—C4—C5—C1	-177.4 (2)

*Table 20: Selected hydrogen-bond parameters for **MS8**; Symmetry code(s): (i) x+1, y, z; (ii)-x+2, -y+1, -z+1; (iii) x+1/2, -y+3/2, z+1/2; (iv) -x+3/2, y+1/2, -z+1/2; (v) -x, -y+1, -z.*

D—H···*A*	*D*—H (Å)	H···*A* (Å)	*D*···*A* (Å)	*D*—H···*A* (°)
N2—H2A···Cl2^{i}	0.91	2.75	3.2886 (19)	119.2
N2—H2A···Cl2^{ii}	0.91	2.50	3.2887 (19)	145.4
N2—H2B···O2^{iii}	0.91	2.91	3.303 (2)	107.8
N2—H2B···Cl2	0.91	2.25	3.0952 (19)	153.5
N2—H2C···Cl1^{iv}	0.91	2.30	3.1610 (19)	158.7
C6—H6B···Cl2^{ii}	0.99	2.68	3.443 (2)	133.6
C8—H8B···O2	0.98	2.35	2.794 (3)	107.0
O1—H1···Cl1	0.89 (3)	2.13 (3)	3.0164 (17)	175 (3)
O2—H2···Cl1^{v}	0.87 (4)	2.25 (4)	3.0763 (19)	160 (4)
O2—H2···O1	0.87 (4)	2.36 (4)	2.694 (2)	103 (3)

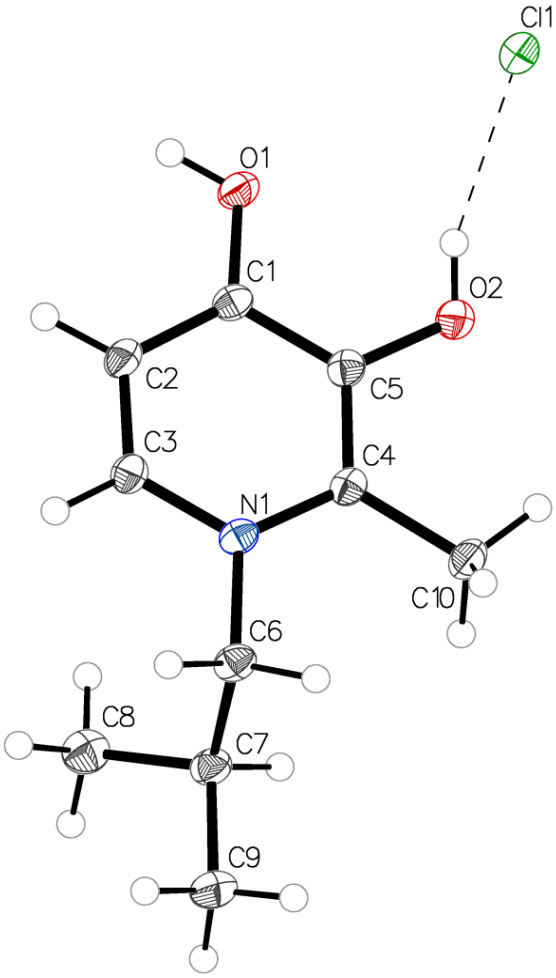

*Figure 100: ORTEP diagram for **MS9***

*Table 21: Crystallographic data for **MS9**.*

Crystal data	
Chemical formula	$Cl \cdot C_{10}H_{16}NO_2$
M_r	217.69
Crystal system, space group	Triclinic, *P*1
Temperature (K)	150
a, *b*, *c* (Å)	7.656 (3), 8.364 (3), 9.385 (6)
α, β, γ (°)	85.387 (13), 77.367 (18), 69.698 (9)
V (Å^3)	550.0 (5)
Z	2
Radiation type	Mo *K*α
μ (mm^{-1})	0.32
Crystal size (mm)	× ×
Data collection	
Diffractometer	Bruker *APEX*-II CCD
Absorption correction	Multi-scan *SADABS2016*/2 (Bruker,2016/2) was used for absorption correction. wR2(int) was 0.1345 before and 0.0964 after correction. The Ratio of minimum to maximum transmission is 0.7373. The λ/2 correction factor is Not present.
T_{min}, T_{max}	0.550, 0.746
No. of measured, independent and observed [$I > 2\sigma(I)$] reflections	21075, 2512, 2351
R_{int}	0.064
$(\sin \theta/\lambda)_{max}$ (Å^{-1})	0.650
Refinement	
$R[F^2 > 2\sigma(F^2)]$, $wR(F^2)$, S	0.033, 0.093, 1.09
No. of reflections	2512
No. of parameters	138
H-atom treatment	H atoms treated by a mixture of independent and constrained refinement
$\Delta\rho_{max}$, $\Delta\rho_{min}$ (e Å^{-3})	0.44, −0.40

*Table 22: Bond lengths and angles for **MS9**.*

O1—C1	1.3301 (15)	C2—C3	1.3720 (17)
O2—C5	1.3563 (15)	C4—C5	1.3894 (17)
N1—C3	1.3528 (16)	C4—C10	1.4968 (17)
N1—C4	1.3712 (16)	C6—C7	1.5327 (17)
N1—C6	1.4909 (15)	C7—C8	1.524 (2)
C1—C2	1.3980 (17)	C7—C9	1.5340 (18)
C1—C5	1.4093 (17)		
C3—N1—C4	121.19 (10)	N1—C4—C10	120.17 (11)
C3—N1—C6	117.45 (10)	C5—C4—C10	121.10 (11)
C4—N1—C6	121.36 (10)	O2—C5—C1	120.92 (11)
O1—C1—C2	124.68 (11)	O2—C5—C4	118.44 (11)
O1—C1—C5	116.80 (11)	C4—C5—C1	120.61 (11)
C2—C1—C5	118.51 (11)	N1—C6—C7	113.61 (10)
C3—C2—C1	119.19 (11)	C6—C7—C9	107.30 (11)
N1—C3—C2	121.73 (11)	C8—C7—C6	112.26 (10)
N1—C4—C5	118.73 (11)	C8—C7—C9	109.99 (11)
O1—C1—C2—C3	-179.00 (11)	C3—N1—C4—C10	-178.88 (10)
O1—C1—C5—O2	-1.23 (16)	C3—N1—C6—C7	89.52 (13)
O1—C1—C5—C4	-179.21 (10)	C4—N1—C3—C2	0.56 (18)
N1—C4—C5—O2	-179.99 (10)	C4—N1—C6—C7	-89.81 (13)
N1—C4—C5—C1	-1.95 (16)	C5—C1—C2—C3	0.89 (17)
N1—C6—C7—C8	-60.57 (14)	C6—N1—C3—C2	-178.77 (10)
N1—C6—C7—C9	178.48 (10)	C6—N1—C4—C5	-179.45 (10)
C1—C2—C3—N1	-1.64 (18)	C6—N1—C4—C10	0.42 (16)
C2—C1—C5—O2	178.88 (11)	C10—C4—C5—O2	0.14 (16)
C2—C1—C5—C4	0.89 (17)	C10—C4—C5—C1	178.17 (10)
C3—N1—C4—C5	1.25 (16)		

*Table 23: Selected hydrogen-bond parameters for **MS9**; Symmetry code(s): (i) -x+1, -y+1, -z+1; (ii) -x+2, -y+1, -z+1.*

D—H···*A*	*D*—H (Å)	H···*A* (Å)	*D*···*A* (Å)	*D*—H···*A* (°)
C8—H8C···O1^{i}	0.98	2.61	3.437 (2)	142.6
C10—H10B···O2	0.98	2.35	2.8099 (19)	108.1
O2—H2···Cl1	0.83 (2)	2.26 (2)	3.0511 (16)	158.5 (18)
O2—H2···O1	0.83 (2)	2.39 (2)	2.7061 (17)	103.3 (15)
O1—H1···Cl1^{ii}	0.84 (2)	2.13 (2)	2.9701 (14)	179 (2)

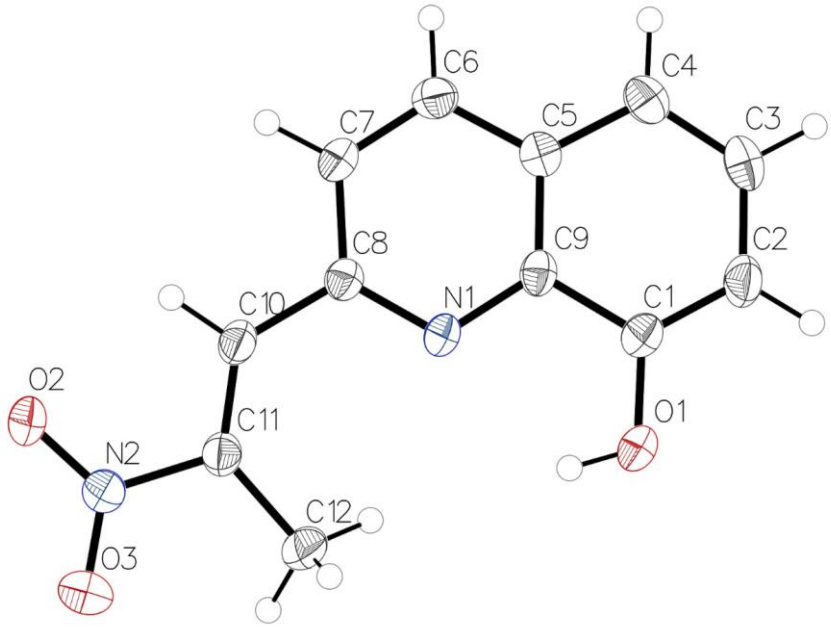

Figure 101: ORTEP diagram for 2-(-2-nitroprop-1-en-1-yl)quinoline-8-ol

Table 24 Crystallographic data for 2-(-2-nitroprop-1-en-1-yl)quinoline-8-ol

Crystal data	
Chemical formula	$C_{12}H_{10}N_2O_3$
M_r	230.22
Crystal system, space group	Monoclinic, $P2_1/n$
Temperature (K)	150
a, b, c (Å)	13.0598 (12), 6.3565 (6), 13.7985 (13)
β (°)	110.237 (4)
V (Å^3)	1074.77 (18)
Z	4
Radiation type	Mo $K\alpha$
μ (mm^{-1})	0.11
Crystal size (mm)	0.18 × 0.08 × 0.03
Data collection	
Diffractometer	Bruker D8Quest
Absorption correction	Multi-scan *SADABS2016*/2 (Bruker,2016/2) was used for absorption correction. wR2 (int) was 0.1752 before and 0.0900 after correction. The Ratio of minimum to maximum transmission is 0.9115. The λ/2 correction factor is Not present.
T_{min}, T_{max}	0.680, 0.746
No. of measured, independent and observed [$I > 2\sigma(I)$] reflections	26876, 2473, 1731
R_{int}	0.098
$(\sin \theta/\lambda)_{max}$ (Å^{-1})	0.651
Refinement	
$R[F^2 > 2\sigma(F^2)]$, $wR(F^2)$, S	0.058, 0.131, 1.06
No. of reflections	2473
No. of parameters	156
H-atom treatment	H-atom parameters constrained
$\Delta\rho_{max}$, $\Delta\rho_{min}$ (e Å^{-3})	0.29, −0.27

Table 25: Bond length and angles for 2-(-2-nitroprop-1-en-1-yl)quinoline-8-ol

C1—O1	1.355 (3)	C4—C5	1.419 (3)
C1—C2	1.364 (3)	C5—C6	1.408 (3)
C1—C9	1.421 (3)	C5—C9	1.411 (3)
N1—C8	1.325 (3)	C6—H6	0.9500
N1—C9	1.358 (3)	C6—C7	1.363 (3)
O1—H1	0.8400	C7—H7	0.9500
C2—H2	0.9500	C7—C8	1.417 (3)
C2—C3	1.403 (3)	C8—C10	1.466 (3)
N2—O2	1.222 (2)	C10—H10	0.9500
N2—O3	1.224 (2)	C10—C11	1.328 (3)
N2—C11	1.473 (3)	C11—C12	1.486 (3)
C3—H3	0.9500	C12—H12A	0.9800
C3—C4	1.368 (3)	C12—H12B	0.9800
C4—H4	0.9500	C12—H12C	0.9800
O1—C1—C2	121.5 (2)	C7—C6—H6	120.3
O1—C1—C9	118.1 (2)	C6—C7—H7	119.9
C2—C1—C9	120.4 (2)	C6—C7—C8	120.1 (2)
C8—N1—C9	117.67 (18)	C8—C7—H7	119.9
C1—O1—H1	109.5	N1—C8—C7	122.1 (2)
C1—C2—H2	120.2	N1—C8—C10	119.90 (19)
C1—C2—C3	119.6 (2)	C7—C8—C10	117.99 (19)
C3—C2—H2	120.2	N1—C9—C1	116.24 (19)
O2—N2—O3	121.9 (2)	N1—C9—C5	124.10 (19)
O2—N2—C11	119.90 (19)	C5—C9—C1	119.7 (2)
O3—N2—C11	118.17 (19)	C8—C10—H10	116.0
C2—C3—H3	119.0	C11—C10—C8	128.0 (2)
C4—C3—C2	121.9 (2)	C11—C10—H10	116.0
C4—C3—H3	119.0	N2—C11—C12	114.56 (19)
C3—C4—H4	120.2	C10—C11—N2	115.06 (19)
C3—C4—C5	119.5 (2)	C10—C11—C12	130.4 (2)
C5—C4—H4	120.2	C11—C12—H12A	109.5
C6—C5—C4	124.5 (2)	C11—C12—H12B	109.5
C6—C5—C9	116.6 (2)	C11—C12—H12C	109.5
C9—C5—C4	118.9 (2)	H12A—C12—H12B	109.5
C5—C6—H6	120.3	H12A—C12—H12C	109.5
C7—C6—C5	119.3 (2)	H12B—C12—H12C	109.5

Table 26: Selected hydrogen-bond parameters for 2-(-2-nitroprop-1-en-1-yl)quinoline-8-ol; Symmetry code(s): (i) -x+2, -y+1, -z+1; (ii) -x+2, -y, -z+1; (iii) x-1/2, -y+3/2, z-1/2; (iv) -x+1, -y+2, -z+1.

D—H···*A*	*D*—H (Å)	H···*A* (Å)	*D*···*A* (Å)	*D*—H···*A* (°)
O1—H1···N1	0.84	2.18	2.660 (2)	116.4
O1—H1···O1^{i}	0.84	2.73	3.127 (4)	110.5
C2—H2···O1^{ii}	0.95	2.52	3.354 (3)	146.1
C6—H6···O3^{iii}	0.95	2.49	3.305 (3)	144.1
C7—H7···O2^{iv}	0.95	2.47	3.349 (3)	153.4
C10—H10···O2	0.95	2.24	2.652 (3)	105.5
C12—H12B···N1	0.98	2.40	2.986 (3)	117.9

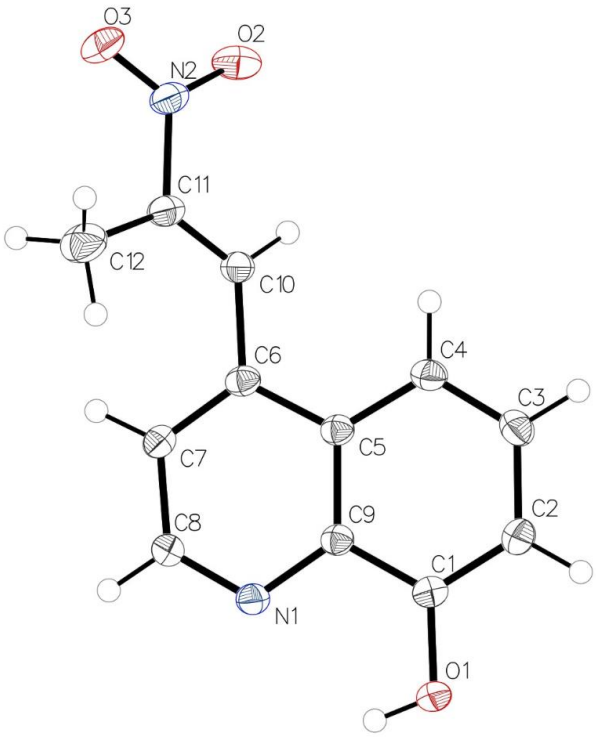

Figure 102: ORTEP diagram for 4-(-2-nitroprop-1-en-1-yl)quinoline-8-ol

Table 27: Crystallographic data for 4-(-2-nitroprop-1-en-1-yl)quinoline-8-ol

Crystal data	
Chemical formula	$C_{12}H_{10}N_2O_3$
M_r	230.22
Crystal system, space group	Triclinic, *P*1
Temperature (K)	150
a, *b*, *c* (Å)	6.6710 (3), 8.0412 (4), 10.5537 (6)
α, β, γ (°)	100.492 (2), 90.759 (2), 108.475 (2)
V (Å^3)	526.45 (5)
Z	2
Radiation type	Mo *K*α
μ (mm^{-1})	0.11
Crystal size (mm)	0.41 × 0.09 × 0.03
Data collection	
Diffractometer	Bruker D8Quest
Absorption correction	Multi-scan *SADABS2016*/2 (Bruker,2016/2) was used for absorption correction. wR2 was 0.1607 before and 0.0769 after correction. The Ratio of minimum to maximum transmission is 0.7562. The λ/2 correction factor is Not present.
T_{min}, T_{max}	0.564, 0.746
No. of measured, independent and observed [$I > 2\sigma(I)$] reflections	42186, 2449, 2106
R_{int}	0.059
$(\sin \theta/\lambda)_{max}$ (Å^{-1})	0.654
Refinement	
$R[F^2 > 2\sigma(F^2)]$, $wR(F^2)$, S	0.035, 0.106, 1.08
No. of reflections	2449
No. of parameters	156
H-atom treatment	H-atom parameters constrained
$\Delta\rho_{max}$, $\Delta\rho_{min}$ (e Å^{-3})	0.27, −0.27

Table 28: Bond lengths and angles for 4-(-2-nitroprop-1-en-1-yl)quinoline-8-ol

C1—O1	1.3563 (13)	C3—C4	1.3699 (17)
C1—C2	1.3746 (16)	C4—C5	1.4174 (16)
C1—C9	1.4255 (15)	C5—C6	1.4276 (15)
N1—C8	1.3202 (15)	C5—C9	1.4249 (14)
N1—C9	1.3695 (14)	C6—C7	1.3729 (16)
C2—C3	1.4104 (16)	C6—C10	1.4790 (14)
N2—O2	1.2305 (14)	C7—C8	1.4119 (15)
N2—O3	1.2250 (14)	C10—C11	1.3279 (16)
N2—C11	1.4854 (14)	C11—C12	1.4836 (17)
O1—C1—C2	118.88 (10)	C5—C6—C10	120.03 (10)
O1—C1—C9	120.76 (10)	C7—C6—C5	118.64 (10)
C2—C1—C9	120.35 (10)	C7—C6—C10	121.28 (10)
C8—N1—C9	117.17 (9)	C6—C7—C8	119.67 (10)
C1—C2—C3	119.95 (11)	N1—C8—C7	124.00 (10)
O2—N2—C11	119.52 (10)	N1—C9—C1	117.70 (10)
O3—N2—O2	123.17 (10)	N1—C9—C5	123.38 (10)
O3—N2—C11	117.30 (11)	C5—C9—C1	118.91 (10)
C4—C3—C2	121.54 (11)	C11—C10—C6	123.42 (10)
C3—C4—C5	119.67 (10)	C10—C11—N2	116.01 (10)
C4—C5—C6	123.34 (10)	C10—C11—C12	129.95 (11)
C4—C5—C9	119.56 (10)	C12—C11—N2	114.03 (10)
C9—C5—C6	117.10 (10)		

Table 29: Selected hydrogen-bond parameters for 4-(-2-nitroprop-1-en-1-yl)quinoline-8-ol; Symmetry code(s): (i) -x+2, -y+1, -z.

D—H···*A*	*D*—H (Å)	H···*A* (Å)	*D*···*A* (Å)	*D*—H···*A* (°)
O1—H1···N1	0.84	2.30	2.7562 (13)	114.4
O1—H1···N1^{i}	0.84	2.19	2.8511 (13)	135.4
C8—H8···O1^{i}	0.95	2.46	3.0005 (14)	116.2
C10—H10···O2	0.95	2.30	2.6768 (14)	102.8

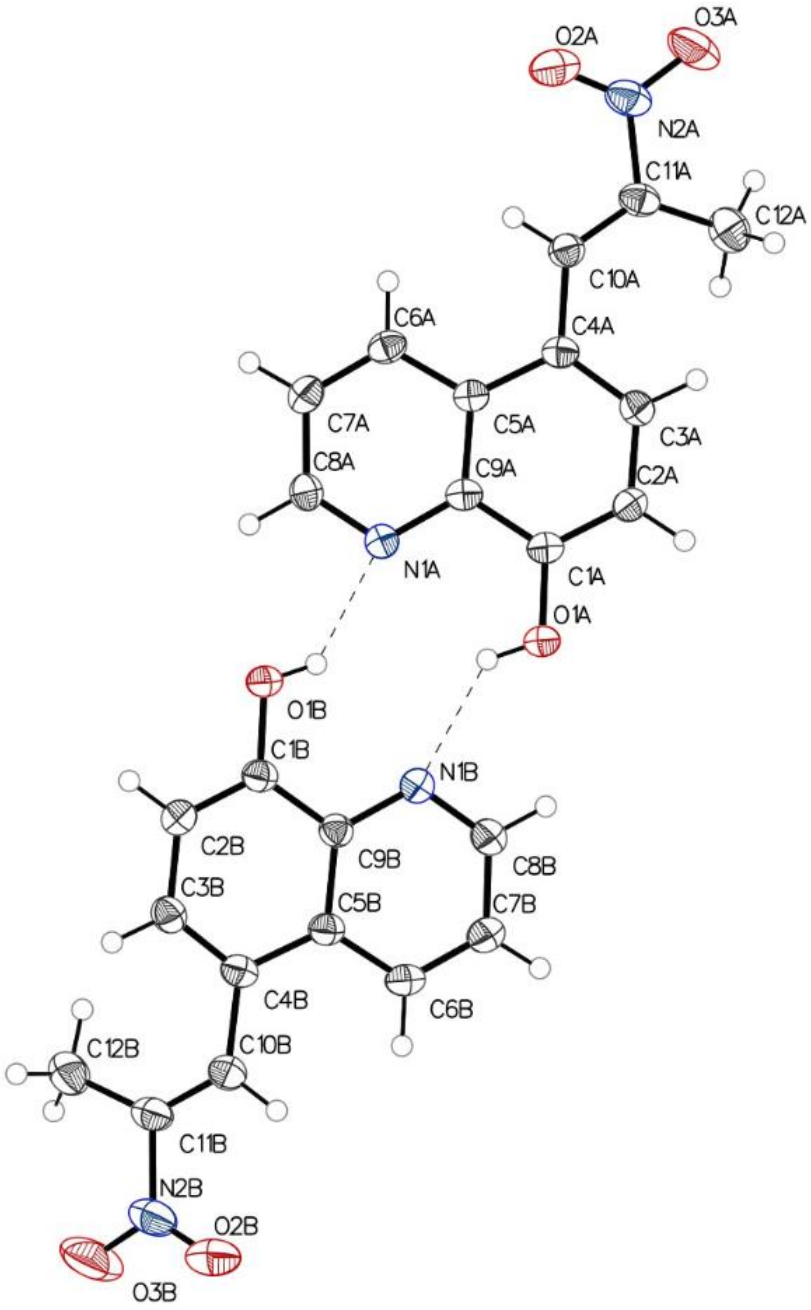

Figure 103: ORTEP diagram for 5-(-2-nitroprop-1-en-1-yl)quinoline-8-ol

Table 30: Crystallographic data for 5-(-2-nitroprop-1-en-1-yl)quinoline-8-ol

Crystal data	
Chemical formula	$2(C_{12}H_{10}N_2O_3)$
M_r	460.44
Crystal system, space group	Triclinic, *P*1bar
Temperature (K)	150
a, *b*, *c* (Å)	7.0189 (13), 10.9644 (19), 14.234 (3)
α, β, γ (°)	80.648 (6), 88.802 (6), 75.050 (6)
V (Å^3)	1044.0 (3)
Z	2
Radiation type	Mo *K*α
μ (mm^{-1})	0.11
Crystal size (mm)	0.15 × 0.11 × 0.09
Data collection	
Diffractometer	Bruker D8Quest
Absorption correction	Multi-scan *SADABS2016*/2 (Bruker,2016/2) was used for absorption correction. wR2(int) was 0.1385 before and 0.0899 after correction. The Ratio of minimum to maximum transmission is 0.8765. The λ/2 correction factor is Not present.
T_{min}, T_{max}	0.654, 0.746
No. of measured, independent and observed [$I > 2\sigma(I)$] reflections	45104, 4817, 2810
R_{int}	0.120
$(\sin\theta/\lambda)_{max}$ (Å^{-1})	0.652
Refinement	
$R[F^2 > 2\sigma(F^2)]$, $wR(F^2)$, S	0.057, 0.154, 1.02
No. of reflections	4817
No. of parameters	311
H-atom treatment	H-atom parameters constrained
$\Delta\rho_{max}$, $\Delta\rho_{min}$ (e Å^{-3})	0.31, −0.32

Table 31: Bond lengths and angles for 5-(-2-nitroprop-1-en-1-yl)quinoline-8-ol

C1A—O1A	1.348 (3)	C1B—O1B	1.359 (3)
C1A—C2A	1.370 (3)	C1B—C2B	1.367 (3)
C1A—C9A	1.420 (3)	C1B—C9B	1.415 (3)
N1A—C8A	1.317 (3)	N1B—C8B	1.318 (3)
N1A—C9A	1.369 (3)	N1B—C9B	1.372 (3)
C2A—C3A	1.397 (3)	C2B—C3B	1.405 (3)
N2A—O2A	1.221 (3)	N2B—O2B	1.227 (3)
N2A—O3A	1.224 (3)	N2B—O3B	1.223 (3)
N2A—C11A	1.475 (3)	N2B—C11B	1.485 (3)
C3A—C4A	1.384 (3)	C3B—C4B	1.374 (4)

C4A—C5A	1.431 (3)	C4B—C5B	1.436 (3)
C4A—C10A	1.464 (3)	C4B—C10B	1.472 (3)
C5A—C6A	1.417 (3)	C5B—C6B	1.413 (4)
C5A—C9A	1.428 (3)	C5B—C9B	1.424 (3)
C6A—C7A	1.364 (3)	C6B—C7B	1.364 (4)
C7A—C8A	1.407 (3)	C7B—C8B	1.409 (3)
C10A—C11A	1.335 (3)	C10B—C11B	1.329 (4)
C11A—C12A	1.485 (4)	C11B—C12B	1.490 (4)
O1A—C1A—C2A	118.3 (2)	O1B—C1B—C2B	118.2 (2)
O1A—C1A—C9A	121.7 (2)	O1B—C1B—C9B	121.7 (2)
C2A—C1A—C9A	120.1 (2)	C2B—C1B—C9B	120.1 (2)
C8A—N1A—C9A	117.61 (19)	C8B—N1B—C9B	117.8 (2)
C1A—C2A—C3A	120.6 (2)	C1B—C2B—C3B	120.3 (2)
O2A—N2A—O3A	123.1 (2)	O2B—N2B—C11B	119.5 (2)
O2A—N2A—C11A	118.8 (2)	O3B—N2B—O2B	122.8 (2)
O3A—N2A—C11A	118.1 (2)	O3B—N2B—C11B	117.8 (3)
C4A—C3A—C2A	122.2 (2)	C4B—C3B—C2B	122.0 (2)
C3A—C4A—C5A	118.2 (2)	C3B—C4B—C5B	118.6 (2)
C3A—C4A—C10A	122.4 (2)	C3B—C4B—C10B	121.3 (2)
C5A—C4A—C10A	119.2 (2)	C5B—C4B—C10B	120.1 (2)
C6A—C5A—C4A	124.2 (2)	C6B—C5B—C4B	123.8 (2)
C6A—C5A—C9A	116.2 (2)	C6B—C5B—C9B	117.0 (2)
C9A—C5A—C4A	119.6 (2)	C9B—C5B—C4B	119.2 (2)
C7A—C6A—C5A	120.2 (2)	C7B—C6B—C5B	119.9 (2)
C6A—C7A—C8A	119.1 (2)	C6B—C7B—C8B	119.0 (2)
N1A—C8A—C7A	123.8 (2)	N1B—C8B—C7B	123.8 (2)
C1A—C9A—C5A	119.3 (2)	C1B—C9B—C5B	119.7 (2)
N1A—C9A—C1A	117.57 (19)	N1B—C9B—C1B	117.9 (2)
N1A—C9A—C5A	123.1 (2)	N1B—C9B—C5B	122.5 (2)
C11A—C10A—C4A	126.8 (2)	C11B—C10B—C4B	124.5 (2)
N2A—C11A—C12A	114.6 (2)	N2B—C11B—C12B	114.2 (2)
C10A—C11A—N2A	115.5 (2)	C10B—C11B—N2B	115.7 (2)
C10A—C11A—C12A	129.9 (2)	C10B—C11B—C12B	130.0 (2)

Table 32: Selected hydrogen-bond parameters for 5-(-2-nitroprop-1-en-1-yl)quinoline-8-ol; Symmetry code(s): (i) x, y+1, z-1; (ii) -x+2, -y+1, -z+1.

D—H···*A*	*D*—H (Å)	H···*A* (Å)	*D*···*A* (Å)	*D*—H···*A* (°)
O1A—H1A···N1A	0.84	2.31	2.762 (3)	114.1
O1A—H1A···N1B	0.84	2.09	2.772 (3)	138.0
C8A—H8A···O1B	0.95	2.60	3.020 (3)	107.1
C10A—H10A···O2A	0.95	2.24	2.641 (3)	104.6
C12A—H12A···O3A	0.98	2.30	2.685 (4)	102.5
O1B—H1B···N1A	0.84	2.09	2.776 (2)	139.0
O1B—H1B···N1B	0.84	2.33	2.771 (3)	113.7
C6B—H6B···O2A^{i}	0.95	2.30	3.243 (3)	170.3
C8B—H8B···O1A	0.95	2.56	3.014 (3)	109.4
C10B—H10B···O2A^{i}	0.95	2.54	3.309 (4)	138.1
C10B—H10B···O2B	0.95	2.30	2.675 (3)	102.8
C12B—H12E···O3A^{ii}	0.98	2.65	3.361 (3)	129.6

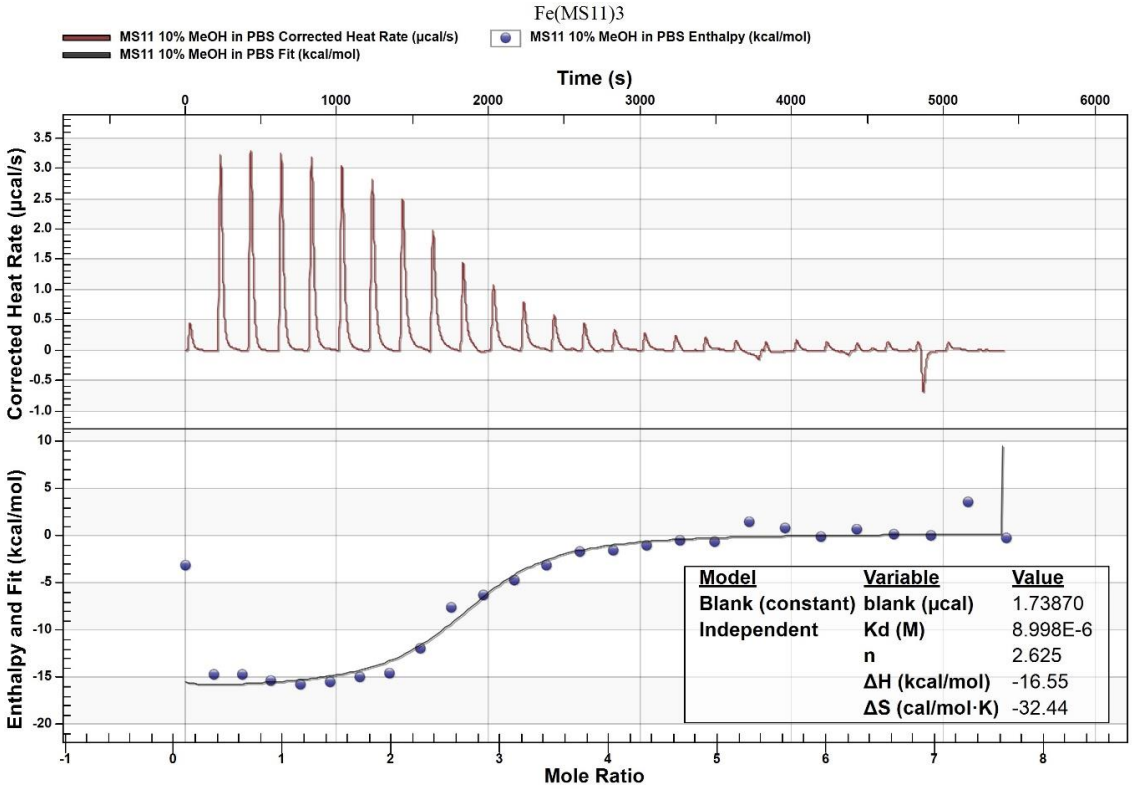

*Figure 104: ITC (**MS11**)$_3$:Fe; **MS11** titrating into iron*

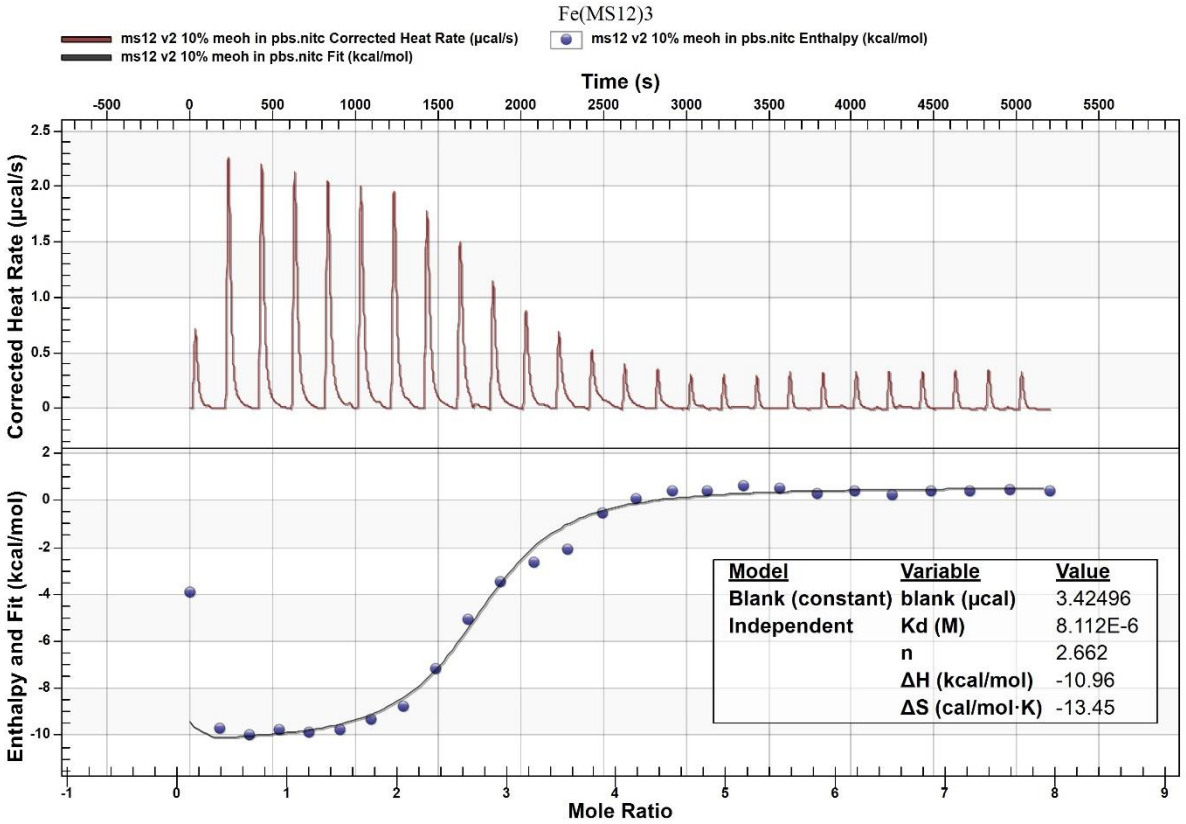

*Figure 105: ITC (**MS12**)$_3$:Fe; **MS12** titrating into iron*

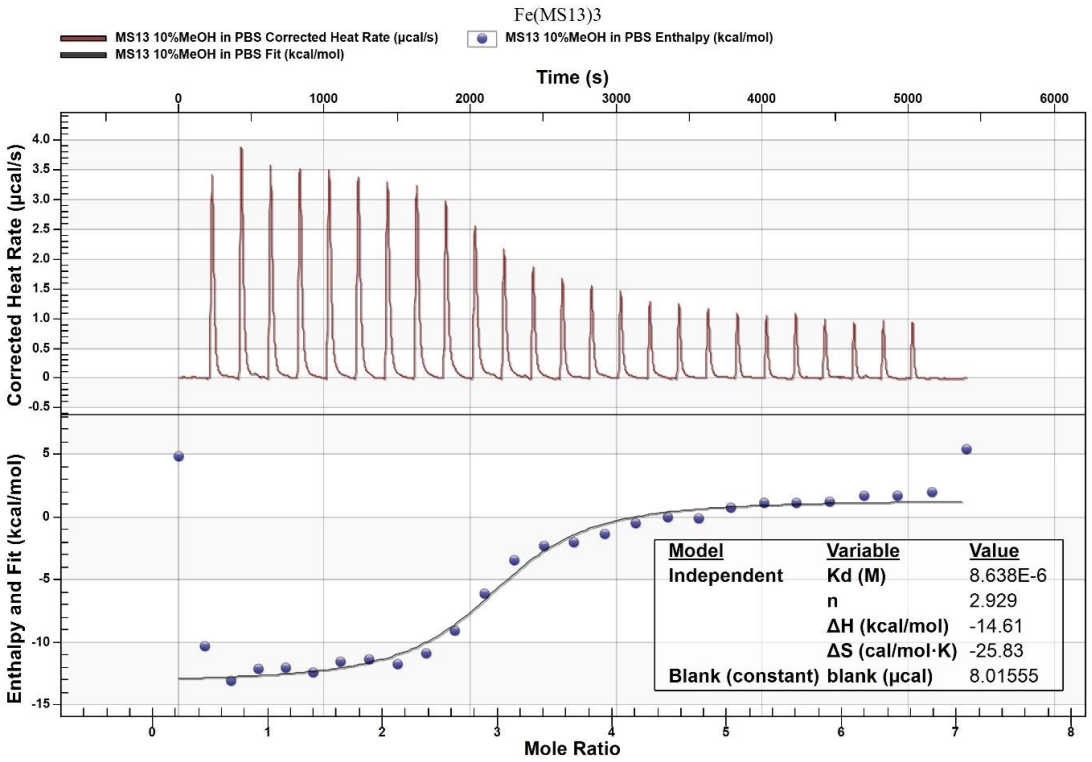

*Figure 106: ITC (**MS13**)$_3$:Fe; **MS13** titrating into iron*

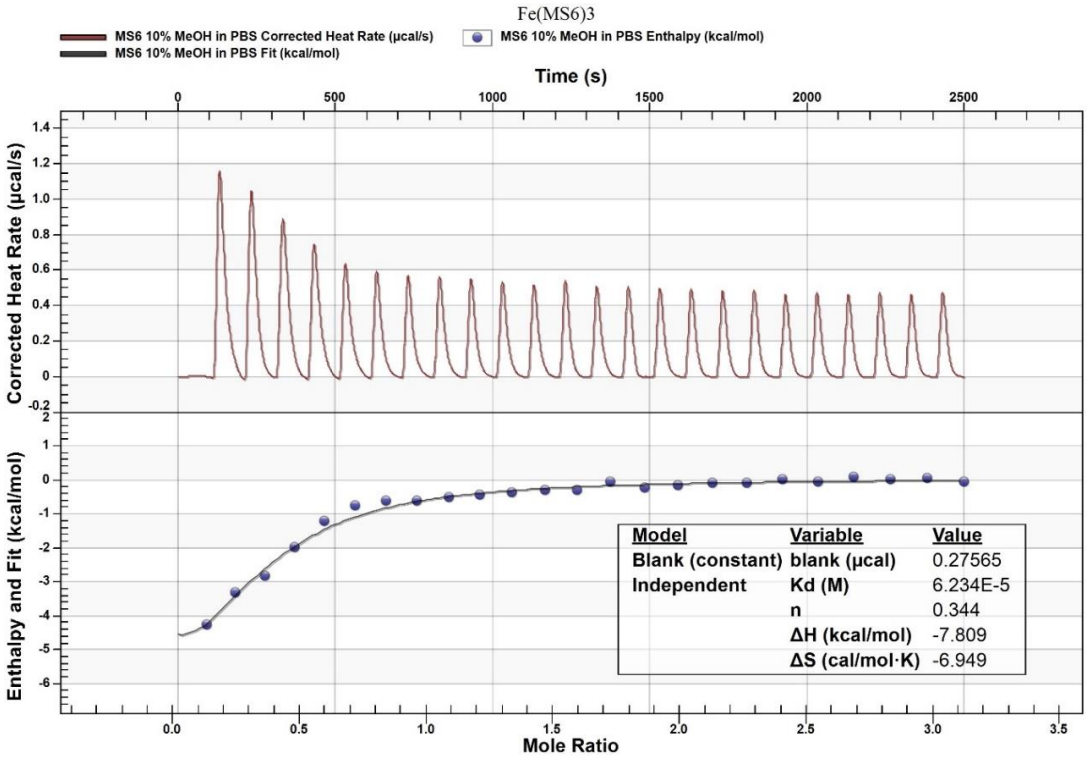

*Figure 107: ITC (**MS6**)$_3$:Fe; iron titrating into **MS6***

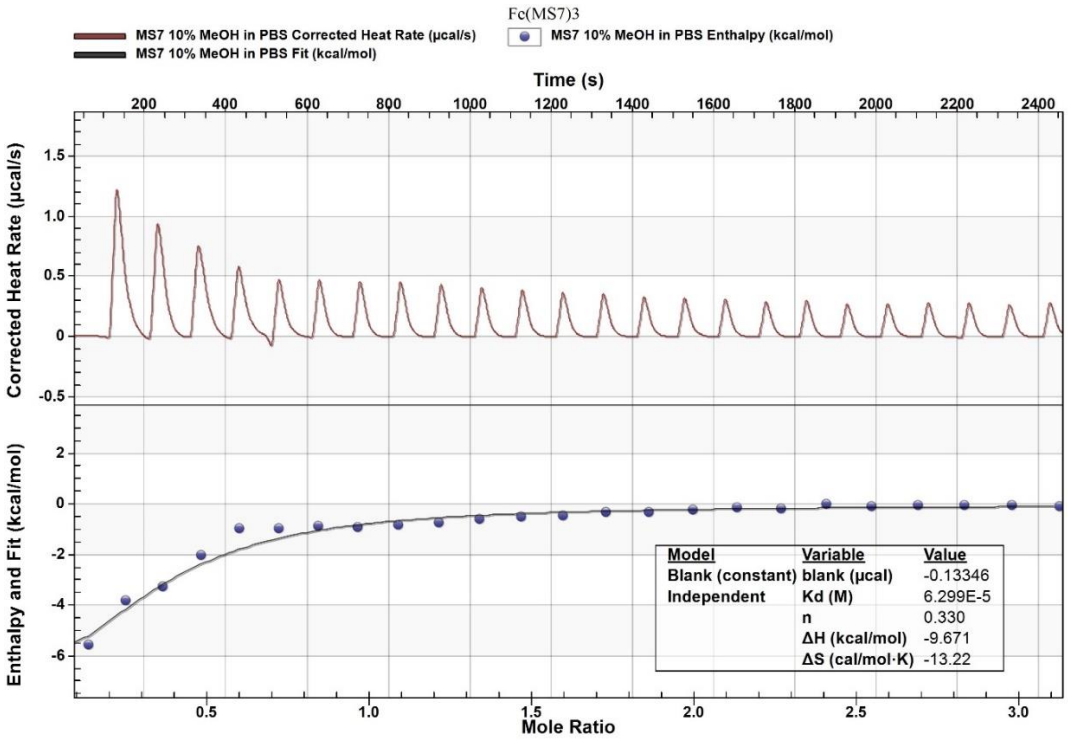

*Figure 108: ITC (**MS7**)$_3$:Fe; iron titrating into **MS7***

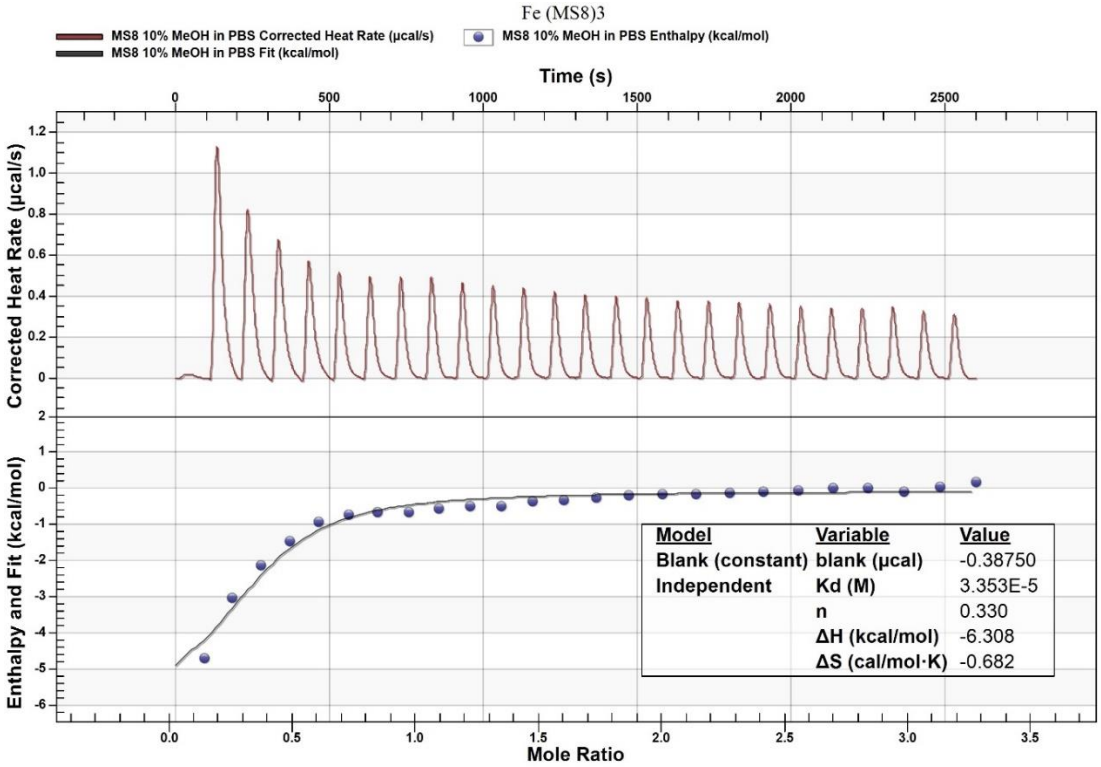

*Figure 109: ITC (**MS8**)$_3$:Fe ; iron titrating into **MS8***

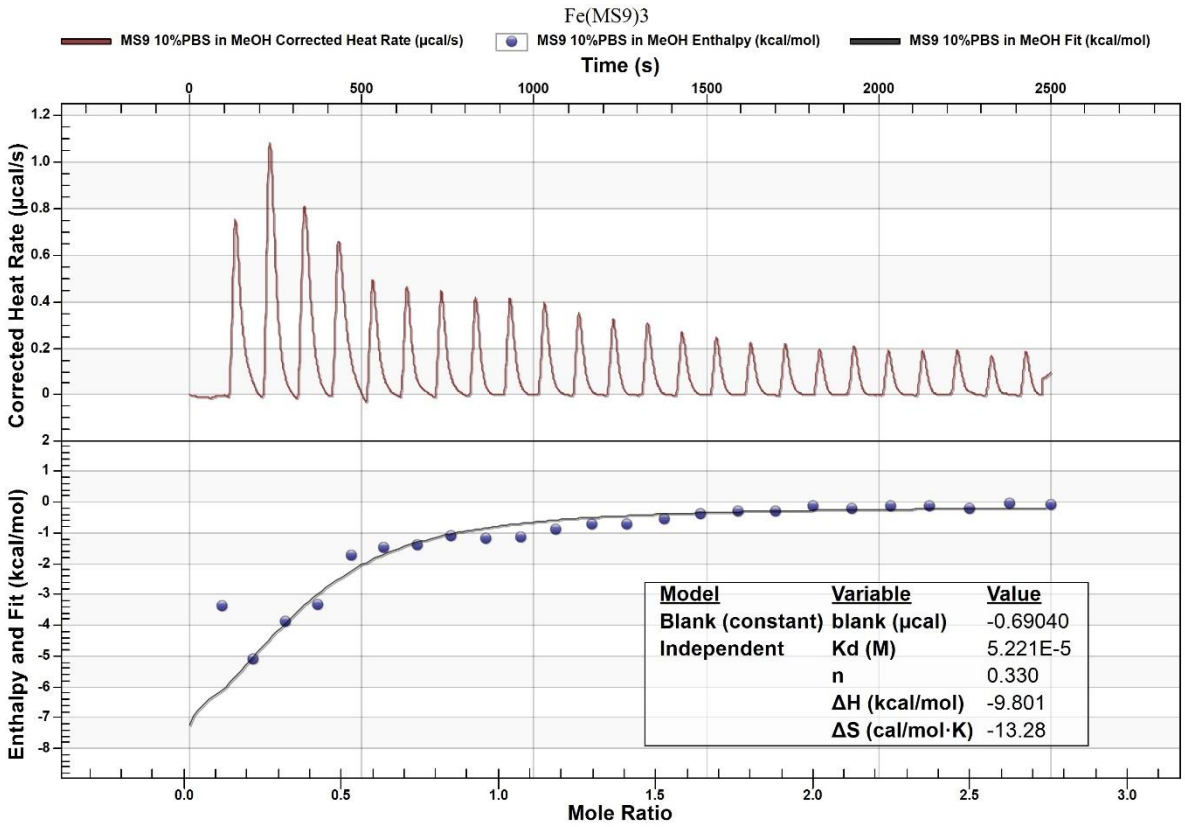

*Figure 110: ITC (**MS9**)$_3$:Fe ; iron titrating into **MS9***

Table 33: IC_{50} data from DPPH assays.

Compound	IC_{50} (µM)
Vit. C	22 ± 3
MS5	536 ± 25
MS6	391± 14
MS7	499± 18
MS8	710± 21
MS9	635± 25
MS10	123± 8
MS11	219± 15
MS12	80± 14
MS13	302± 28

Appendix 2

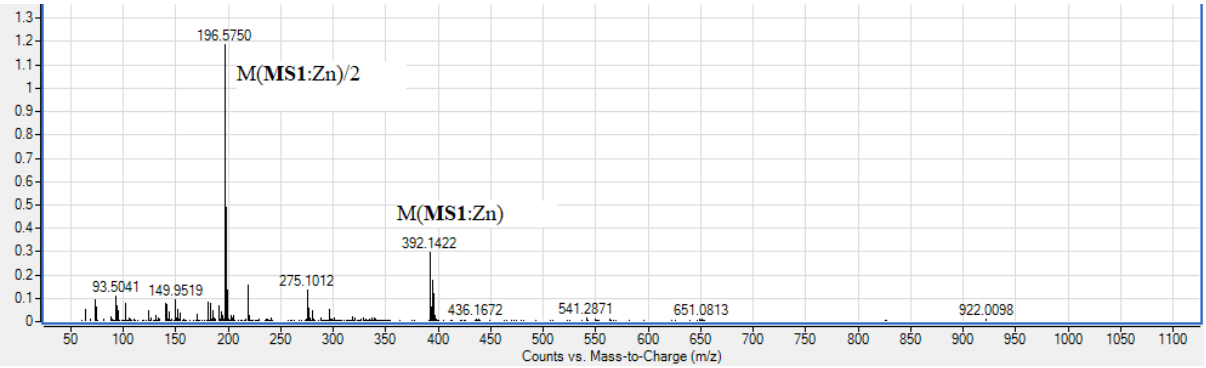

*Figure 111: Mass spectrum for m/z **MS1**:Zn*

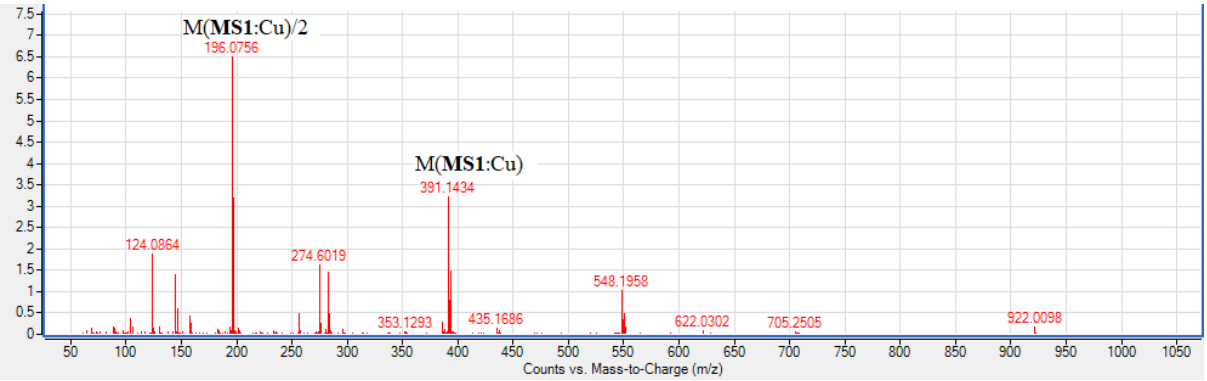

*Figure 112: Mass spectrum for m/z **MS1**:Cu*

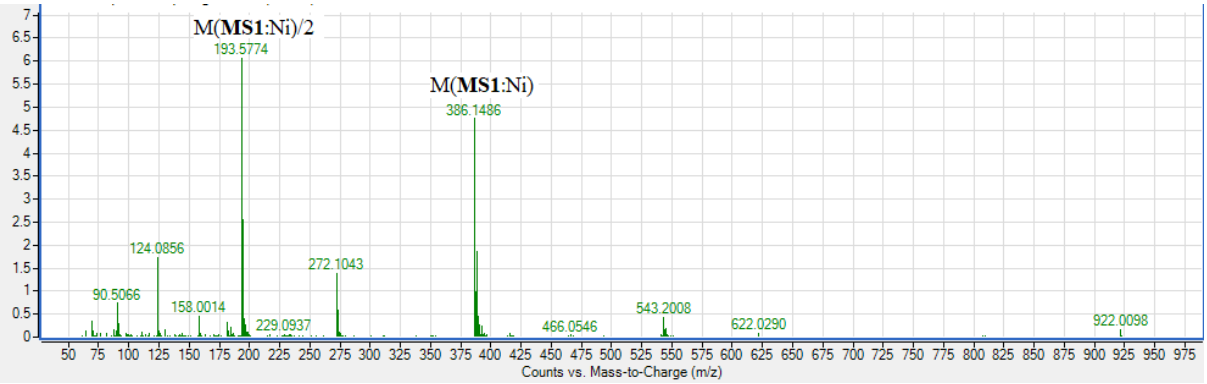

*Figure 113: Mass spectrum for m/z **MS1**:Ni*

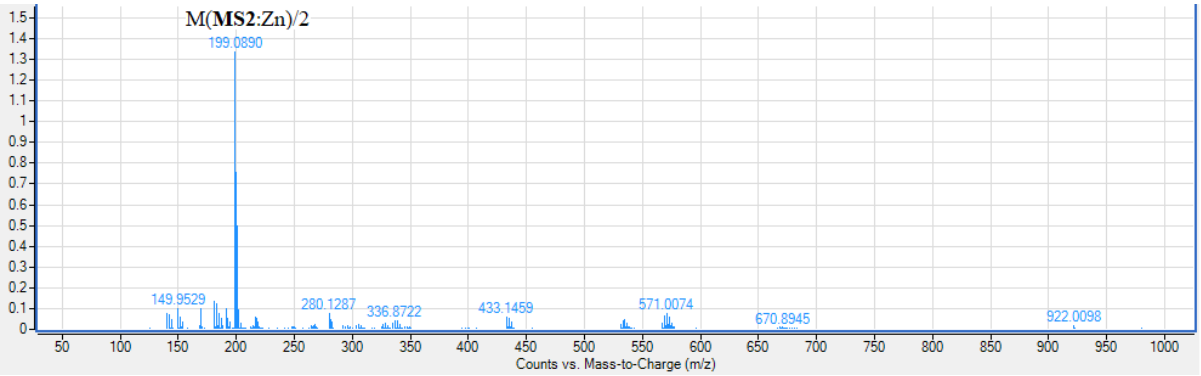

*Figure 114: Mass spectrum for m/z **MS2**:Zn*

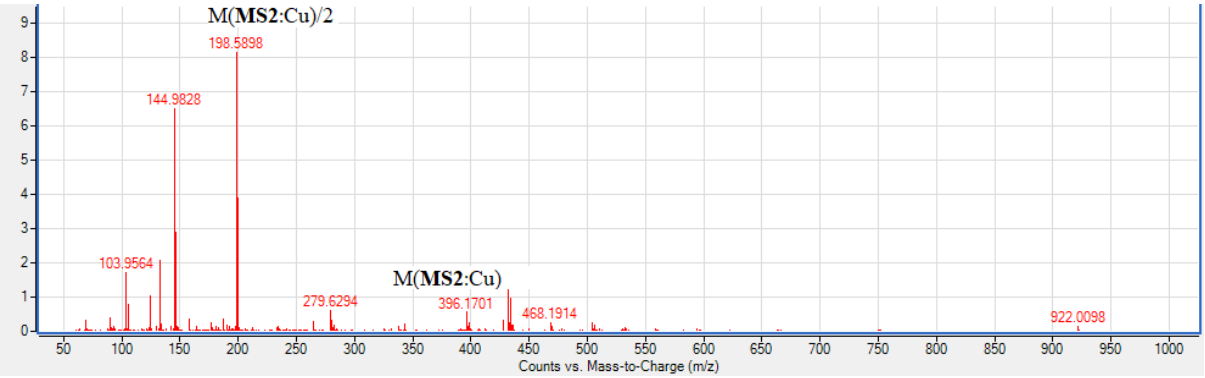

*Figure 115: Mass spectrum for m/z **MS2**:Cu*

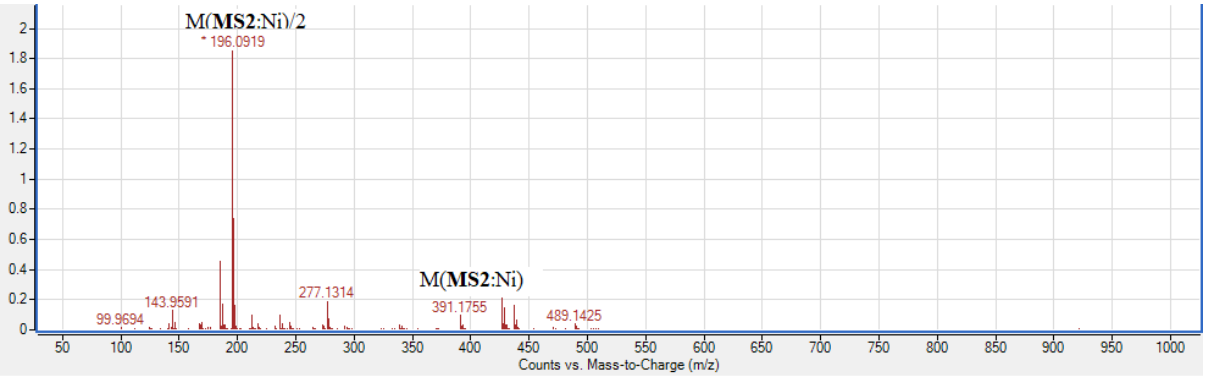

*Figure 116: Mass spectrum for m/z **MS2**:Ni*

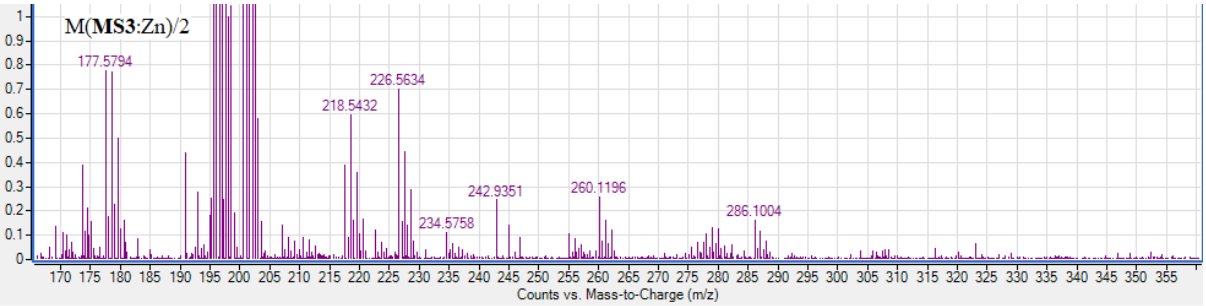

*Figure 117: Mass spectrum for m/z **MS3**:Zn*

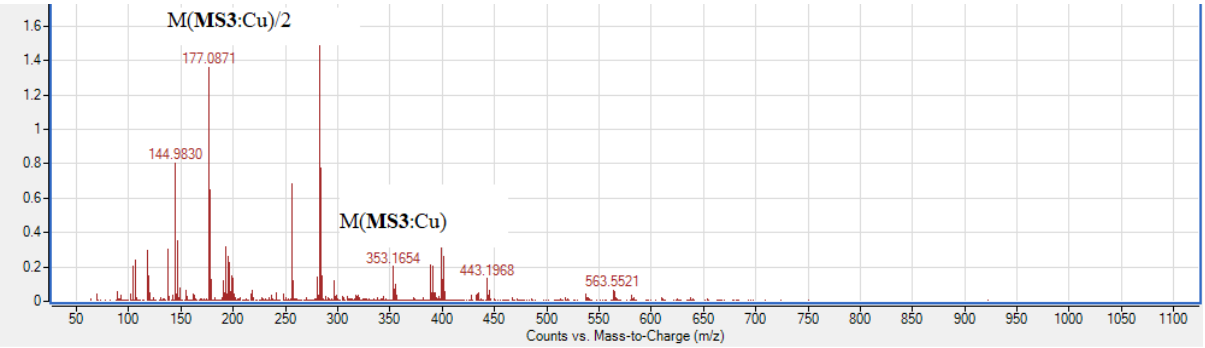

*Figure 118: Mass spectrum for m/z **MS3**:Cu*

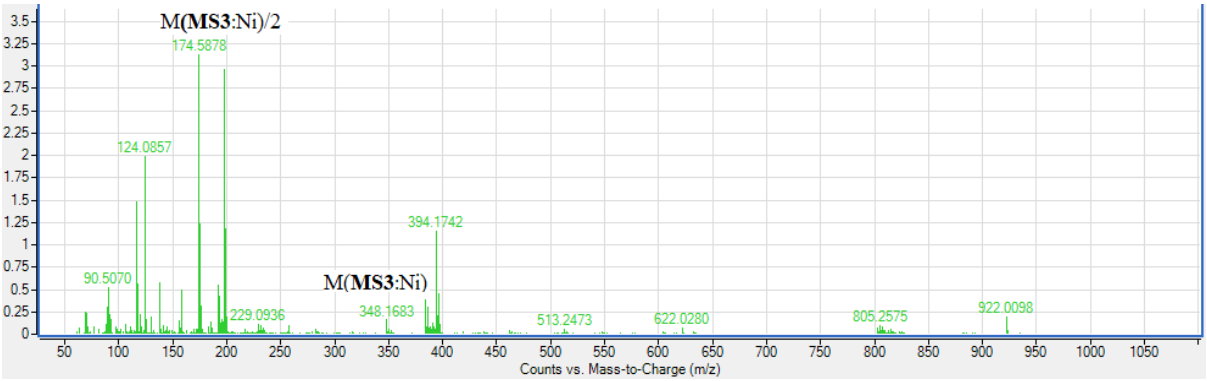

*Figure 119: Mass spectrum for m/z **MS3**:Ni*

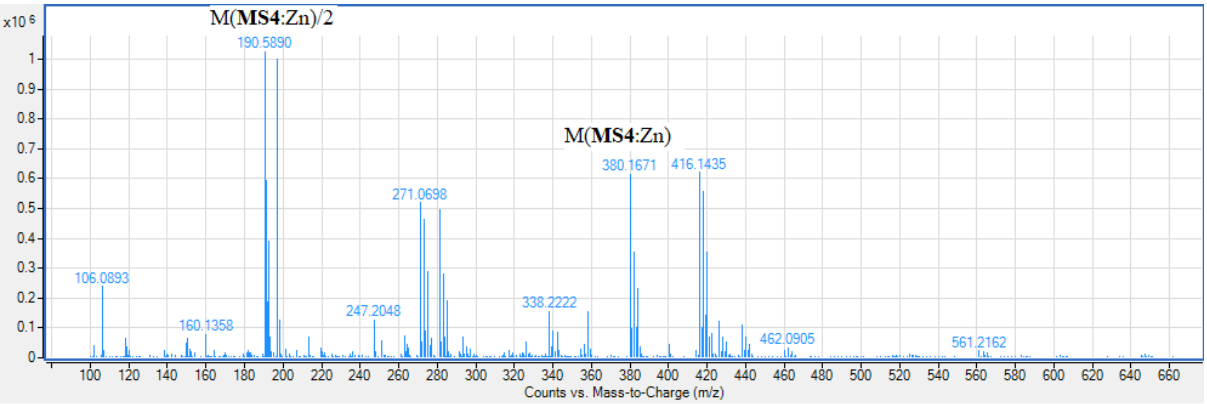

*Figure 120: Mass spectrum for m/z **MS4**:Zn*

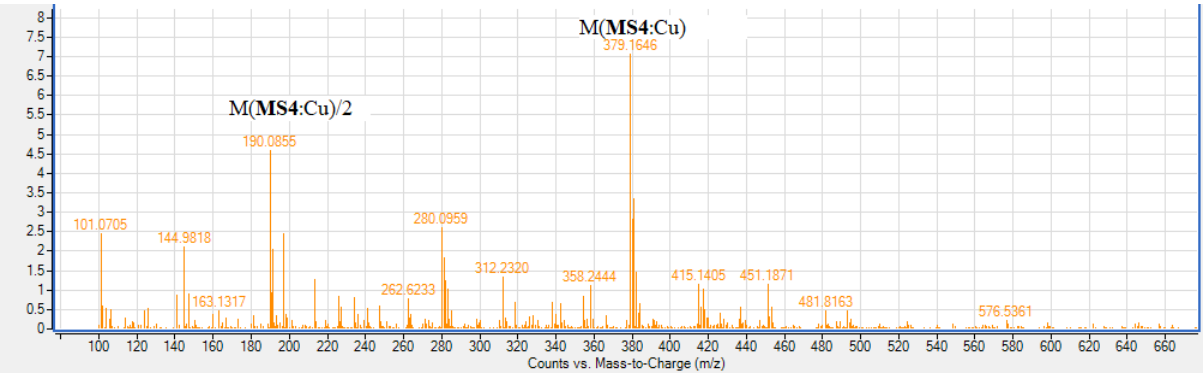

*Figure 121: Mass spectrum for m/z **MS4**:Cu*

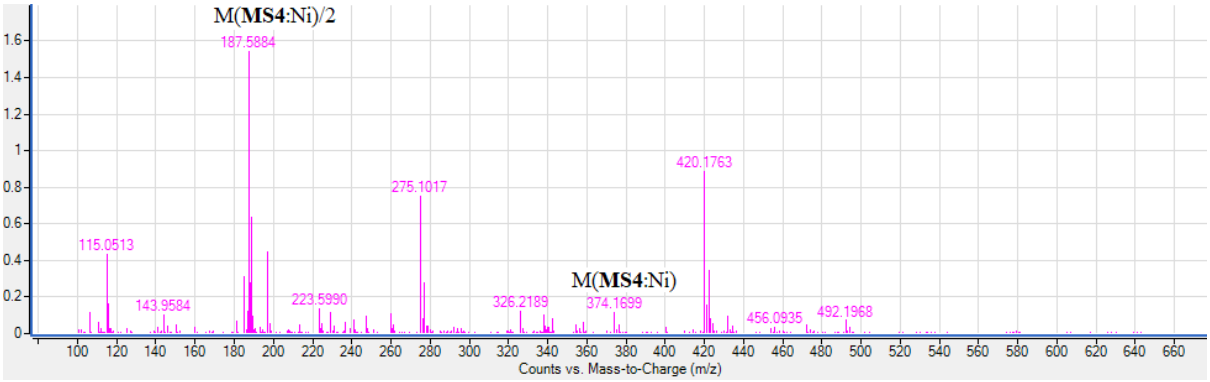

*Figure 122: Mass spectrum for m/z **MS4**:Ni*

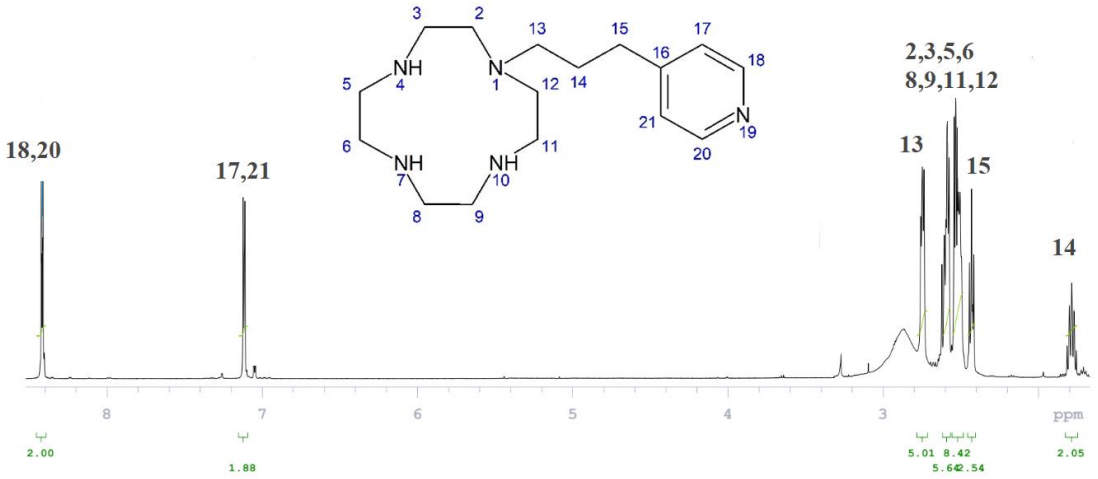

Figure 123: [1]HNMR for MS3

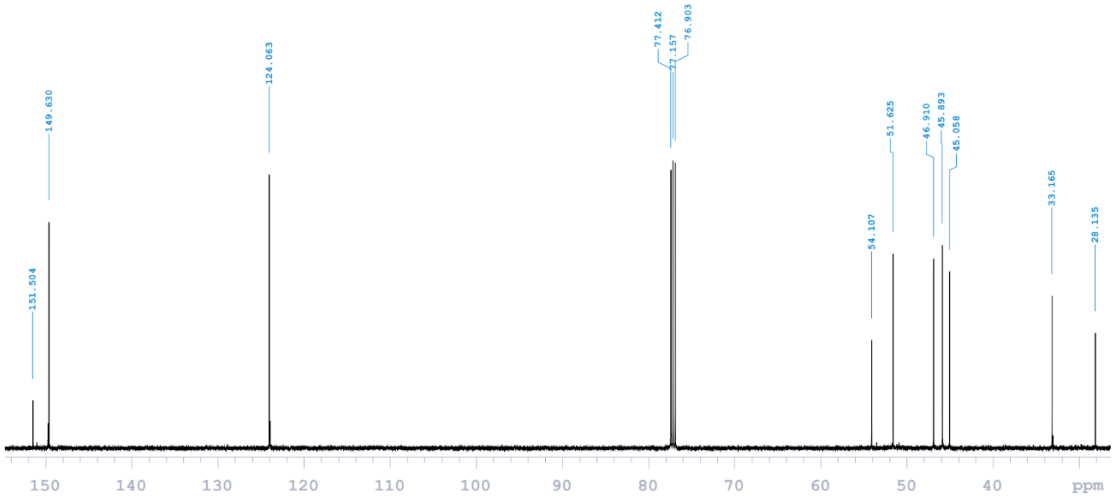

Figure 124: [13]CNMR for MS3

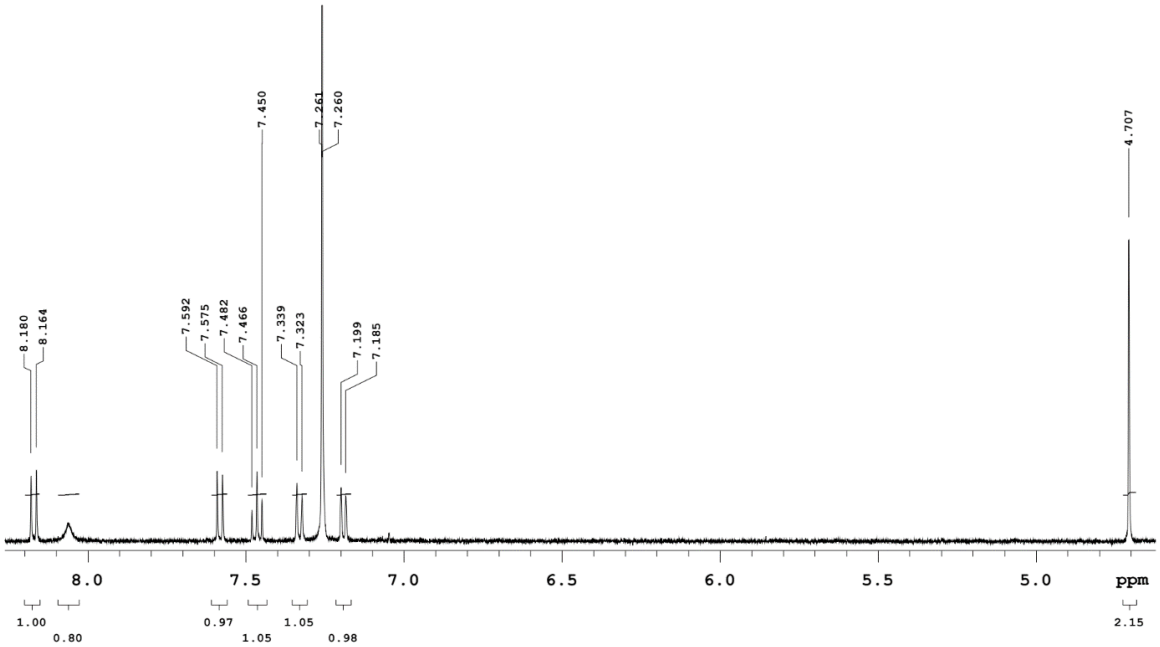

*Figure 125: [1]HNMR for **MS1B***

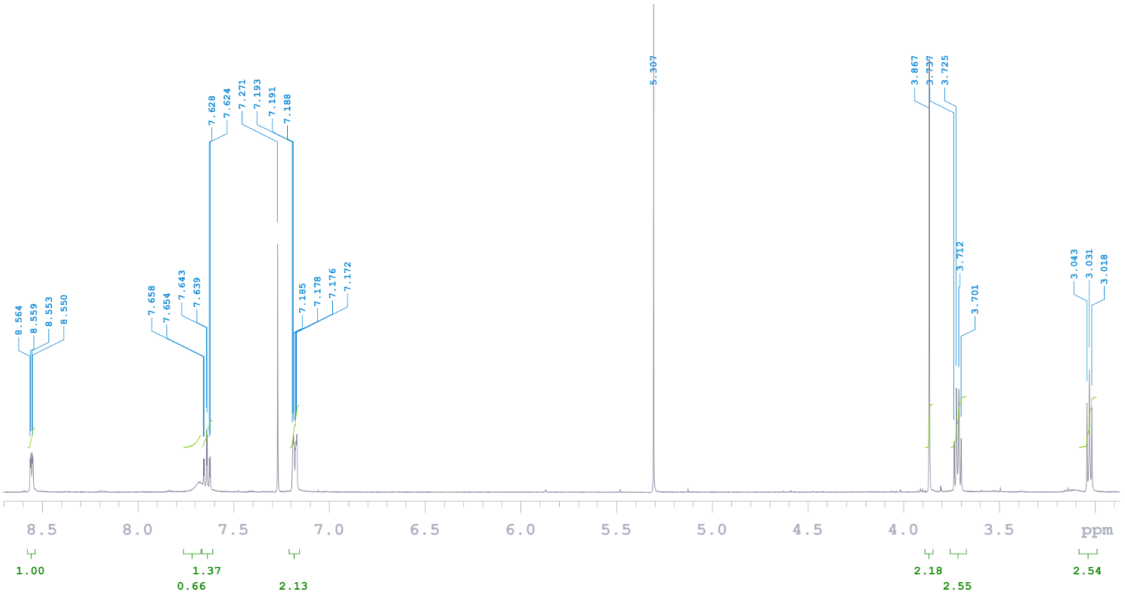

*Figure 126: [1]HNMR for **MS2A***

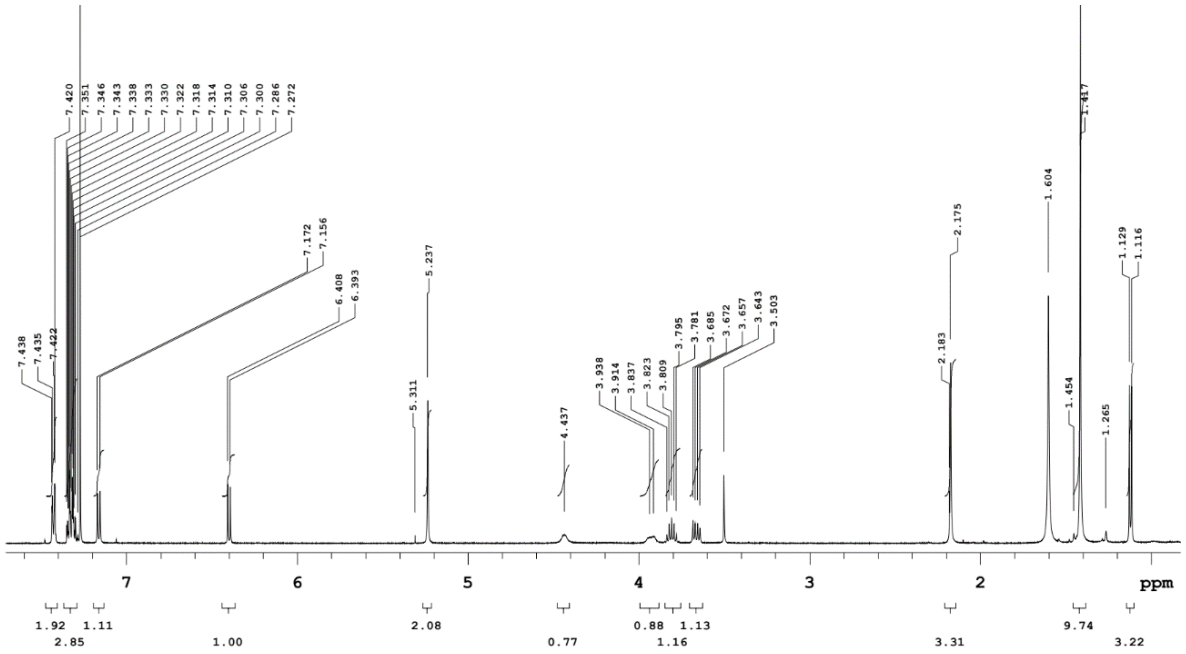

*Figure 127: [1]`HNMR **MS5A***

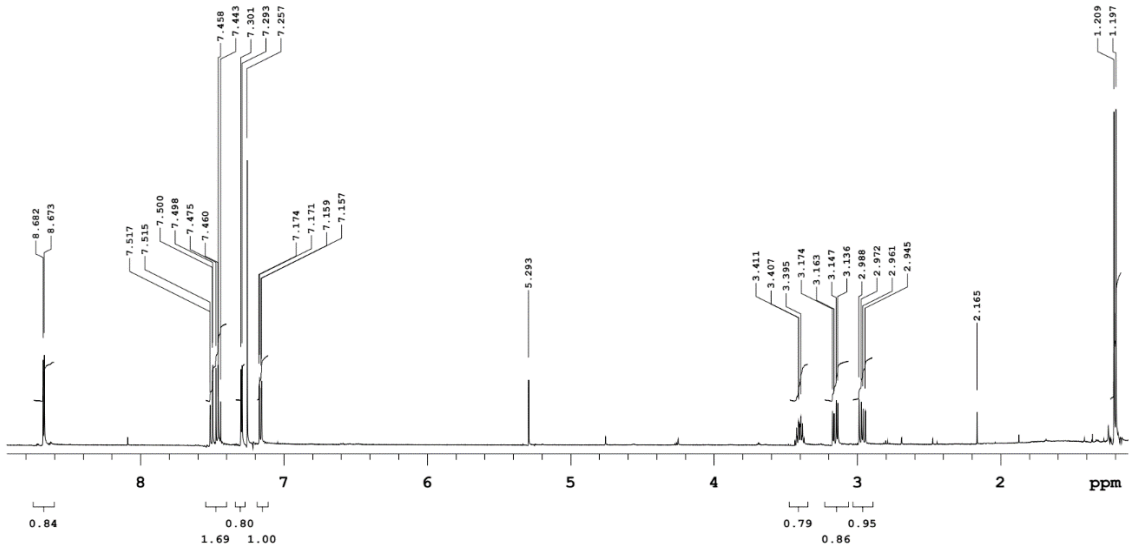

*Figure 128: [1]HNMR **MS11***

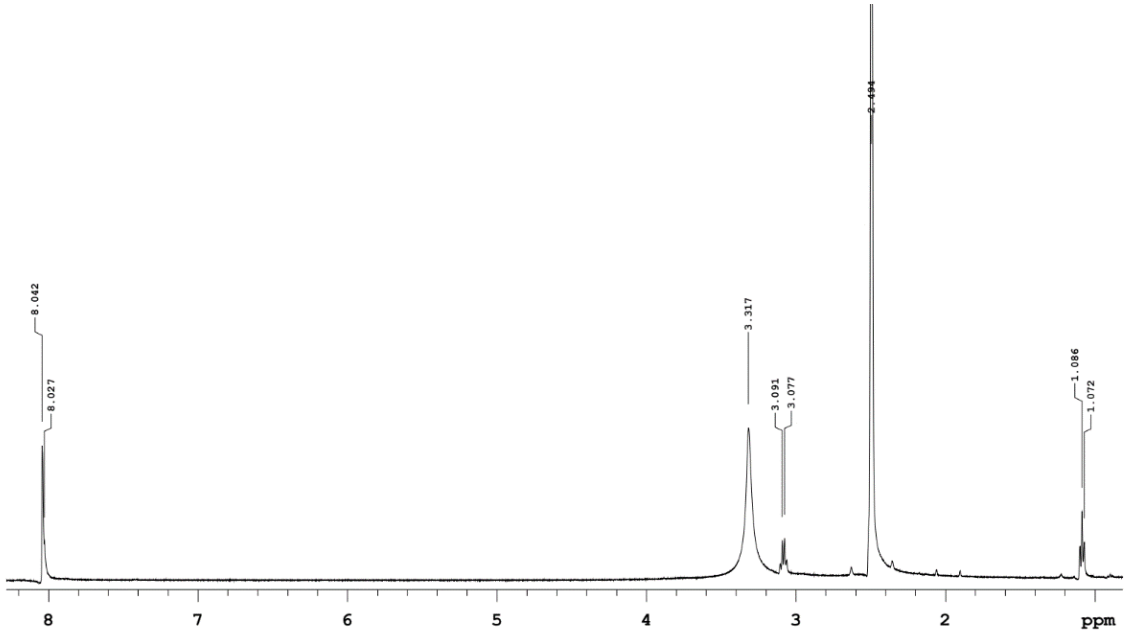

*Figure 129: [1]HNMR **MF4***

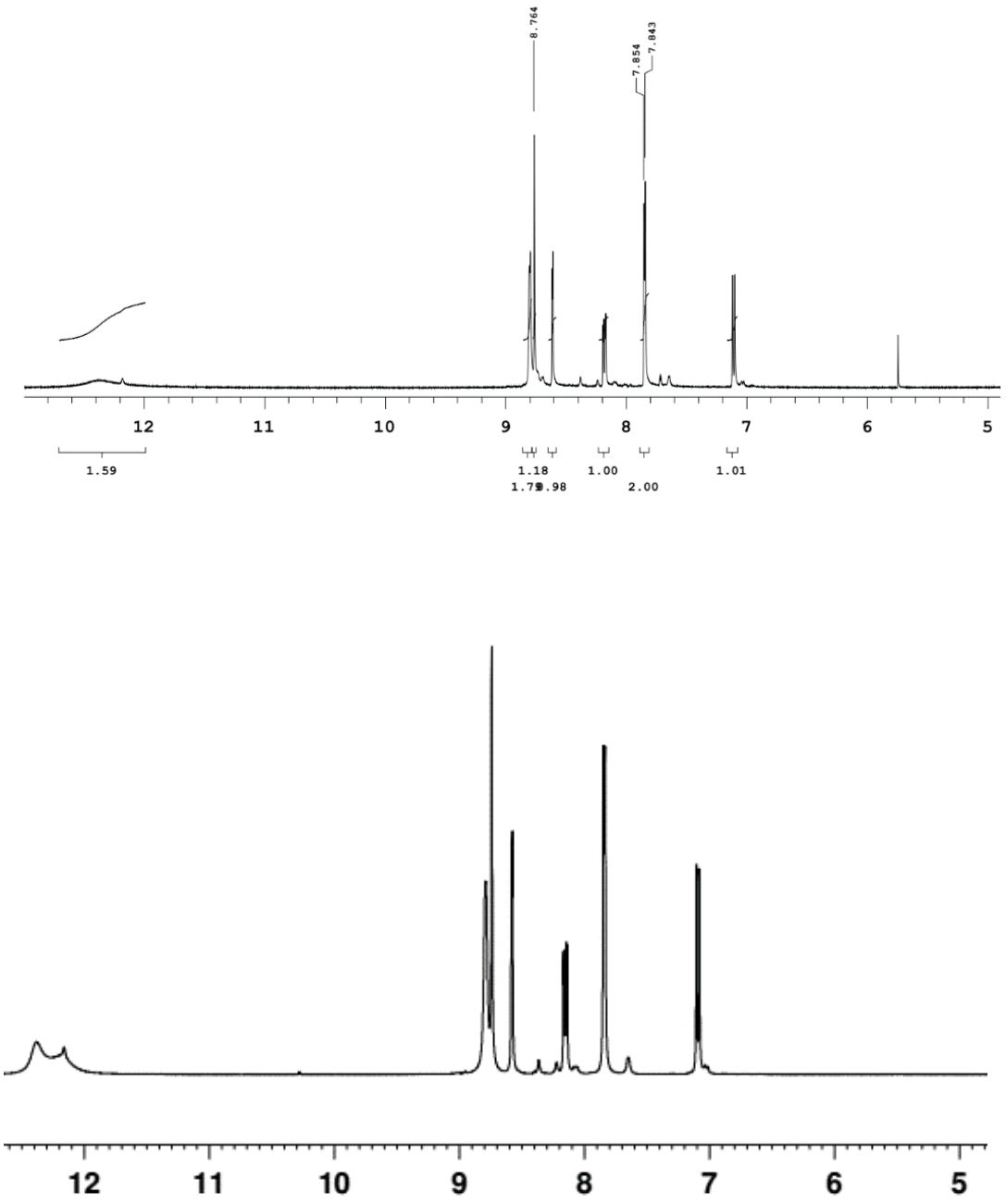

*Figure 130: Above is [1]HNMR for **MF9**, below is [1]HNMR that was reported by yuan et al.*

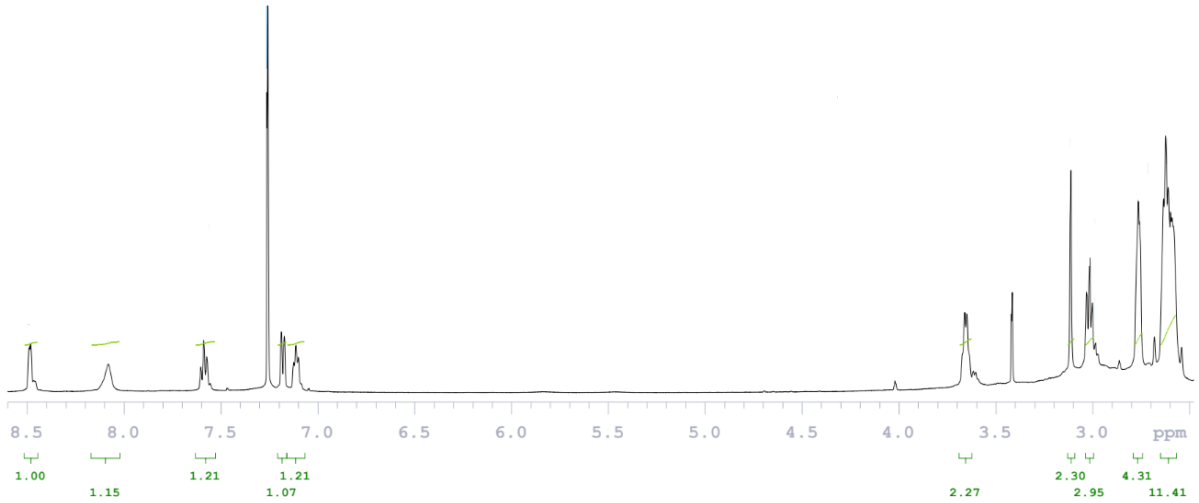

Figure 131: [1]HNMR for MS2